INTERACTIONS BETWEEN THE IMMUNE SYSTEM, INFLUENZA A VIRUS, AND BACTERIAL PNEUMONIA

by

Ericka Danielle Keef

B.S.B.M.E., Western New England University, 2011

Submitted to the Graduate Faculty of the

Kenneth P. Dietrich School of Arts and Sciences in partial fulfillment

of the requirements for the degree of

Doctor of Philosophy

University of Pittsburgh

2016

UNIVERSITY OF PITTSBURGH

DIETRICH SCHOOL OF ARTS AND SCIENCES

This dissertation was presented

by

Ericka Danielle Keef

It was defended on

April 4, 2016

and approved by

Dr. Gilles Clermont, Department of Critical Care Medicine, UPMC

Dr. G. Bard Ermentrout, Professor, Department of Mathematics

Dr. Christopher James Langmead, Associate Professor, Carnegie Mellon University

Dissertation Advisor: Dr. David Swigon, Associate Professor, Dept of Mathematics

INTERACTIONS BETWEEN THE IMMUNE SYSTEM, INFLUENZA A VIRUS, AND BACTERIAL PNEUMONIA

Ericka Keef, PhD

University of Pittsburgh, 2016

Influenza and pneumonia continue to be leading causes of morbidity and mortality in the United States each year. These pathogens can be lethal on their own, but they are particularly dangerous if encountered simultaneously in an influenza-pneumonia superinfection. The severity of the infection can be controlled by the strength of the host's immune response, which is often dependent on the age and species of the host. In this work, the intrahost immune response to respiratory infections is explored with mathematical modeling. We first examine how different species of mice react to an identical *Streptococcus pneunoniae* infection. A low-order ordinary differential equation (ODE) model is used to model data from four strains of mice, each of which represents a distinct phenotype in response to the infection. By changing only a small number of parameters, representing variations in the strength of the immune response, the output of the model can change significantly. We next examine the complementary study, in which the host species remains constant but the strain of bacteria administered is different. Again adjusting only a few parameters in our small ODE model, we can again reproduce several phenotypes of responses to these varied infections. We then examine the immune response to influenza infection. First, we develop a large ODE model to fit to data from mice infected with either a sublethal or lethal dose of H1N1. The model is the first of its kind to include a detailed study of the inflammatory response to infection. Next we use a Boolean network model to study data taken from adult and elderly mice infected

with influenza to assess differences in the immune response that arise with age. Finally, we propose an ODE model of influenza-pneumonia superinfection. In each of these five studies, we discuss the implications of our work for further experiments and identify potential avenues for future research.

TABLE OF CONTENTS

LIST OF TABLES

LIST OF FIGURES

LIST OF EQUATIONS

PREFACE

I would like to thank my committee for their support throughout my graduate school experience. First, thank you to David Swigon, for reading my resume as an undergraduate and seeing in it my potential for success as a graduate student. To Gilles Clermont, for providing funding and plenty of M&M donuts to get me through the 4+ years I spent as a grad student. To Bard Ermentrout, for attending to my meetings every single week and helping me to succeed, even though I was never technically your advisee. And finally, to Christopher Langmead, for allowing me a chance to be a teaching assistant twice and letting me give a guest lecture, solidifying my decision to focus my career on teaching.

I am forever grateful to my sweet husband Tyler for providing endless amounts of coffee, encouragement, and chocolate to get me through even the toughest parts of research.

To my parents Jeff and Sharon Mochan and my siblings Alyssa, Alexa, and Daniel for always encouraging and believing in my academic exploits.

To Lidia Pacira, who inspired this PhD in more ways than one. Rest in peace.

And finally, to Kristina Buschur and Tim Song, for innumerable coffee breaks together, providing a support system for which I will always be grateful.

1.0 INTRODUCTION

Mathematical modeling of biological systems has grown in recent years as larger biological data sets have become increasingly available. These models let us predict the behavior of physiological systems under a variety of conditions, allowing for the answers to questions which cannot yet be addressed using traditional experimental methods. This work focuses primarily on modeling the mechanisms through which the immune system responds to infectious respiratory disease, specifically influenza A virus and bacterial pneumonia infection. The following sections give an overview of the immune response to infection and the mathematical modeling tools with which we model these physiological processes.

1.1 IMMUNE RESPONSE TO RESPIRATORY INFECTION

The immune response can be divided into three parts: innate immunity, adaptive immunity, and humoral immunity. Each response has a distinct role in the resolution of an infection, involving different cells, cytokines, and receptors for its activation. This section outlines these three responses and their involvement in the resolution of a respiratory infection.

1.1.1 Innate immunity

Mechanical clearance of microbes from the host is among the first of the non-specific line of defenses of the body. The mucociliary elevator acts in the lungs to physically remove pathogens from the body via coughing and sneezing [1,2]. The flow of mucus tends to be comparatively slow, with an average speed of around 2 μm/s, and thus these nonspecific defenses can be easily overwhelmed if the bacterial population is large [3]. Epithelial cells will also release antimicrobial peptides, such as defensins, to inhibit the reproduction of the antigen [1].

The innate immune response is the second line of defense against infection. Innate immunity is always ready to act and does not act in an epitope-specific fashion. The primary components of an innate immune response are the soluble components, such as cytokines, chemokines, complement, and interferons, and cellular components, such as neutrophils, macrophages, dendritic cells, and natural killer (NK) cells [4]. These components act in a nonspecific manner against any microbe present in the host. Innate immune components are present constitutively in the body, and as such they are able to act very quickly when an infection begins.

One important element of innate immunity is phagocytosis, the killing of foreign agents in the body by cellular ingestion and lysosomal degradation. Neutrophils and macrophages are the primary effectors of phagocytosis, with neutrophils initially circulating in the blood and macrophages patrolling tissues. Once an infection has been detected, these cells will move via chemotaxis to the site of infection to increase immune defenses at that site. Chemotaxis is instigated by the upregulation of chemokines, such as interleukin (IL)-8 or macrophage inflammatory protein (MIP). These chemical messengers bring phagocytes and other immune cells to the site of infection. These cells, along with epithelial cells in the tissue, also release cytokines,

chemical messengers that activate the immune cells. Cytokines are classified as either pro-inflammatory or anti-inflammatory, depending on whether they activate or deactivate the immune cells. Cytokines like tumor necrosis factor (TNF) and IL-1 are common examples of pro-inflammatory cytokines, as they serve to increase inflammation locally. IL-10 is a common example of an anti-inflammatory cytokine and is used often in this work to inhibit further inflammation. Some cytokines, such as IL-6, can serve as either pro- or anti-inflammatory, depending on the specific cells with which they are interacting [5]. This system of checks and balances in the cytokine response helps to curb excess inflammation, which is linked to tissue damage, causing further symptoms in the host. Tightly regulated control of the inflammatory response is a vital part of survival of an infection, as we will see in Chapter 4 of this work.

Interferons are a type of cytokine particularly important for antiviral immunity. Type I interferons include all subtypes of interferon-α and interferon-β [6]. These interferons are secreted by a variety of cell types, including plasmacytoid dendritic cells (pDCs) and infected epithelial cells. These cells secrete interferon to help protect surrounding epithelial cells from infection. Interferon induces an antiviral state in a cell, protecting it from viral infection by initiating the production of two proteins: MXC and PKR. These proteins stop the cellular machinery from allowing transcription and translation of DNA, which prevents a virus from taking advantage of the cell and replicating itself [4]. Type II interferon, also known as interferon-γ, is released by natural killer cells and T cells [7–10]. Type II interferon helps to increase pathogen recognition, antigen presentation, and immunomodulation [7].

In addition to neutrophils and macrophages, NK cells and dendritic cells are also essential elements of the nonspecific immune response. Natural killer cells are so named for their innate ability to kill infected cells to control an infection. Dendritic cells are professional antigen-

presenting cells [11], acting as a link between the innate immune responses and the later adaptive immune responses. In lung tissue, dendritic cells form a tightly regulated network of sentinel cells, recognizing antigen and adjusting the ensuing immune response to levels necessary to ward off infection [11–14].

1.1.2 Adaptive immunity

The adaptive immune response is characterized by the actions of T cells and B cells. These cells are lymphocytes which cannot carry out their antiviral activity until they have clonally expanded and differentiated. In a viral infection, the T and B cell immune responses primarily target infected cells and free virus particles. T cell-mediated immunity is an important source of clearance of infected cells; killing these cells helps prevent further viral replication and keeps the infection in check [4]. There are two types of T lymphocytes that play a major role in this work: CD4+ T helper cells (T_H cells) and CD8+ cytotoxic T cells (CTLs). CTLs kill other cells infected with foreign matter. T_H cells work to activate T and B lymphocytes to generate the adaptive immune response, and they also produce important cytokines to help regulate the innate immune response [4]. T_H cells can be divided into two groups: T_H-1 cells and T_H-2 cells. T_H-1 cells primarily secrete IL-2, IL-12, and interferon-γ, promoting further cytotoxic responses. T_H-2 cells primarily secrete IL-4, IL-5, IL-9, IL-10, and IL-13, all of which can control inflammatory responses.

B cell-mediated immunity is also known as *humoral immunity*, and it is predominantly defined by actions of antibodies produced by plasma cells. When a resting B lymphocyte is activated through its B cell receptor, it is stimulated to differentiate into a plasma cell. These plasma cells produce immunoglobulins which neutralize virus particles in a viral infection.

1.2 MATHEMATICAL MODELING OF PHYSIOLOGICAL SYSTEMS

The complex series of immune response interactions described above are modeled in this work with either a series of differential equations or a network model, depending on the problem which we seek to solve. The difficulty in developing mathematical models lies in the ability to generate a model structure to replicate biological phenomena given a particular data set. Much of this process depends on the values assigned to parameters of the model. The inverse problem is solved by identifying parameter sets of the model which replicate the given data [15]. Inferring the parameters from the data is an ill-posed problem, meaning it does not yield a unique solution and is not statistically identifiable [16]. A well-posed problem would involve a large amount of experimental data, and would allow us to ascertain a single parameter set which would minimize the error associated with this data. However, uncertainty in both the parameter values and the experimental data lead us to use a probabilistic approach to the inverse problem.

Traditional parameter fitting algorithms involve finding a single parameter set that minimizes the objective function. A single parameter set may not adequately describe a true biological phenomenon, however. Many biological data sources, including those used in this work, are derived from a pool of measurements collected from different hosts subjected to identical experimental conditions. Because smaller animal hosts like mice need to be sacrificed in order to properly measure all the data, these animals cannot be followed for the full length of the experiment, making true longitudinal data impossible to generate. Larger animal hosts like pigs or nonhuman primates can be used to generate longitudinal data, but these experiments are quite expensive by comparison. For this reason, smaller animal models are often used, and multiple animals are sacrificed at pre-determined times and measured for the variables of interest. These experiments assume that animals of the same species undergoing identical infections would react

very similarly. Inter-individual variability in the hosts can lead to large differences in the measurements between these hosts, however, invalidating this assumption.

To mitigate this problem, Bayesian parameter inference is commonly used to compute a distribution of values in which the parameters of the model may exist [15,17–22]. This probability density of distribution describes the likelihood of a parameter set taking on a particular value. The distribution is meant to incorporate the behavior of an entire population, not just of one individual. For this reason, Bayesian inference may be more appropriate to describe the pooled data than a single parameter set would be.

Bayesian parameter inference yields the posterior probability density, which is defined as the probability that the model has a particular parameter set given the data. Thus we are choosing parameters most likely to make the model fit well to the data. The calculation of the posterior distribution depends on the definition of the prior distribution of the parameters, or the information known about the parameters' values before the experimental data are considered [22]. For the purposes of this work, the prior distributions of all parameters are taken to be a uniform distribution in log space between the upper and lower bounds of each parameter [23]. Bounds are typically defined from biological references where possible, and estimated for parameters unable to be directly measured in experiments.

We sample from within these parameter bounds to yield the collections of parameter sets which comprise the distributions and make up an *ensemble* of models. Each parameter set is applied to the system of differential equations used to the model the given experimental data, and the output is a potential predicted trajectory of each variable of the model. The likelihood that a particular parameter set occurs in the posterior distribution is equivalent to the likelihood that the

corresponding predicted trajectory has contributed to the experimental data. Thus, ensemble modeling allows us to account for the uncertainty in the data.

1.3 OVERVIEW

First, mathematical models of the intrahost immune response to bacterial pneumonia caused by *Streptococcus pneumoniae* are explored. Ordinary differential equation (ODE) models are used to simulate the trajectories of the bacterial count and phagocytic cell response. Both host organism and bacterial strains are varied to determine the impact of each on the outcome of the infection.

The intrahost immune response to influenza infection is next investigated using two different types of models: ODE and Boolean. Two age groups and two inocula are tested so that conclusions may be drawn as to the effectiveness of a host's immune response to varied amounts of virus as the host ages. First, a large-scale ODE model is used to simulate a detailed look at both branches of immunity. Then, a Boolean network model is used to study and contrast the interactions between various immune components in both older and younger hosts.

Finally, a *superinfection* of influenza A virus and bacterial pneumonia is explored *in silico*. A superinfection is defined as an infection in which the first infectious agent is not fully cleared from the system before a second infectious agent is introduced. We investigate hypotheses as to the mechanisms responsible for the increased likelihood of morbidity and mortality associated with influenza-pneumonia superinfection, and we also study the lethal synergism between these two pathogens.

2.0 EFFECT OF HOST SPECIES ON INTRAHOST IMMUNE RESPONSE TO BACTERIAL PNEUMONIA INFECTION

2.1 OVERVIEW

The seriousness of pneumococcal pneumonia in mouse models has been shown to depend both on bacterial serotype and murine strain. We here present a simple ordinary differential equation model of the intrahost immune response to bacterial pneumonia that is capable of capturing diverse experimentally determined responses of various murine strains. We discuss the main causes of such differences while accounting for the uncertainty in the estimation of model parameters. We model the bacterial population in both the lungs and blood, the cellular death caused by the infection, and the activation and immigration of phagocytes to the infected tissue. The ensemble model suggests that inter-strain differences in response to streptococcus pneumonia inoculation reside in the strength of nonspecific immune response and the rate of extrapulmonary phagocytosis. This work has been previously published in Journal of Theoretical Biology [24].

2.2 BIOLOGICAL OVERVIEW

Pneumonia is the most significant cause of death of children worldwide, killing over one million children under the age of five every year, mostly in developing countries [25], and is the most prevalent infectious disease in the elderly in developing countries [26], often complicating respiratory viral infections. Pneumonia is an inflammatory condition of the lung affecting

primarily the alveoli, caused by bacterial or viral infection, or to a lesser extent other micro-organisms or chemicals. *Streptococcus pneumoniae*, also known as pneumococcus, is the most common cause of bacterial pneumonia [25]. Pneumococcus is estimated to permanently colonize the upper respiratory system of about 10% of adults and 20 – 40% of children [27]. While the bacteria remain in the nasal cavities, carriers do not show signs of infection and are not considered to be ill. Pneumonia begins when bacteria move from the upper to lower respiratory tract and grow, which may or may not be contained by the ensuing immune response.

The first line of defense against microbes in the upper respiratory tract is the mucociliary layer, which can mechanically clear bacteria via directed mucus flow [2] or the production of antimicrobial peptides [1]. Mucociliary flow is rather slow (about 2 μm/s), and pneumococcal strains have been found to impair the flow by disrupting the F-actin cytoskeleton of epithelial cells [3], so larger bacterial challenges can overwhelm the mechanical defenses. Once pneumococci reach the lower respiratory tract, they will adhere to the epithelial cell surface via platelet-activating factor receptor [28], which is quickly internalized by the cell together with the bacteria. The bacteria damage the host epithelial cells primarily via the action of pneumolysin, a pore-forming cytotoxin that is lytic to the cells at sufficiently high concentrations [2]. A pneumolysin-deficient pneumococcus mutant is less likely to cause lethal infection than wild type and reaches overall lower levels in both lung and blood [29]. Once the epithelial cell wall is disrupted, the bacteria can cross into the bloodstream.

Alveolar macrophages are the first immune cell type to recognize and phagocytose low numbers of pneumococci [30,31]. If the pneumococcal population grows quickly, macrophage phagocytic activity can be overwhelmed. Macrophages also orchestrate the inflammatory response by producing pro-inflammatory cytokines such as Il-1 or TNF-α, which are involved in the

recruitment of neutrophils and other phagocytic cells [31]. Neutrophils are the primary phagocytic agent for clearing the infection. [32]. They are activated in the blood and then move toward the infected tissue, and though they will digest bacteria found in the bloodstream along the way, most of their work will be performed in the tissue. Once in the bloodstream, pneumococcus can cause bacteremia and spread to other tissues, a particularly deadly complication of localized infection. Extrapulmonary phagocytosis in the blood is an important factor in determining survival or nonsurvival in response to infection [33]. Once bacteria are cleared from the lung, newly recruited macrophages enter the alveoli to clear neutrophils and cellular debris [34,35]. Macrophages themselves then apoptose after phagocytosis [36].

The purpose of this study is to use a model-based approach to provide insight as to why distinct murine strains elicit distinct phenotypes in response to the same load of an identical strain of pneumococci. It has been observed, for example, that when infected by D39 strain, CBA/Ca and MF1 mice succumb to the infection after 1 – 2 days, while the BALB/c and C57BL/6 mice are generally able to overcome the infection quickly [37–39] Moreover, the progression of infection in the lung differs from a mild increase (CBA/Ca), to a decline followed by sharp increase (MF1), to a constant level followed by a decline (BALB/c), to a sharp decline (C57BL/6). In particular, the origin of a sharp increase following the decline in MF1 strain has not yet been satisfactorily explained [29]. In this chapter, we will employ mathematical modeling techniques to explain what facets of the immune response are primarily responsible for these four different phenotypic responses to identical bacteria.

2.3 LITERATURE REVIEW

Previous work in the intrahost response to pneumonia has led to several ODE models. Smith et al. used models of increasing complexity to model the intrahost immune response of BALB/c mice to three initial doses of pneumonia [40]. These models divide the immune response into three successive stages: resident alveolar macrophage response, neutrophil and cytokine response, and recruited monocyte-derived macrophage response. Using a single equation to model the alveolar macrophage response, a low inoculum of bacteria can be cleared. Adding in complexity with recruited neutrophils and macrophages, the authors develop a target cell-limited model of pneumonia infection. The more complex model can clear higher doses of bacteria from the system, but at a cost of depleting the susceptible cell population. The model is fit to only one host species and one pathogen species, but it could be generalized to other bacterial infections by changing the value of the parameters.

Another study by Romanyukha et al. used ODEs to study the amount of energy required by the human body to clear an infection [41]. A host must expend energy not only to fight an infection, but also to maintain homeostasis. These authors found the maintenance of a fever is the greatest energy cost, followed by the maintenance of phagocytic cells.

Pilyugin and Antia studied the influence of the handling time, or time required to complete ingestion of bacteria, of phagocytic cells [42]. The model operates under the assumption that the time required for phagocytosis to occur can hinder the overall effectiveness of immune cells against the pathogen, particularly if the number of recruited cells is low. The equations and parameters of their model are not specific to any species but provide guidance as to how to incorporate this handling time into simple ODE models.

All of these previously published studies focus on different aspects of the immune system and provide parameters based on experimental data for a single combination of bacterial and mouse strains. Thus, characterizing distinctive immune response across strains using a model-based approach has not been previously attempted. None of the models differentiate between bacteria in the lung and bacteria in the blood, a feature that we find especially important for description of various types of responses.

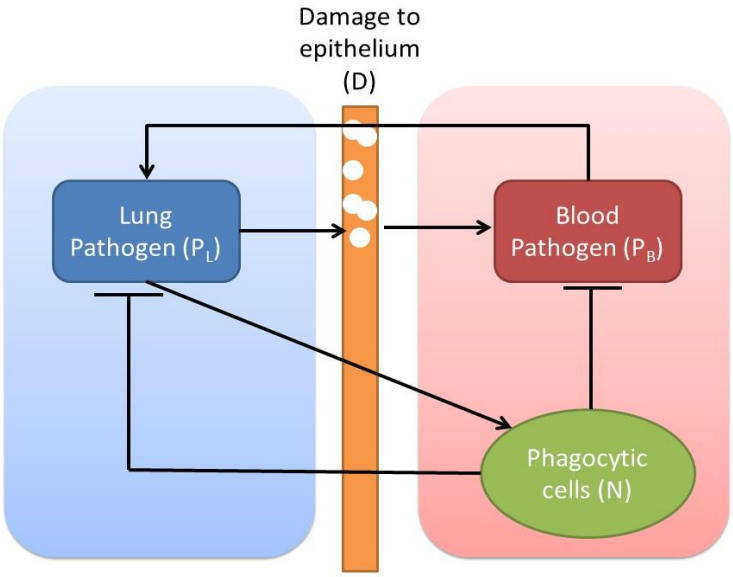

Figure 1. Graphic representation of the interactions between the bacteria and the host.

2.4 MODEL DEVELOPMENT

The four equations comprising the ODE model represent interactions between the bacteria, the host tissue, and the immune system, as shown in Figure 1. The model simulates four variables:

bacteria levels in the lungs (P_L), bacteria levels in the blood (P_B), activated phagocytic cells (N), and damage to the lung epithelium (D).

2.4.1 Bacteria equations

$$\frac{dP_L}{dt} = k_l P_L - \frac{\nu P_L}{\mu + P_L} - \frac{\xi_{nl} N P_L}{1 + \xi_2 P_L} + f[(bD + a)P_B - bDP_L] \quad 2.1$$

$$\frac{dP_B}{dt} = k_b P_B \left(\frac{P_B - \varepsilon}{P_B + \varepsilon}\right)\left(1 - \frac{P_B}{K}\right) - \frac{\xi_{nb} N P_B}{1 + \xi_2 P_B} - (bD + a)P_B + bDP_L \quad 2.2$$

Equation 2.1 represents the bacterial population in the lungs (P_L). Lung bacteria grow at a constant rate of k_l. Two terms represent the impact of the immune system on the lung bacteria population. First, a saturating term expresses the rate at which the nonspecific immune response initially controls the bacteria levels in the tissue. Parameters ν and μ control these dynamics, which represent responses such as the mucociliary elevator and complement-driven removal of bacteria. These parameters are tuned such that they can lead to the eradication of the bacteria from the lungs without the influx of neutrophils. However, if the initial burden of bacteria is too high, other immune responses will be necessary to clear the body of infection. The third term in the equation denotes the effect of immune cells (N) on the bacterial population. Immune cells phagocytose the bacteria at a rate ξ_{nl}. Higher rates of phagocytosis are more likely to fully clear the bacteria from the lung tissue.

The last two terms in the equation describe the effects of exchange between the lung and blood pathogen populations. Parameter f represents the volumetric difference between the blood and lung compartments. Blood bacteria (P_B) can move from the bloodstream back to the lungs in two ways: damage-dependent motion and damage-independent motion. Parameter b represents the

permeability of the epithelial membrane to the bacteria, which is determined by the level of damage (D) in the tissue. Parameter a represents the damage-independent motion of the blood bacteria into the lung compartment. Bacteria circulating in the bloodstream exhibit a tendency to attach to capillary walls in the lung tissue and concentrate at this location [43], so parameter a denotes this increased probability of bacteria moving from blood to the tissue. The final term ($-bDP_L$) denotes the movement of the bacteria in the lung to the bloodstream, which is a damage-dependent motion.

Equation 2.2 denotes the change in blood pathogen (P_B) over time. Equation 2.2 has a similar structure to Equation 2.1, but with a few key differences. Blood bacteria grow logistically at a rate k_b, limited by the carrying capacity K and the Allee threshold ε. Blood pathogen is removed by phagocytes in the blood at a rate ξ_{nb}, proportional to the pathogen population. Like the previous equation, the final terms describe damage-dependent and damage-independent motion of bacteria between the two compartments.

There is no logistic growth term necessary in the lung bacteria equation, as the bacterial data used in this study never approach carrying capacity in the lungs. However, bacteria in the blood do seem to reach carrying capacity as they extravasate to other organs. Bacteria also tend to grow more quickly in the nutrient-rich environment of the blood as compared to the relatively sterile environment of lung tissue. Thus, two different bacterial growth terms are used to justify differences in bacterial reproduction in each compartment.

2.4.2 Damage equation

$$\frac{dD}{dt} = qP_L(1 - D) - cD \qquad 2.3$$

Equation 2.3 describes the increase in damage to the lung epithelium as a result of bacterial infection. When bacteria interact with epithelial cells, they release toxins such as pneumolysin, causing cell apoptosis. In this model, these interactions occur at a rate q, proportional to the amount of bacteria present in the lung. The host can repair this damage at a rate c. Damage is meant to represent a percentage of the epithelial tissue injured by the pathogen, and as such it varies only between 0 and 1.

2.4.3 Immune cells equation

$$\frac{dN}{dt} = \left(-N + \frac{hP_L}{n_h + P_L}\right)\left(\frac{1}{\tau_N}\right) \qquad 2.4$$

Equation 2.4 describes the change in the lung population of activated phagocytes (primarily composed of neutrophils). Parameter τ_N denotes the time to activation of the phagocytes, and this activation is proportional to the population of lung bacteria. Activation occurs with Michaelis-Menten dynamics, with a rate constant of h and a half-maximum of n_h. In reality, this activation is a much more complicated mechanism, involving pro-inflammatory cytokines and receptors on the surface of the immune cells. For the sake of simplicity, we do not model these cytokines explicitly, but instead assume they would be produced proportionally to the bacteria present.

2.4.4 Model parameters

Table 1 summarizes the 17 model parameters and their biological interpretations, as well as the bounds and units for each of their values.

Table 1. Biological interpretation of bacteria ODE model parameters.

Parameter	Meaning	Units	Bounds
τ_N	Time to activation of phagocytes	hours	0.01 – 10
n_h	Steady-state value of phagocyte population	cells	10^2 – 10^4
μ	Michaelis-Menten rate of nonspecific immunity	CFU/ml	10^5 – 10^7
ξ_2	Inhibition of phagocyte phagocytosis	ml/CFU	10^{-13} – 10^{-11}
h	Activation of phagocytes due to P_L population	cells/CFU/ml	10^5 – 10^8
K	Carrying capacity of blood pathogen	CFU/ml	10^7 – 10^8
k_l	Growth rate of pathogen in lung tissue	$hour^{-1}$	0.1 – 5
k_b	Growth rate of pathogen in blood	$hour^{-1}$	20 – 40
q	Rate of increase of damage due to P_L	$hour^{-1}$	10^{-9} – 10^{-7}
ε	Threshold value of P_B	CFU/ml	1 – 10
a	Directionality of movement from P_B to P_L	$hour^{-1}$	0.1 – 10
f	Volumetric ratio	dimensionless	10 – 50
b	Effect of D on movement rates	$hour^{-1}$	0.01 – 10
v	Rate of clearance of P_L by nonspecific immunity	CFU/ml/hour	10^4 – 10^9
ξ_{nl}	Rate of phagocyte phagocytosis in lung tissue	$cell^{-1}$ $hour^{-1}$	10^{-9} – 10^{-4}
ξ_{nb}	Rate of phagocyte phagocytosis in blood	$cell^{-1}$ $hour^{-1}$	10^{-9} – 10^{-4}
c	Rate of repair of damage	$hour^{-1}$	0.01 – 1

Parameters for this model can be divided into two groups: mouse-strain-independent, and mouse-strain-dependent. Four of the seventeen parameters fall into the mouse-strain-dependent group: h, the rate at which phagocytes migrate to lung tissue; ν, the rate at which pathogen is cleared from the lungs by non-specific immunity, and ξ_{nl} and $\xi_{nb,}$ the rate at which phagocytes clear pathogen from lungs and blood, respectively. These are defined as the parameters which will differ between each type of mouse examined in this study, and as such, these are the parameters that will be responsible for creating the four different phenotypes seen in the experimental data used.

The parameters defined as strain-independent are those which would not necessarily change with host species. These include parameters inherent to the bacteria (bacterial growth rates k_l and k_b as well as carrying capacity K), steady-state and threshold parameters ($\varepsilon, \mu, n_h, \xi_2$), phagocyte activation time constant τ_n, and parameters controlling bacterial infiltration of the lung (b, f, a, q, c).

The bounds on each of these parameters were defined in biological ranges where literature values could be ascertained, and approximated for the other parameters. Bacterial growth parameters were approximated from doubling times reported in both tissue and blood [44,45]. The phagocyte activation rate was also estimated from literature [46]. Most other parameters were allowed to vary over two orders of magnitude. Sampling was performed across log space. The four strain-dependent parameters were given very wide ranges such that their behavior could be more fully understood.

2.4.5 Initial conditions of the system variables

Since the simulations begin just as the bacteria reach the lung tissue, it is assumed that there is no appreciable damage in the lungs initially, and no activated phagocytes have yet made their way to the tissue. There is also no bacteria in the blood initially. The only non-zero initial value therefore is the initial condition for P_L, which is equal to the dose given to the mice in each experiment (10^6 CFU for the CBA/Ca, MF1, and BALB/c mice, and 10^5 CFU for the C57BL/6 mice).

For the purposes of model fitting, the activated neutrophil data must be assumed to be zero at day 0. The initial value of *N* data, therefore, is subtracted from all subsequent data points, such that each have been shifted down by N_0.

2.5 MARKOV CHAIN MONTE CARLO SAMPLING PROCEDURE

As in Battogtokh et al. [47] we use Bayesian inference to estimate the likely values of the parameters of the system. If **p** represents the list of all parameters and **y** represents the vector of the data, then the posterior distribution $\rho(\mathbf{p}|\mathbf{y})$, reporting on the probability that the system has parameters **p** given the data **y,** is given by the Bayes formula $\rho(\mathbf{p}|\mathbf{y}) = Q^{-1}L(\mathbf{y}|\mathbf{p})\theta(\mathbf{p})$ where $L(\mathbf{y}|\mathbf{p})$ is the likelihood of observing **y** for a model with parameters **p**, $\theta(\mathbf{p})$ is the prior distribution based on information about the parameter distribution available before the data is collected, and $Q = \int L(Y|\mathbf{p})\theta(\mathbf{p})$ is the normalizing constant. The likelihood function used in the generation of posterior distribution is the exponential of the negative sum of squared errors, i.e.

$$L(Y|\mathbf{p}) = \exp\left(-\sum_{i,j}\frac{(\bar{y}_{i,j} - y_{i,j})^2}{2\sigma_{i,j}^2}\right) \quad 2.5$$

where $\bar{y}_{i,j}$ is the mean of variable j at time i, and $\sigma_{i,j}^2$ is its standard deviation. For prior distribution $\theta(\mathbf{p})$ we choose a product of uncorrelated bounded Jeffreys prior distributions for p_i which are equivalent to uniform distributions for $\log(p_i)$ between 0.01 and100 times a biologically reasonable logged baseline value .

Three heuristics were also added to the likelihood function to ensure biologically relevant solutions were found. First, we require that the system is stable with no pathogen, meaning the healthy state is stable. We also require complete clearance of bacteria at a low inoculum of 10^2 CFU/ml within 2 days post inoculation. Lastly, for the BALB/c mice, the system must be able to clear lung pathogen within 2 days post inoculation at an inoculum of 10^5 CFU/ml. Smith et al., [40] showed this to be true experimentally, so we use this requirement as well. If a parameter set does not fulfill any of these heuristics, a large penalty is added to the overall cost, essentially eliminating any chances this parameter set will be accepted.

A sample of parameter sets which represents the posterior distribution $\rho(\mathbf{p}|\mathbf{y})$ over the parameter space was found by using the Metropolis-Hastings Monte Carlo method (MHMC) (sometimes also called Markov Chain Monte Carlo). We generate parameter sets for all strains of mice simultaneously, with **p** consisting of 13 strain-independent parameters that are applied to all 4 strains' parameter vectors, and four sets of 4 strain-dependent parameters, one for each strain. This results in a total of 29 parameters generated at every step of the simulation. The error is calculated for each strain's fit, and the likelihood $L(\mathbf{y}|\mathbf{p})$ is taken to be the product of likelihoods of individual strain fits.

To facilitate full sampling of the 29-dimensional space, we use a parallel tempering technique [48–50], in which chains move through parameter space in steps analogous to their assigned energies, with larger steps taken at higher energies. We generated two million parameter sets and tested convergence of the chains with a Gelman-Rubin diagnostic [51] and a Geweke test [52].

2.6 EXPERIMENTAL DATA

The model was calibrated to data from literature [37–39], in which female mice of four strains (CBA/Ca, MF1, BALB/c, and C57BL/6) were intranasally infected by *Streptococcus pneumoniae* strain D39. D39, a serotype 2 strain of *Streptococcus*, is known to be particularly virulent in murine models of pneumonia, and as such it is often employed as the infectious agent in these studies. These studies provided data for the bacterial population in the lungs post-infection, and all but one study (C57BL/6) also provided data for neutrophil counts and bacteria levels in the blood.

BALB/c is an inbred albino mouse strain mainly used for hybridoma development, monoclonal antibody production and infectious disease studies. The CBA/Ca strain is commonly used for brain development, neurochemistry, and behavioral studies. The MF1 strain is suitable for general use in toxicology, pharmacology, physiology, and behavioral science. C57BL/6 strain is used for diet-inducing obesity, transgenic/knockout model development, safety and efficacy testing, and immunology. All four strains have very different origins, and it is therefore not surprising that they should exhibit contrasting phenotypes under challenges they were not specifically engineered to withstand [53]. CBA/Ca are the most susceptible to infection, as they succumb to the infection about 24 hours post inoculation and exhibit no appreciable decrease in

bacteria levels in either the lung or blood compartment. MF1 are moderately susceptible mice. In the first twelve hours, these mice are able to mount a defense in the lung tissue through nonspecific immunity, but the blood pathogen levels rise too quickly for the phagocytes to control. MF1 mice are known to die about 48 hours post inoculation.

C57BL/6 and BALB/c mice are resistant to the infection at these inocula. Female C57BL/6 mice are able to keep lung pathogen levels under control immediately, clearing the infection within 24 hours post inoculation. Only lung pathogen data was available for this strain, and we have only 48 hours of data from the experiment. BALB/c mice are also able to survive their challenge to the end of the seven day experiment.

2.7 ENSEMBLE FITS OF MODEL TO DATA

Model ensembles for each strain comprised two million parameter sets. Figure 2 shows the ensemble trajectories for each of the four strains. The solid black line represents the median value, at a given time point, of all trajectories computed from parameter sets comprising the ensemble, not any particular or best fitting trajectory. The darker shadowed area corresponds to the interval between 25th and 75th percentile of trajectory values, and the lighter outside shadows the interval between 5th and 95th percentile. The data and their standard deviations are also displayed.

The most variation seen in the CBA/Ca mice tends to occur in the overall level of damage. The other trajectories are tight, as the bacteria levels will rise quickly and settle at the carrying capacity by day 2. The model predicts that these mice should show the most damage to the epithelium, as would be expected given their high morbidity. In the first twelve hours, pathogen levels remain relatively constant as a result of the nonspecific immunity. High pathogen levels in

tissue encourage movement to the blood, where bacteria reproduce rapidly. Simultaneously, pathogen increases in the lung due to the infiltration through the damaged epithelium, leading to high sustained pathogen levels in both compartments. Since phagocyte levels are proportional to lung pathogen, the phagocyte trajectories are also tight and held essentially constant over the seven day simulation. In experiments, CBA/Ca mice were found moribund within 24 hours post inoculation.

MF1 mice are also killed by pneumococcus, but infection evolved more slowly following inoculation. We see an initial decay in P_L levels as the nonspecific immunity in the lung fights the initial dose of bacteria and the remaining bacteria invade the tissue and the blood. Then, as P_B levels rise, the pathogen will infiltrate back into the lungs and will enter a phase of uncontrolled reproduction. The phagocytes are not strong enough to overcome the infection, and mice die, despite the high level of activated phagocyte levels.

The BALB/c and C57BL/6 mice were both able to overcome the infection. BALB/c mice controlled the blood pathogen levels during the full course of the infection. The peak of P_B is several orders of magnitude lower for BALB/c than either the MF1 or CBA/Ca. The majority of P_L and P_B trajectories generated for the BALB/c ensemble will decay to zero eventually, though some will stay at a chronic level. Endpoints of the trajectories are largely influenced by the strength of parameters directing movement between tissue and blood in these populations; those with strong tendencies for infiltration will tend to be unable to clear the infection. Lung bacteria populations are also largely dependent on blood bacteria, given that tissue infiltration is the major contributing factor to P_L levels. BALB/c mice also show little damage since the bacterial levels are brought under control so quickly.

The C57BL/6 trajectories show little variation, given the few data points available for this strain. The data show lung bacteria clearance by 24 hours post inoculation, and because of this rapid clearance, there is no appreciable blood bacteria and no tissue damage. Phagocytes are the only factor showing variation in the ensemble. Phagocyte levels are proportional to lung pathogen by a factor of h. The width of this ensemble reflects the width of the posterior distribution on h for C57BL/6 mice.

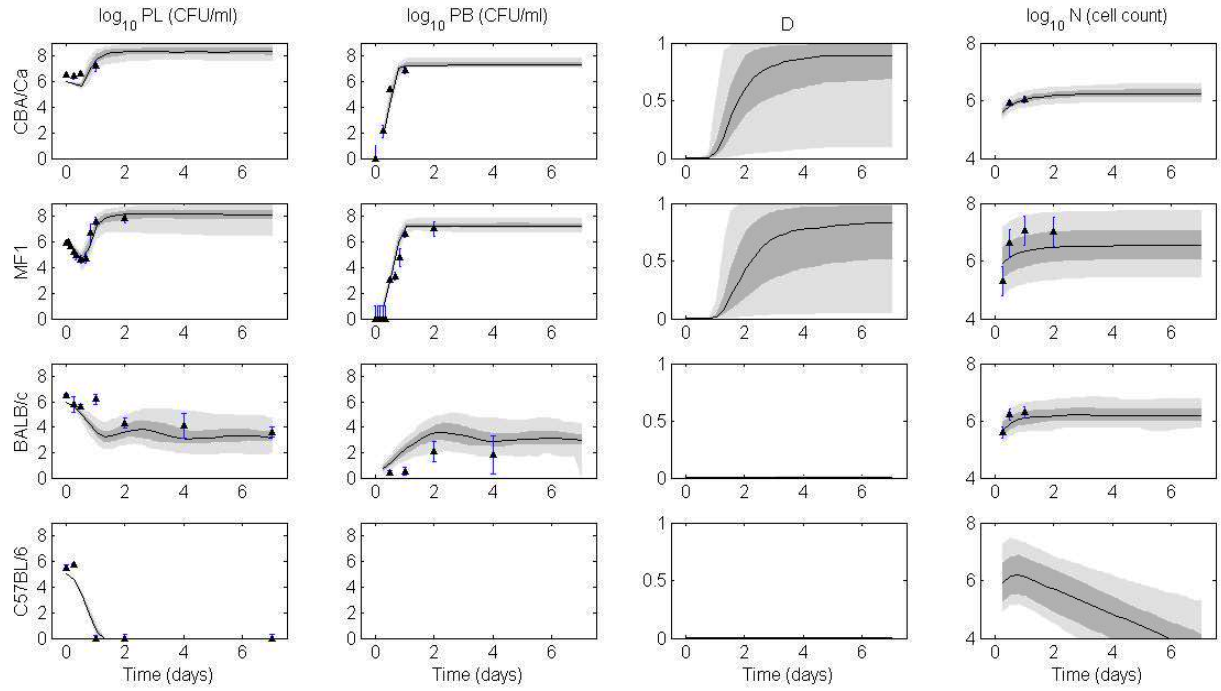

Figure 2: Ensemble fits of each murine strain for lung pathogen (PL), blood pathogen (PB), epithelial damage (D), and activated phagocytic cells (N).

The black line represents the median trajectory, the inner dark gray area represents the 25th to 75th quantiles of trajectories, and the outer light gray envelope represents 90% of the trajectories (5th to 95th quantiles). Data points with standard deviations are represented by the black triangles with error bars. Trajectories are simulated over 7 days, with infection occurring on day 0. Each row denotes the ensembles for a different strain of mouse: CBA/Ca, MF1, BALB/c, and C57BL/6, respectively.

2.8 POSTERIOR DISTRIBUTIONS OF PARAMETERS EXPLAIN FOUR PHENOTYPES IN DATA

2.8.1 Full marginal distributions

To characterize the ensembles generated for each of the four murine strains, the full marginal posterior distributions for each parameter are analyzed and compared. These distributions are plotted as histograms of the value which each parameter takes on in the fitting procedure. Figure 3 shows the one-dimensional parameter distributions of the strain-independent parameters of the model. The left and right sides of the plots are the lower and upper bounds of each parameter, respectively, as defined in Table 1. These parameter distributions are identical for all 4 murine strains used in this study.

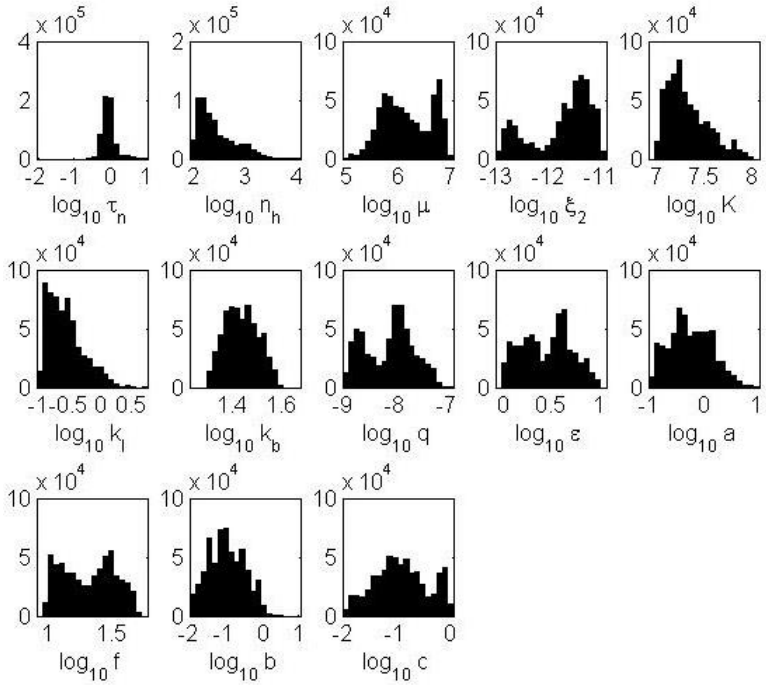

Figure 3: Full marginal parameter distributions of strain-independent parameters.

The parameter distributions for the strain-dependent parameters are shown in Figure 4. Each row represents one strain of mouse, and each column corresponds to one parameter. Comparing down a column shows how different these distributions can be between the four phenotypes studied here. Column 1 shows the distributions for parameter h, the rate at which the immune cells are activated in response to presence of bacteria. C57BL/6 mice (bottom row) tend to exhibit a high rate of phagocyte activation, while each of the other three strains show a similar and lower h distribution. The data for the C57BL/6 mice did not include neutrophil counts. However, there is a sharp decrease in bacteria counts in the lungs almost immediately after the onset of infection. It is likely that this decrease is caused, at least in part, by a high number of activated phagocytic cells present in the tissue.

The h distribution for the BALB/c mice had an average value of $3.4\ x\ 10^6$ cells/CFU/ml, while the average for the CBA/Ca mice was $2.1\ x\ 10^6$ cells/CFU/ml. The source of the data for these two strains [38] reports that BALB/c did exhibit a higher overall rate of neutrophil influx than did the CBA/Ca mice, which aligns with our findings.

Figure 4, column 2 shows the distributions for the parameter ν, the rate of mechanical clearance of lung pathogen. These posterior distributions can be divided into two subgroups: those with a higher ν (MF1 and BALB/c) and those with lower ν values (CBA/Ca and C57BL/6). Data for MF1 mice show a strong decay of lung bacteria in the first twelve hours post-infection, likely controlled by ν. BALB/c mice also exert strong control over the bacteria in the first twelve hours, again showing the importance of these nonspecific defenses in resistance to bacterial infection. Interestingly, C57BL/6 mice have the lowest overall ν values, despite the quick decay of lung pathogen values seen in these data. The immune cell response must then be strong enough to

eradicate the bacteria levels without the need for much other intervention via nonspecific immunity.

The final two columns describe the posterior distributions of ξ_{nl} and ξ_{nb}, the rates of phagocytosis of immune cells in the lungs and blood, respectively. The ξ_{nl} distribution again divides the mice into two sets of two. BALB/c and CBA/Ca mice both tend towards the lower bound, while MF1 and C57BL/6 tend to have higher values. BALB/c mice have the highest values for ξ_{nb}, showing a strong immune response in the bloodstream as a distinct characteristic of their resistant phenotype. CBA/Ca mice again tend towards the lower bound on the phagocytosis rate, underlining their susceptibility to the bacterial infection. MF1 and C57BL/6 mice do not show much of a pattern in the ξ_{nb} distributions.

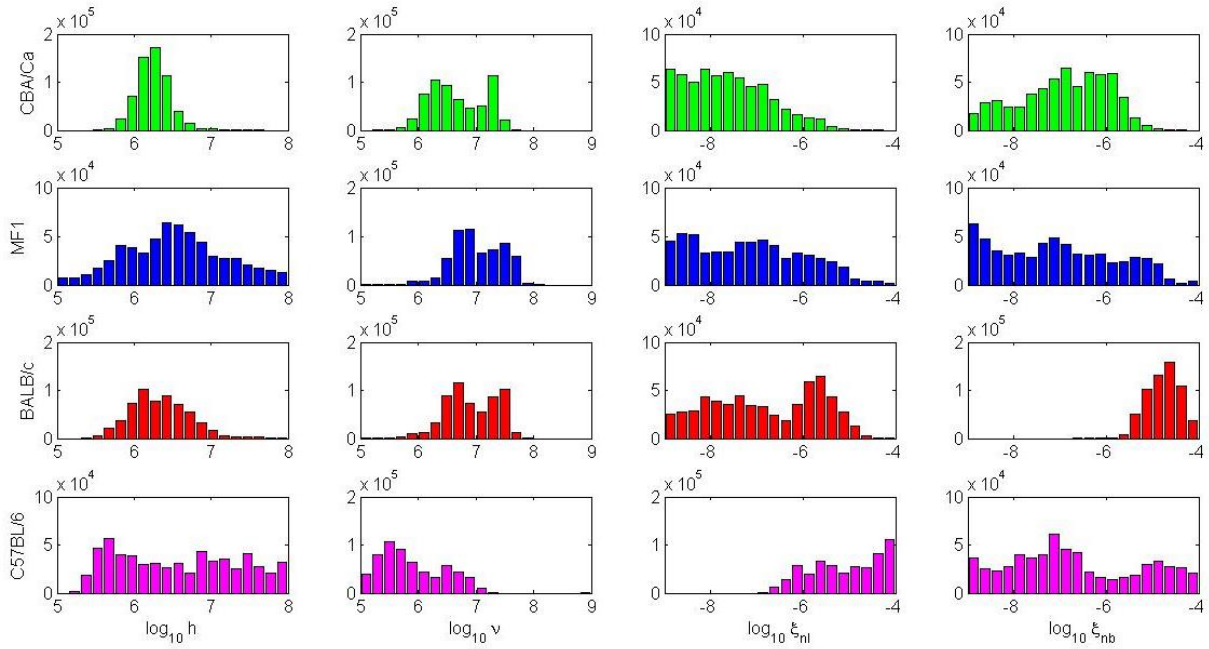

Figure 4: Full marginal parameter distributions of strain-dependent parameters.

Each row represents one strain of mouse, and each column contains a histogram showing the values each strain-dependent parameter takes on in the corresponding ensemble.

2.8.2 Two-dimensional parameter distributions show important correlations

Two-dimensional parameter distributions demonstrate any correlations between pairs of these strain-dependent parameters. Figure 5 shows these parameter correlations for all four strains of mice. These plots were generated using the scattercloud function in MATLAB, which plots pairs of values as a scatterplot between defined bounds (in this case, the upper and lower bound of the parameter of interest), and it uses a Gaussian smoothing technique to create a cloud of points, showing where most of the parameter distribution mass is concentrated. The scattercloud is plotted for all parameter pairs within our four strain-dependent parameter subset.

Panel A shows these correlations for the CBA/Ca mice. These clouds show no strong correlations between any of the parameters. These highly susceptible mice tend to have parameter values only on the lower end of the spectrum, thus creating very little correlation between parameter pairs.

The other three strains show more interesting trends. A negative correlation exists between ξ_{nl} and h, which is most clearly visible in the C57BL/6 parameter space (Panel D). This negative correlation implies that if the actual activation rate of phagocytes is high and more will be brought to the infected tissue, the strength of the phagocytosis does not need to be as high as if there were fewer phagocytes present to fight the infection.

There is also a negative correlation evident in both MF1 and BALB/c mice between parameters ξ_{nb} and h C57BL/6 mice do not show this trend, as the distribution for ξ_{nb} spans the entire allowable range. Again, if more phagocytes are brought in to eliminate bacteria, their

individual efficacy does not need to be as high. Other parameter pairs here do not show much of a correlation in these ensembles.

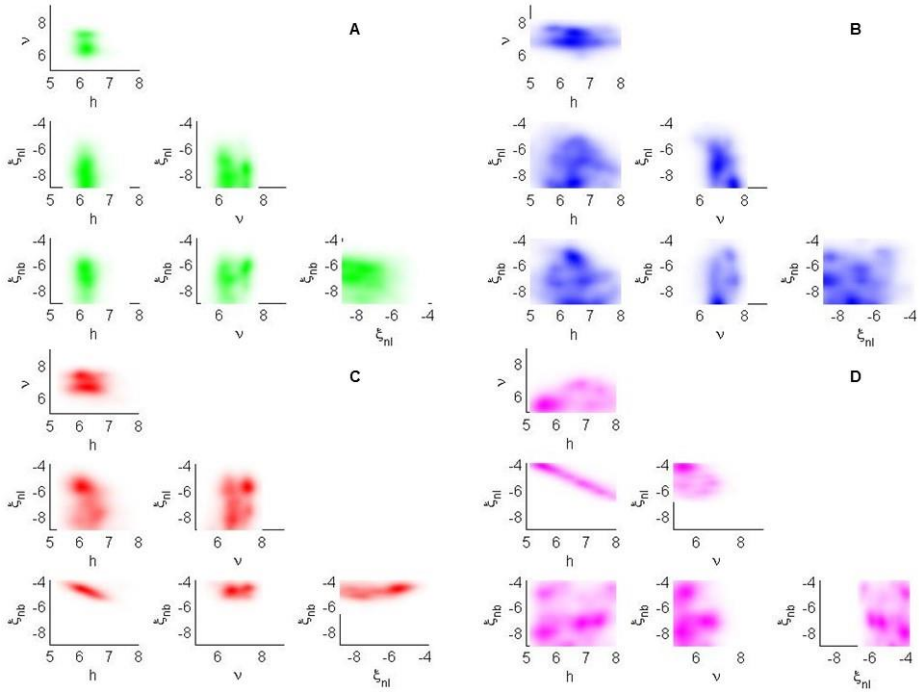

Figure 5: Two-dimensional parameter correlations:

for strain-dependent parameters for (A) CBA/Ca, (B), MF1, (C) BALB/c, and (D) C57BL/6 mice.

2.8.3 Principal component analysis of ensembles

Principal component analysis (PCA) applied to the ensembles will identify the parameters which describe the most sensitive directions in parameter space. Moving along these sensitive directions (i.e. changing these most sensitive parameters in a particular direction) will have a great impact on the trajectory output.

PCA was performed using a singular value decomposition (SVD). SVD is a factorization of a matrix, in which our data matrix $\mathbf{X}$ is factorized into the form $\mathbf{X} = \mathbf{U\Sigma V^T}$, where $\mathbf{U}$ is a unitary

matrix, $\mathbf{\Sigma}$ is a diagonal matrix, and $\mathbf{V}^T$ is the transpose of unitary matrix $\mathbf{V}$. The elements of $\mathbf{\Sigma}$ are the singular values of $\mathbf{X}$, and columns of $\mathbf{V}$ yield the principal directions. The 17 parameters in this model yield 17 principal components. The singular values associated with each of the 17 principal components (Figure 6) show a significant difference between principal components 16 and 17, denoting a sharp increase in sensitivity at the last principal component [54]. Therefore, principal component 17 characterized a very stiff direction in parameter space, indicating that parameters contributing large coefficients to this principal component are particularly sensitive.

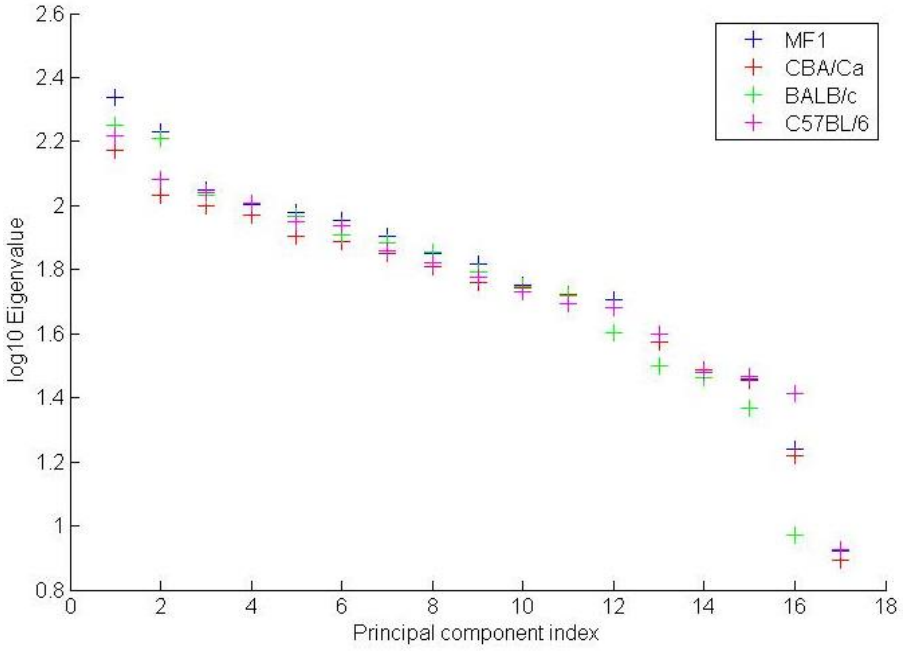

Figure 6: Eigenvalues associated with each principal component for mouse ensembles.

The makeup of this principal component is shown in pie charts in Figure 7. The larger a piece of the pie, the more sensitive the ensemble is to that parameter. CBA/Ca mice show the most sensitivity to the activation rate of phagocytes and the nonspecific clearance rate. If either of these

factors was increased, the CBA/Ca mice would have a better chance of fighting off the infection and the phenotype would be altered. The posterior distributions for these parameters tend to include low rates for both of these parameters, however, keeping the CBA/Ca mice from being able to clear pathogen from the lungs.

MF1 mice are most sensitive to the nonspecific immunity, with some contribution from the activation rate of phagocytes. Nonspecific defenses are responsible for the initial decline in lung pathogen numbers in these mice, and thus are the primary factor to creating this phenotype.

The variation in the trajectories of BALB/c mice is most sensitive to the blood pathogen phagocytosis rate and the nonspecific immunity. BALB/c mice are primarily able to resist the infection because they can keep the blood bacteria levels under control, and are therefore able to limit movement back into the lungs and survive the infection. The initial decline in lung pathogen levels is driven by nonspecific clearance, accounting for the large contribution of ν to the sensitivity.

C57BL/6 mice are most sensitive to the lung pathogen phagocytosis and the phagocyte activation rate. Since these mice clear all bacteria from the lungs before there can be any significant movement into the blood component, the variation in this phenotype will be predominantly subject to the lung phagocytosis parameters. Thus, the stiff directions identified in the strain-specific ensembles point to biological drivers for each of the phenotypes.

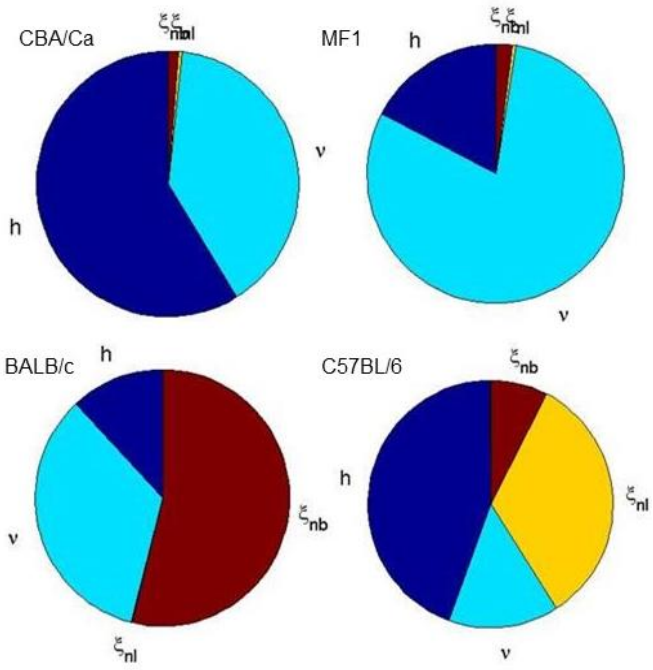

Figure 7: PCA results for mouse strain study:

Composition of the principal component associated with the smallest eigenvalue for each mouse strain. The larger the fraction represented by a parameter, the more sensitive the population is to that parameter.

2.9 MODEL VALIDATION

To ensure the ODE model is not overfit to the data previously presented, more data from literature searches were used to test the model. PubMed searches for published data from experiments in which one of these four murine strains were infected with D39 *S. pneumoniae* lung and/or blood bacteria data. No comparable data could be found for the CBA/Ca mice.

Smith et al. [40] published data for BALB/c mice infected intranasally with D39 strain pneumococcus at three different inocula: 10^4 CFU/ml, 10^5 CFU/ml, and 10^6 CFU/ml. At the low inoculum, the mice clear the bacteria within a few hours, but at a higher inoculum there are appreciable bacteria levels over the first few days. We simulated this system with all parameter

sets previously generated for BALB/c but with the three initial conditions listed (Figure 8). The mice clear bacteria within 2 days post inoculation for both 10^4 CFU/ml and 10^5 CFU/ml. At 10^6 CFU/ml the predicted trajectories are those originally generated by the BALB/c mice ensemble (Figure 2). Given the large standard deviations in the data, the ensemble fits these data generally well, except on the first day, as our predicted trajectories all decrease immediately after inoculation, contrary to these observations. There may be an uncertainty in the actual starting inoculation levels due to different technique of delivery in the Smith et al. experiments compared to those used for calibration of the model.

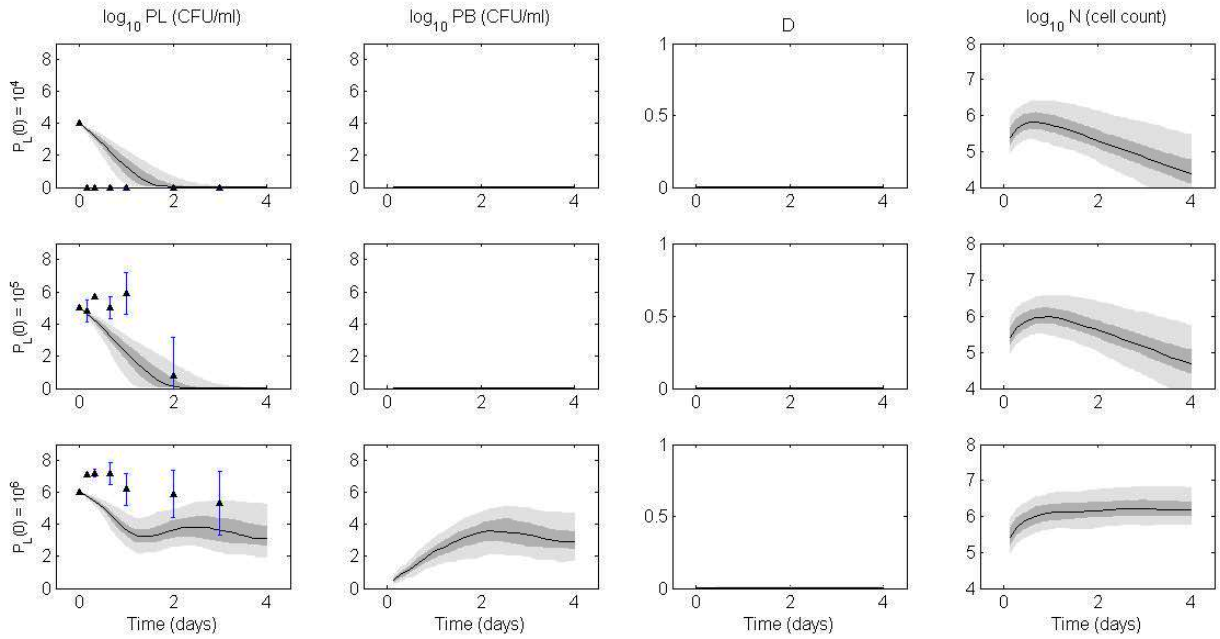

Figure 8: Model validation on test data for BALB/c mice.

The black line represents the median trajectory, the inner dark gray area represents the 25th to 75th quantiles of trajectories, and the outer light gray envelope represents 90% of the trajectories (5th to 95th quantiles). Data points with standard deviations are represented by the black triangles with error bars. Trajectories are simulated over 4 days, with infection occurring on day 0. Each row represents a different initial bacterial load modeled: 10^4 CFU, 10^5 CFU, and 10^6 CFU, respectively.

We also validated predictions in MF1 mice on data in which MF1 mice were infected with a higher dose of D39 strain pneumococcus (10^8 CFU/ml) [55]. Only lung pathogen data is reported for this testing set, obtained over the first 24 hours post inoculation. Qualitatively, the data look similar to our training set, with a smaller initial dip in lung pathogen populations but the same general timeframe of events. At this higher inoculum, innate immunity will not be as effective, and so the initial clearance is not as noticeable as in the training data. Yet, the ensemble of trajectories fit the data well, again validating our ensemble as biologically relevant (Figure 9).

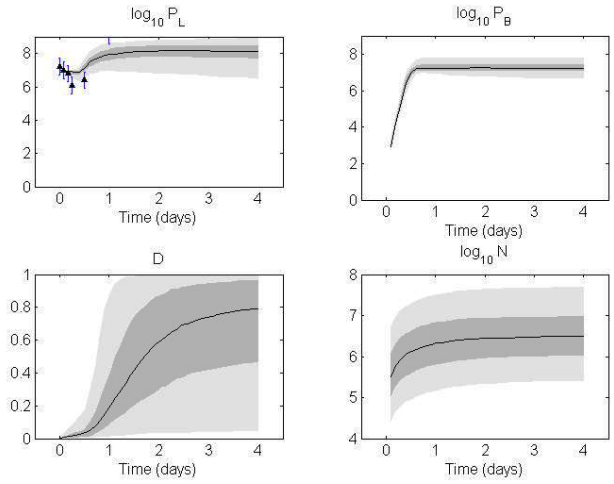

Figure 9: Model validation on test data for MF1 mice.

The black line represents the median trajectory, the inner dark gray area represents the 25th to 75th quantiles of trajectories, and the outer light gray envelope represents 90% of the trajectories (5th to 95th quantiles). Data points with standard deviations are represented by the black triangles with error bars. Trajectories are simulated over 4 days, with infection occurring on day 0.

Kadioglu et al. provided data for female C57BL/6 mice after challenges of both 10^5 and 10^6 CFU/ml [39]. We train our set on the lower inoculum, and then validate on the higher inoculum (Figure 10). We have only four data points for lung bacteria levels, but the trajectories generally

fit these points well. Gingles et al. provided a count of blood pathogen 24 hours post inoculation for the C57BL/6 mice, estimating about 2 – 3 log CFU/ml [38]. This estimate aligns with our simulated fit (Figure 10) as well, also validating predictions from the ensemble. Mean survival time given in the Gingles et al. study was about 72 hours post inoculation for this strain. Most of the trajectories at this higher initial condition will cause sustained high lung pathogen levels, but a small percentage of the trajectories will be able to clear within a few days. In this situation, the strength of our inference is limited by available data: without late data, it is impossible to discern how many of these trajectories that predict bacterial clearance would, in reality, be associated with dead mice. However, following trends seen in the training set for shapes of trajectories and mean time to death, this test again seems to support that inferences using our approach is robust.

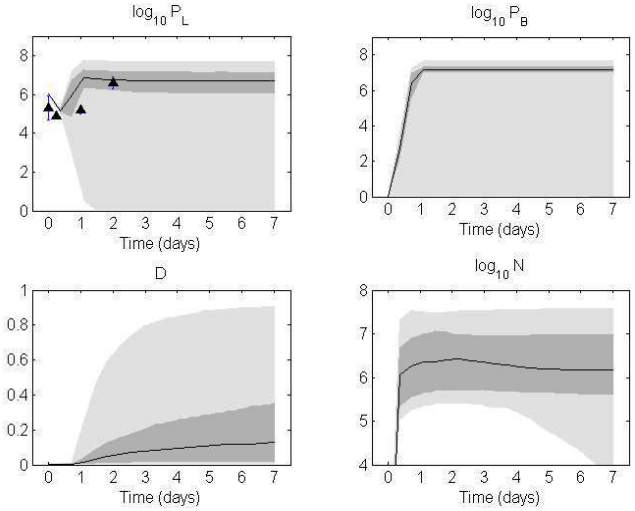

Figure 10: Model validation on test data for C57BL/6 mice.

The black line represents the median trajectory, the inner dark gray area represents the 25th to 75th quantiles of trajectories, and the outer light gray envelope represents 90% of the trajectories (5th to 95th quantiles). Data points with standard deviations are represented by the black triangles with error bars. Trajectories are simulated over 7 days, with infection occurring on day 0.

2.10 DISCUSSION

We developed an ensemble model of intrahost immune dynamics of pneumococcal pneumonia in four murine strains, where each strain is represented as a model ensemble, a large collection of parameter sets compatible with experimental data. With only four equations and 17 parameters, the model expresses phenotypic differences across strains as differences in parametric distributions across the corresponding ensembles. These differences in immune response crystalize in four strain-dependent parameters governing different aspects of the immune response. Variance in the phenotypes can also be explained biologically through the principal component analysis described in Figure 7.

Two of the strains studied in this work, BALB/c and C57BL/6, were resistant to the pneumococcal infection and able to survive the inoculum, but the model suggests that their immune systems handled the infection in different ways. BALB/c mice first appear to control lung pathogen levels through a strong nonspecific immunity, showing a sharp decay in bacteria levels in the first day. This component of immunity may include mechanisms such as mucociliary clearance, a specific characteristic of respiratory epithelial cells conveying resistance to bacterial attachment, alveolar macrophage activity, or the presence of other participants to mucosal immunity such as defensins [56]. As infiltration into the blood increases, blood and extrapulmonary pathogen clearance become the strongest influence on the ability of bacteria to propagate infection. C57BL/6 mice, on the other hand, control bacterial populations by recruiting phagocytes quickly and maintaining a high level of efficacy of phagocytosis in tissue.

We see separate trends for the strains that do not survive the infection. CBA/Ca mice have low bacterial clearance rates both by leukocytic phagocytosis and by nonspecific immunity, explaining their tendency to die soon after inoculation with a high pathogen load. MF1 have strong

nonspecific immune defenses, but phagocytes cannot effectively control excess pathogens and therefore do not overcome the infection.

We have also shown that our model does not overfit the four experimental datasets used to compute the strain-specific ensembles, as predictions generated from those ensembles produced good fit of testing data, both qualitatively and quantitatively. Important conclusions from literature, such as survival times and strength of cytokine signaling, can be validated with the parameter ensembles, supporting the biological and mathematical relevance of our model.

It is also clear that containing blood and extrapulmonary bacteria to low levels is vital to surviving an infection. Several studies suggest that resistant mice have a higher rate of influx of phagocytes than the susceptible mice, corresponding to our parameter h [57–59]. The ensembles show the highest rates of influx in C57BL/6 and MF1 mice, and the lowest rates for CBA/Ca mice. In the future, flow cytometry could be performed to test the number of activated phagocytes in the blood of each of these strains. We could then determine if this difference in phagocytosis rates is due to an increase in the number of phagocytes in the blood compartment, or whether the same number of phagocytes is more efficient in clearing bacteria in the BALB/c mice. We would predict that, as phagocyte number is driven by bacterial counts, higher phagocyte counts would be associated with worse outcomes. Of course, profound immune failure associated with extremely low blood phagocytes would also be associated with a poor outcome. Support for these predictions can be found in several reports, where successful containment of infection was associated with a strong immune response at the site of infection, with limited expansion of the inflammatory response beyond this site [60,61]. Our model explains the data for all testing and training sets well and provides biological mechanisms associated with these varying phenotypes. Our equations greatly simplify the dynamics of the system. We summarize the immune system with only three

components: one term for the nonspecific removal of pathogen, one term encompassing all phagocytosis in the lung tissue, and one term for the phagocytosis in blood. In reality, these mechanisms are more complex, involving macrophages, neutrophils, plasma cells and other adaptive immune components, and many cytokines and chemokines for signaling. The model could be adapted to include more of these components explicitly. Incorporating more mechanistic details could allow the models to further elucidate the biological underpinning of phenotypic differences. Such enhancements provide a path for future improvements but may be limited by available experimental data.

Mice are typically sacrificed whenever data were collected, although methods to collect data longitudinally in smaller animals are expanding. Extending the model-based approach to truly longitudinal data would improve the robustness of inference. The ensemble methodology is not an attempt to construct a synthetic population of individuals. Rather, it simply attempts to reflect data sparsity and uncertainty into model uncertainty, and therefore prediction uncertainty [16]. The posterior distribution, because it is computed from a limited number of individuals, represents an underestimate of population variability. Whether access to longitudinal data would impose more constraints on this distribution remains an open question. In the context of precision medicine, comparison of human phenotypes could be possible with simple models as well. Differences in human susceptibility to pneumonia and other lung diseases can be partially attributed to differences in the inflammatory response [11,62]. Our model can distinguish between phenotypes with high and low neutrophil recruitment, which may lend insight to mechanisms distinguishing severe from mild infections, for comparable pathogen loads.

Traditionally, contrasting phenotypes is accomplished through data analysis, from which speculative mechanisms explaining differences are inferred [11,38,63–67]. Our ensemble-based

approach determines putative mechanisms *a priori*, and quantifies their relative importance in explaining various phenotypes through distributional differences in phenotype-specific ensemble. Our approach has two main limitations. Potential mechanisms can only be included *a priori*, and mathematical models have limited complexity owing to data sparsity. If quantification of some of the mechanisms can be supported by data, a model-based approach would also offer more detailed and robust insight. Both approaches, data-first and model-first, are in fact complementary. The richness of the data should determine the level of detail with which individual mechanisms can be modeled. Yet, a model-based approach may lead to mechanistic insight more naturally, and provide direct intuition as to the structure of the ensuing experimental agenda.

3.0 A THREE-TIERED STUDY OF DIFFERENCES IN MURINE INTRAHOST IMMUNE RESPONSE TO MULTIPLE PNEUMOCCAL STRAINS

3.1 OVERVIEW

Using the pneumonia ODE model presented in the previous chapter, we present a complementary study in which we vary the species of pathogen while keeping the host species constant. We first explore the response to D39 (serotype 2) bacteria missing portions of the pneumolysin protein controlling either the hemolytic activity (H2-/C+) or complement-activating activity (H+/C-) [68]. Next, we model the response to D39 bacteria deficient in either NanA or NanB [55]. Lastly, we explore the response to three different serotypes of pneumococcus: D39 (serotype 2), 0100993 (serotype 3), and TIGR4 (serotype 4) bacteria [69]. Notably, a change in few key parameters expressing the activity of immune response components and virulence factors in our 4-variable ODE model captures the differences in the progression of infection exhibited by each phenotype of bacteria. This work has been previously published in PLOS One [70].

3.2 VIRULENCE OF PNEUMOCOCCUS

The capsule of pneumococcal bacteria, composed almost entirely of polysaccharides, shields the bacteria from several host defense mechanisms and contributes significantly to the virulence of pneumococci [71–73]. In fact, encapsulated strains are about 100,000 times more virulent than strains without a capsule [74,75].

The virulence of encapsulated bacteria depends on capsule thickness and chemical composition. A thicker capsule is advantageous in that it allows the bacteria to evade phagocytosis by immune cells such as neutrophils or macrophages [76]. However, thicker capsules also impede the ability of the bacteria to migrate from lung tissue to the bloodstream, decreasing their ability to cause bacteremia [77]. Bacteria in blood tend to proliferate faster than in tissue [44,45], and the number of activated phagocytes in the blood is proportionally lower than the number which migrate into infected tissue. Thus, even though a thinner capsule leaves the bacteria more vulnerable to phagocytosis, a thin capsule may also be advantageous for survival in some host species. Because of this dichotomy, pneumococcal serotypes have evolved with a range of capsule thicknesses.

In addition to capsule thickness, the chemical composition of the capsule is significant to bacterial fitness. Serotypes of pneumococcus are distinguished by the presence of specific glycoprotein motifs present on the surface of the capsule that influence the activation of the complement [78,79], degradation of complement components [80], and resistance to phagocytosis [81]. To date, over 90 serotypes of pneumococcus have been identified [82]. Each serotype can induce a different reaction from the immune system, depending on the makeup of the capsule and the activity of virulence factors associated with the bacterial surface [83].

In addition to the capsule, other virulence factors, present both on the surface and within the bacterium, play an important role in the ability of the bacteria to evade the immune system. Examples of such virulence factors are pneumolysin and neuraminidase. Pneumolysin is a pore-forming toxin expressed by virtually all serotypes of pneumococcus [84]. In early stages of the infection, when bacteria exist in low levels in the body, pneumolysin is cytotoxic, causing apoptotic activity in the epithelial cells [85] and activation of the complement system [86]. As the

infection progresses and pneumolysin concentration reaches higher levels, it is lytic to any cell with cholesterol in the membrane [87]. This lytic action causes damage to the tissue, and surrounding epithelial cells will increase the cytokine signaling to activate immune cells. In the absence of pneumolysin, the influx of phagocytic cells is delayed and decreased [37]. Neuraminidase is a surface protein that promotes the attachment of the bacteria to the epithelium. Neuraminidase cleaves the terminal sialic acid from glycolipids and glycoproteins, which damages the epithelium, exposes more potential binding sites for the bacteria, and promotes colonization [88,89]. Pneumococci have two neuraminidases on their surfaces: neuraminidase A (NanA) and neuraminidase B (NanB) [55]. Though bacteria deficient in either NanA or NanB are unable to cause sepsis in mice, NanA-deficient ($NanA^{-}$) bacteria have been shown to cause less damage than $NanB^{-}$ bacteria [55].

3.3 OVERVIEW OF METHODS

The ODE model used for the bacteria strain study is identical to that used in the murine strain study presented in Chapter 2. In each of our three studies (pneumolysin activity study, neuraminidase study, and serotype study), we define a subset of the model parameters as "bacterial-strain-dependent". These parameters are chosen based on existing knowledge of the mechanisms of immune response regulation so as to account for expected phenotypic differences seen in the progression of disease caused by each strain of bacteria modeled in the study. All other parameters are defined as "bacterial-strain-independent"; these parameters, which include parameters governing phagocyte lifespan, bacteria growth rates, threshold parameters, and parameters

inherent to host tissue, are assumed not to differ across strains of bacteria. Table 2 summarizes these parameter choices for each of the three studies. These choices are justified in Section 3.4.

Table 2: Summary of bacteria-strain-dependent parameters in each study.

Study	Parameters varied between strains	Reference
Pneumolysin activity	$h, q, \nu, \xi_{nl}, \xi_{nb}$	[68]
Neuraminidase	$q, \nu, a, \xi_{nl}, \xi_{nb}$	[55]
Serotype	$h, q, \nu, a, \xi_{nl}, \xi_{nb}$	[69]

3.4 EXPERIMENTAL DATA

This work is divided into three sub-studies, each with its own corresponding set of experimental data taken from literature. Here, the data used in each study and the method by which it was retrieved are summarized for the reader.

3.4.1 Pneumolysin activity study data

Data for the first study comes from a 2003 paper on the effect of pneumolysin on the survival of bacteria in the host [68]. Female MF1 mice were infected with D39 *S. pneumoniae* bacteria. The study involved wild-type D39 and two mutant strains: H+/C-, in which pneumolysin lacks its complement-activating activity, and H2-/C+, in which pneumolysin has substantially reduced hemolytic (pore-forming) activity. The C location on the pneumolysin protein activates the

classical complement pathway [90]. Decreased activation of complement leads to decreased phagocytic activity in both compartments and decreased activation of nonspecific immunity. In our model, these effects are controlled by h, the rate at which phagocytes are activated by lung bacteria; v, the rate of nonspecific clearance of bacteria from the lungs by mucociliary clearance and resident macrophages; ξ_{nl}, the rate at which phagocytes clear bacteria from the lungs; and ξ_{nb}, the rate at which phagocytes clear bacteria from the blood. The H segment of the pneumolysin controls the hemolytic activity of the bacteria, and hence the rate at which damage to the epithelium increases due to the presence of bacteria in the lungs, which is in our model represented by parameter q, We therefore fit the model to the pneumolysin study data by allowing only h, v, ξ_{nl}, ξ_{nb} and q to vary across the bacterial strains.

3.4.2 Neuraminidase study data

Data for the neuraminidase study was drawn from a 2006 study on the impact of both neuraminidase A and neuraminidase B on the survival of bacteria in the host [55]. Mice were infected intranasally with 10^7 CFU of either wild-type, NanA$^-$, or NanB$^-$ D39 pneumococcus. NanA$^-$ bacteria are cleared from the lungs by 12 hours post-infection, while NanB$^-$ bacteria persist for up to 48 hours post-infection but are eventually cleared by the immune system. Wild-type bacteria overwhelm the immune system and cause death about 24 hours post-infection. The wild-type D39 data is the same data used to calibrate the MF1 mouse model in Chapter 2.

We select the following parameters to explain the behavior of neuraminidase in the intranasal infection: q, the rate of increase of damage to epithelium; ξ_{nl}, the rate of intrapulmonary phagocytosis; and v, the nonspecific clearance of bacteria in the lungs. Changes in q and v would

represent a decreased ability of the bacteria to bind to the epithelium in the absence of neuraminidase, and some studies also suggest neuraminidase can stimulate resistance to opsonization by neutrophils [91], which would impact the value of ξ_{nl}. We hypothesize that the wild-type bacteria should cause the most damage to the epithelium, as this strain has full ability to bind to the epithelium. We would expect higher rates of clearance and lower damage creation from the mutant strains.

Following the intranasal infection, neither NanA$^-$ nor NanB$^-$ bacteria were able to be isolated from the blood [55]. To better explore the role of neuraminidase in the blood vessels, Manco *et al*. also infected MF1 mice intravenously with 10^5 CFU of one of these bacterial strains. Again, the neuraminidase-deficient bacteria are unable to cause a serious infection, as they are cleared from the blood within 2 days post-infection. Wild-type bacteria, however, are again able to cause serious bacteremia and therefore lead to morbidity around 2 days post-infection. We select a, the damage-independent rate of bacterial migration from blood to tissue, and ξ_{nb}, the rate of extrapulmonary phagocytosis, to explain the results of the intravenous infection experiment. Neutrophil opsonization would again be limited by the presence of neuraminidase in the wild-type bacteria, and neuraminidase-deficient bacteria would not be able to migrate between compartments easily, as they lack a basic component of adhesion to the epithelial wall.

3.4.3 Serotype study data

The final set of data was taken from a 2004 study featuring three serotypes of *S. pneumoniae*. [69]. In this experiment, mice were intranasally infected with wild-type strains of either D39 (serotype 2), 0100993 (serotype 3), or TIGR4 (serotype 4) pneumococcus. Data were taken at 12, 24, and

48 hours post-infection. Three mice were sacrificed at each time point and their bacteria and cell counts were averaged to provide the experimental data.

These serotypes differ primarily in their capsule thicknesses and virulence. Capsule thickness is a major contributor to the ease with which bacteria can move through the epithelial barrier. In this study, we selected 6 parameters as bacteria-strain-dependent: h, q, a, ν, ξ_{nl} and ξ_{nb}, since these parameters control the degree to which bacteria can move between lung tissue and blood (q and a), as well as the degree to which the host is able to fight these particular strains of pneumococcus ($h, \nu, \xi_{nl}, \xi_{nb}$).

3.5 PNEUMOLYSIN ACTIVITY STUDY

In accord with experimental conditions, we set the initial condition for lung bacteria to 10^6 CFU, and all other variables were initially set to 0. Figure 11 displays the ensemble fits to data for wild-type, H+/C-, and H2-/C+ D39 bacteria. On each ensemble trajectory plot, we represent the median trajectory as a solid black line, with the 25 – 75% quantiles in dark gray and 5 – 95% percentiles in light gray. Mean experimental data are represented by the black triangles, with standard deviations presented by the error bars.

In both lung and blood, each strain exhibits distinct behavior in the first 12 hours post-infection. The H+/C- bacteria stay at a near constant high level for the first 12 hours and reach the bloodstream in only 2 hours. The H2-/C+ bacterial population remains essentially level in the lungs until a sharp decrease at 12 hours, while showing negligible levels in the blood during that time. Bacterial populations in both compartments then begin to rise quickly, as transport between compartments increases and the bacteria can more easily avoid the immune system. The wild-type

bacteria exhibit a gradual, steady decline in lung population levels. Wild-type bacteria reach the blood in about 6-8 hours post-infection. As Figure 11 shows, the model captures all these behaviors within the ensemble.

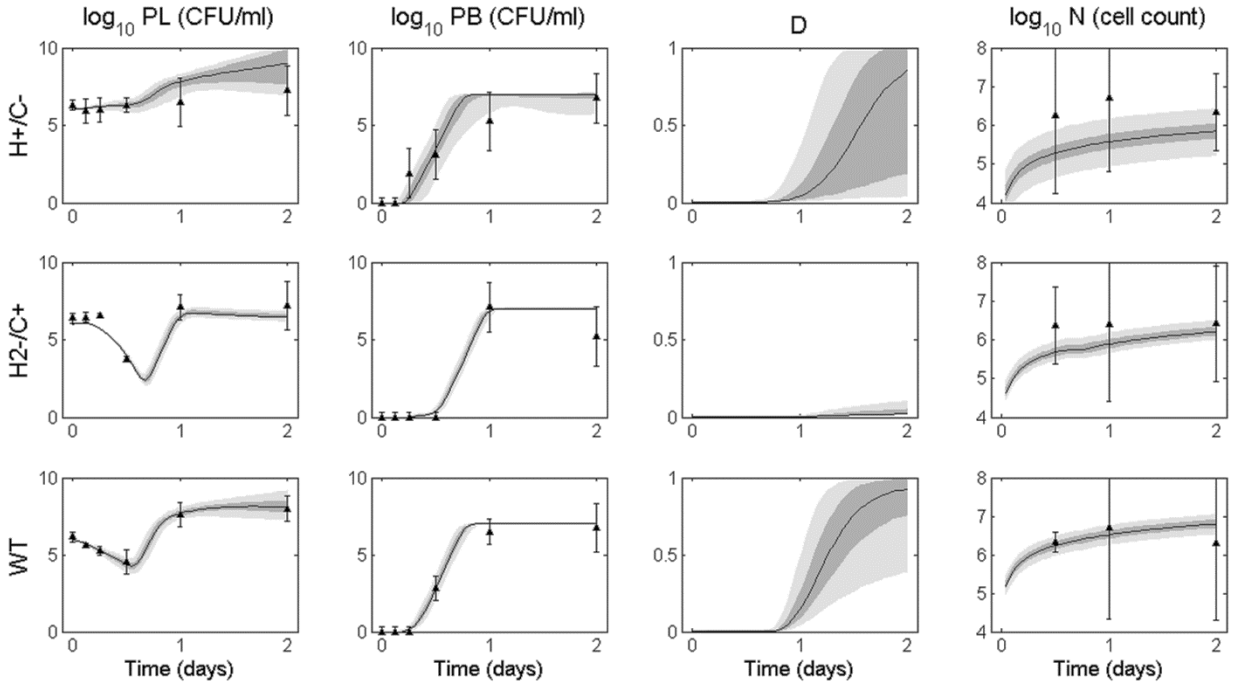

Figure 11: Ensemble fits of each strain for lung pathogen (PL), blood pathogen (PB), epithelial damage (D), and activated phagocytic cells (N) for pneumolysin activity study.

The black line represents the median trajectory, the inner dark gray area represents the 25th to 75th quantiles of trajectories, and the outer light gray envelope represents 90% of the trajectories (5th to 95th quantiles). Data points with standard deviations are represented by the black triangles with error bars. Data were taken at 0, 3, 6, 12, 24, and 48 hours post-infection with ten mice in each group. Trajectories are simulated over two days, with infection occurring on day 0. The top row shows ensembles for H+/C- bacteria, the middle row shows ensembles for H2-/C+ bacteria, and the bottom row shows ensembles for the wild-type (WT) bacteria.

We next explore differences in the posterior distributions of the bacteria-strain-dependent parameters (Figure 12). H+/C- bacteria distributions (Figure 12, top row) show a bimodal response of the phagocytes, and the pairwise parameter correlations in Figure 15 indicate these parameters are inversely correlated. Thus, when lung phagocytosis rates (ξ_{nl}) are high, blood phagocytosis (ξ_{nb}) tends to be less effective, and vice versa. Since this strain lacks complement activation, we would expect a generally low level of phagocytic activity. Interestingly, even though this strain has full hemolytic activity, the distribution of the damage production rate q exists in the lower half of its bounds. This likely occurs because lung bacteria levels remain high throughout the full course of the infection, and thus the values for q do not need to be exceedingly high in order to produce movement into the blood compartment.

H2-/C+ bacteria distributions (Figure 12, middle row) have full complement-activating capability, so they show relatively high levels of phagocytic activation (h) and response (ξ_{nl}). Nonspecific clearance (ν) tends to be low for this strain, allowing the bacteria to persist in the lungs at a constant level for the first 8 hours post-infection. The lack of hemolytic activity in this bacterial strain is associated with a low level of damage production q. In contrast, wild-type bacteria distributions (Figure 12, bottom row) exhibit high levels of damage production, phagocytic activation, and nonspecific clearance. The pneumolysin of this strain possesses its full hemolytic and complement-activating activity. Clearance of the wild-type bacteria in the blood is low, as the bacteria reach the blood and remain at high levels after about 12 hours post-infection.

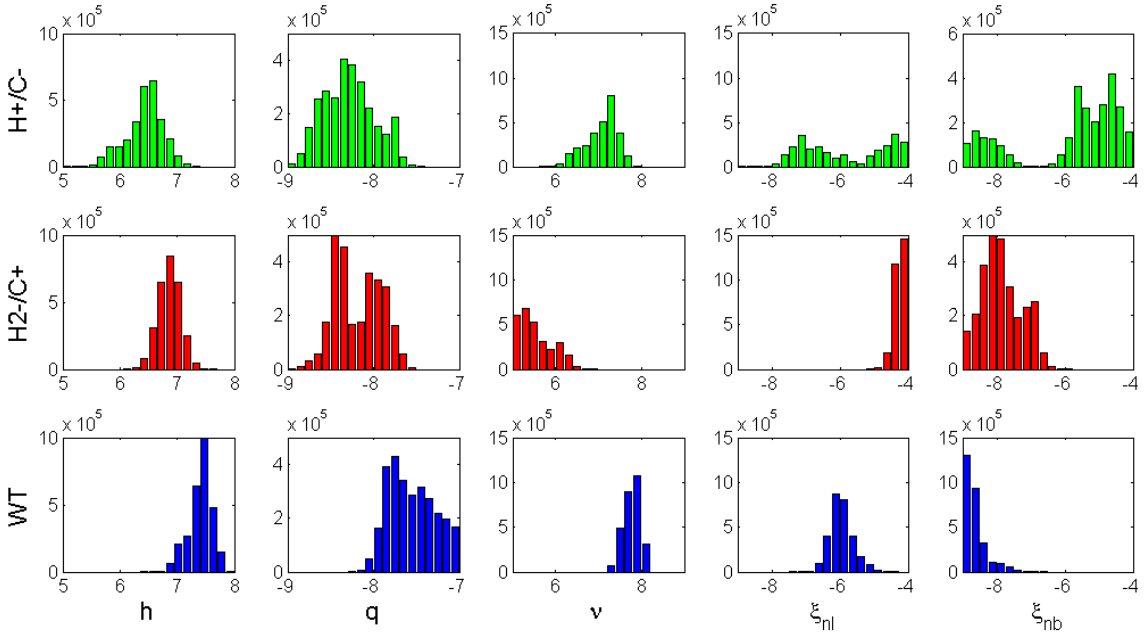

Figure 12: Full marginal parameter distributions for strain-dependent parameters in pneumolysin activity study. Each row represents one strain used in this study, and each column contains histograms for one of the strain-dependent parameters in this study ($\boldsymbol{h}, \boldsymbol{q}, \boldsymbol{\nu}, \boldsymbol{\xi_{nl}}, \boldsymbol{\xi_{nb}}$).

The strain-independent parameters include all other parameters of the model, with the exception of carrying capacity *K*, which is kept at a constant value of 10^8 CFU in this experiment. Histograms for the strain-independent parameters are shown in Figure 13. All three ensembles in the pneumolysin activity study have identical distributions for these ten parameters. Bounds on these parameters are identical to those presented in Table 2.

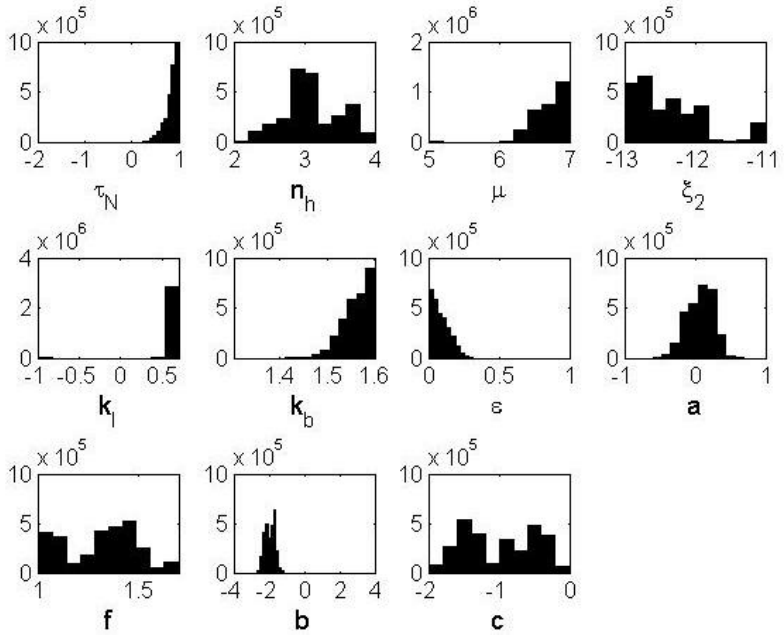

Figure 13: Full marginal parameter distributions for strain-independent parameters in pneumolysin activity study. All parameter values are given in $\log_{10}$ space, and upper and lower bounds on the graphs correspond to upper and lower bounds given to each parameter in the MCMC procedure (**Table 1**).

We next study the eigenvalues of the system through singular-value decomposition (Figure 14). Since there is no large difference in the singular values associated with the final two principal components, we conclude that a principal component analysis would not be beneficial to this study, as there is no clear stiff direction in parameter space.

We instead present two-dimensional parameter correlations for the strain-dependent parameters for each bacteria strain (Figure 15). Figure 15, left panel more clearly shows the bimodality exhibited by ξ_{nl} and ξ_{nb} in the H+/C- ensemble. The ensembles for H2-/C+ (Figure 15, middle) and wild-type (Figure 15, right) show few correlations of interest, as these distributions tend to be tighter than those of the H+/C- ensemble.

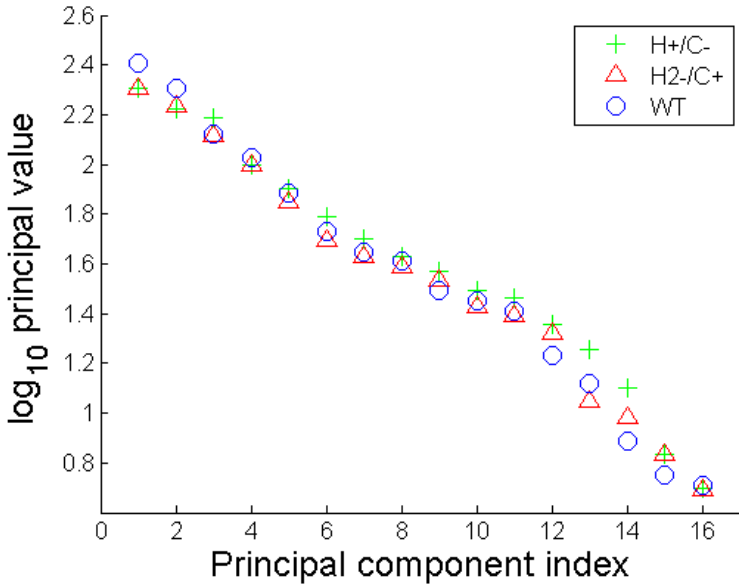

Figure 14: Eigenvalues and associated principal components for pneumolysin activity study.

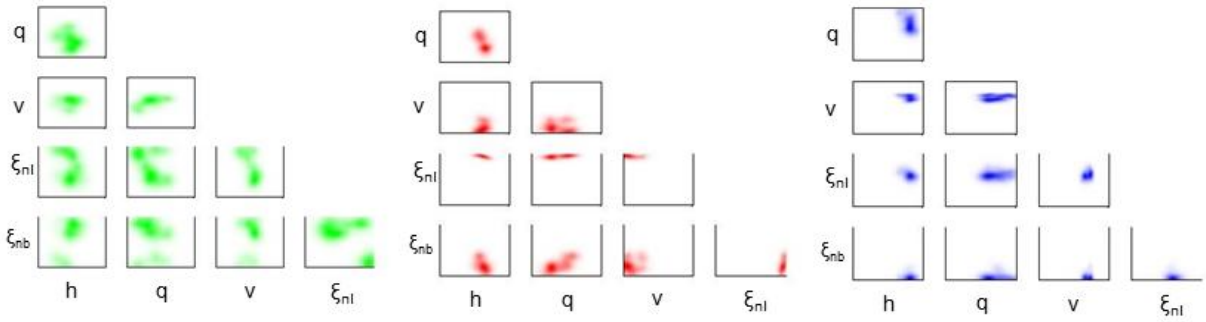

Figure 15: Two-dimensional parameter correlations for pneumolysin activity study.

(Left) H+/C-, (Center) H2-/C+ , (Right) WT parameter correlations. Each dot represents a single pair of parameter values in the ensemble.

3.6 NEURAMINIDASE STUDY

As explained in Section 3.4.2, the neuraminidase study includes experimental data for both an intranasal and an intravenous bacterial infection. We fit both the intranasal and intravenous data simultaneously for all three strains of bacteria. For the intranasal case, we use an initial condition of 10^7 CFU for P_L and 0 CFU for P_B, and for the intravenous case, we use an initial condition of 0 CFU for P_L and 10^5 CFU for P_B, consistent with experimental conditions. The model is fit to data for both cases simultaneously, thus generating only one set of parameter distributions for each strain of mouse in the neuraminidase study.

Figure 16 shows the ensemble fits to intranasal infection data for wild-type, $NanA^-$, and $NanB^-$ D39 bacteria. $NanA^-$ bacteria are unable to adequately bind to the epithelium, and they are cleared from the lungs within 12 hours. $NanA^-$ bacteria are unable to cause any appreciable damage or sustain a population in the blood for more than a few hours in our predicted trajectories. Experiments verified that these bacteria were not detected in the blood at any point in the experiments. $NanB^-$ bacteria can persist in the lungs longer than $NanA^-$, but these bacteria will eventually clear as well. While our ensembles show some presence of bacteria in the blood, these bacteria are cleared within about one day, thus not causing severe bacteremia, again aligning with the findings of the authors [55]. The wild-type bacteria are highly virulent, causing sepsis and eventual death to the mice about 1 day post-infection. Our ensembles match the lung data well and show a quick rise in blood bacteria levels as well as epithelial damage. Though the activated phagocytic cell population is highest in the simulated wild-type bacteria ensemble, these cells are unable to contain the bacterial population in either compartment.

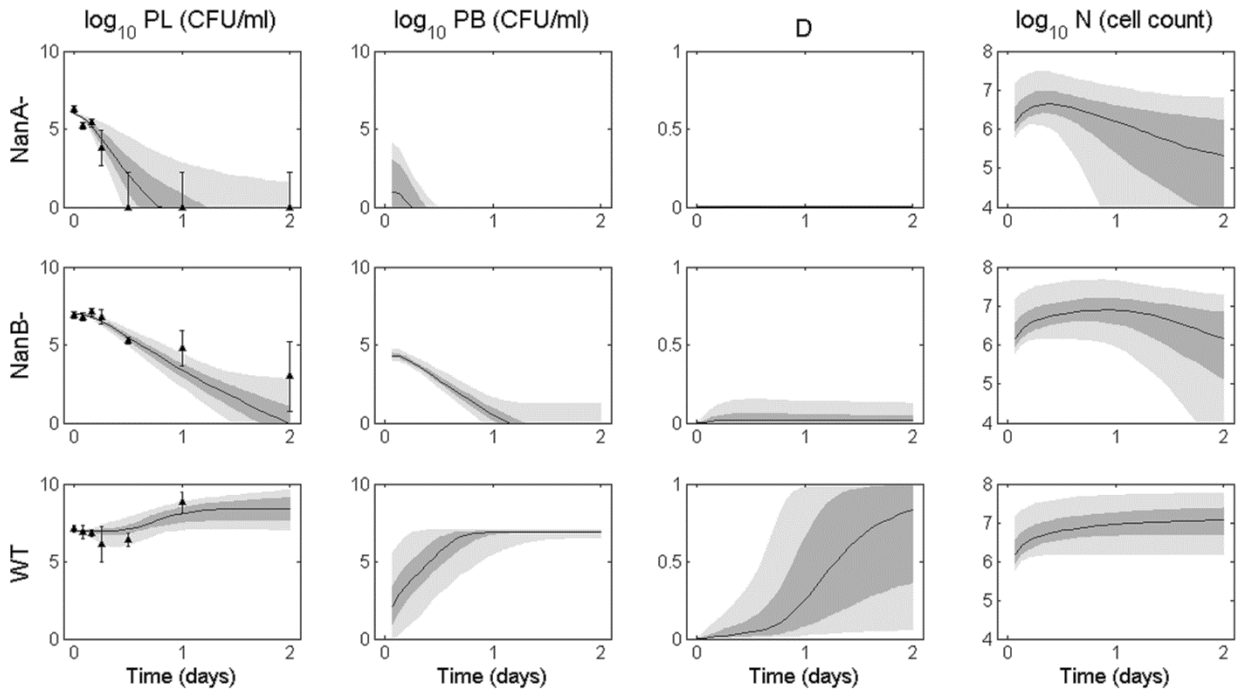

Figure 16: Ensemble fits of each strain for lung pathogen (PL), blood pathogen (PB), epithelial damage (D), and activated phagocytic cells (N) for intranasal infection in neuraminidase study.

The black line represents the median trajectory, the inner dark gray area represents the 25th to 75th quantiles of trajectories, and the outer light gray envelope represents 90% of the trajectories (5th to 95th quantiles). Data points with standard deviations are represented by the black triangles with error bars. Data were taken at 0, 2, 4, 6, 12, 24, and 48 hours post-infection with ten mice in each group. Trajectories are simulated over two days, with infection occurring on day 0. The top row shows ensembles for $NanA^-$ bacteria, the middle row shows ensembles for $NanB^-$ bacteria, and the bottom row shows ensembles for the wild-type (WT) bacteria.

Figure 17 demonstrates the ensemble solutions for the intravenous infection experiments. Bacteria are introduced into the blood at day 0 at an initial level of 10^5 CFU. $NanA^-$ bacteria are cleared from the blood within about 12 hours post-infection, and while they are able to reach the lungs relatively quickly, they are cleared from the tissue quickly as well. $NanB^-$ bacteria show an

initial steep drop in blood levels as they move into the lungs. These bacteria are not fully cleared from the blood until about 2 days post-infection. While the lung bacteria levels have not been eliminated at this point, all trajectories will eventually lead to total clearance of bacteria from both compartments. Again, the wild-type bacteria are the most virulent in these experiments. These are the only bacteria able to cause significant damage, and as such the bacteria levels in both compartments rise over the first 12 hours until they hit a carrying capacity in the blood and cause morbidity of the host.

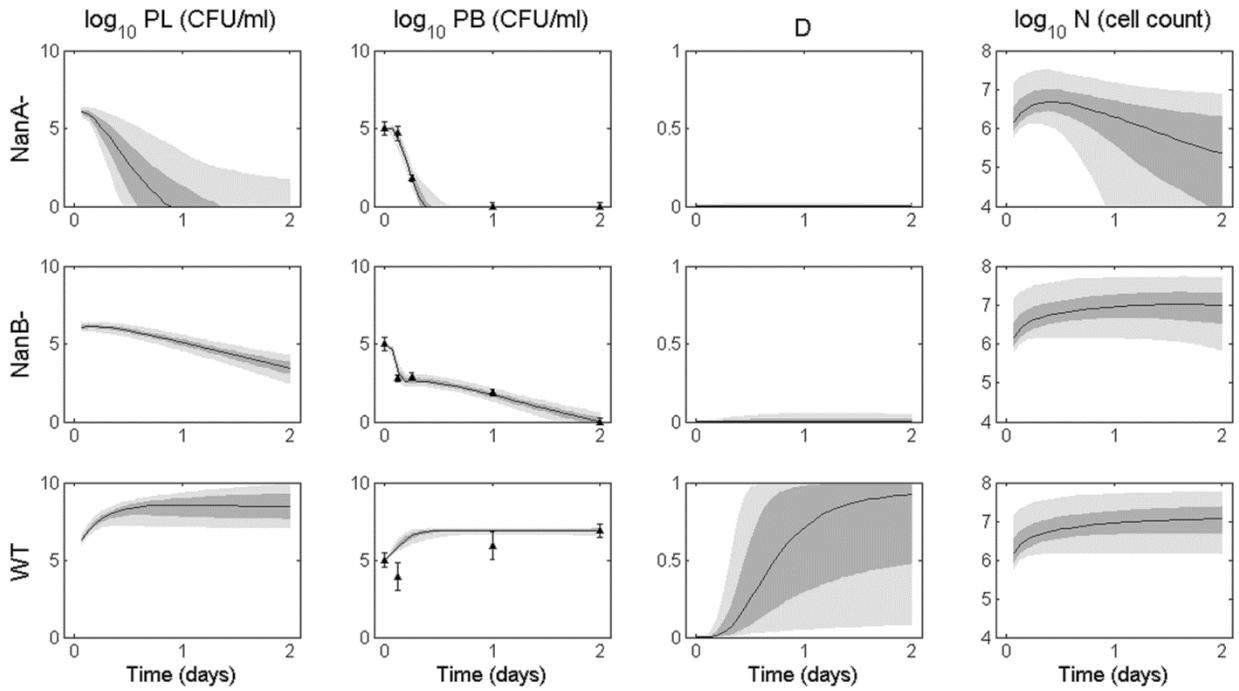

Figure 17: Ensemble fits of each strain for lung pathogen (PL), blood pathogen (PB), epithelial damage (D), and activated phagocytic cells (N) for intravenous infection in neuraminidase study.

The black line represents the median trajectory, the inner dark gray area represents the 25th to 75th quantiles of trajectories, and the outer light gray envelope represents 90% of the trajectories (5th to 95th quantiles). Data points with standard deviations are represented by the black triangles with error bars. Data were taken at 0, 3, 6, 24 and 48 hours post-infection with ten mice in each group. Trajectories are simulated over two days, with infection occurring

on day 0. The top row shows ensembles for NanA⁻ bacteria, the middle row shows ensembles for NanB⁻ bacteria, and the bottom row shows ensembles for the wild-type (WT) bacteria.

Distributions of our bacteria-dependent parameters show marked differences across these three strains (Figure 18). NanA⁻ bacteria are essentially insensitive to q and a, as the bacteria are unable to maintain their population for more than a few hours in either the intranasal or the intravenous experiments. Clearance rates of the NanA⁻ bacteria both by nonspecific means (ν) and by phagocytic cells (ξ_{nl}, ξ_{nb}) tend towards the upper end of the spectrum, meaning these bacteria are easily cleared by the immune system. This result is further verified by the evidence that NanA prevents opsonization by neutrophils [91].

NanB⁻ bacteria show the most sensitivity to a, the damage-independent movement of bacteria from blood to lungs, as this distribution is the most narrow. Pulmonary clearance of the NanB⁻ bacteria (ν, ξ_{nb}) tends to be lower than that of the NanA⁻ bacteria. It is unclear whether NanB has the same effect on opsonization as NanA; further experiments on the interactions of NanB and neutrophils are needed in order to verify this prediction biologically. The clearance of NanB⁻ bacteria in the blood is generally very high, explaining the fast initial drop in blood levels in the intravenous infection data.

The distributions for the wild-type bacteria differ most from the neuraminidase-deficient bacteria in the values of a and ξ_{nb}, both of which are much lower than the distributions seen in the other two strains. Both of these results align with our initial hypotheses; the presence of NanA allows the wild-type bacteria additional resistance to phagocytosis, and the ability to bind the epithelium and cause excess damage means the bacteria require less damage-independent motion to overwhelm the lung and blood compartments. Interestingly, all three strains show an

insensitivity to q, despite the known increased ability of the wild-type bacteria to adhere to the epithelium and create damage. The effect of this phenomenon is absorbed in the parameter a; higher values of a imply lower levels of damage created.

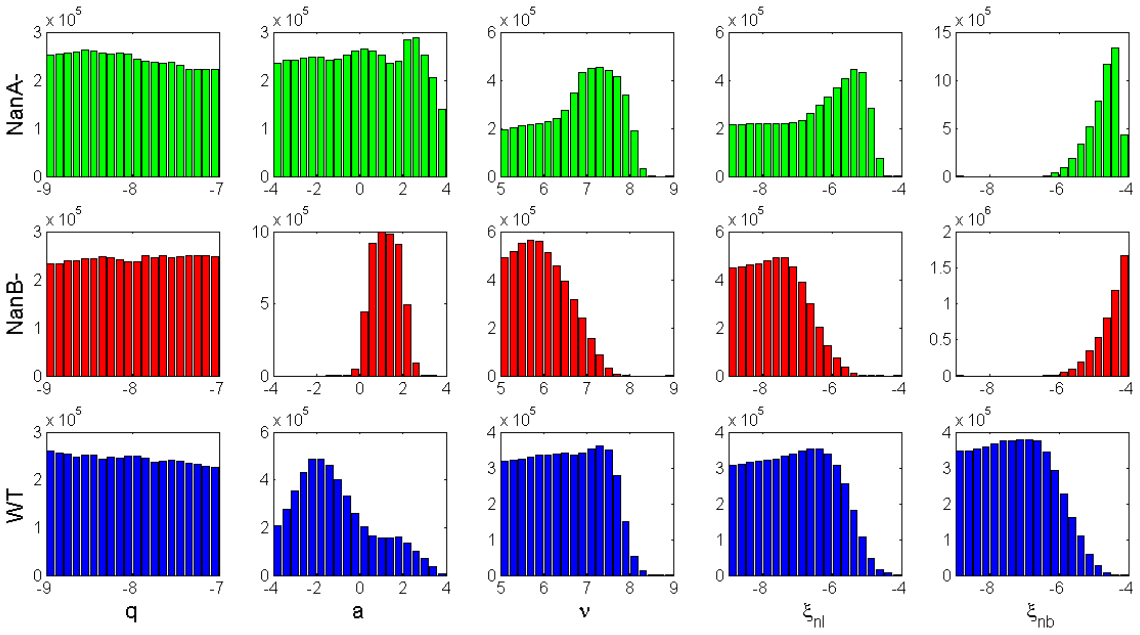

Figure 18: Full marginal parameter distributions for strain-dependent parameters in neuraminidase study. Each row represents one strain used in this study, and each column contains histograms for one of the strain-dependent parameters in this study ($\boldsymbol{q, a, \nu, \xi_{nl}, \xi_{nb}}$).

Strain-independent parameters are shown in Figure 19. Most parameters fully span their bounds, allowing a wide range of phenotypes in the output, given a particular set of strain-dependent parameters from Figure 18.

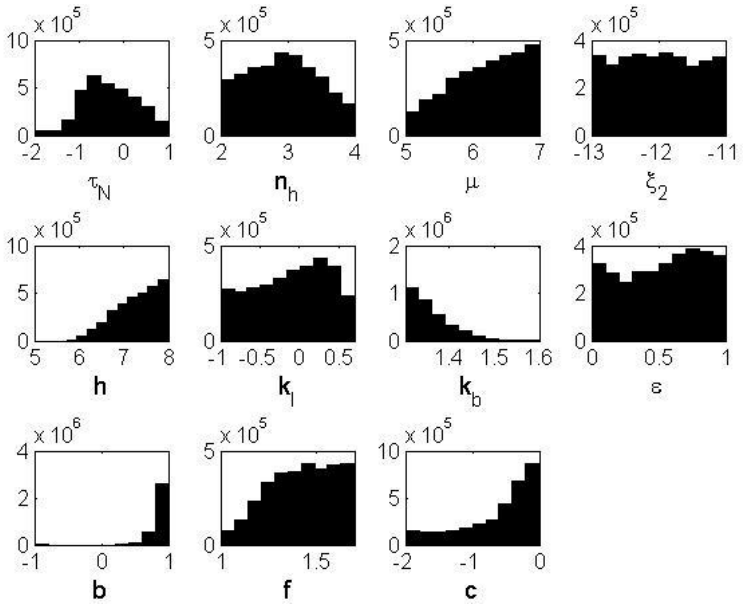

Figure 19: Full marginal parameter distributions for strain-independent parameters in neuraminidase study. All parameter values are given in $\log_{10}$ space, and upper and lower bounds on the graphs correspond to upper and lower bounds given to each parameter in the MCMC procedure (**Table 1**).

The principal values of the system again show no significant difference between the final two components (Figure 20), so a principal component analysis would not provide interpretable results. The two-dimensional parameter correlations (Figure 21) show a few noteworthy patterns. NanA⁻ bacteria (green) exhibit a switching behavior with ν, a, and ξ_{nl}. When ν is high, then a and ξ_{nl} are low, and vice versa. In other words, when nonspecific clearance of bacteria in the lungs is high, phagocyte-dependent clearance can be low to achieve the same overall clearance from the lungs.

In addition, both NanB⁻ (red) and wild-type bacteria (blue) show a strong negative correlation between q and a. As we saw in Figure 18, much of the effects of q become absorbed

in parameter a, as low damage creation can imply a large percentage of bacteria movement is damage-independent.

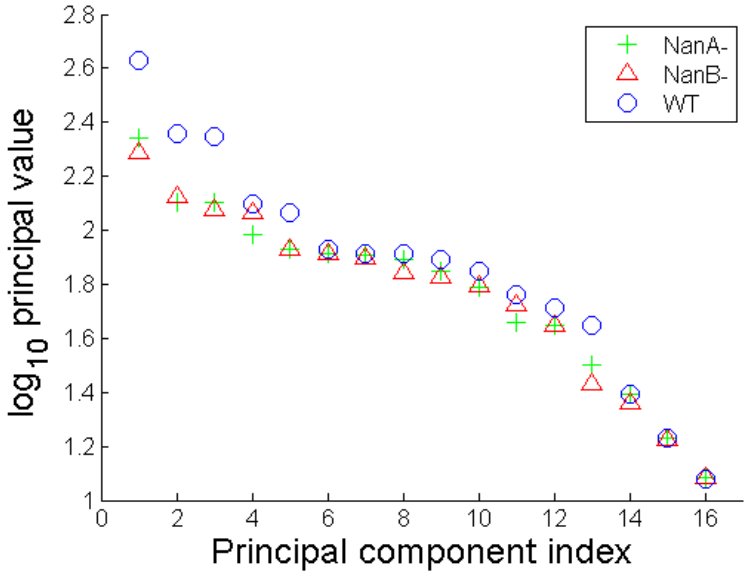

Figure 20: Eigenvalues and corresponding principal components for neuraminidase study.

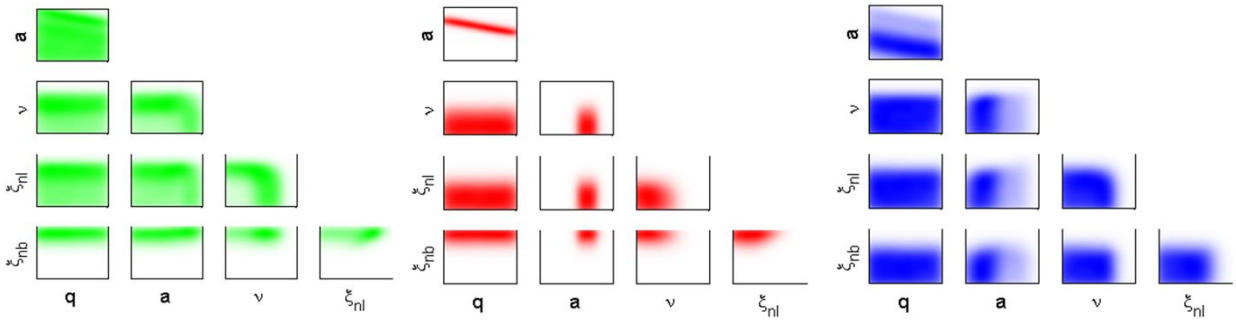

Figure 21: Two-dimensional parameter correlations for neuraminidase study.

(Left) NanA^{--} -, (Center) NanB^{--}, (Right) WT parameter correlations. Each dot represents a single pair of parameter values in the ensemble.

3.7 SEROTYPE STUDY

In the serotype study, each strain of bacteria was given in a different dose to the mice, reflecting their widely varied virulence in murine hosts. Because of this, we have three separate sets of initial conditions used to simulate the ODEs. Lung bacteria begins at 10^6 CFU for D39, 10^7 CFU for 0100993, or 10^5 CFU for TIGR4 pneumococcus. As in the previous studies, all other variables begin at 0.

Figure 22 shows the ensemble trajectories fit to data for D39, 0100993, and TIGR4 bacteria up to 48 hours post-infection. Trajectories generally fit data tightly, with most variation in predicted trajectories occurring in D and N. TIGR4 tend to create the most damage, while very little damage is seen for the D39 ensemble. Each strain varies significantly in the first 12 hours, represented by the first data point. 0100993 bacteria remain relatively high, exhibiting little nonspecific clearance. TIGR4 and D39 bacteria levels in the lung decrease by several orders of magnitude during the first 12 hours, showing both a greater susceptibility to this initial clearance and faster movement into the bloodstream.

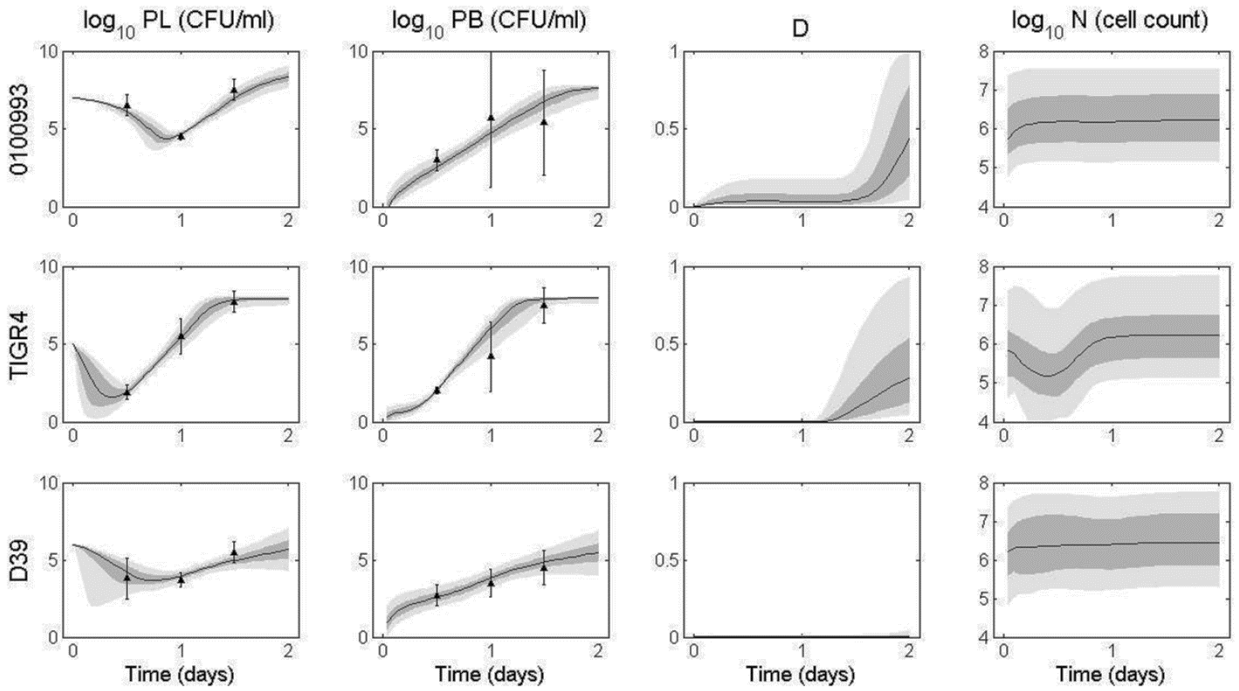

Figure 22: Ensemble fits to data in serotype study.

The black line represents the median trajectory, the inner dark gray area represents the 25th to 75th quantiles of trajectories, and the outer light gray envelope represents 90% of the trajectories (5th to 95th quantiles). Data points with standard deviations are represented by the black triangles with error bars. Data were taken at 12, 24 and 48 hours post-infection with ten mice in each group. Trajectories are simulated over two days, with infection occurring on day 0. The top row shows ensembles for 0100993 bacteria, the middle row shows ensembles for TIGR4 bacteria, and the bottom row shows ensembles for the D39 bacteria.

Figure 23 shows the distributions of bacteria-strain-dependent parameters for each of the three serotypes. The largest disparities between strains exist in distributions for a, ξ_{nl}, ξ_{nb} and ν populations. 0100993 bacteria tend to have a low value for a, the damage-independent movement of bacteria from the bloodstream to the tissue. Since these serotype 3 bacteria typically remain higher in the lung tissue than in the blood, we would expect the effect of this motion to be minimal.

In contrast, TIGR4 bacteria tend to have a high a value, as these bacteria readily cause sepsis. D39, known to cause both severe pneumonia and sepsis in MF1 mice, have a values concentrated between these two extremes.

Each serotype also differs in its resistance to clearance by both mucosal immunity and phagocytic activity. The distribution for D39 ν aligns with the MF1 output from our previous work [24]. Higher values of ν are evident in 0100993 and TIGR4 bacteria. Phagocytosis rates (ξ_{nl} and ξ_{nb}) also vary between these serotypes. Phagocytosis in the tissue tends to be low for the 0100993 bacteria, high for TIGR4, and D39 lies somewhere in the middle. Extrapulmonary phagocytosis is high in both 0100993 (mean of 1.3×10^{-5}) and D39 (mean of 1.8×10^{-5}), and it is slightly lower for TIGR4 (mean of 3.6×10^{-6}).

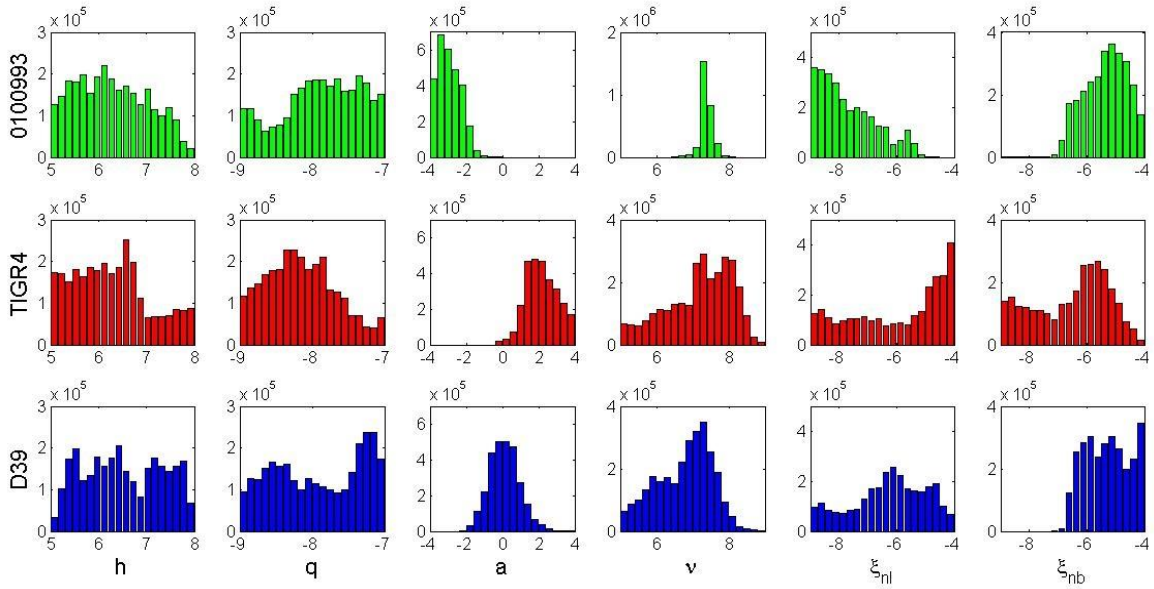

Figure 23: Full marginal parameter distributions for serotype study.

Each row represents one strain used in this study, and each column contains histograms for one of the strain-dependent parameters in this study.

Strain-independent parameters are shown in Figure 24. Bacterial reproduction rates k_l and k_b, as well as neutrophil activation time τ_N, tend to be low, but the other parameters generally can take on any value in their allowed ranges.

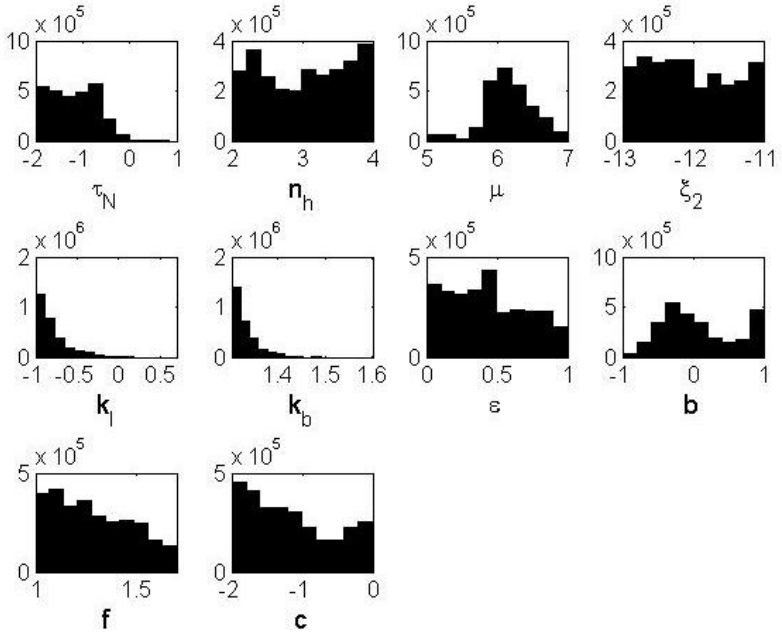

Figure 24: Full marginal parameter distributions for strain-independent parameters in serotype study. All parameter values are given in $\log_{10}$ space, and upper and lower bounds on the graphs correspond to upper and lower bounds given to each parameter in the MCMC procedure (**Table 1**).

We performed singular value decomposition on the ensemble, and from the output determine the makeup of each principal component and eigenvalues associated with each. The steep drop in the magnitude of the eigenvalue associated with the final principal component suggests that the composition of the final principal component explains most of the sensitivity of the model (Figure 25). We studied the makeup of this vector to determine which parameters contribute most to this sensitivity (Figure 26). The relative contribution of each element to the

vector is represented in a pie chart, and the color of each piece denotes whether the parameter has a positive (cool colors) or negative (warm colors) contribution.

Strain 0100993 is most sensitive to ν. Serotype 3 strains tend to stay in the lungs to cause severe pneumonia [92], so a sensitivity to clearance in the tissue is expected. The TIGR4 ensemble is most sensitive to ν, ξ_{nb}, q and a. TIGR4 bacteria are known to cause bacteremia and sepsis very quickly in mice, and eventually progress to cross the blood-brain barrier, leading to meningitis [92]. These sensitive parameters control the ability of the bacteria to proliferate in the lungs, cause epithelial damage, and move between the lung and blood compartments. Lastly, the D39 ensemble is most sensitive to q. D39 is known to be highly virulent to mice, often leading to both sepsis and severe pneumonia [92,93]. Since bacterial replication in lung tissue is highly dependent on the ability of the bacteria to move to the blood and evade phagocytosis, we would expect the rate of damage creation to be critical to explain the data.

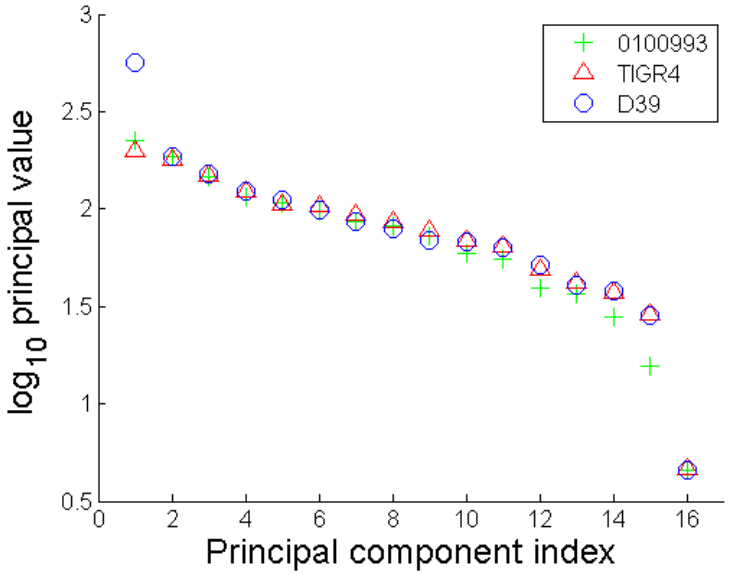

Figure 25: Eigenvalues and associated principal components for serotype study.

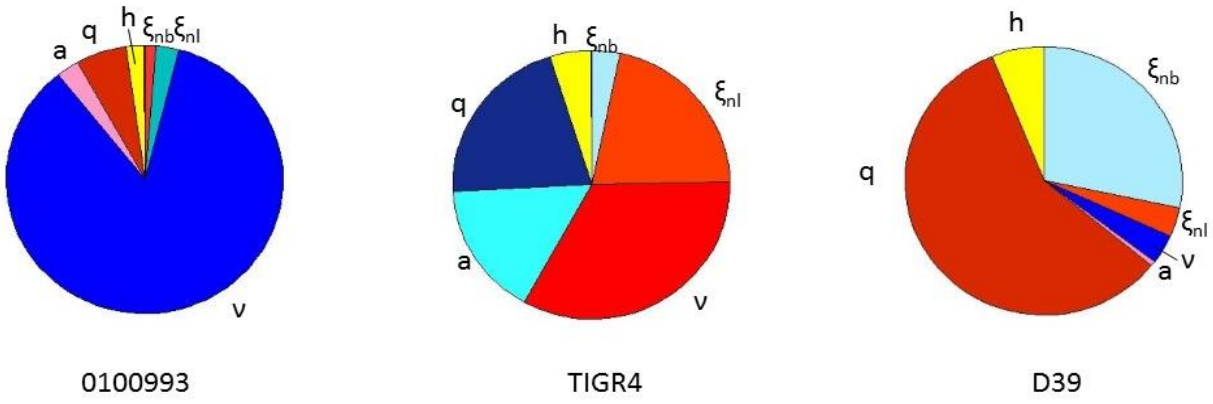

Figure 26: PCA output for the serotype study.

Each pie chart demonstrates the makeup of principal component 16 for each of the three strains used in this study. (Left) PCA for 0100993 strain shows high sensitivity to ν. (Center) TIGR4 PCA shows a high sensitivity to parameters $\boldsymbol{a}, \boldsymbol{\nu}, \boldsymbol{q}, \boldsymbol{\xi_{nl}}$. (Right) PCA for D39 strain shows high sensitivity to q.

3.8 DISCUSSION

In this study we further developed the ODE model of intrahost immune response to pneumococcal pneumonia presented in Chapter 2 and previously published in Journal of Theoretical Biology [24]. We demonstrate the selection of a parsimonious subset of parameters that can define primary differences between bacterial strains. We here show that the model is capable of capturing differences not only across murine strains, but also across bacterial strains. Our model identifies differences in immune response to infection by bacteria missing a portion of a protein (pneumolysin activity study), a whole protein (neuraminidase study), or entirely different serotypes (serotype study). The model can also describe initial decay and subsequent dramatic rise in the number of pneumococci in the lungs, which has been observed experimentally as coordinated with a similar rise in the blood.

While a different subset of five or six parameters was identified as bacteria-dependent in each study, four parameters were consistently bacteria-dependent in all of our three studies: ν, q, ξ_{nl} and ξ_{nb}. The parameter ν incorporates nonspecific clearance mechanisms such as mucociliary clearance, alveolar macrophage activity, defensins and other proteins active in mucosal immunity. The pneumolysin study demonstrated differences in ν for all three bacterial strains, with high ν values seen in the wild-type bacteria ensembles and low ν values in the H2-/C+ ensembles. Absence of hemolytic activity in the H2-/C+ bacteria could be responsible for a decreased activation of the alveolar macrophages, thereby decreasing the overall rate of clearance by ν. In the neuraminidase study, ν tended to be lowest for NanB^{-} bacteria. These bacteria have not been studied extensively, so reasons for this difference are unclear.

In the serotype study, ν stood out as a highly sensitive parameter for both TIGR4 and 0100993 bacteria. TIGR4 bacteria are highly virulent, so likely the host must have strong nonspecific defenses to control TIGR4 levels from the beginning of the infection. Another virulence factor impacting the nonspecific clearance is choline-binding protein. Choline-binding proteins allow bacteria to anchor themselves to the epithelial surface, increasing their ability to avoid non-specific clearance mechanisms. Brooks-Walter *et al*. showed that about 25% of pneumococcal strains do not express choline-binding protein A (CbpA, also known as PspC or SpsA), which can limit virulence [94]. It has been shown that another serotype 3 strain, A66.1, does not express CbpA, so it is possible that our serotype 3 strain, 0100993, also does not. This would explain the need for such a high inoculum to generate survival rates similar to those seen in the other infections; an inoculum of 10^7 CFU of 0100993 was required, compared to only 10^5 CFU of TIGR4, suggesting decreased virulence in the serotype 3 strain.

The parameter q, the rate at which lung bacteria create damage to the epithelium, was found to be strain-dependent in all three studies. While q was not an influential parameter in the neuraminidase study, it was crucial to the ensemble fits for the wild-type D39 bacteria in the pneumolysin and serotype studies. D39 is often used in murine models of pneumonia because it is known to be highly virulent to mice, leading to both severe pneumonia and bacteremia. We would therefore expect to see damage creation as a highly important factor in the phenotype associated with D39 infection. The $q$distribution for wild-type D39 tends to be skewed high in the pneumolysin study but exists over the full parameter range in the serotype study. We can see large differences in the D39 bacteria levels between the two studies, possibly due to different laboratory conditions, different protocols used, or different sources of the materials and specimens used in the study. These differences are enough to induce distinct parameter distributions for each wild-type ensemble.

The rates of phagocytic clearance in lung tissue and blood (ξ_{nl} and ξ_{nb}, respectively) were also found to be bacteria-dependent parameters in each of the three studies. Many virulence factors present on the bacterial surface allow the bacteria to avoid phagocytosis, and since the presence and efficacy of these virulence factors varies across strains, we would expect these parameters to greatly influence the ensembles. In the pneumolysin study, because the biggest variations in the data occur in the first 12 hours, phagocytic cells do not control the major differences in the ensembles; these effects are felt more strongly later in the course of the infection. In the neuraminidase study, wild-type bacteria are not cleared effectively in the blood, while the neuraminidase-deficient strains show very high levels of blood clearance. Neuraminidase A is known to decrease efficacy of neutrophil killing [91], so it is possible neuraminidase B has a similar effect on the host. Our ensembles do not demonstrate such a stark contrast in the

intrapulmonary phagocytosis rates, however. A lower intensity of immune response in the lungs is sufficient to clear the bacteria.

We have utilized experimental data for neutrophil levels and for bacterial levels in the lungs and in the blood to calibrate the model. We have not fit the trajectory of the damage variable to any data and therefore this trajectory is a prediction of the model that can be potentially used to validate our results. There are several ways that damage to epithelium can be monitored; one possibility is by means of a biomarker such as decreased lung capacity or decreased epithelial cell cilia [95,96]. The other possibility is to use histological samples to assess the level of epithelial damage. The addition of damage level data to future uses of the model could change the distributions of q, possibly making them to be tighter to adhere to a particular range of data.

The ensemble model approach to data analysis can accommodate uncertainty in data, but it does have limitations. Our equation-based model might be considered complex by some researchers (it requires 17 parameters), yet, even so, it greatly simplifies the actual biology of the immune response. For example, parameter ν lumps several different mechanisms involved in mucosal immunity, only one type of immune cells is assumed to remove pathogens, and we do not directly account for intercellular signaling. Unfortunately, experimental datasets required to parametrize more complex and biologically accurate models describing these mechanisms currently do not exist. Accordingly, we perceive our contribution as hypothesis-generating and as a basis for guiding future mechanistically-based experimentation. Future iterations of the model could address some of these simplifying assumptions, perhaps providing for a more detailed account of the host immune system. Another important assumption of the model is that, within the lung or blood compartments, the system is well-mixed. In reality, there is a spatial component to

bacterial infections that this simple model is unable to capture. Future models may allow for this spatial heterogeneity to be incorporated into the dynamics.

3.9 CONCLUSIONS FROM PNEUMONIA MODEL STUDIES

Throughout Chapters 2 and 3, we have demonstrated the biological relevance of the ODE model presented in Equations 2.1-2.4. First, Chapter 2 showed that the model is capable of depicting four very different reactions to an identical inoculum. By defining a few parameters as mouse-strain-dependent, we can generate ensembles in which only four parameters change value in order to change the phenotype. Blood bacteria levels were shown to be an important factor in determining whether a host will survive a pneumococcal infection; if blood bacteria are allowed to reproduce too quickly, they will overrun the host and cause quick morbidity and mortality. Strong extrapulmonary phagocytosis rates, however, can contain blood bacteria to manageable levels, allowing the infection to be resolved.

Chapter 3 presents an important extension of our previously proposed model that shows its utility not only in modeling how different hosts response to the same bacterial infection, but also how identical hosts respond to multiple types of bacterial infections. Our model is able to capture the initial decay followed by quick rise in lung bacterial loads associated with a rise in blood bacterial loads. We have demonstrated how the parameters of our model can be used to analyze and predict the immune responses of the host to each type of bacteria. This work provides a path forward for future work modeling the response to different bacterial strains or adding complexity to the model by incorporating more components of the immune system explicitly in the equations.

4.0 ORDINARY DIFFERENTIAL EQUATION MODEL OF THE INTRAHOST IMMUNE RESPONSE TO INFLUENZA A VIRAL INFECTION

4.1 OVERVIEW

Influenza A virus continues to be a leading cause of morbidity and mortality worldwide. While the virus itself can often be lethal, the host's immune response, particularly the inflammatory response, is often a major contributor to the lethality of disease. An ordinary differential equation model of the intrahost immune response to influenza infection is presented here. The model was calibrated to experimental data from mice infected with H1N1 at either a survivable or nonsurvivable dose. Using Markov chain Monte Carlo simulations, we generated an ensemble of parameters fit to these data. Parameters were then used to study survivability of influenza infection, as well as the effect of the inflammatory response on the immune system as a whole. This work has been published in Journal of Theoretical Biology [97].

4.2 PREVIOUS WORK

Many mathematical models of the immune response to IAV infection have been developed with varying degrees of detail [98–116]. Some of the simplest model of IAV infection describe only dynamics of epithelial cells interacting directly with the virus [102,103]. These models are fit only to viral titer data, and they employ many simplifying assumptions to limit the number of parameters in the model.

Some slightly more complex models will focus on one aspect of the immune response, such as type I interferons [117] or T cells [105,118]. Other larger ODE models will include several arms of immune response [106,119–121]. Likewise, systemic inflammation has been studied using mathematical modeling, also with varying degree of detail, ranging from conceptual models, to more detailed models leveraging rich biological datasets linking cytokine expression and organ dysfunction [65,122–125].

Most published ODE models of viral infection are target cell-limited models, meaning the initial population of susceptible epithelial cells can decrease as the infection spreads, but these target cells can never regenerate. This monotonic decline in target cell populations makes the equation simple, but ensures that by the end of the simulation, all target cells in the infected tissue will be dead, implying that even if the virus is cleared from the host, the lungs will have completely decayed. While this assumption allows for a simpler model to be used, it is not biologically sound.

The model of in-host response to influenza presented in this chapter is a comprehensive model that includes all major cellular and molecular components of the immune response and inflammation. The model accounts for the classical mechanisms of antiviral immune response as represented by several arms of immunity described in the literature, including the innate, adaptive, and humoral (antibody) responses [126]. As a novel component, the model also includes the basic pathways of systemic inflammation, comprised of macrophages, pro-inflammatory and anti-inflammatory cytokines, chemokines attracting neutrophils, and toxins utilized by cytokines.

4.3 EXPERIMENTAL DATA

The experimental data for this work was obtained by Franklin Toapanta and Ted Ross and published in their previous work [127]. Female BALB/c mice, age 12-16 weeks, were given an intranasal dose of influenza A/8/PR/34 (H1N1). Mice were given either a sublethal dose of 50 plaque-forming units (PFU) or a lethal dose of 500 PFU. Those given the sublethal dose were observed for up to 19 days post-infection, and those given the lethal dose could only be observed for up to 7 days post-infection, after which time there were no surviving subjects. Toapanta and Ross collected data at day 0 (before the infection began) and at days 1, 2, 3, 5, and 7 for all mice, plus days 9, 11, 15, and 19 post-infection for the mice in the sublethal cohort. However, since the virus is cleared around day 9 and is fully eradicated by day 11, we do not include the data for days 15 and 19. At each time point, three mice were sacrificed and data were measured from these mice. We use these measurements to generate a mean and standard deviation for each variable at each measurement day. This provides us with a pooled data set; because mice need to be sacrificed in order to obtain all necessary measurements, we cannot obtain longitudinal data for murine infection studies.

Table 3 summarizes the types of data and method for measuring each variable in the system of ODEs. Of the 20 variables modeled in the system, only four have no measured data against which to calibrate them: blood neutrophils, reactive oxygen species, target epithelial cells, and infected epithelial cells. We use weight loss data as a proxy for dead epithelial cells, as these cannot be directly measured. In addition, the macrophages, antibodies, and antigen presenting cells were reported only for the sublethal cohort, so we have three fewer variables with data associated in the lethal fits than we do in the sublethal case.

Table 3: Variables and corresponding measured data for influenza model

	Variable	Units	Measured data	Measurement type
TNF	T	pg/ml	TNF	Luminex
IL-10	L	pg/ml	IL-10	Luminex
Chemokines	C	pg/ml	MCP and MIP-1β	Luminex
Macrophages	M	cell count	CD11c- CD11b+ CD40+ GR-1 dim F4/80-	Flow cytometry
Blood neutrophils	$\tilde{N}$	cell count	None	N/A
Tissue neutrophils	N	cell count	Gr-1+ (high) CD11b+ (high)	Flow cytometry
Reactive oxygen species	X	pg/ml	None	N/A
Target epithelial cells	H	cell count	Recovery/mortality	Heuristic
Infected epithelial cells	I	cell count	None	N/A
Damaged epithelial cells	D_H	cell count	Weight loss	Weight
Virus	V	pfu/ml	Influenza A/PR/8/34	Plaque assay
Type I interferon	F	pg/ml	IFN-α and IFN-β	ELISA
Type II interferon	G	pg/ml	IFN-γ	Luminex
Natural killer cells	K	cell count	CD49b(DX5)+ CD69+	Flow cytometry
Antigen presenting cells	P	cell count	CD11c+ CD11b+ CD40+ GR-1 dim	Flow cytometry
B cells	B	cell count	CD19+ CD69+	Flow cytometry
CD8+ T cells	E	cell count	CD3+ CD8+ CD69+	Flow cytometry
IL-12	W	pg/ml	IL-12	Luminex
CD4+ T cells	O	cell count	CD3+ CD4+ CD69+	Flow cytometry
Antibodies	A	pg/ml	IgM antibodies	HAI

4.4 ODE MODEL

The ODE model used to simulate the immune response to influenza infection contains 20 equations and 94 parameters. This model incorporates all branches of immunity, as well as variables for target, infected, and damaged epithelial cells. Figure 27 gives a graphical representation of this system, denoting the inflammatory response versus the remainder of the immune response. The equations used in this model are summarized below along with their biological justifications. The full list of parameters, their biological interpretations, and the bounds for each are listed in

Appendix A. Parameter bounds were taken from literature where possible, and others were estimated from previous modeling efforts.

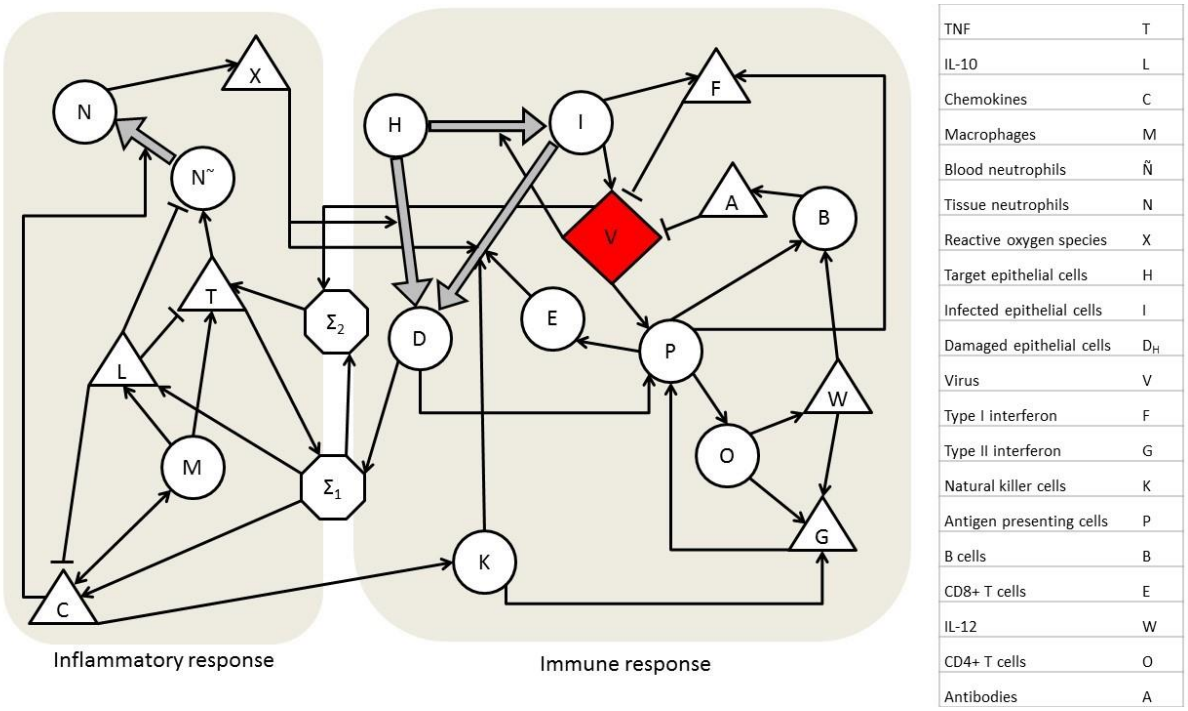

Figure 27: Graphic of interactions between variables in the influenza ODE model.

Neutrophils (Equations 4.1 and 4.2) are modeled in two separate groups: active free neutrophils (Ñ) and active neutrophils at the site of infection (N). Two processes are required for activation and recruitment of neutrophils. First, the inactive neutrophils receive a stimulation by pro-inflammatory cytokine TNF (T), but this process is inhibited by the anti-inflammatory mediator IL-10 (L). Then, chemokines (C) draw the active neutrophils to the site of infection via a chemokine gradient, driving neutrophils from the Ñ population to the N population. Both types of neutrophils have a natural decay rate of μ_n, and both populations are zero at baseline.

$$\bar{N}' = \frac{b_{nt}T}{a_{nt} + a_{nl}L + T} - \frac{g_{nc}\bar{N}C}{a_{nc} + C} - \mu_n\bar{N} \quad 4.1$$

$$N' = \frac{g_{nc}\bar{N}C}{a_{nc} + C} - \mu_n N \quad 4.2$$

Neutrophil phagocytosis produces a reactive nitric oxygen species (NOS) byproduct [128]. NOS (X) is taken up by surrounding tissue and has toxic effects on these cells [129–131]. NOS is assumed to be zero initially.

$$X' = \frac{b_{xn}N}{a_{xn} + N} - g_{xh}HX - g_{xi}IX - \mu_x X \quad 4.3$$

The macrophage population (M) is comprised of two groups: the resident alveolar macrophages and the recruited blood macrophages. Resident macrophages are represented by the nonzero initial condition, b_m. Recruited macrophages enter the tissue via a chemokine gradient, here represented by a Hill term. The cells deactivate after several days [132].

$$M' = \frac{b_{mc}C^{h_c}}{{a_{mc}}^{h_c} + C^{h_c}} - \mu_M(M - b_m) \quad 4.4$$

An important function of macrophages is the production of pro- and anti-inflammatory cytokines. We assume macrophages produce these cytokines in responses to a stimulus, represented by Σ_1 and Σ_2. The stimuli are comprised of a linear combination of pro-inflammatory signals, including TNF [133], damaged tissue (D) [134], and virus (V) [135]. The virus term in Σ_2 saturates for a low level of virus, representing the role of resident alveolar macrophages to detect and respond to the small initial presence of virus in the host.

$$\Sigma_1 = a_{11}T + a_{12}D$$

$$\Sigma_2 = \Sigma_1 + \frac{a_{21}V}{a_{22} + V}$$

Macrophages produce the pro-inflammatory cytokine TNF in proportion to all three inflammatory stimuli (Σ_2) in a Michaelis-Menten type equation. IL-10 (L) inhibits TNF production to maintain an inflammatory balance in the tissue. Both the maximum production rate of TNF and the substrate affinity are tempered by IL-10. The half-life of TNF is on the order of minutes [136].

$$T' = \frac{b_t M \Sigma_2}{\Sigma_2 + \left(\Sigma_2 + \frac{g_1 L + g_2}{L + d_2}\right)\left(\frac{k_1 L + k_2}{L + d_1}\right)} - \mu_t T \qquad 4.5$$

IL-10 production is proportional to exogenous TNF and damage only (Σ_1). Target epithelial cells (H) also produce a low level of IL-10 at baseline to maintain homeostasis in the lungs. IL-10 half-life is 1.1 – 2.6 hours [137].

$$L' = \frac{b_l M \Sigma_1}{\Sigma_1 + \left(\frac{g_1 L + g_2}{L + d_2}\right)} - \mu_l (L - b_{lh}\,(1 - R_F)\,H) \qquad 4.6$$

Chemokine production by macrophages is also modeled as a Michaelis-Menten function of inflammatory signal Σ_1, inhibited by a function of IL-10. The chemokine population decays on the order of minutes [138].

$$C' = \frac{b_c M \Sigma_1}{\Sigma_1 + \left(\frac{g_1 L + g_2}{L + d_2}\right)} - \mu_c C \qquad 4.7$$

Type I interferon (F) is primarily produced by infected cells and antigen presenting cells (P) [139]. Interferon levels decrease in one of two ways. Infected cells can absorb free interferon, or interferons can decay naturally.

$$F' = b_{fi}(1 - R_F)I + b_{fp}P - g_{fi}IF - \mu_f F \qquad 4.8$$

Interferon production by infected cells is limited by saturation term R_F. R_F is an algebraic term representing the saturation of type I interferon in the system [7,117,140], where $R_F = \frac{F}{a_{rf} + F}$. R_F can take on values between 0 and 1. The R_F term was derived from the resistant class of cells used in the Hancioglu et al. model, from which this model was derived [119]. In the Hancioglu model, epithelial cells can be divided into healthy, infected, or resistant cells. Resistant cells are unable to be infected by virus due to an influx of type I interferon preventing viral replication in the cell. However, defining a class of epithelial cells as "resistant" to viral infection is a bit simplistic; even epithelial cells with high interferon present can become infected. Instead, we define a R_F to represent the percentage of epithelial cells affected by interferon. Type I interferon is so named because it interferes with the cellular reproduction machinery, halting viral reproduction within the cell.

Target epithelial cells (H) are stimulated to reproduce by nearby dead or damaged epithelial cells ($D_H + D_I$). Type I interferons, however, slow this reproduction by interfering with mitosis; this process is represented by the $(1 - R_F)$ term in the epithelial cell reproduction term. At baseline, target cells are at their maximum value, H_{max}. The target cell reproduction term also contains an Allee threshold θ. The Allee threshold is defined as the population size below which a reproduction term will become negative [141], i.e. if $H < \theta$, $(H - \theta)$ becomes negative and the

healthy cell population will decay. When H is above θ, healthy cells may regenerate, eventually returning to H_{max} in the event of a survivable infection.

$$H' = b_h H(1 - R_F)(D_H + D_I)\left(\frac{H - \theta}{H_0}\right) - g_{hv} VH - \frac{g_{hx} HX^{h_x}}{{a_{hx}}^{h_x} + X^{h_x}} \quad 4.9$$

Infected epithelial cells arise as target cells interact with the virus. We assume an infected cell will not undergo mitosis [142]. Thus, the virus must be present for the infected cell population to continue growing. Both NK cells and cytotoxic T cells (E) clear infected cells from the lungs. A Hill term is used to denote the death of infected cells as a byproduct of interaction with NOS. Infected cells are presumed to be zero before the infection begins.

$$I' = g_{HV} VH - \frac{g_{ix} IX^{h_x}}{{a_{ix}}^{h_x} + X^{h_x}} - b_{ik} R_F IK - b_{ie} R_F IE - \mu_i (1 - R_F) I \quad 4.10$$

Virus (V) is produced by infected cells, hindered by the presence of type I interferon. Free virus is depleted when interacting with a target cell to create a new infected cell, and virus can also decay naturally. Two immune responses are included in the viral equation. We include a saturating term representing the mechanical clearance of virus from the lungs via mucociliary action at rate g_v[143]. This term is analogous to the ν term in the pneumonia model presented in Chapters 2 and 3. Virus can also be cleared by interaction with antibodies (A).

$$V' = g_{vi}(1 - R_F) I - g_{vh} HV - \frac{g_v V}{1 + a_v V} - g_{va} AV - \mu_v V \quad 4.11$$

Uninfected, damaged target epithelial cells (D_H) arise as a result of an interaction between NOS and healthy target cells, which we model with a Hill function. Damaged cells are cleared as healthy cells regenerate.

$$D_H' = \frac{g_{hx} H X^{h_x}}{{a_{hx}}^{h_x} + X^{h_x}} - b_h(H)(1 - R_F)(D_H)\left(\frac{H - \theta}{H_{\max}}\right) \quad 4.12$$

There also exists a population of infected damaged cells (D_I). Assuming H_{max} is the maximum number of epithelial cells in the lungs, the number of infected damaged cells can be calculated with an algebraic expression, assuming the total number of epithelial cells remains constant: $D_I = Hmax - H - I - D_H$.

Cytotoxic T cells (E) exist endemically at low levels and are recruited to the site of infection by antigen presenting cells, represented by a Hill term. CTLs decay naturally on the order of days [144,145]. In addition, some CTLs deactivate as a result of infected cell lysis. CTLs can become fatigued after removing infected cells from the host, rendering them less effective against the virus [146]. The infected cell removal is also multiplied by the R_F term, since CTLs affect infected cells that are in the presence of interferon [117].

$$E' = \frac{b_{ep} P^{h_e}}{{a_{ep}}^{h_e} + P^{h_e}} - b_{ei} R_F I E - \mu_e E \quad 4.13$$

B cells (B) also exist endemically at low levels in the tissue (represented by b_b). B cells mature from a pool of undifferentiated B cells (B_0), aided by antigen presenting cells (P) and regulatory cytokine IL-12 (W). B cells have a long half-life but deactivate on the order of days.

$$B' = b_b + b_{bp} W P\ (B_0 - B) - \mu_b B \quad 4.14$$

Antibodies (A) are produced in proportion to the population of mature B cells. Antibodies decay naturally after several weeks [147]. Those that come in contact with virus will also be removed from the system. Antibodies are assumed to start at a low initial level of b_a.

$$A' = b_a + b_{ab}B - g_{av}AV - \mu_a A \tag{4.15}$$

Natural killer (NK) cells (K) are present in low quantities in the lung in the absence of infection, which we model with a nonzero baseline value of b_k. NK cells are primarily brought to the lungs by the chemokine gradient [148], modeled here with a Hill function. The NK cells are depleted either naturally or after lysing infected epithelial cells (I) at a rate g_{ki} [8,9,145,148,149].

$$K' = b_k + \frac{b_{kc}C^{h_k}}{{a_{kc}}^{h_k} + C^{h_k}} - g_{ki}R_F IK - \mu_k K \tag{4.16}$$

Several types of cells can be classified as an antigen presenting cell (APC). Macrophages and dendritic cells both possess antigen presentation capability. Here, we differentiate in the experimental data between the macrophage modeled in equation 4.4 and the APC by the presence of cluster-differentiation factor 11c (CD11c+) [150]. The formulation of the APC equation is similar to that in the Hancioglu model [107]. APCs (P) are largely recruited to the lungs after exposure to virus or damaged infected cells, aided by the presence of type II interferon (G). APCs deactivate on the order of days [151] and begin at a nonzero level equivalent to parameter b_p.

$$P' = P_0\left(\frac{g_{pv}V}{a_{pv} + V} + g_{pd}D_I\right)\left(g_p + \frac{b_{pg}G}{a_{pg} + G}\right) - \mu_p(P - b_p) \tag{4.17}$$

IL-12 (W) is produced by APCs as they interact with T helper cells (O). We use a Michaelis-Menten term here to denote the saturation of available receptors for T helper cells on the APC surface. IL-12 exists endemically in the tissue, represented by nonzero initial condition b_w, and it decays naturally at rate μ_W.

$$W' = b_w + \frac{b_{wo}O}{a_{wo} + O}P - \mu_w W \tag{4.18}$$

Type II interferon (G) is produced primarily by NK cells [8,9] and T_H1 cells [7,10], enhanced by the presence of IL-12. Type II interferon has a relatively short half-life, decaying after several hours [7,8,140].

$$G' = \frac{b_{go}W + g_{go}}{a_{go} + W}O + \frac{b_{gk}W + g_{gk}}{a_{gk} + W}K - \mu_g G \tag{4.19}$$

T_H1 cells (O) are recruited by the presence of APCs, represented here by a Hill function. T_H1 cells have a half-life on the order of days [152].

$$O' = \frac{b_{op}P^{h_o}}{{a_{op}}^{h_o} + P^{h_o}} - \mu_o O \tag{4.20}$$

These twenty equations together comprise the influenza ODE model. Table 4 gives a summary of each variable and its initial condition used in simulations. Many initial conditions are defined as relationships between parameters of the model, determined algebraically. The initial level of target epithelial cells, H_{max}, is defined as 2.5×10^5 cells, an approximation generated from the volume of a mouse's lungs. The initial level of virus is either 50 or 500 PFU, depending on whether we are simulating the sublethal or lethal infection condition.

Table 4: Initial conditions in the influenza ODE model.

	Variable	Initial condition
Blood neutrophils	$\tilde{N}$	$\tilde{N}_0 = 0$
Tissue neutrophils	N	$N_0 = 0$
Reactive oxygen species	X	$X_0 = 0$
Macrophages	M	$M_0 = b_m$
TNF	T	$T_0 = 0$
IL-10	L	$L_0 = b_{lh} H_{max}$
Chemokines	C	$C_0 = 0$
Type I interferon	F	$F_0 = b_p b_{fp} / \mu_f$
Target epithelial cells	H	$H_0 = H_{max}$
Infected epithelial cells	I	$I_0 = 0$
Virus	V	$V_0 = 50 \text{ or } 500$
Damaged, uninfected epithelial cells	D_H	$D_{H0} = 0$
CD8+ T cells	E	$\frac{\left(b_{ep}/\mu_e\right) b_p^{h_e}}{b_p^{h_e} + a_{ep}^{h_e}}$
B cells	B	$B_0 = \frac{b_b + b_{bp} b_p W_0 b_0}{b_{bp} b_p W_0 + \mu_b}$
Antibodies	A	$A_0 = (b_a + b_{ab} B_0)/\mu_a$
Natural killer cells	K	$K_0 = b_k$
Antigen presenting cells	P	$P_0 = b_p$
IL-12	W	$\frac{\left(b_p/\mu_w\right) b_{wo} O_0}{O_0 + a_{wo}}$
Type II interferon	G	$G_0 = \frac{\left(\frac{O_0}{\mu_w}\right)\left(b_{go} W_0\right)}{W_0 + a_{go}} + \frac{\left(\frac{K_0}{\mu_g}\right)\left(b_{gk} W_0\right)}{W_0 + a_{gk}}$
CD4+ T cells	O	$\frac{\left(b_{eo}/\mu_o\right) b_p^{h_o}}{b_p^{h_o} + a_{ep}^{h_o}}$

4.5 MODEL PARAMETERS AND HEURISTICS

In total the model contains 94 parameters, each with a distinct biological interpretation and boundaries between which we allow the parameters to vary in the MCMC procedure. These

parameters are summarized in Appendix A. The bounds on each parameter are determined from literature where available, or estimated from previous modeling efforts.

Three heuristic requirements are also included in the fitting procedure, constraining the admissible parameter values further. First, small perturbations from baseline (i.e. viral loads less than 1 virion) will always heal without requiring a full immune response. Second, sublethal viral loads clear completely, and cytokine levels and healthy epithelial cells must return to their baseline levels within 15 days. Lastly, the target epithelial cell population must decay to zero after a lethal inoculum. In this study, time of death is defined as the time at which healthy cells drop below 10% of their baseline value [153]. When the number of healthy cells falls below this threshold, the reproduction term in Equation 4.9 becomes negative, so healthy cells decay to zero. A potential solution which does not obey all three heuristic behaviors will have a large penalty added to its overall associated error. Unless the solution was found with a high-energy chain (in which solutions with larger errors are more likely to be accepted), this solution will end up rejected.

4.6 MARKOV CHAIN MONTE CARLO SIMULATIONS

To calibrate the model to the data, we utilize MCMC techniques (please see Section 2.5 for more details). We fit the sublethal and lethal cases simultaneously, generating a total energy for each fit that is comprised of a sum of the error of the fit to the sublethal data and the error for the fit to the lethal data. Energy is defined as the sum of errors between the predicted trajectory of the variable and the data associated with it. A set of parameters will ideally minimize the distance between the trajectory in both the sublethal and lethal fits, as well as obey a set of pre-defined heuristic behaviors integral to the qualitative behavior of the simulation.

Figure 28 represents the ensemble by plotting each parameter combination in the ensemble as a point in the objective space, where the objective values report the relative error of the fit of the trajectory for that parameter combination to either sublethal or lethal data when starting at the appropriate initial condition. Typically in multi-objective optimization, there is no single solution of the model which will yield the optimal solution for both objectives concurrently [154]. Here, that implies there is no single parameter set in the sample that would represent the optimum for both the sublethal and the lethal objectives taken from data across multiple subjects. As is common with multi-objective optimization, the optimization yields a Pareto boundary (shown as a dashed polygonal curve) which represents a collection of parameter sets that cannot improve in one objective without increasing the other objective value [154].

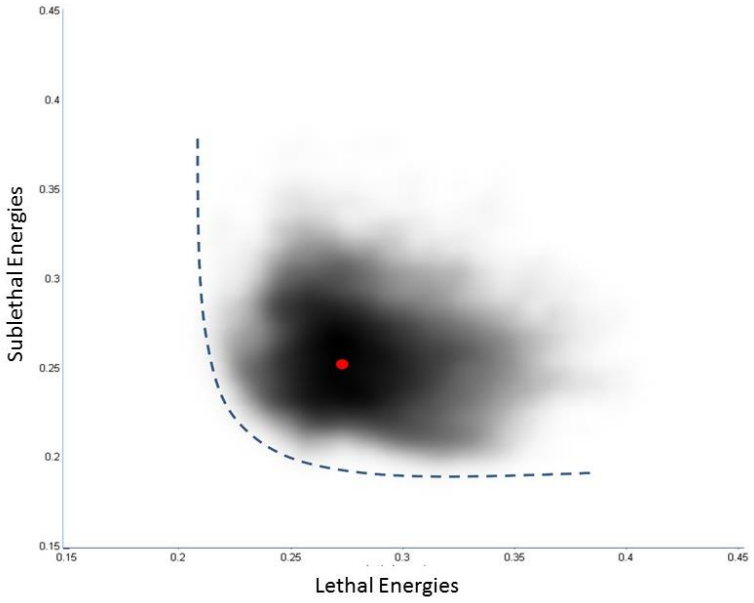

Figure 28: Distribution of energies from sublethal vs lethal fits to data.

Each dot on the graph represents a single pair of sublethal and lethal energies associated with one parameter set in the ensemble. Red dot represents the center of mass of the energy pairs. Dashed line represents Pareto boundary.

4.7 ENSEMBLE FITS TO EXPERIMENTAL DATA

4.7.1 Sublethal infection ensembles

Graphs of the ensemble trajectories for all variables for the sublethal inoculum are shown in Figure 29. The black line shows the median of the trajectories at each time point, the dark grey shows the range from 25% of trajectories above and below the median, and the light grey shows the range from 5% to 95%. Black crosses indicate the mean and standard deviation of the experimental data for each analyte.

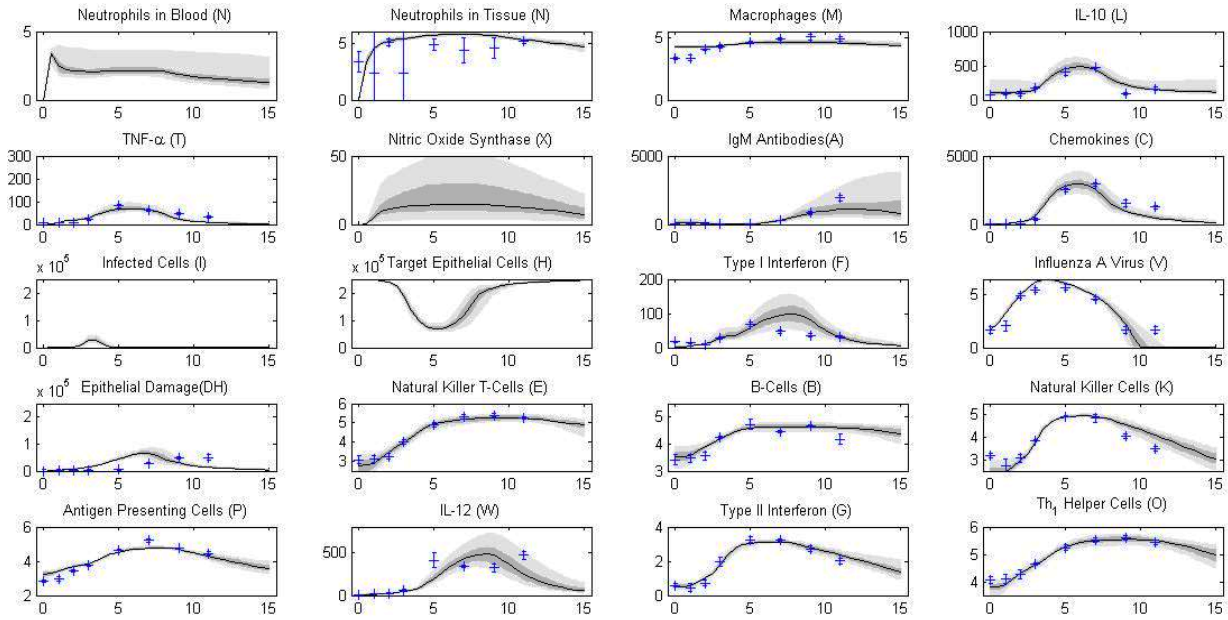

Figure 29: Ensemble fits to data for sublethal simulations of influenza ODE model. Experimental data are represented by the blue crosses, with standard deviations expressed in the error bars. Data are measured at days 0, 1, 2, 3, 5, 7, 9, and 11. The black line signifies the median trajectory, the dark gray envelope signifies 25-75% confidence, and the light gray envelope signifies 5-95% confidence.

Our predicted trajectories are generally in accord with the experimental data. Blood neutrophils (panel 1) do not have experimental data to which we fit the trajectories, but the tissue neutrophils (panel 2), which arise from chemotaxis of blood neutrophils, are matched to data. Most neutrophil data points have very large standard deviations, especially at days 1 and 3, though there are two points (at days 2 and 11) with very tight distributions. These two points drive the overall shape of the ensemble trajectories.

Macrophages (row 1, column 3) are not well matched to the first two data points. Data show the macrophages rise almost two full logs from baseline to the endpoint; our fits, however, miss the initial value of M by about one order of magnitude. Experiments to force the baseline value of M to the data value were ineffective, hurting the overall fit of several other variables while slightly improving the macrophage fit (data not shown).

Macrophages are a major source of IL-10, TNF, and chemokines. IL-10 (row 1, column 4) and TNF (row 2, column 1) both fit well to their corresponding data. TNF trajectories rise until about day 6, and then fall back to baseline around day 11. IL-10 trajectories peak a day later than TNF, around day 7. IL-10 tends to be very tightly distributed, with the greatest variation seen in the initial level of IL-10, corresponding to variation in parameter b_{lh}. Chemokines (row 2, column 4) are matched to data for total levels of MCP-1 and MIP-1β, both of which recruit macrophages to the site of infection. Chemokine trajectories peak around day 7 and then quickly fall back to baseline levels as the inflammatory response begins to wane. The other cytokine modeled here is IL-12 (row 5, column 2). IL-12 data is bimodal, with a peak at day 5, a small decline to day 9, and then a second peak at day 11. Our ensemble instead peaks at day 9 and misses the points at days 5 and 9.

The virus (row 3, column 4) rises continuously for the first four days post-infection, peaks at day 4, and then falls for the next five days, leading to its clearance around day 9. The peak of the ensemble is almost a full log higher than the peak exhibited in the data. Infected cells (row 3, column 1) peak around the same time as the virus, at around 20% of H_{max}.

Target epithelial cells (row 3, column 2) begin at H_{max}, which we set at $2.5 \, x \, 10^5$. Target cell levels begin decaying quickly after the start of the infection, reaching a minimum around day 5, falling to about 40% of the initial value. Our system is not a target cell-limited model, so the target cells are able to regenerate and eventually return to H_{max} about two weeks after the infection began. Target cell-limited models are common [102,112,116,155,156], and in each the susceptible cell population decays to zero over time, which depletes the potential source of infected cells, ensuring the virus will eventually clear even without immune response intervention. Importantly, our model forces the virus to clear without depleting the epithelial cell population; influenza infection leads to a heterogeneous infection, with some areas of the lung more severely damaged than others, but there always remains a population of epithelial cells at the end [157]. Thus the influenza model makes an important step towards more accurately modeling the true biology of the immune response to infection.

Trajectories for damaged cells (row 4, column 1) peak at day 7, coinciding with the peak of the majority of NOS trajectories (row 2, column 2). However, the data do not peak until day 9, suggesting that our use of weight loss as a proxy for epithelial damage may not be appropriate for this model.

Antibodies (row 2, column 3) are the major source of viral clearance. They remain at or below the level of detection for the first five days, and then rise steadily until day 11, at which point about half the trajectories begin to fall while the others continue to rise. B cells (row 3,

column 3) are the source of antibodies in this model. B cells fit their data well, rising quickly for five days, and then remaining relatively stagnant for the remainder of the experiment, in accord with the data.

CTLs, T_H1 cells, and APCs all fit their corresponding data very well. NK cells (row 4, column 4) fit the rise of the data over the first 7 days, but the simulated trajectories are slower to return to baseline than the data imply.

Type II interferon (row 5, column 3) follows the data tightly. Type I interferon follows the first five days of data well, but the simulated trajectories continue to rise until day 8, whereas the data fall after day 5. Our model therefore misses the peak of type I interferon by around 3 days. The equation for type I interferons (Equation 4.8) includes two production terms. First, infected cells produce the majority of interferons, and then as the infection progresses and infected cells die out, antigen presenting cells are the major contributor to interferon production. The APC production of interferon drives the late peak, and as such, the reliance on APC production of interferon in the model may be too high to accurately predict the biology.

4.7.2 Lethal infection ensembles

Figure 30 shows the ensemble fits to the lethal infection data. In these simulations, death is defined as the point when target cells are depleted, which occurs here at day 7, in accord with experiments. Subplots are shown in the same order as Figure 29. Most predictions seem to fit to data well, though a few variables do not.

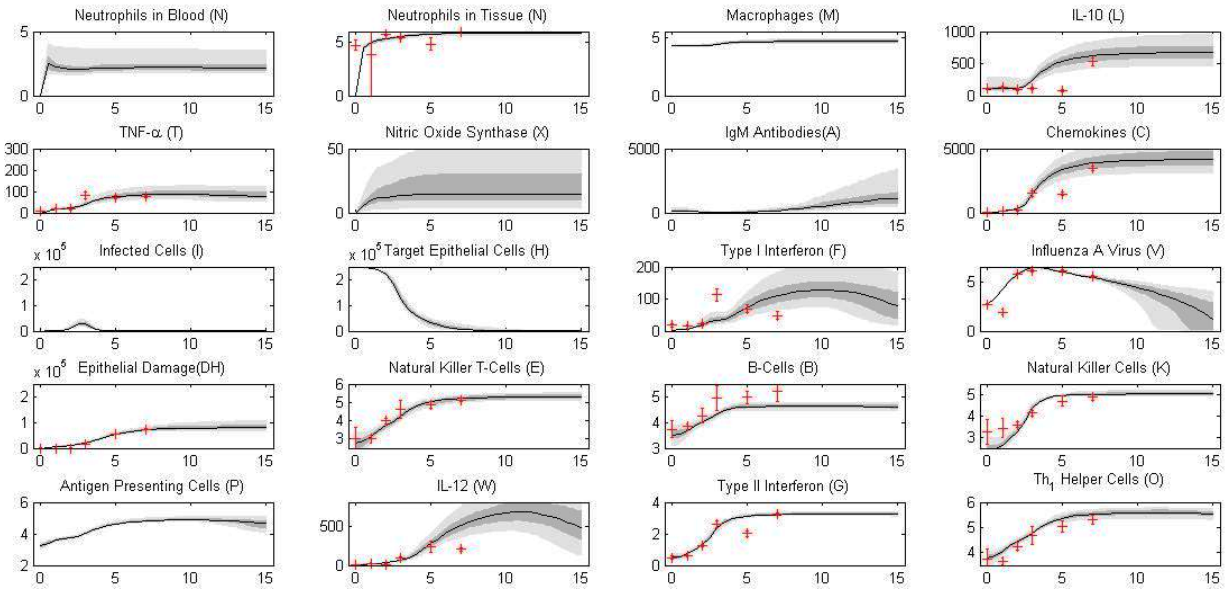

Figure 30: Ensemble fits to data for lethal simulations of influenza ODE model.

Experimental data are represented by the red crosses, with standard deviations expressed in the error bars. Data are measured at days 0, 1, 2, 3, 5, and 7. The black line signifies the median trajectory, the dark gray envelope signifies 25-75% confidence, and the light gray envelope signifies 5-95% confidence.

In the first row, we see blood neutrophils have a predicted trajectory similar to that in the sublethal case, but the neutrophil level remains high throughout the simulation, rather than dropping off as in the sublethal trajectories. Tissue neutrophils rise quickly and stay high, in accord with experimental data. There is no data given for macrophages in the lethal case, but the prediction shows a macrophage trajectory very similar to that in the sublethal case. IL-10 trajectories begin rising about three days before the data do. Since the data measure only free IL-10, it may be that more IL-10 receptors are activated in response to the high virus levels, thus decreasing the amount of free IL-10 without actually denoting a decrease in anti-inflammatory activity in response to virus. IL-10 receptors are found on most myeloid and lymphoid cell lineages [136], so it is unclear which cell types would exhibit the increased receptors.

TNF trajectories fit well to the data, as do the chemokines. NOS and antibodies do not have data to which trajectories are matched in the lethal case. As in the sublethal, NOS rises quickly and hits its peak around day 6, but in the lethal case NOS does not drop off over time. Antibodies begin rising around day 7 and stay high through the end of the simulation.

Infected cells peak earlier in the lethal simulations, corresponding to a higher initial dose of virus, and their peak value is slightly higher than in the sublethal cohort. Virus rises quickly after the onset of infection, reaching a peak around day 4, and then dropping through the remainder of the experiment. Our simulations miss the second viral data point, which shows an initial decrease in viral load one day after infection. This decay would indicate an eclipse period, a time between infection and the production of free virions by epithelial cells, which lasts about 6 – 8 hours [158]. We do not include the eclipse phase in the model, but future iterations of this work may include it to more accurately predict this data.

Type I interferon is again poorly predicted by the ensemble, as the data peak on day 3, while the ensemble comes to a slow peak around day 10. The interferon data peak two days earlier after a lethal infection than a sublethal infection, and with such tight standard deviations on the data, these features are difficult for the ensemble to accurately capture.

Damaged cells, CTLs, and NK cells all generally predict the data well. B cell predictions tend to be a bit lower than the data suggest; our ensemble misses the peak value but follows the general shape of the data well. Antibodies, which do not have corresponding data in the lethal cohort, stay low until day 5 and then rise steadily to the end of the experiment, much like the sublethal predictions.

APCs were not measured in the lethal infection, and their predicted trajectories generally look similar to those predicted in the sublethal case. Type II interferon and helper T cells follow

the data well. IL-12 predicts the first four data points well, but the second half of the infection is not well calibrated. The peak of the data occurs at day 5, while the ensemble continues to rise until day 11 and peaks at a value much higher than the data imply.

Overall, Figure 30 shows a well-calibrated model that follows the trends defined by the experimental data. The peak level of the virus is about 3 times higher in the lethal condition than in the sublethal condition. We also see higher peak values in the cytokines and chemokines after the lethal inoculum, leading to a subsequently higher inflammatory response and increased rate of epithelial damage.

4.8 MARGINAL DISTRIBUTIONS FOR ALL PARAMETERS

Shown in Figure 31 are the marginal distributions for all 94 parameters of the model. The upper and lower bounds of the horizontal axis of each subplot are equal to the bounds within which the parameter was allowed to vary. These bounds are listed explicitly in Appendix A. Sensitivity of individual parameters can be inferred from these marginal distributions; the more narrow the distribution, the more sensitive the system is to that parameter's value.

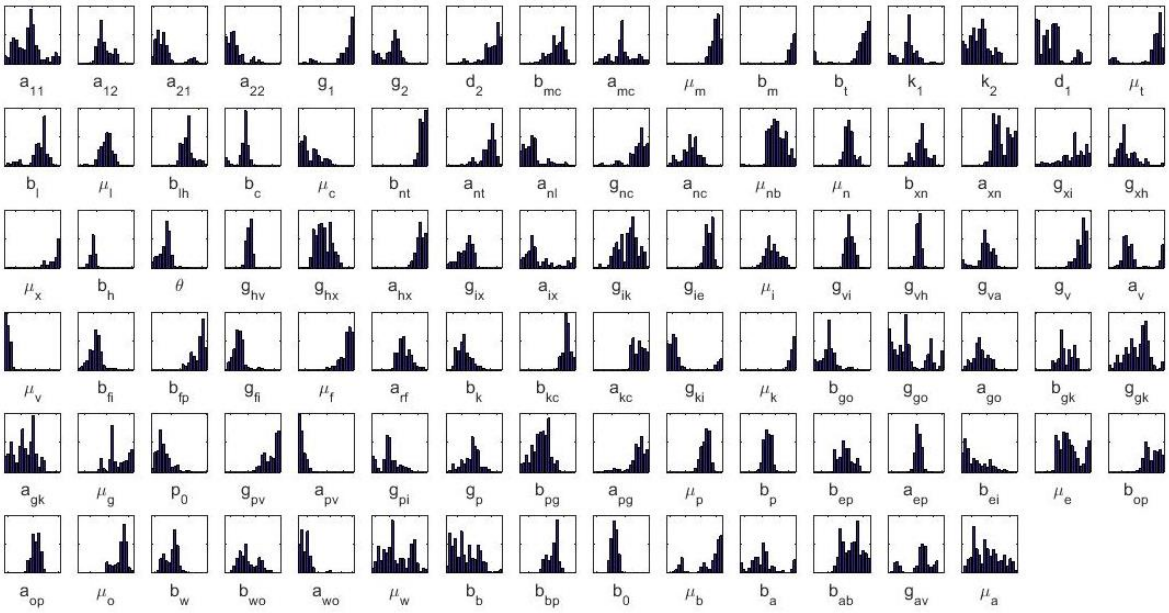

Figure 31: Posterior distributions for all parameters of the influenza ODE model.

4.9 PREDICTING HOST SURVIVAL

Though our experimental data includes only predictions for host response after 50 PFU and 500 PFU doses of virus, we want to determine how our model reacts to other viral inocula to see at what point the behavior of the ensemble changes from survival to nonsurvival. In Figure 32, we show how changing the inoculum changes the outcome of the infection by tracking the change in target cell population over time. Other published influenza ODE models do not include dynamics of epithelial cells such that the acan be used to track symptomaticity of infection. Our ODE model is the first to be calibrated such that changing only the initial condition of the virus allows for a change in the trajectory of the target cell population corresponding to severity of infection.

Using one representative parameter set from the ensemble, we simulated the system of ODEs at each of 11 different viral inocula. These simulations denote three distinct regimes of behavior:

(1) A very low inoculum (5 PFU in this example) leads to an asymptomatic infection, in which there is no discernable change in the target epithelial cell population. With no excess damage detected in the simulations, we can conclude that the virus is cleared by nonspecific immunity, without the need for adaptive or humoral responses to be activated. The virus will monotonically decay to be fully cleared after only a few days.

(2) A moderate inoculum (here, between 25 PFU and 150 PFU) will lead to a sublethal infection, defined as a loss of target cells followed by an increase in target cells leading to a full recovery. The substantial loss of target cells corresponds to an infection in which the virus was able to persist, meaning the immune system would have been activated. After reaching a minimum around a week after the infection began, the target cells will quickly regenerate, eventually reaching their starting value H_{max} again.

(3) A large inoculum (here, 175 PFU and above) will lead to a lethal infection. Death in this model is defined as the point at which target cells have been fully depleted. Unlike the sublethal infection examples, target cells monotonically decay as the virus population overwhelms the tissue and inflammation causes excess damage.

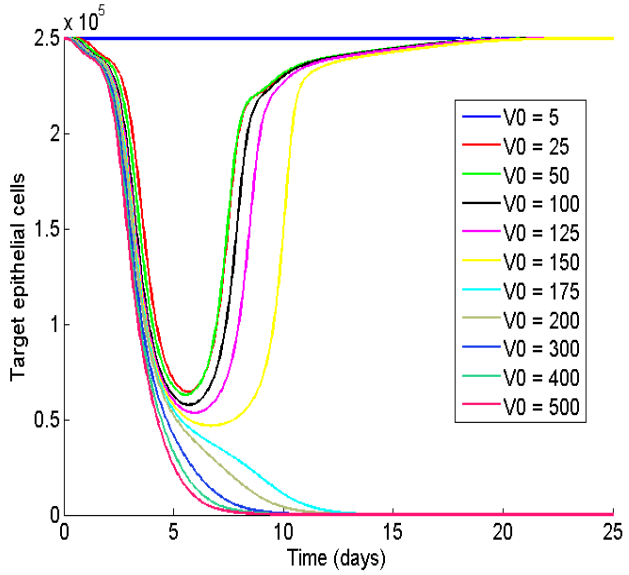

Figure 32: Effect of varying initial virus level in influenza ODE model.

Each line indicates one representative target cell trajectory using a single parameter set with a particular initial value of V. The curves identify three regimes of behavior: asymptomatic infection, sublethal infection, and lethal infection, depending upon the viral load given to the host.

In contrast to Figure 32, the next analysis utilizes the full ensemble to study the delineation between these three behaviors of the model. Figure 33 shows the thresholds between each of these regimes for our ensemble. As the initial viral load is varied from 0.01 PFU to 1000 PFU, the proportion of the ensemble exhibiting asymptomatic, sublethal, or lethal infections is calculated and plotted. In our calibrated model, any infection beginning with 0.1 PFU or less will lead to an asymptomatic infection. Likewise, an inoculum of 500 PFU or higher will always lead to a lethal infection. The variation between these two extremes corresponds to variation in the parameters of the ensemble.

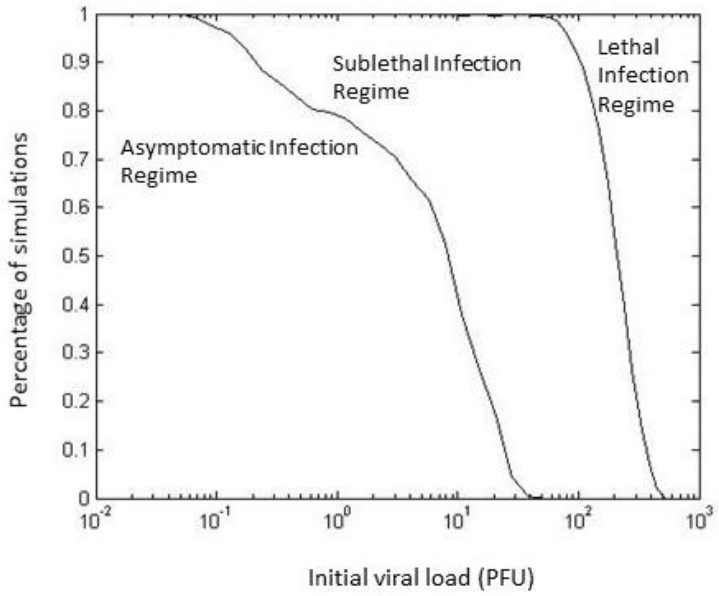

Figure 33: Regimes of behavior as identified by the ensemble.

When beginning a simulation with the initial condition of the virus equal to the value on the horizontal axis, we can calculate what percentage of the parameter sets in the ensemble would lead to either an asymptomatic, symptomatic sublethal, or lethal infection. Lines on the As the amount of initial virus increases, the likelihood of a symptomatic infection also increases.

Finally, the probability of survival over time can also be calculated for the ensemble. Survival curves, plotted in Figure 34, demonstrate the likelihood of a lethal infection after a particular viral dosage, ranging from 50 PFU to 750 PFU. As the inoculum increases, the time at which a percentage of the ensemble begins to die decreases, meaning a larger inoculum leads to faster morbidity. A dosage of about 210 PFU leads to about 50% survival at day 15. At 750 PFU, the highest inoculum tested in this study, only about 50% of the population can survive 5 days post-infection, and all members of the ensemble are predicted to be deceased by day 7. Since we used 500 PFU as the dosage at which to calibrate a lethal infection, we would expect any dosage

higher than 500 PFU would lead to death by at most 7 days post-infection. The survival curves validate this.

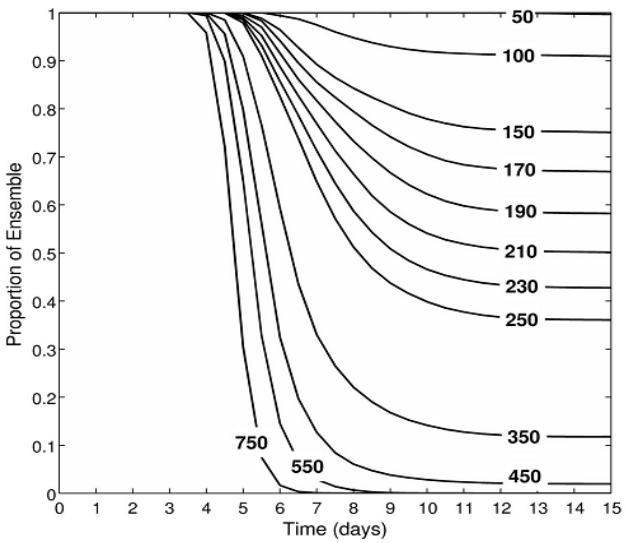

Figure 34: Survival curves.

Each curve represents the predicted length of survival of the ensemble for varied viral dosages. At the sublethal calibration dose, 50 PFU, 100% of the population survives for 15 days post-infection. As the dosage increases, the likelihood of survival to 15 days decreases. At the highest tested dose, 750 PFU, the ensemble predicts only about 50% of the population would survive to 5 days, and all members of the population are dead by day 7.

4.10 EFFECT OF SELECTED IMMUNE RESPONSE DELETIONS ON HOST SURVIVAL

As described in Section 4.4, the stimuli Σ_1 and Σ_2 represent linear combinations of pro-inflammatory signals that initiate the inflammatory response. TNF, IL-10, and chemokines are directly stimulated by these signals, and other effects like NK cell stimulation and NOS production are impacted by Σ_1 and Σ_2 further down the inflammatory cascade. The addition of the in-depth

inflammatory component in the model is an important physiological feature of the immune system, and as such we experiment with knockouts of various components of the inflammatory response to judge their impact on the system as a whole. Figure 35 demonstrates the effect of these knockouts on a select set of model variables: IL-10, TNF, NOS, infected cells, target cells, virus, and NK cells. Each row represents one variable, while each column denotes a separate knockout experiment. To perform the knockouts, one or more variables are forced to remain at their baseline level by setting the right hand side of the corresponding equation to zeros (i.e. $dY/dt = 0$ for some variable Y). In every experiment, the inoculum used was 50 PFU, previously identified as a survivable dose for these hosts.

Column 1 shows the wild-type behavior of the ensemble for comparison. These trajectories are identical to those shown previously in Figure 29, as no equation is altered in this experiment. Column 2 shows the behavior of the model if the inflammatory response is completely shut off. To do this, we turn off both Σ_1 and Σ_2, which prevents the inflammation from ever turning on. Without this arm of the immune response, the system is unable to heal, as we see a monotonic decay of target cells and high levels of virus, corresponding to higher peak values of infected cells.

The two major effectors of inflammatory feedback in the model are NK cells and NOS. In columns 3 and 4, we turn off each of these components individually to judge their overall impact on the system. Without an increase in NK cells (column 3), the system is again unable to heal, though death is reached about one day slower than in the "no inflammation" case. When NOS is fixed at zero, a similar result occurs. NK cells and NOS both keep the infected cell population in check; without them, it may be that the infected cell population cannot be controlled by the remaining components of the model. Increased infected cells levels will lead to much higher levels of virus, and the host will not be able to survive the infection [159,160].

In column 5, we study the effect of keeping IL-10, the anti-inflammatory mediator in the system, at its baseline value. Without the suppressive effects of IL-10, TNF peaks higher than in the wild-type. The lack of increased IL-10 does not have much of an effect on the remainder of the variables shown in Figure 35, however. In the majority of the parameter sets, fixed IL-10 leads to faster viral clearance and faster healing of target cells. In 5-25% of the ensemble, however, the increased inflammation will lead to increased target cell damage and eventual death of the host.

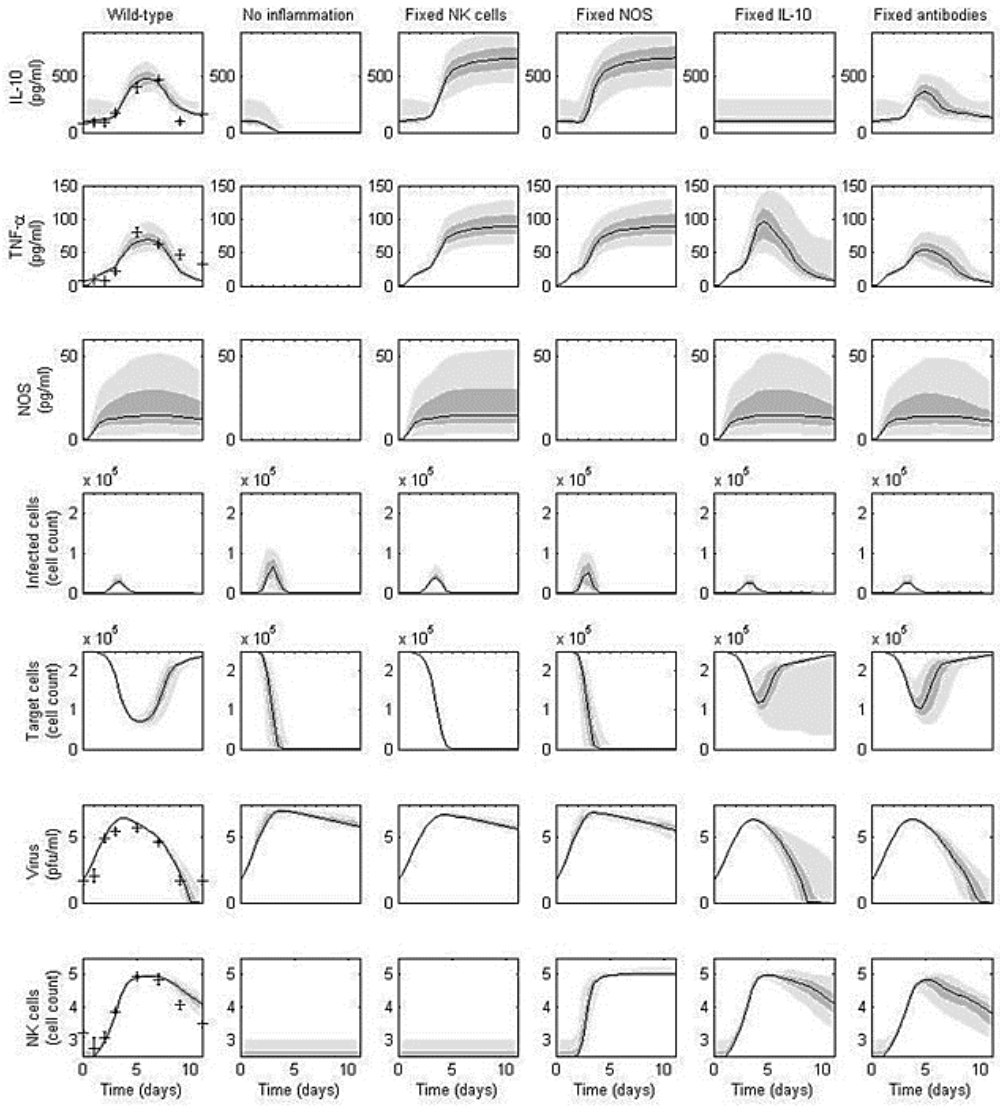

Figure 35: Immune response response deletions study for influenza model.

We also tested one non-inflammatory response knockout in column 6 of Figure 35: antibody knockout. Antibodies are critical to the clearance of viral infection. In our ODE model, however, a fixed baseline level of antibodies does not lead to prolonged viral infection. In fact, healthy target cells actually regenerate faster in the absence of antibodies. This would imply a problem with the viral clearance terms in the model. One possibility is the nonspecific clearance of virus (parameters g_{vh}, g_v, a_v, and μ_v) is too strong, meaning the importance of antibodies in viral clearance is minimized in this ensemble. Another possibility is antibody clearance of viral load is overly simplified in our $g_{av}AV$ term of the virus equation (Equation 4.11). Future iterations of this model may improve upon this antibody-virus interaction to better reflect biology.

4.11 DISCUSSION

The ensemble model of the intrahost immune response to influenza infection presented here incorporated an in-depth look at innate, adaptive, humoral, and inflammatory responses to infection. The model was calibrated to a large, detailed data set including the time-dependent responses of cells, chemokines, and cytokines to the viral infection [127]. This data set allows for a comprehensive look at the immune response, unlike many other influenza ODE models, which focus on only one or two immune responses [102–105,108,112,156,161].

A major contribution of this work is the addition of the inflammatory component to the model. In Figure 35, the importance of the inflammatory component is demonstrated, as it clearly has an impact on survival of the host. Inflammation provides a stimulus to two important effectors of infected cell control (NK cells and NOS), but unchecked inflammation can lead to excess tissue damage, ultimately causing the death of the host [162].

This ODE model was necessarily large and complex, with 20 equations and 94 parameters governing its behavior. The large body of data provided, however, necessitates a complex model to best capture the behavior of the immune system as a whole. Of the 20 variables used in the model, only four are not fit to any data, and three more are fit only in the sublethal condition. These variables (target cell count, infected cell count, NOS levels, and blood neutrophil count) were essential for accurate portrayal of the immune response and were included in the model despite their lack of corresponding measurements. The primary criticism of such large models is a concern about a lack of parameter identifiability. In these cases, we must weigh the importance of identifiability of parameters against physiological accuracy and clinical significance. Physiological systems are inherently complex, and even large models like this one are forced to simplify the biology for computational feasibility. It is impossible to uniquely estimate the parameters of this model; rather, we rely on an ensemble of potential solutions to the model. Every measurement of rate constants, half-lives, and other parameters used in this model have an inherent uncertainty built in. Ensemble models exploit this uncertainly by allowing every parameter to exist over a range of values, rather than forcing every parameter to one value. Thus we attain a posterior distribution of parameters rather than a single best-fit parameter set.

Another important feature of this model is the absence of target cell limitation. Viral clearance is possible without a total depletion of target cells, in contrast with other published models [102,156]. Physiologically, a loss of target cells is analogous to a depletion of the lung epithelium, which would certainly lead to death of the host, even if the virus is cleared from the system. Thus our model reflects an important component of host recovery not seen in many other published models.

One disadvantage of this model is the computation time needed to fully explore the parameter space. With a 94-dimensional model space, weeks were required to generate the ensemble. Though we used parallel tempering techniques to explore the space more thoroughly, the time needed for this model may be prohibitive for some future projects.

5.0 DISCRETE DYNAMICAL MODELING OF INTRAHOST INFLUENZA INFECTION SUGGESTS AGE-DEPENDENT DIFFERENCES IN IMMUNE RESPONSES

5.1 INTRODUCTION

Influenza A virus leads to about 36,000 deaths every year in the United States [163]. The elderly population is highly susceptible to influenza infection, accounting for about 90% of all influenza deaths [164]. The increased susceptibility of the elderly to infections leads to enormous medical costs; the elderly account for about half the hospital stays and a third of the prescription drug use in the United States [165]. These costs will likely continue to increase well into this century, as the elderly population is predicted to triple by 2050, reaching about 2 billion individuals worldwide [165].

The elderly are known to exhibit increased morbidity and mortality in response to influenza infection due to a weakening of the immune response with age, called immunosenescence [166]. Immunosenescence is a complicated remodeling of the immune response, leading to an overall weakened response to pathogens, particularly those which have not been encountered by the host previously. Both innate and adaptive responses are impacted by immunosenescence [167]. Both mice and humans have been shown to exhibit dysregulated inflammation in response to infection due to immunosenescence [168]. The elderly generally experience a delayed onset of innate immunity and a prolonged inflammatory response, causing excess inflammatory damage to the body and thus more persistent symptoms. Elderly hosts tend to have higher baseline levels of pro-inflammatory cytokines, a condition recently termed “inflamm-aging” [169]. Elevated cytokines

are correlated with increased inflammatory damage. In fact, elevated IL-6 post-infection is the most accurate predictor of morbidity and mortality [167]. Phagocytosis by immune cells also tends to decrease with age in human hosts, particularly in neutrophils, though neutrophil efficacy has not been shown to decrease in elderly mice [170]. The specific changes to neutrophil secretion of various cytokines and chemokines are still largely unknown in either human or murine hosts. Changes to macrophage phagocytic function are also unclear, as some reports have shown no changes to macrophage phagocytosis [171], while others have shown evidence of a decline [172,173]. Decreased chemotactic responses have also been shown in macrophages [164].

The function of both T cells and B cells has been shown to decline with age, leading to an overall decline in the efficacy of flu vaccines [164]. Age-related thymic involution also causes a decrease in the number of naïve T lymphocytes [166], limiting the ability of the host to mount a defense against novel pathogens. Helper T cell function declines with age, as does the overall number of B cells in the host [174]. The number of IgG and IgA antibodies have been shown to increase with age, though the efficacy of antibodies against specific pathogens decreases [175].

To investigate further the changing immune mechanisms that arise in immunosenescence in response to influenza A virus, we have constructed a network model of the intrahost immune response to viral infection to elucidate the differences in immune response of older and younger hosts. Variables included in the model represent cell types, cytokines, chemokines, interferons, antibodies, and viral loads. The model features components from innate, adaptive, and humoral immunity. Cell types include macrophages, neutrophils, natural killer (NK) cells, conventional and plasmacytoid dendritic cells, T cells, B cells, and epithelial cells. To activate and recruit these cells we include cytokines and chemokines, such as interleukins IL-1α, IL-1β, IL-6, IL-10, IL-12, type I and type II interferons, tumor necrosis factor (TNF)-α, transforming growth factor (TGF)-β,

RANTES, monocyte chemotactic protein (MCP-1), and macrophage inflammatory protein (MIP)-1β., and keratinocyte chemoattractant (KC). The model also incorporates antibodies to clear the virus from the host. Interactions between virus, cells, cytokines, chemokines, and interferon comprise the early phases of the immune response, until eventually antibodies are upregulated and clear the virus. Our Boolean model investigates the structure of these interactions and compares interactions between young and older hosts.

Unlike the previous chapters, which employ systems of ODEs to model physiological systems, this study instead uses a Boolean network to model interactions between immune components. A discrete, rule-based model allows for an intuitive look at the relationship between virus, cells, chemokines, and cytokines. Rules of the model can be as simple or as complex as the user wishes, but they are perhaps more readable and more easily interpreted than an ODE. The rule-based model also has no parameters to fit, eliminating a large, time-consuming facet of ODE modeling. The most difficult part of rule-based modeling is determining the rules themselves. These are generally derived from literature knowledge, but the nature of rule-based modeling allows for data-driven rules as well. In this way, we can identify novel interactions between model components, or verify proposed immune mechanisms, with minimal computation time.

Boolean network models have previously been shown to generate important conclusions regarding the host immune response to other infections [176–179], and we now present a model of influenza infections as well. Initiated by the presence of a viral load in the lungs, the network propagates a number of processes activated to fight the infection. We match the trajectories of each component of the immune system to rich time-series data from a murine model of influenza infection [127]. Studying the time evolution of the immune response allows for analysis of the

initiation and duration of activation of these immune components and the differences seen in young and older hosts.

5.2 EXPERIMENTAL DATA

Data to which the model is calibrated were measured from BALB/c mice subjected to influenza A viral infection. Mice were in one of two age groups: adult (younger) at 12-16 weeks of age, or elderly (older) at 72-76 weeks of age. Within each of these age groups, mice were further subdivided into two cohorts based on viral dosage: sublethal (50 pfu dose) or lethal (500 pfu) [127]. (The data for the younger mice is the same data used to calibrate the ODE model presented in Chapter 4.)

In the sublethal cohort, data were taken at days 0, 1, 2, 3, 5, 7, 9, 11, 15, and 19. In the lethal cohort, data were taken at days 0, 1, 2, 3, 5, and 7, at which point the remaining mice succumbed to the infection. At each time point, three mice were sacrificed for the data measurements, and from these three mice we generated a mean and standard deviation of each measurement. We used these statistics to transform the data from real-valued measurements to Boolean values. Using the day 0 measurements as a baseline, we performed an ANOVA to test if a data point for variable X at time T is significantly larger than the value of variable X at baseline ($p < 0.05$). If a significant difference is observed, variable X is assigned a value of 1 at time T; otherwise, the variable is assigned a 0. We performed this process for all variables across all cohorts, yielding a total of 347 Boolean-valued data points with which the model can be calibrated.

5.3 GENERATION OF A BOOLEAN NETWORK

We have constructed a rule-based model of the immune response to influenza infection based on both literature and our experimental data. Our model consists of 25 variables representing viral load, immune cells, cytokines, chemokines, antibodies, and infected epithelial cells. The model is capable of capturing the complex interactions between the immune system and the virus, leading to either viral clearance or death of the host, depending on the inoculum. Table 5 summarizes the variables used in the network and the abbreviations used for each.

Each variable represents a single node of the model, with a total of 25 nodes. Each variable's trajectory over time is governed by a Boolean transfer function, or rule, which defines the conditions under which the variable should turn on at the next time step. The model is a strict two-state Boolean system, and at each time step, the rules are evaluated synchronously to set each node to one of two states: 0 (at or near baseline) or 1 (significantly above baseline). These rules are relatively simple and involve a combination of ANDs, ORs, and NOTs. If two or more components are required for the activation of a particular variable, the rule will include an AND. If one component inhibits another, the rule will include a NOT. If one of multiple sources is sufficient to activate a variable, that rule will include an OR. Because the two age groups feature distinct patterns in their data sets (in particular, there is a 1 to 2 day delay in the onset of many inflammatory components), we use different rules to model each age group's response to the infection. These two rule sets allow us to capture these differences in a data-driven manner and will provide conclusions on the impact of immunosenescence on the immune response to influenza infection. A more detailed look at the interactions known between these components is presented in the following sections.

Table 5: Variables and associated abbreviations for the Boolean network model.

Immune component	Variable name	Immune component	Variable name
Activated macrophages	ActiveM	Interferon-γ	IFNg
Tumor necrosis factor (TNF)-α	TNF	Activated neutrophils	ActiveN
Interleukin (IL)-1α	IL1a	Interferon-α/β	IFNab
IL-1β	IL1b	Activated cytotoxic T cells (CTLs)	ActiveCTL
IL-6	IL6	Plasmacytoid dendritic cells	pDC
IL-10	IL10	Activated conventional dendritic cells	ActivecDC
IL-12p70	IL12p70	Activated helper T cells	ActiveTh
RANTES	RANTES	Activated B cells	ActiveB
Monocyte chemotactic protein (MCP)-1	MCP1	Antibodies	Ab
Macrophage inflammatory protein (MIP)-1β	MIP1b	Low virus	Vlow
Keratinocyte chemoattractant	KC	High virus	Vhigh
Transforming growth factor (TGF)-β	TGFb	Infected epithelial cells	IEC
Activated natural killer (NK) cells	ActiveNK		

5.3.1.1 Innate immunity and inflammation

The first line of defense against influenza infection is the innate immune system. The presence of the virus in the respiratory tract activates the epithelial cells lining the lungs, promoting the expression of cytokines and chemokines to attract and activate innate immune cells. Neutrophils, macrophages, and dendritic cells will response to these chemical messengers, infiltrating the lungs

and promoting further inflammation through the expression of pro-inflammatory cytokines, such as IL-1α, IL-1β, TNF, and IL-6. The cells also produce chemokines to recruit more cells to the site of infection, including macrophage inflammatory protein 1b (MIP-1β, also known as CCL4), monocyte chemotactic protein 1 (MCP-1, also known as CCL2), keratinocyte chemoattractant (KC, also known as CXCL1), and RANTES (Regulated on Activation, Normal T cell Expressed and Secreted, also known as CCL5). To temper the inflammatory response, anti-inflammatory markers like TGF-β and IL-10 are upregulated as well.

Interferons (IFNs) are also upregulated early in the infection. Type I IFN (IFN-α and IFN-β) is released by infected cells and plasmacytoid dendritic cells (pDCs) and instigates an antiviral state in nearby target epithelial cells, preventing their infection. Type II IFN (IFN-γ) is important for the activation of components of the adaptive immune response, as well as NK cells.

5.3.1.2 Adaptive immunity

The adaptive immune response initiates a few days post-infection and is aimed specifically at the viral infection, whereas the innate immune response is a more general defense against pathogens. The adaptive response to viral infection is primarily composed of T cells. In this model we include responses from both CD8+ cytotoxic T cells (CTLs) and CD4+ T helper cells (T_H cells). CTLs are an important regulator of the infection, killing infected cells to keep them from spreading the infection further. T_H cells release cytokines to attract more cells to the site of infection. They also bridge the gap between adaptive and humoral immunity, activating the B cells to initiate the humoral immune response. Once B cells are activated, they differentiate into plasmablasts and plasma cells, which then begin to produce antibodies specific to the virus. These antibodies are the principal factor in viral clearance. In our model, antibody function can be hindered by the presence of IL-10 [180].

5.3.1.3 Virus and epithelium

The viral population variable is split into two variables: V_{low} and V_{high}, representing the different viral loads used as inocula in the experiments to generate the sublethal and lethal responses. A high level of virus implies that a low level is also present, but a low level of virus does not necessarily imply a V_{high} is active. Virus is cleared from the system by antibodies and is produced by the presence of free virus or infected cells.

5.3.2 Network formation

To assemble the rules of the Boolean model, we first generated a library of potential rules for each of the 25 variables. For example, the pro-inflammatory cytokine tumor necrosis factor (TNF) can be produced by neutrophils, macrophages, dendritic cells, and epithelial cells. The time at which TNF turns on dictates which of these potential producers will be most influential in its trajectory. Thus choices for TNF rules included combinations of these cells. Rule choices were generated primarily from literature, but some are also data-driven. Both adult and elderly mouse data were fit from the same library of 57 total rule choices.

5.4 OPTIMIZATION OF NETWORK RULES

In order to fit the Boolean data, we find the optimal set of rules which fit the data with the fewest total errors. We generate a separate set of rules for the older and younger mice, but only one rule set is used to model the sublethal and lethal data within one age group. To get these rule sets, we reformulated the rule discovery problem into an integer linear programming problem [181,182].

The objective function is the minimized difference between the model prediction and the measured data. The objective was then linearized using dummy variables $A_{t,s}$, given by equation 5.1.

$$\begin{aligned} &\min \sum_{s\in S}\sum_{t\in T_s} A_{t,s} \\ &\text{subject to } D_{t,s} - M_{t,s} \leq A_{t,s} \\ &D_{t,s} - M_{t,s} \geq -A_{t,s} \end{aligned} \qquad 5.1$$

where $D_{t,s}$ and $M_{t,s}$ represents the measured data and model, respectively, for state *s* at time *t*.

5.4.1.1 Formulation of Boolean rules

All Boolean rules can be expressed in the conjunctive normal form, which is comprised of a series of AND clauses: Rule $R = Q_1 \wedge Q_2 \wedge \cdots \wedge Q_N$ where Q_i is a series of inclusive OR terms: $Q_i = P_1 \vee P_2 \vee \cdots \vee P_M$ [183]. Each term P is the name of a variable in the system with or without a NOT operator preceding it, depending on whether the term has a positive or negative effect on the clause.

Let y_i represent the Boolean value of P_i. Each of the Q_i logical OR constraints can be expressed as:

$$y_1 + y_2 + \cdots + y_r \geq 1 \qquad 5.2$$

In other words, at least one y_i must be a value of 1 in order for the OR constraint to be satisfied. The AND constraint, *R*, does not need to be explicitly stated because Equation 5.2 ensures that each subclause, Q_i, is true, and if R is comprised of a series of true clauses, R must be satisfied.

The NOT clauses, $\neg P_i$, can be expressed as $(1 - y_i)$. Implications, e.g. $P_1 \Rightarrow P_2$, can be expressed as $\neg P_1 \vee P_2$, which is an OR constraint:

$$1 - y_1 + y_2 \geq 1 \quad (5.3)$$

Using this framework, we can formulate this as a mixed integer linear program (MILP) [181,182]. Potential rules are always of the form: $S_{i,t+1} \leftarrow S_t$, where S_t represents a series of logical operations acting upon the state *s* at the current time *t*. This logical clause will generate an update in the *i*-th state S_i at time $t + 1$. If this rule were true, $S_{i,t+1} \Leftrightarrow S_t$ for all time *t*. Applying the above equivalences, we obtain:

$$\neg S_{i,t+1} \vee S_t \quad (5.4)$$

$$\neg S_t \vee S_{i,t+1} \quad (5.5)$$

which we expand into the conjunctive normal form and apply the appropriate linear constraints.

Finally, in order to perform rule optimization, Boolean decision variables, D_{ij}, are initialized for every rule *j* each state *i*. The *k* OR constraints generated from the conjunctive normal form of the *ij*-th rule is now represented as:

$$\text{Constraint 1: } y_1 + y_2 + \cdots + y_r \geq D_{ij} \quad (5.6)$$

$$\text{Constraint 2: } y_1 + y_2 + \cdots + y_r \geq D_{ij}$$

...

$$\text{Constraint k: } y_1 + y_2 + \cdots + y_r \geq D_{ij}$$

We here modify the rule laid out in Equation 5.2 to allow the optimizer to turn a rule on or off, depending on how well it fits to the experimental data. If decision variable D_{ij} is 0, the values of

y_i are unconstrained and potential rule ij does not apply. If D_{ij} is 1, the rule applies. A final constraint is set such that each state may only have 1 rule selected:

$$\sum_{j=1}^{J} D_{ij} == 1 \tag{5.7}$$

Now we will look at a detailed example of constraint formation from the first potential rule listed in Table 9: ActiveM(t + 1) ← KC(t) ∧ IL6(t). This rule is equivalent to the following constraints:

$$\begin{aligned} &\text{ActiveM(t + 1)} \Rightarrow [\text{KC(t)} \wedge \text{IL6(t)}] = \neg\text{ActiveM(t + 1)} \vee [\text{KC(t)} \wedge \text{IL6(t)}] \\ &= [\neg\text{ActiveM(t + 1)} \vee \text{KC(t)}] \wedge [\neg\text{ActiveM(t + 1)} \vee \text{IL6(t)}] \end{aligned} \tag{5.8}$$

$$1 - \text{ActiveM(t + 1)} + \text{KC(t)} \geq \text{D} \tag{5.9}$$

$$1 - \text{ActiveM(t + 1)} + \text{IL6(t)} \geq \text{D} \tag{5.10}$$

$$\begin{aligned} &[\text{KC(t)} \wedge \text{IL6(t)}] \Rightarrow \text{ActiveM(t + 1)} = \neg[\text{KC(t)} \wedge \text{IL6(t)}] \vee \text{ActiveM(t + 1)} \\ &= \text{ActiveM(t + 1)} \vee \neg\text{KC(t)} \vee \neg\text{IL6(t)} \end{aligned} \tag{5.11}$$

$$\text{ActiveM(t + 1)} + 1 - \text{KC(t)} + 1 - \text{IL6(t)} \geq \text{D} \tag{5.12}$$

5.4.1.2 Python solver

A Python (version 3.5) package was written to accept Boolean data and a list of potential rules for each state. This package reformulates the inputs into an integer linear program for use with the Python Optimization Modeling Objects package (Pyomo) [184,185]. Pyomo then converts this script into a solver-friendly file, which was then solved by the IBM ILOG CPLEX

optimization studio. CPLEX was set to populate all optimum solutions. Finally, our Python package parses through this solution pool and generates the rule selection frequency identified in the results. The GLPK solver was also considered, but was unable to populate a solution pool, and an important aspect of our work is the identification of equivalent rule sets, which produce the same number of errors on the data set but are comprised of different rules for at least 1 variable in the system.

5.4.2 Simulation of the Boolean network

The Boolean network was simulated with the optPBN software package in MATLAB [186]. Error is defined as the total number of data points incorrectly predicted by the simulation. Each time step represents one day, and we simulate the system for 7 days for the lethal cohort and 19 days for the sublethal cohort. The Boolean model simulates the infection with synchronous updates. At time 0, only the virus is set to 1; all other variables are considered "off" initially. In the sublethal simulations, only V_{low} is on initially, whereas in the lethal simulations, both V_{low} and V_{high} are on initially. Within each age group, sublethal and lethal cohorts are simulated with the same set of rules; only the initial condition is changed in order to generate the trajectories predicting survival or nonsurvival of the infection.

5.4.3 Bootstrapping

To test the robustness of the rules we have presented, we performed a bootstrapping test on our data. We generated 100 new datasets by removing randomly 10% of the raw data (making sure that at least two data points remain at each time point for each variable) and recalculating the

Boolean levels for each of the 25 variables. Optimization was performed in the same way as in the full data set.

5.5 OPTIMIZED NETWORKS FOR ADULT AND ELDERLY MICE

5.5.1 Fits to adult mice data

Figure 36 shows graphically the rules chosen for the adult mice. Green lines represent two or more variables combined in an AND condition, and the black arrow represents the output of the AND rules. Blue arrows represent direct relations between two variables. Each arrow pointing into a box represents an OR condition. For example, we see KC is turned on by ActiveM OR V_{low}. Red blunted arrows represent NOT conditions. For example, V_{low} is turned off by Ab (antibodies). Dashed lines represent rules that exist in some, but not all, models that comprise the optimum solution.

Our rules for the adult mice are 95% accurate for the experimental data, missing only 11 data points in the sublethal simulations (Figure 37A and C) and 5 in the lethal simulations (Figure 37B and D). Only two of the variables (RANTES and ActiveCTL) could be simulated with more than one rule to achieve this optimal result. Each of these variables has two rules that yield identical outputs in this system. The four combinations of these alternatives yields four possible models, described in Table 6.

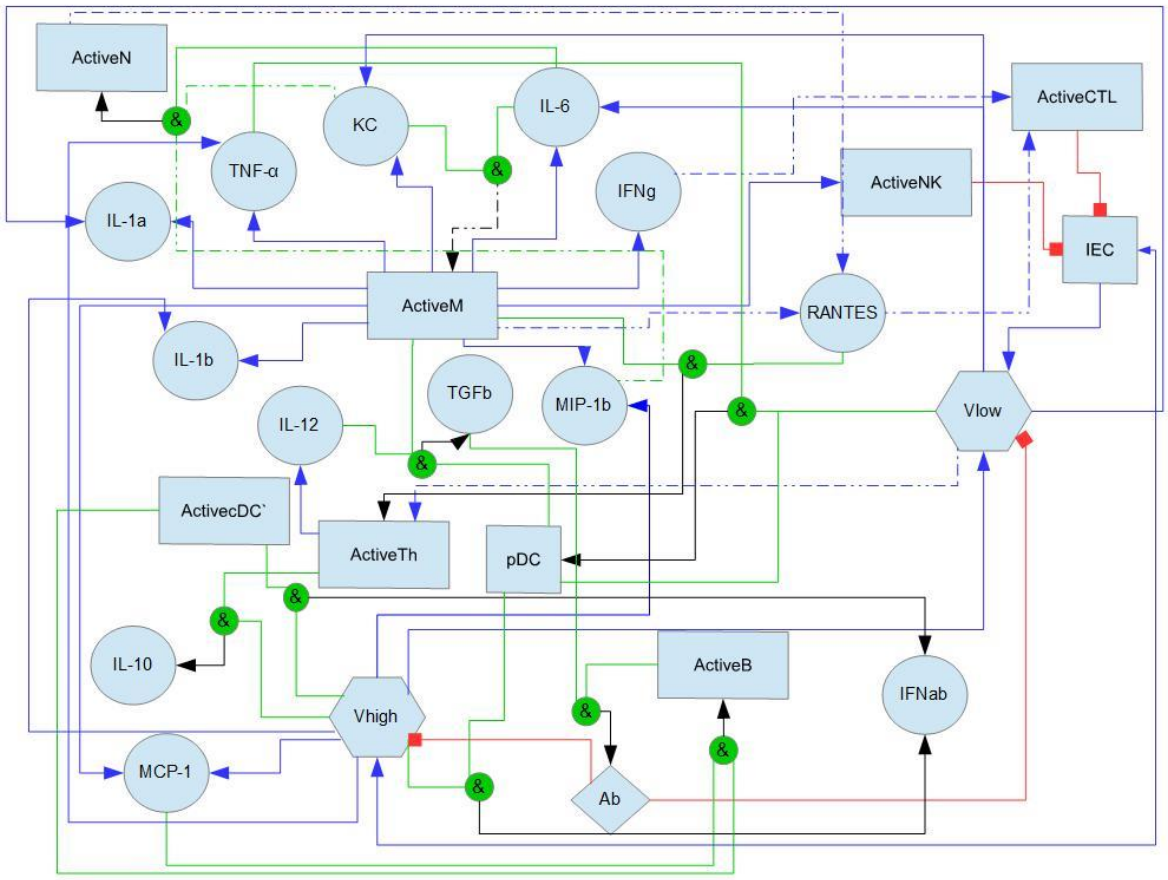

Figure 36: Graphical representation of adult mouse network model.

Diagram of adult (younger) mice rule choices for full data set. Blue arrows indicate direct relation between two components. More than one blue arrow into a variable indicates an OR condition. Green lines indicate two or more components activate another through an AND operator. Black arrows indicate the output of the AND. Red blunted arrows indicate a NOT condition. Rectangles represent cell populations, circles represent cytokines and chemokines, hexagons represent viral loads, and the diamond represents antibodies. Dashed lines represent rule alternatives that exist in some, but not all, models that comprise the optimum solution.

Table 6: Optimum rule choices for the adult mouse model.

Rule	Frequency
ActiveM ← KC & IL6	100%
TNF ← ActiveM | Vhigh	100%
IL1a ← ActiveM | Vlow	100%
IL1b ← ActiveM | Vhigh	100%
IL6 ← ActiveM | Vlow	100%
IL10 ← ActiveTh & Vhigh	100%
IL12p70 ← ActiveTh	100%
RANTES ← ActiveN	50%
RANTES ← ActiveM	50%
MCP1 ← ActiveM | Vhigh	100%
MIP1b ← ActiveM | Vhigh	100%
KC ← ActiveM | Vlow	100%
TGFb ← ActiveM & pDC & IL12p70	100%
ActiveNK ← ActiveM	100%
IFNg ← ActiveM	100%
ActiveN ← (KC | MIP1b) & IL6	100%
IFNab ← ((pDC & Vhigh) | (ActivecDC & Vhigh))	100%
ActiveCTL ← IFNg	50%
ActiveCTL ← IFNg | RANTES	50%
pDC ← (Vlow | Vhigh | pDC) & TNF	100%
ActivecDC ← Vlow | IFNg	100%
ActiveTh ← ActiveM & RANTES	100%
ActiveB ← ActivecDC & MCP1	100%
Ab ← (ActiveB & TGFb) | Ab	100%
Vlow ← (IEC | Vlow | Vhigh) & ~Ab	100%
Vhigh ← (IEC | Vhigh) & ~Ab	100%
IEC ← (Vlow | Vhigh) & ~ActiveCTL & ~ActiveNK	100%

In the sublethal case (Figure 37A), we see the first components to turn on after the infection begins are IL-1α, IL-6, KC, infected epithelial cells (IEC), and activated conventional dendritic cells (ActivecDC), each of which respond directly to the presence of the virus. Direct response to

virus represents an activated or upregulated by lung epithelial cells [187]; since we do not have data for these cells, we represent this mechanism with a simple interaction between virus and the cytokine. Dendritic cells also respond directly to the virus, implying an early influx and activation of these cells, consistent with clinical observations [13]. The presence of virus also produces a population of infected cells, which further increase the virus level in the lung tissue, creating a high level of virus at day 2.

Also on day 2, high levels of IL-6 and KC lead to the activation and migration of macrophages and neutrophils. Interferon (IFN)-γ is also activated on day 2 in response to the dendritic cells, leading to an increase in cytotoxic T cells (CTLs) at day 3. Macrophages, dendritic cells, and neutrophils increase activation of several other cytokines and chemokines on day 3, including TNF-α, IL-1β, RANTES, MCP-1, and MIP-1β. Macrophages also instigate the influx of natural killer cells.

Day 4 brings an increase in the plasmacytoid dendritic cell (pDC) population and the activation of helper T (T_H) cells and B cells. The CTLs and NK cells decrease the infected cell population on day 4, though free virus levels remain high. On day 5, the anti-inflammatory cytokines turn on, including IL-10 and TGF- β, though our rules miss this first data point for TGF-β. IL-12 also turns on at day 5 in response to the T_H cells.

The next significant event is the activation of antibodies at day 7. Antibodies clear virus levels immediately after they turn on. Virus activates pDCs to produce type I IFN, so once the virus leaves the system, IFN-α/β turns off as well. The remaining variables all remain on throughout the course of the simulation, though our data shows IL-6, IL-12, KC, and IFN-γ will turn off at day 19. There are also zeroes in TGF-β at day 15 and in NK cells at day 11. Our rules

are unable to capture these behaviors, leading to six errors in the final stages of the infection simulation.

In the lethal case (Figure 37B), many of the cytokines and chemokines turn on immediately after infection, whereas only KC, IL-1α and IL-6 were on day 1 in the sublethal case. Macrophages and neutrophils are again activated on day 2. The data also show CTLs turn on day 2, but our rules do not capture this point. pDCs are also turned on at day 2, two days earlier than in the sublethal condition.

Day 3 brings RANTES, NK cells, and type I and type II IFN. IL-10 and antibodies turn on at day 5, though our data show IL-10 is delayed until day 7. Virus levels remain high through day 7, at which point the host succumbed to the infection.

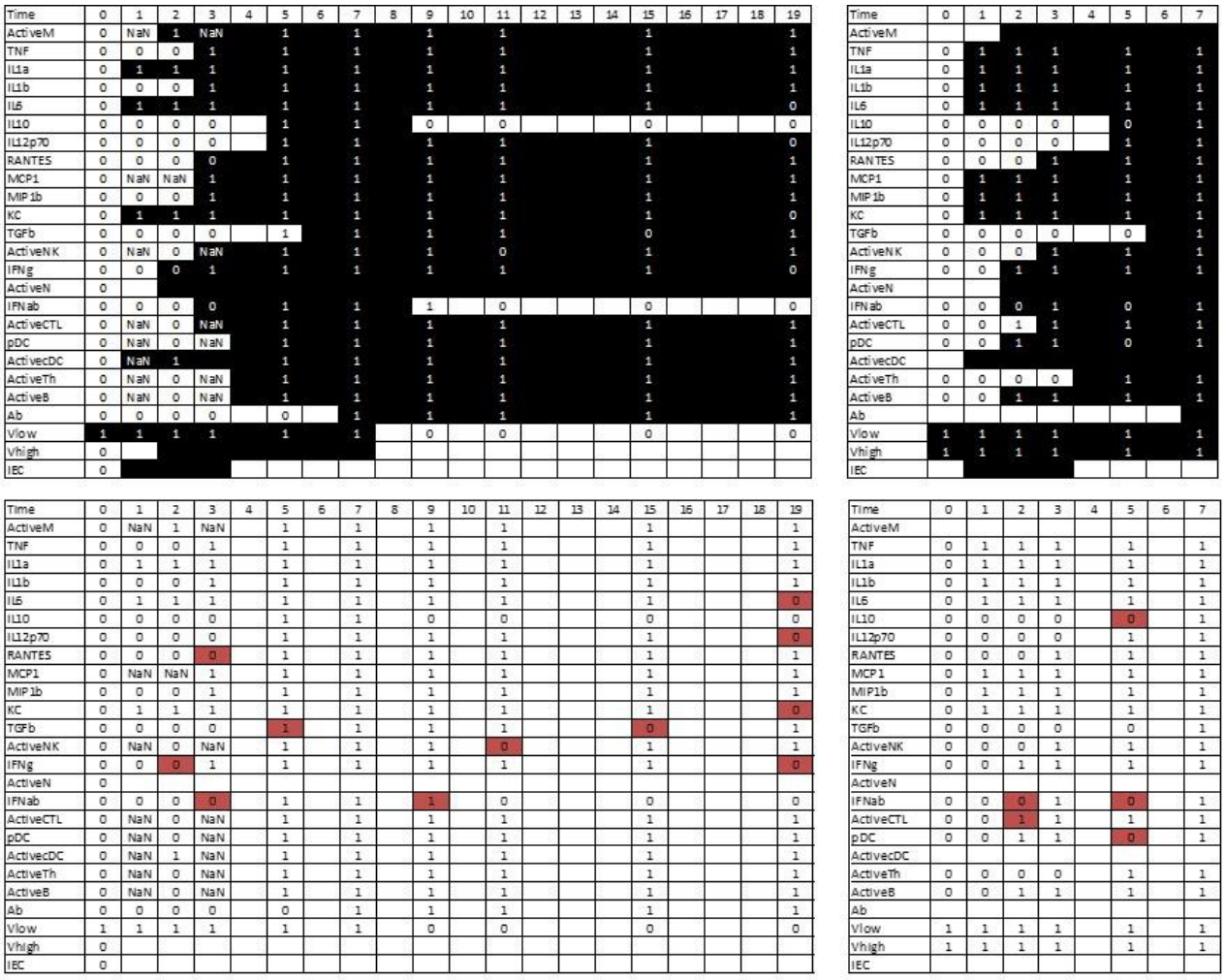

Time	0	1	2	3	4	5	6	7	8	9	10	11	12	13	14	15	16	17	18	19
ActiveM	0	NaN	1	NaN		1		1		1		1				1				1
TNF	0	0	0	1		1		1		1		1				1				1
IL1a	0	1	1	1		1		1		1		1				1				1
IL1b	0	0	0	1		1		1		1		1				1				1
IL6	0	1	1	1		1		1		1		1				1				0
IL10	0	0	0	0		1		1		0		0				0				0
IL12p70	0	0	0	0		1		1		1		1				1				0
RANTES	0	0	0	0		1		1		1		1				1				1
MCP1	0	NaN	NaN	1		1		1		1		1				1				1
MIP1b	0	0	0	1		1		1		1		1				1				1
KC	0	1	1	1		1		1		1		1				1				0
TGFb	0	0	0	0		1		1		1		1				0				1
ActiveNK	0	NaN	0	NaN		1		1		1		0				1				1
IFNg	0	0	0	1		1		1		1		1				1				0
ActiveN	0																			
IFNab	0	0	0	0		1		1		1		0				0				0
ActiveCTL	0	NaN	0	NaN		1		1		1		1				1				1
pDC	0	NaN	0	NaN		1		1		1		1				1				1
ActivecDC	0	NaN	1			1		1		1		1				1				1
ActiveTh	0	NaN	0	NaN		1		1		1		1				1				1
ActiveB	0	NaN	0	NaN		1		1		1		1				1				1
Ab	0	0	0	0		0		1		1		1				1				1
Vlow	1	1	1	1		1		1		0		0				0				0
Vhigh	0																			
IEC	0																			

Time	0	1	2	3	4	5	6	7
ActiveM								
TNF	0	1	1	1		1		1
IL1a	0	1	1	1		1		1
IL1b	0	1	1	1		1		1
IL6	0	1	1	1		1		1
IL10	0	0	0	0		0		1
IL12p70	0	0	0	0		1		1
RANTES	0	0	0	1		1		1
MCP1	0	1	1	1		1		1
MIP1b	0	1	1	1		1		1
KC	0	1	1	1		1		1
TGFb	0	0	0	0		0		1
ActiveNK	0	0	0	1		1		1
IFNg	0	0	1	1		1		1
ActiveN								
IFNab	0	0	0	1		0		1
ActiveCTL	0	0	1	1		1		1
pDC	0	0	1	1		0		1
ActivecDC								
ActiveTh	0	0	0	0		1		1
ActiveB	0	0	1	1		1		1
Ab								
Vlow	1	1	1	1		1		1
Vhigh	1	1	1	1		1		1
IEC								

Time	0	1	2	3	4	5	6	7	8	9	10	11	12	13	14	15	16	17	18	19
ActiveM	0	NaN	1	NaN		1		1		1		1				1				1
TNF	0	0	0	1		1		1		1		1				1				1
IL1a	0	1	1	1		1		1		1		1				1				1
IL1b	0	0	0	1		1		1		1		1				1				1
IL6	0	1	1	1		1		1		1		1				1				0
IL10	0	0	0	0		1		1		0		0				0				0
IL12p70	0	0	0	0		1		1		1		1				1				0
RANTES	0	0	0	0		1		1		1		1				1				1
MCP1	0	NaN	NaN	1		1		1		1		1				1				1
MIP1b	0	0	0	1		1		1		1		1				1				1
KC	0	1	1	1		1		1		1		1				1				0
TGFb	0	0	0	0		1		1		1		1				0				1
ActiveNK	0	NaN	0	NaN		1		1		1		0				1				1
IFNg	0	0	0	1		1		1		1		1				1				0
ActiveN	0																			
IFNab	0	0	0	0		1		1		1		0				0				0
ActiveCTL	0	NaN	0	NaN		1		1		1		1				1				1
pDC	0	NaN	0	NaN		1		1		1		1				1				1
ActivecDC	0	NaN	1	NaN		1		1		1		1				1				1
ActiveTh	0	NaN	0	NaN		1		1		1		1				1				1
ActiveB	0	NaN	0	NaN		1		1		1		1				1				1
Ab	0	0	0	0		0		1		1		1				1				1
Vlow	1	1	1	1		1		1		0		0				0				0
Vhigh	0																			
IEC	0																			

Time	0	1	2	3	4	5	6	7
ActiveM								
TNF	0	1	1	1		1		1
IL1a	0	1	1	1		1		1
IL1b	0	1	1	1		1		1
IL6	0	1	1	1		1		1
IL10	0	0	0	0		0		1
IL12p70	0	0	0	0		1		1
RANTES	0	0	0	1		1		1
MCP1	0	1	1	1		1		1
MIP1b	0	1	1	1		1		1
KC	0	1	1	1		1		1
TGFb	0	0	0	0		0		1
ActiveNK	0	0	0	1		1		1
IFNg	0	0	1	1		1		1
ActiveN								
IFNab	0	0	0	1		0		1
ActiveCTL	0	0	1	1		1		1
pDC	0	0	1	1		0		1
ActivecDC								
ActiveTh	0	0	0	0		1		1
ActiveB	0	0	1	1		1		1
Ab								
Vlow	1	1	1	1		1		1
Vhigh	1	1	1	1		1		1
IEC								

Figure 37: Boolean model fits to experimental data for adult mice.

Experimental data are indicated with the 0s and 1s. Variables for which no data was measured are indicated with "NaN". The simulated trajectories are indicated with shading of the table cell, where black rectangles represent a variable being on at that time point, and white rectangles represent the variable being off at that point. Thus, if a black rectangle overlaps a 1, the simulation correctly predicts that variable's trajectory at that point. A white rectangle overlapping a 0 is also a correct prediction. Incorrectly predicted data points have been highlighted in panel (C) for the sublethal condition and panel (D) for the lethal condition. NaN data and blank cells can predict either a 0 or 1 without penalty. A total of 16 data points are missed in the optimum fit.

5.5.2 Fits to elderly mice data

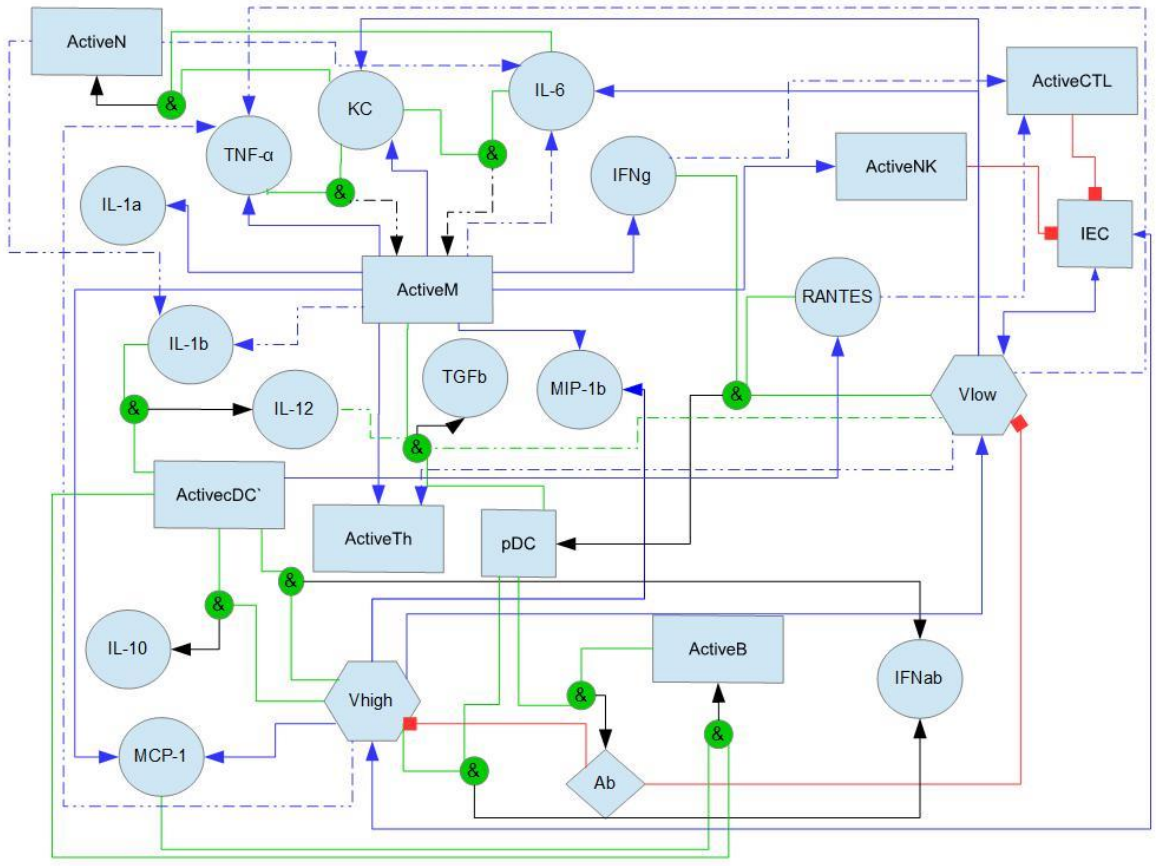

Figure 38: Graphical representation of elderly mouse network model.

Diagram of elderly (older) mice rule choices for full data set. Blue arrows indicate direct relation between two components. More than one blue arrow into a variable indicates an OR condition. Green lines indicate two or more components activate another through an AND operator. Black arrows indicate the output of the AND. Red blunted arrows indicate a NOT condition. Rectangles represent cell populations, circles represent cytokines and chemokines, hexagons represent viral loads, and the diamond represents antibodies. Dashed lines represent rule alternatives that exist in some, but not all, models that comprise the optimum solution.

Table 7: Optimum rule choices for the elderly mice model.

Rule	Frequency
ActiveM ← KC & IL6	50%
ActiveM ← KC & TNF	50%
TNF ← ActiveM | Vhigh	25%
TNF ← ActiveM | Vlow	75%
IL1a ← ActiveM | ActiveN	100%
IL1b ← ActiveN	37.5%
IL1b ← ActiveM	62.5%
IL6 ← ActiveM | Vlow	75%
IL6 ← ActiveM | ActiveN | ActivecDC	25%
IL10 ← ActivecDC & Vhigh	100%
IL12p70 ← (ActiveTh & Vhigh) | (ActivecdC & IL1b)	100%
RANTES ← ActivecDC	100%
MCP1 ← ActiveM | Vhigh	100%
MIP1b ← ActiveM | ActiveN | ActivecDC	100%
KC ← ActiveM | Vlow	100%
TGFb ← ActiveM & pDC & Vlow	33.3%
TGFb ← ActiveM & pDC & IL12p70	66.7%
ActiveNK ← ActiveM	100%
IFNg ← ActiveM	100%
ActiveN ← (KC | MIP1b) & IL6	100%
IFNab ← ((pDC & Vhigh) | (ActivecDC & Vhigh))	100%
ActiveCTL ← IFNg	50%
ActiveCTL ← IFNg | RANTES	50%
pDC ← IFN & RANTES & Vlow	100%
ActivecDC ← ActiveNK	100%
ActiveTh ← ActiveM | Vlow | Vhigh	100%
ActiveB ← ActivecDC & MCP1	100%
Ab ← (ActiveB & pDC) | Ab	100%
Vlow ← (IEC | Vlow | Vhigh) & ~(Ab & ~IL10)	100%
Vhigh ← (IEC | Vhigh) & ~Ab	100%
IEC ← (Vlow | Vhigh) & ~ActiveCTL & ~ActiveNK	100%

Experimental data for the elderly mice show many differences in the activation and upregulation of immune system components as compared to the younger mice, particularly in the inflammatory response (Figure 38). Our rules fit the data with 94% accuracy, missing 10 data points in the sublethal simulation and 12 in the lethal simulation (Figure 39). There are 48 models that produce outputs with the same number of errors, though the exact data points which are missed may differ between these outputs. Table 7 summarizes the rule choices for the elderly mouse optimum fit.

KC and T_H cells respond directly to the virus level in 100% of simulations after the sublethal infection (Figure 39A). Depending on the rule chosen, other models can also cause TNF and IL-6 to turn on at day 1. The data for TNF show it turns off on day 2 before turning on again at day 3, remaining on for the remainder of the experiment. The zero point at day 2 is likely an anomaly in the data, and we cannot capture this point with our rules.

The combination of KC with a pro-inflammatory cytokine brings in the activated macrophages and neutrophils, which then initiate the production of the other pro-inflammatory cytokines and chemokines, as well as type II IFN and NK cells. The dendritic cells and CTLs turn on at day 4, bringing IL-10, type I IFN, and B cells on day 5 and pDCs on day 6. At day 7, TGF-β and antibodies turn on. On day 8, antibodies bring down the virus level so that only V_{low} remains on. Once IL-10 turns off, the antibodies can turn off V_{low} as well. Removal of the virus turns off IL-10, TGF-β, IFN-α/β, and pDCs between days 9 and 11.

In the lethal simulations (Figure 39B), we see the higher viral inoculum changes the dynamics of the system substantially. Our simulations show TNF, MCP-1, and active all turn on immediately after infection. These drive the activation and upregulation of macrophages, IL-12,

IFN-gamma, and active B cells. At day 3, the other cytokines and chemokines turn on, bringing in neutrophils on day 4.

Interestingly, in our experimental data, IL-10 never turns on after the lethal dose. In this case, the T_H cells standard deviations associated with the measured data were so large that we cannot discern a statistical difference between any of the data points with baseline. In our simulations, however, IL-10 turns on at day 5, causing an error at the day 5 and 7 data points. We also have an anomaly in the TGF-β data, where this cytokine is on between days 1 and 2, then off again between days 3 and 5, and then turns back on at day 7. The rules are set so that the data at days 1 and 2 are ignored, leading to an activation of TGF- β at days 6 and 7 only.

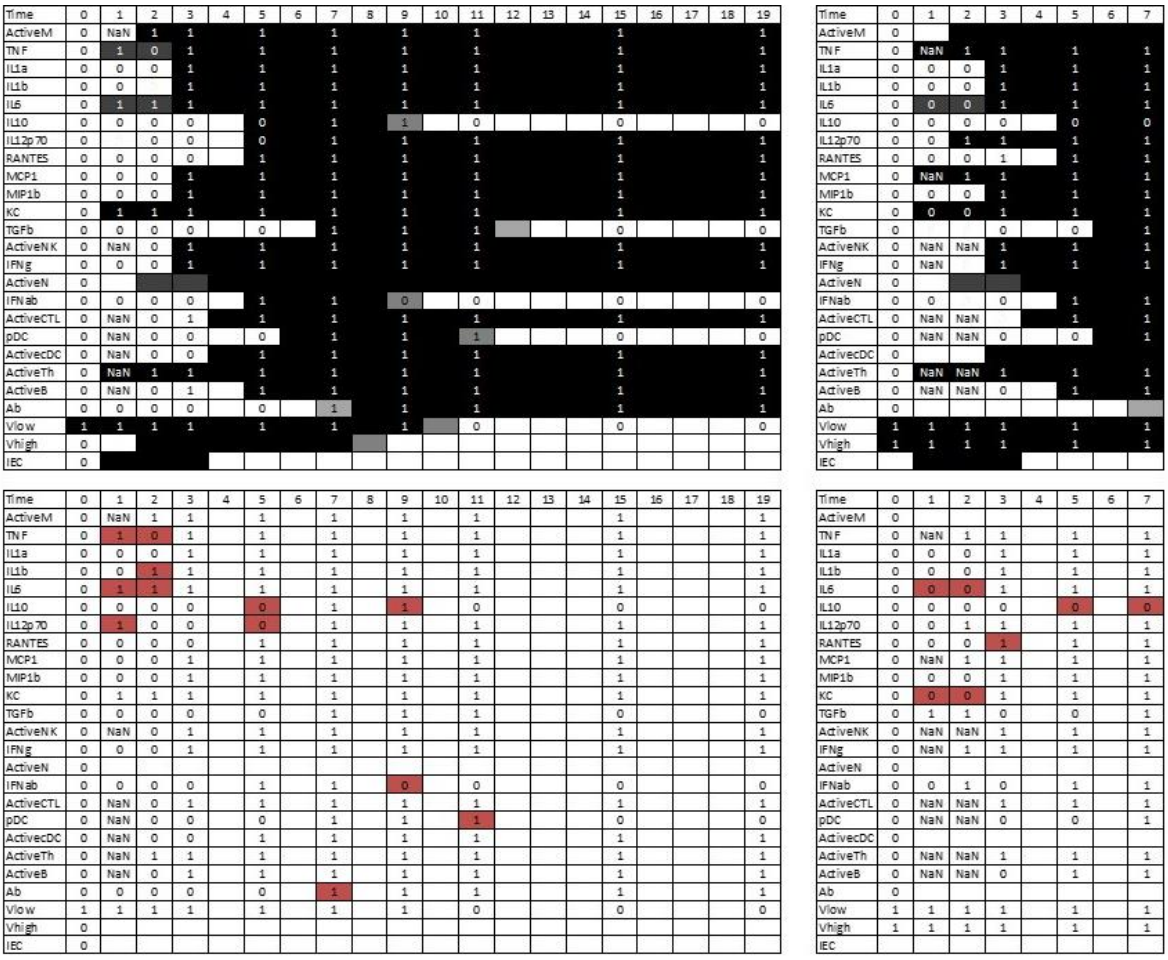

Time	0	1	2	3	4	5	6	7	8	9	10	11	12	13	14	15	16	17	18	19
ActiveM	0	NaN	1	1		1		1		1		1				1				1
TNF	0	1	0	1		1		1		1		1				1				1
IL1a	0	0	0	1		1		1		1		1				1				1
IL1b	0	0		1		1		1		1		1				1				1
IL6	0	1	1	1		1		1		1		1				1				1
IL10	0	0	0	0		0		1		1		0				0				0
IL12p70	0		0	0		0		1		1		1				1				1
RANTES	0	0	0	0		1		1		1		1				1				1
MCP1	0	0	0	1		1		1		1		1				1				1
MIP1b	0	0	0	1		1		1		1		1				1				1
KC	0	1	1	1		1		1		1		1				1				1
TGFb	0	0	0	0		0		1		1		1				0				0
ActiveNK	0	NaN	0	1		1		1		1		1				1				1
IFNg	0	0	0	1		1		1		1		1				1				1
ActiveN	0																			
IFNab	0	0	0	0		1		1		0		0				0				0
ActiveCTL	0	NaN	0	1		1		1		1		1				1				1
pDC	0	NaN	0	0		0		1		1		1				0				0
ActivecDC	0	NaN	0	0		1		1		1		1				1				1
ActiveTh	0	NaN	1	1		1		1		1		1				1				1
ActiveB	0	NaN	0	1		1		1		1		1				1				1
Ab	0	0	0	0		0		1		1		1				1				1
Vlow	1	1	1	1		1		1		1		0				0				0
Vhigh	0																			
IEC	0																			

Time	0	1	2	3	4	5	6	7
ActiveM	0							
TNF	0	NaN	1	1		1		1
IL1a	0	0	0	1		1		1
IL1b	0	0	0	1		1		1
IL6	0	0	0	1		1		1
IL10	0	0	0	0		0		0
IL12p70	0	0	1	1		1		1
RANTES	0	0	0	1		1		1
MCP1	0	NaN	1	1		1		1
MIP1b	0	0	0	1		1		1
KC	0	0	0	1		1		1
TGFb	0			0		0		1
ActiveNK	0	NaN	NaN	1		1		1
IFNg	0	NaN		1		1		1
ActiveN	0							
IFNab	0	0		0		1		1
ActiveCTL	0	NaN	NaN			1		1
pDC	0	NaN	NaN	0		0		1
ActivecDC	0							
ActiveTh	0	NaN	NaN	1		1		1
ActiveB	0	NaN	NaN	0		1		1
Ab	0							
Vlow	1	1	1	1		1		1
Vhigh	1	1	1	1		1		1
IEC								

Time	0	1	2	3	4	5	6	7	8	9	10	11	12	13	14	15	16	17	18	19
ActiveM	0	NaN	1	1		1		1		1		1				1				1
TNF	0	1	0	1		1		1		1		1				1				1
IL1a	0	0	0	1		1		1		1		1				1				1
IL1b	0	0	1	1		1		1		1		1				1				1
IL6	0	1	1	1		1		1		1		1				1				1
IL10	0	0	0	0		0		1		1		0				0				0
IL12p70	0	1	0	0		0		1		1		1				1				1
RANTES	0	0	0	0		1		1		1		1				1				1
MCP1	0	0	0	1		1		1		1		1				1				1
MIP1b	0	0	0	1		1		1		1		1				1				1
KC	0	1	1	1		1		1		1		1				1				1
TGFb	0	0	0	0		0		1		1		1				0				0
ActiveNK	0	NaN	0	1		1		1		1		1				1				1
IFNg	0	0	0	1		1		1		1		1				1				1
ActiveN	0																			
IFNab	0	0	0	0		1		1		0		0				0				0
ActiveCTL	0	NaN	0	1		1		1		1		1				1				1
pDC	0	NaN	0	0		0		1		1		1				0				0
ActivecDC	0	NaN	0	0		1		1		1		1				1				1
ActiveTh	0	NaN	1	1		1		1		1		1				1				1
ActiveB	0	NaN	0	1		1		1		1		1				1				1
Ab	0	0	0	0		0		1		1		1				1				1
Vlow	1	1	1	1		1		1		1		0				0				0
Vhigh	0																			
IEC	0																			

Time	0	1	2	3	4	5	6	7
ActiveM	0							
TNF	0	NaN	1	1		1		1
IL1a	0	0	0	1		1		1
IL1b	0	0	0	1		1		1
IL6	0	0	0	1		1		1
IL10	0	0	0	0		0		0
IL12p70	0	0	1	1		1		1
RANTES	0	0	0	1		1		1
MCP1	0	NaN	1	1		1		1
MIP1b	0	0	0	1		1		1
KC	0	0	0	1		1		1
TGFb	0	1	1	0		0		1
ActiveNK	0	NaN	NaN	1		1		1
IFNg	0	NaN	1	1		1		1
ActiveN	0							
IFNab	0	0	1	0		1		1
ActiveCTL	0	NaN	NaN	1		1		1
pDC	0	NaN	NaN	0		0		1
ActivecDC	0							
ActiveTh	0	NaN	NaN	1		1		1
ActiveB	0	NaN	NaN	0		1		1
Ab	0							
Vlow	1	1	1	1		1		1
Vhigh	1	1	1	1		1		1
IEC								

Figure 39: Boolean model fits for elderly mice.

Experimental data are indicated with the 0s and 1s. Variables for which no data was measured are indicated with "NaN". The simulated trajectories are indicated with shading of the table cell, where black rectangles represent a variable being on at that time point, and white rectangles represent the variable being off at that point. Thus, if a black rectangle overlaps a 1, the simulation correctly predicts that variable's trajectory at that point. A white rectangle overlapping a 0 is also a correct prediction. Incorrectly predicted data points have been highlighted in panel (C) for the sublethal condition and panel (D) for the lethal condition. NaN data and blank cells can predict either a 0 or 1 without penalty. A total of 22 data points are missed in the optimum fit.

5.5.3 Aged-based rule differences

Figure 40 summarizes the differences between rules chosen for younger (orange arrows) and older (purple arrows) mice in this model. Only rules chosen for one age group but not the other are included in this figure. Components with no arrows in are governed by the same rules in each network. In total, 11 of the 25 components rely on different rules to simulate the Boolean data.

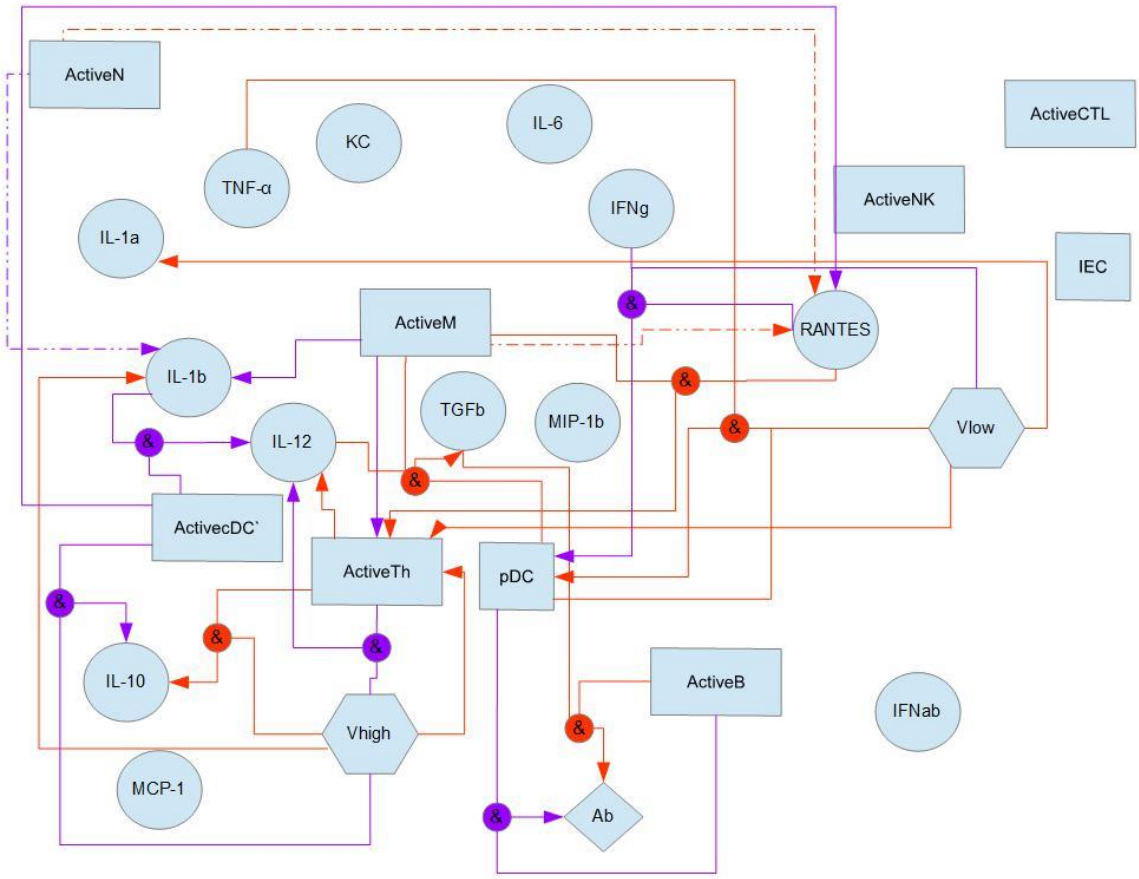

Figure 40: Aged-based differences in rules for Boolean models.

Differences in rule choices between age groups. Orange arrows represent rules seen in adult mouse model but not in elderly mouse model. Purple arrows represent rules seen in elderly mouse model but not in adult mouse model. Shapes without incoming arrows have identical rules between age groups.

These age-dependent variables are also summarized below in Table 8.

Table 8: Summary of age-dependent rules in best fit solutions to adult and elderly mice data.

Variable	Adult Rule	Elderly Rule
IL-1α	IL1a ← ActiveM | Vlow	IL1a ← ActiveM | ActiveN
IL-1β	IL1b ← ActiveM | Vlow	IL1b ← ActiveM | ActiveN
IL-10	IL10 ← ActiveTh & Vhigh	IL10 ← ActivecDC & Vhigh
IL-12	IL12p70 ← ActiveTh	IL12p70 ← (ActiveTh & Vhigh) | (ActivecdC & IL1b)
RANTES	RANTES ← ActiveM | ActiveN	RANTES ← ActivecDC
MIP-1β	MIP1b ← ActiveM | Vhigh	MIP1b ← ActiveM | ActiveN | ActivecDC
ActivecDC	ActivecDC ← Vlow | IFNg	ActivecDC ← ActiveNK
pDC	pDC ← (Vlow | Vhigh | pDC) & TNF	pDC ← IFN & RANTES & Vlow
ActiveTh	ActiveTh ← ActiveM & RANTES	ActiveTh ← ActiveM | Vlow | Vhigh
Ab	Ab ← (ActiveB & TGFb) | Ab	Ab ← (ActiveB & pDC) | Ab
Vlow	Vlow ← (IEC | Vlow | Vhigh) & ~Ab	Vlow ← (IEC | Vlow | Vhigh) & ~(Ab & ~IL10)

IL-1α is produced in the presence of macrophages or low levels of virus in the adult mice, but only by macrophages in the elderly mice. Given the high level of dysregulation of cytokine production in elderly hosts, this discrepancy can be explained by an inability of epithelial cells to respond quickly amount of virus present. A similar trend is seen in the IL-1β rule choices. IL-1β can respond to active macrophages in either age group, but in adult mice it can also respond to high virus levels. This discrepancy implies epithelial cells in the lungs of younger mice can

produce high levels of IL-1β in response to a large viral load, but lung epithelial cells in older mice are unable to produce IL-1β at the same rate.

Cytokine dysregulation may also account for rule differences in IL-10, IL-12, and TGF-β. IL-10 responds to dendritic cells in the presence of high virus levels in the elderly mice, but it responds to T helper cells and high virus in the younger mice. In both data sets, IL-10 turns off immediately after the virus is lowered, implying a dependence of IL-10 on high virus levels. The cell type primarily responsible for producing IL-10 is also data-driven, depending on which cells activate the day before IL-10 should turn on. T_H cells fit the data appropriately in younger mice. Experimental data measured for CD4+ T cells (T_H cells) included regulatory T cells (T_{reg}), which are known producers of IL-10 [188], accounting for this data-driven rule. In older mice, IL-10 is produced primarily by cDCs.

IL-12p70 is the active heterodimer of IL-12, a regulatory cytokine that operates to connect the innate and adaptive responses through dendritic cells and macrophages. Though IL-12 can be produced by a variety of cell types, in our model, active T_H cells are a major source of IL-12, but they utilize distinct mechanisms for its production between young and old mice. IL-12 is produced by the T_H cells in conjunction with active dendritic cells in the younger mice. This mechanism has previously been shown in young BALB/c mice [189]. In older mice, the rule is more complicated, involving a data-driven mechanism in which T helper cells in conjunction with high virus first produce IL-12, and then when virus is cleared, IL-12 levels are kept high by production from dendritic cells plus IL-1b. Dendritic cells are known to be a major producer of IL-12 in the presence of IL-1b [190].

TGF-β rules are largely data-driven in our model. TGF-β is an anti-inflammatory cytokine that generally exists in a latent form in the body, and macrophages are required to process and

activate the latent form, so both age groups have a TGF-β dependence on activated macrophages. Macrophages can be assisted in this process by one of several cell types, and in this model, pDCs are used to drive TGF-β production. In the elderly mice, because TGF-β turns off after the virus has been cleared from the host, we include a codependence on virus in the rule as well. In adult mice, the TGF-β remains high for the full length of the experiment, so no direct virus dependence is necessary. Instead, to generate the proper timing of TGF-β activation, we include a codependence with IL-12. TGF-β is produced by many T cell types, and since IL-12 activates many of these cells, that may explain this IL-12 dependence for TGF-β production.

Chemokine dysregulation is evident in the elderly mouse rules, as we obtained distinct rules for RANTES and MIP-1β between age groups. Dendritic cells are responsible for most RANTES production in older mice, while macrophages or neutrophils release most RANTES in younger mice. This difference can be attributed to the delay in RANTES activation in older mice; RANTES is off until day 5 in the elderly mouse data, while it turns on at day 3 in the adult mouse data. MIP-1β is produced by macrophages in both age groups, but adult mice have an additional source of MIP-1β from high virus levels, whereas elderly mice have neutrophils and dendritic cells as additional sources of MIP-1β. MIP-1β is delayed in the elderly mice as compared to the younger, so a direct dependence on virus will not suit the data well.

Antibodies are also produced differently in each age group. In the adult mice, antibodies are produced by B cells which have differentiated into plasmablasts and plasma cells in the presence of TGF-β [191,192]. In elderly mice, antibodies are again produced by B cell differentiated into plasmablasts and plasma cells, but here the process is aided by pDCs [193].

Both types of dendritic cells are governed by age-dependent rules. In adult mice, pDCs remain high after activation on day 5, but in elderly mice, pDCs return to baseline after day 11,

justifying a separate rule choice for each cohort. pDCs respond early in younger mice, driven to replicate by a pro-inflammatory cytokine like TNF. pDCs do not activate until day 7 in older mice, possibly related to the well-documented pDC impairment with age [194]. The delayed activation and quick deactivation can be described by a codependence of IFN-γ, RANTES, and low virus. cDCs can activate in response to the virus or to IFN-γ in the younger mice, while they respond directly to NK cells in the older mice. NK cells have previously been shown to aid in dendritic cell maturation in BALB/c mice [14].

T helper cells are the only other cell type to require separate rules per age group. Macrophages in younger mice can activate T_H cells in their capacity as antigen-presenting cells, and the T_H cells are brought to the site of infection by RANTES. Macrophages can also activate T_H cells in aged mice, but the data suggest T_H cells activate at the same time or earlier than macrophages, so another factor must bring in T_H cells as well. Here, we model this with a direct dependence on virus in addition to macrophage activation.

5.6 BOOTSTRAPPING RESULTS

Figure 41 shows the distribution of errors associated with the adult and elderly mice bootstrap results. The adult bootstrap replicates led to an average error of 23.22, with a minimum of 15 and interquartile range (IQR) of 21-28 (Figure 41A). The elderly bootstrap replicates had an average error of 27 with a minimum of 22 and IQR of 24-31 (Figure 41B).

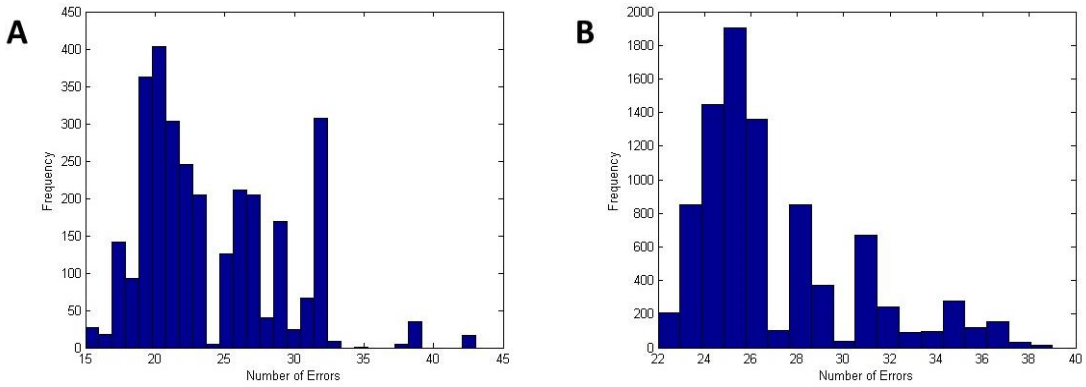

Figure 41: Error distributions for bootstrap replicate output. Distributions of all errors from bootstrap replicates for (A) adult mice (3,016 models) and (B) elderly mice (8,810 models).

As with the original data set, each of the bootstrap replicates had multiple equivalent solutions with different rules but an equal error. For the younger mice, we generated 3,016 solutions, and for the elderly mice we generated 8,810 solutions in total for the 100 datasets tested. Table 9 summarizes the rule choices between age groups, indicating the percent of rule sets that include a particular rule for the full set of bootstrap outputs. Figure 42 and Figure 43 show the average fit of the models generated in the bootstrap experiment. Numbers represent the average value of the data for a particular variable on each day. Darker gray squares represent a greater likelihood each model will predict a variable is on at that point, and lighter gray means a greater likelihood the rule predicts the variable will be off. Figure 42 shows the bootstrap output for the adult mice, and Figure 43 shows the output for the elderly mice.

Table 9: Bootstrapping rule choices for adult and elderly mice.

	ADULT	ELDERLY
ActiveM ← KC & IL6	43.8%	58.7%
ActiveM ← MIP1b & TNF	1.9%	0.0%
ActiveM ← KC & TNF	3.9%	39.5%
ActiveM ← (MIP1b | MCP1) & IL6	51.0%	1.8%
TNF ← ActiveM | Vhigh	70.8%	45.7%
TNF ← ActiveM | Vlow	2.0%	54.1%
TNF ← ActiveM | ActiveN | ActivecDC	27.2%	0.2%
IL1a ← ActiveM | Vhigh	11.8%	0.0%
IL1a ← ActiveM | Vlow	78.1%	0.0%
IL1a ← ActiveM | ActiveN	10.1%	100.0%
IL1b ← ActiveM | Vhigh	95.3%	5.3%
IL1b ← ActiveM	2.0%	49.8%
IL1b ← ActiveN	2.8%	44.8%
IL6 ← ActiveM | Vhigh	5.0%	3.3%
IL6 ← ActiveM | Vlow	88.5%	76.6%
IL6 ← ActiveM | ActiveN | ActivecDC	6.5%	20.1%
IL10 ← ActivecDC & Vhigh	12.1%	28.0%
IL10 ← ActiveTh & Vhigh	87.9%	72.1%
IL12p70 ← (ActiveTh & Vhigh) | (ActivecDC & IL1b)	11.8%	44.6%
IL12p70 ← ActivecDC & IL1b	88.2%	28.2%
IL12p70 ← ActiveTh	0.0%	27.2%
RANTES ← ActiveN	31.1%	12.0%
RANTES ← ActiveM	58.7%	8.1%
RANTES ← ActivecDC	10.3%	79.9%
MCP1 ← ActiveM | Vhigh	1.7%	97.3%
MCP1 ← ActiveM | Vlow	72.8%	0.2%
MCP1 ← ActiveM | ActiveN | ActivecDC	25.5%	2.5%
MIP1b ← ActiveM | Vhigh	50.0%	0.2%
MIP1b ← ActiveM | Vlow	0.0%	0.0%
MIP1b ← ActiveM | ActiveN | ActivecDC	50.0%	99.8%
KC ← ActiveM | Vhigh	8.2%	0.9%
KC ← ActiveM | Vlow	91.8%	99.1%
TGFb ← ActiveM & pDC & Vlow	0.0%	35.6%
TGFb ← ActiveM & pDC & IL12p70	100.0%	66.4%
ActiveNK ← ActiveM	100.0%	100.0%
IFNg ← ActiveM	100.0%	100.0%
ActiveN ← (KC | MIP1b) & IL6	100.0%	100.0%

IFNab ← ((pDC & Vhigh) | (ActivecDC & Vhigh))	100.0%	100.0%
ActiveCTL ← IFNg	40.7%	48.4%
ActiveCTL ← IFNg | RANTES	59.3%	51.6%
pDC ← IFN & RANTES & Vlow	0.0%	97.8%
pDC ← (Vlow | Vhigh | pDC) & TNF	100.0%	2.2%
ActivecDC ← ActiveN	88.0%	3.3%
ActivecDC ← ActiveNK	12.0%	96.7%
ActiveTh ← ActiveM | Vlow | Vhigh	0.0%	26.5%
ActiveTh ← ActiveM & RANTES	84.4%	21.7%
ActiveTh ← ActivecDC | IL12p70	15.6%	51.9%
ActiveB ← ActiveTh	41.0%	12.7%
ActiveB ← ActivecDC & MCP1	59.0%	87.3%
Ab ← (ActiveB & TGFb) | Ab	97.3%	92.1%
Ab ← (ActiveB & pDC) | Ab	2.7%	7.9%
Vlow ← (IEC | Vlow | Vhigh) & ~(Ab & ~IL10)	95.7%	89.5%
Vlow ← (IEC | Vlow | Vhigh) & ~Ab	4.3%	10.5%
Vhigh ← (IEC | Vhigh) & ~Ab	100.0%	100.0%
IEC ← (Vlow | Vhigh) & ~ActiveCTL & ~ActiveNK	100.0%	100.0%

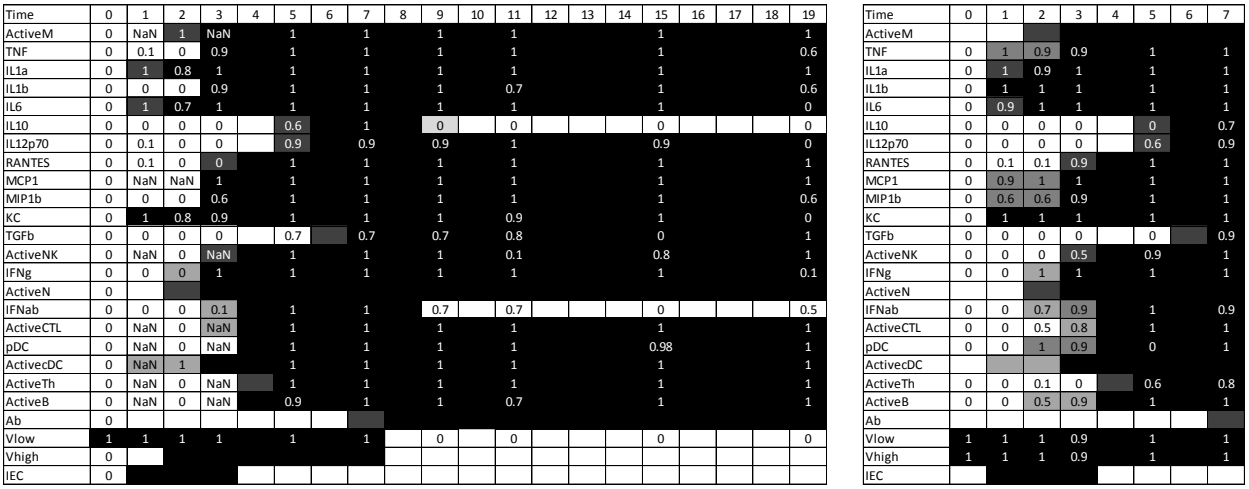

Time	0	1	2	3	4	5	6	7	8	9	10	11	12	13	14	15	16	17	18	19
ActiveM	0	NaN	1	NaN		1		1		1		1				1				1
TNF	0	0.1	0	0.9		1		1		1		1				1				0.6
IL1a	0	1	0.8	1		1		1		1		1				1				1
IL1b	0	0	0	0.9		1		1		1		0.7				1				0.6
IL6	0	1	0.7	1		1		1		1		1				1				0
IL10	0	0	0	0		0.6		1		0		0				0				0
IL12p70	0	0.1	0	0		0.9		0.9		0.9		1				0.9				0
RANTES	0	0.1	0	0		1		1		1		1				1				1
MCP1	0	NaN	NaN	1		1		1		1		1				1				1
MIP1b	0	0	0	0.6		1		1		1		1				1				0.6
KC	0	1	0.8	0.9		1		1		1		0.9				1				0
TGFb	0	0	0	0		0.7		0.7		0.7		0.8				0				1
ActiveNK	0	NaN	0	NaN		1		1		1		0.1				0.8				1
IFNg	0	0	0	1		1		1		1		1				1				0.1
ActiveN	0																			
IFNab	0	0	0	0.1		1		1		0.7		0.7				0				0.5
ActiveCTL	0	NaN	0	NaN		1		1		1		1				1				1
pDC	0	NaN	0	NaN		1		1		1		1				0.98				1
ActivecDC	0	NaN	1			1		1		1		1				1				1
ActiveTh	0	NaN	0	NaN		1		1		1		1				1				1
ActiveB	0	NaN	0	NaN		0.9		1		1		0.7				1				1
Ab	0																			
Vlow	1	1	1	1		1		1		0		0				0				0
Vhigh	0																			
IEC	0																			

Time	0	1	2	3	4	5	6	7
ActiveM								
TNF	0	1	0.9	0.9		1		1
IL1a	0	1	0.9	1		1		1
IL1b	0	1	1	1		1		1
IL6	0	0.9	1	1		1		1
IL10	0	0	0	0		0		0.7
IL12p70	0	0	0	0		0.6		0.9
RANTES	0	0.1	0.1	0.9		1		1
MCP1	0	0.9	1	1		1		1
MIP1b	0	0.6	0.6	0.9		1		1
KC	0	1	1	1		1		1
TGFb	0	0	0	0		0		0.9
ActiveNK	0	0	0	0.5		0.9		1
IFNg	0	0	1	1		1		1
ActiveN								
IFNab	0	0	0.7	0.9		1		0.9
ActiveCTL	0	0	0.5	0.8		1		1
pDC	0	0	1	0.9		0		1
ActivecDC								
ActiveTh	0	0	0.1	0		0.6		0.8
ActiveB	0	0	0.5	0.9		1		1
Ab								
Vlow	1	1	1	0.9		1		1
Vhigh	1	1	1	0.9		1		1
IEC								

Figure 42: Bootstrap output for adult mice.

Average values of bootstrap data are indicated with the numbers, and the simulated trajectories are indicated with color, where black rectangles represent a variable being on at that time point, and white rectangles represent the variable being off at that point. Gray coloring indicates a variable is on at that point for some rule sets, but not for all. Darker gray indicates greater likelihood of an "on" state at that point.

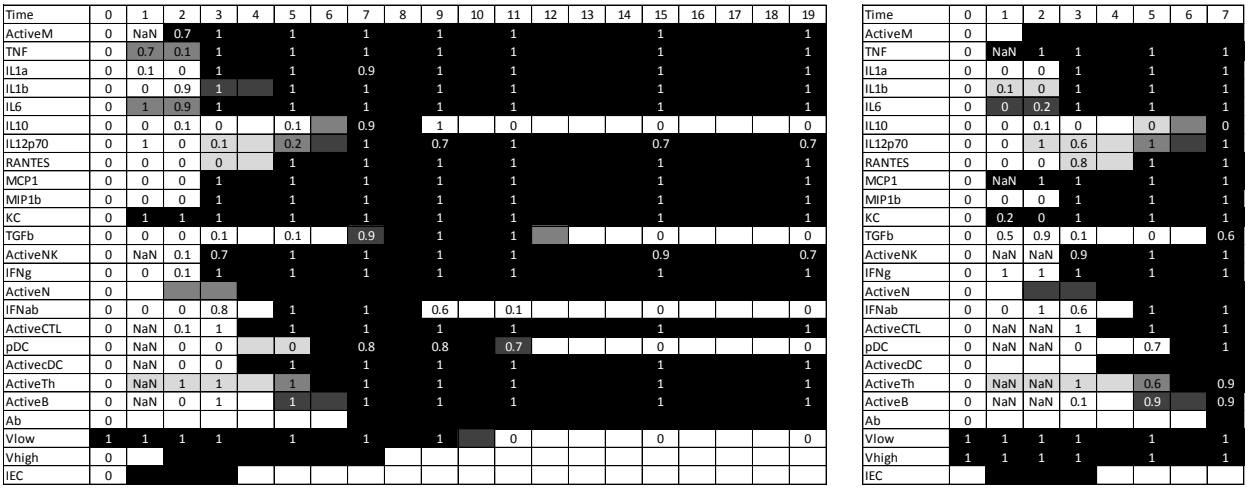

Time	0	1	2	3	4	5	6	7	8	9	10	11	12	13	14	15	16	17	18	19
ActiveM	0	NaN	0.7	1		1		1		1		1				1				1
TNF	0	0.7	0.1	1		1		1		1		1				1				1
IL1a	0	0.1	0	1		1		0.9		1		1				1				1
IL1b	0	0	0.9	1		1		1		1		1				1				1
IL6	0	1	0.9	1		1		1		1		1				1				1
IL10	0	0	0.1	0		0.1		0.9		1		0				0				0
IL12p70	0	1	0	0.1		0.2		1		0.7		1				0.7				0.7
RANTES	0	0	0	0		1		1		1		1				1				1
MCP1	0	0	0	1		1		1		1		1				1				1
MIP1b	0	0	0	1		1		1		1		1				1				1
KC	0	1	1	1		1		1		1		1				1				1
TGFb	0	0	0	0.1		0.1		0.9		1		1				0				0
ActiveNK	0	NaN	0.1	0.7		1		1		1		1				0.9				0.7
IFNg	0	0	0.1	1		1		1		1		1				1				1
ActiveN	0																			
IFNab	0	0	0	0.8		1		1		0.6		0.1				0				0
ActiveCTL	0	NaN	0.1	1		1		1		1		1				1				1
pDC	0	NaN	0	0		0		0.8		0.8		0.7				0				0
ActivecDC	0	NaN	0	0		1		1		1		1				1				1
ActiveTh	0	NaN	1	1		1		1		1		1				1				1
ActiveB	0	NaN	0	1		1		1		1		1				1				1
Ab	0																			
Vlow	1	1	1	1		1		1		1		0				0				0
Vhigh	0																			
IEC	0																			

Time	0	1	2	3	4	5	6	7
ActiveM	0							
TNF	0	NaN	1	1		1		1
IL1a	0	0	0	1		1		1
IL1b	0	0.1	0	1		1		1
IL6	0	0	0.2	1		1		1
IL10	0	0	0.1	0		0		0
IL12p70	0	0	1	0.6		1		1
RANTES	0	0	0	0.8		1		1
MCP1	0	NaN	1	1		1		1
MIP1b	0	0	0	1		1		1
KC	0	0.2	0	1		1		1
TGFb	0	0.5	0.9	0.1		0		0.6
ActiveNK	0	NaN	NaN	0.9		1		1
IFNg	0	1	1	1		1		1
ActiveN	0							
IFNab	0	0	1	0.6		1		1
ActiveCTL	0	NaN	NaN	1		1		1
pDC	0	NaN	NaN	0		0.7		1
ActivecDC	0							
ActiveTh	0	NaN	NaN	1		0.6		0.9
ActiveB	0	NaN	NaN	0.1		0.9		0.9
Ab	0							
Vlow	1	1	1	1		1		1
Vhigh	1	1	1	1		1		1
IEC								

Figure 43: Bootstrap output for elderly mice.

Average values of bootstrap data are indicated with the numbers, and the simulated trajectories are indicated with color, where black rectangles represent a variable being on at that time point, and white rectangles represent the variable being off at that point. Gray coloring indicates a variable is on at that point for some rule sets, but not for all. Darker gray indicates greater likelihood of an "on" state at that point.

Most rule choices in the bootstrapping tend toward the rules chosen in the optimum solutions presented in Table 6 and Table 7. A few variables, however, showed interesting patterns not obvious from the optimal solutions. Macrophages are activated by distinct mechanisms between age groups. Younger mice can recruit macrophages with any chemokine, but IL-6 is required for their activation. Conversely, older mice can only recruit macrophages with the chemokine KC in this model, but any of the pro-inflammatory cytokines can be used for activation. Much of the macrophage's function is dysregulated with age [164]; it is possible macrophages from elderly hosts do not respond as well to MIP-1β or MCP-1, so other chemokines like KC are needed as well to initiate a full macrophage response to viral infection.

IL-10 is initiated by dendritic cells in the original elderly mouse fit, but the bootstrapping results suggest a dependence on T_H cells. As we age, one major change to cellular immunity is a shift in the T cell cytokine production, from a T_H1-focused phenotype to a T_H2 phenotype [167]. T_H2 cells produce IL-10, which implies the bootstrap rule is more likely to represent the underlying biology than the cDC-dependent rule.

IL-12 rules do not match up well between the optimum and the bootstrapping. The original adult mouse model shows T_H cells are the primary source of IL-12. About 88% of bootstrap replicates indicate active cDCs under IL-1β stimulation as the producer of IL-12, however. In elderly mice, there is no clear consensus on which rule most accurately describes IL-12 production. While about 45% of solutions agree with the optimum rule choice from all data, the other 55% of solutions are split evenly between T_H cells and active cDCs with IL-1β. This uncertainty is correlated to the rule choices for T_H cells. IL-12 production by dendritic cells has been shown to decrease with age [195], perhaps requiring a compensatory mechanism through T cell production to maintain this regulatory cytokine throughout the course of the infection.

MCP-1 rules differ in the adult case between optimum and bootstrapping. About 73% of the bootstrap solutions chose an MCP-1 dependence on macrophages and low virus levels, while the optimum solution fit with macrophages and a high virus level. These two rules produce identical outputs in the lethal simulations, but produce a 2 day difference in onset of MCP-1 in the sublethal case. Because we have no measured data at days 1 and 2 for MCP-1, it can turn on at day 1, 2, or 3 without penalty, accounting for this difference in rule choices. Similarly, MIP-1β has quite a bit of uncertainty in its first two data points in the lethal case; about 60% of data sets are on at days 1 and 2. Generally the rules force MIP-1β to turn on at day 3, one day after macrophage activation, leading to an error at these early data points in 60% of cases.

Antibody rules also do not correlate well to the optimal solution for the elderly mice. Because we do not have bootstrap data available for this variable, the antibody trajectory can turn on at any day without penalty. We do have antibody data in the original solution, however, forcing a more rigorous timing to the antibody trajectory. For this reason, the bootstrapping does not reflect the optimum solution for the antibodies in the elderly case.

We also took the most-often chosen model from each age group and tested this model against all 100 bootstrap data sets. The model selected for each age group is presented in Table 10. The simulation output for these model choices is shown in Figure 44 for adult (top panels) and elderly (bottom panels) mice.

Finally, we looked at the best-fit outputs from the bootstrapping replicates, i.e. the rule sets that garnered the lowest overall error on the bootstrap data. Those rule sets are presented in Table 11, and the graphical simulation output is presented in Figure 45.

Time	0	1	2	3	4	5	6	7	8	9	10	11	12	13	14	15	16	17	18	19
ActiveM	0	NaN	1	NaN		1		1		1		1				1				1
TNF	0	0	0	1		1		1		1		1				1				1
IL1a	0	1	1	1		1		1		1		1				1				1
IL1b	0	0	0	1		1		1		1		1				1				1
IL6	0	1	1	1		1		1		1		1				1				0
IL10	0	0	0	0		1		1		0		0				0				0
IL12p70	0	0	0	0		1		1		1		1				1				0
RANTES	0	0	0	0		1		1		1		1				1				1
MCP1	0	NaN	NaN	1		1		1		1		1				1				1
MIP1b	0	0	0	1		1		1		1		1				1				1
KC	0	1	1	1		1		1		1		1				1				0
TGFb	0	0	0	0		1		1		1		1				0				1
ActiveNK	0	NaN	0	NaN		1		1		1		0				1				1
IFNg	0	0	0	1		1		1		1		1				1				0
ActiveN	0																			
IFNab	0	0	0	0		1		1		1		0				0				0
ActiveCTL	0	NaN	0	NaN		1		1		1		1				1				1
pDC	0	NaN	0	NaN		1		1		1		1				1				1
ActivecDC	0	NaN	1			1		1		1		1				1				1
ActiveTh	0	NaN	0	NaN		1		1		1		1				1				1
ActiveB	0	NaN	0	NaN		1		1		1		1				1				1
Ab	0	0	0	0		0		1		1		1				1				1
Vlow	1	1	1	1		1		1		0		0				0				0
Vhigh	0																			
IEC	0																			

Time	0	1	2	3	4	5	6	7
ActiveM								
TNF	0	1	1	1		1		1
IL1a	0	1	1	1		1		1
IL1b	0	1	1	1		1		1
IL6	0	1	1	1		1		1
IL10	0	0	0	0		0		1
IL12p70	0	0	0	0		1		1
RANTES	0	0	0	1		1		1
MCP1	0	1	1	1		1		1
MIP1b	0	1	1	1		1		1
KC	0	1	1	1		1		1
TGFb	0	0	0	0		0		1
ActiveNK	0	0	0	1		1		1
IFNg	0	0	1	1		1		1
ActiveN								
IFNab	0	0	0	1		0		1
ActiveCTL	0	0	1	1		1		1
pDC	0	0	1	1		0		1
ActivecDC								
ActiveTh	0	0	0	0		1		1
ActiveB	0	0	1	1		1		1
Ab								
Vlow	1	1	1	1		1		1
Vhigh	1	1	1	1		1		1
IEC								

Time	0	1	2	3	4	5	6	7	8	9	10	11	12	13	14	15	16	17	18	19
ActiveM	0	NaN	1	1		1		1		1		1				1				1
TNF	0	1	0	1		1		1		1		1				1				1
IL1a	0	0	0	1		1		1		1		1				1				1
IL1b	0	0	1	1		1		1		1		1				1				1
IL6	0	1	1	1		1		1		1		1				1				1
IL10	0	0	0	0		0		1		1		0				0				0
IL12p70	0	1	0	0		0		1		1		1				1				1
RANTES	0	0	0	0		1		1		1		1				1				1
MCP1	0	0	0	1		1		1		1		1				1				1
MIP1b	0	0	0	1		1		1		1		1				1				1
KC	0	1	1	1		1		1		1		1				1				1
TGFb	0	0	0	0		0		1		1		1				0				0
ActiveNK	0	NaN	0	1		1		1		1		1				1				1
IFNg	0	0	0	1		1		1		1		1				1				1
ActiveN	0																			
IFNab	0	0	0	0		1		1		0		0				0				0
ActiveCTL	0	NaN	0	1		1		1		1		1				1				1
pDC	0	NaN	0	0		0		1		1		1				0				0
ActivecDC	0	NaN	0	0		1		1		1		1				1				1
ActiveTh	0	NaN	1	1		1		1		1		1				1				1
ActiveB	0	NaN	0	1		1		1		1		1				1				1
Ab	0	0	0	0		0		1		1		1				1				1
Vlow	1	1	1	1		1		1		1		0				0				0
Vhigh	0																			
IEC	0																			

Time	0	1	2	3	4	5	6	7
ActiveM	0							
TNF	0	NaN	1	1		1		1
IL1a	0	0	0	1		1		1
IL1b	0	0	0	1		1		1
IL6	0	0	0	1		1		1
IL10	0	0	0	0		0		0
IL12p70	0	0	1	1		1		1
RANTES	0	0	0	1		1		1
MCP1	0	NaN	1	1		1		1
MIP1b	0	0	0	1		1		1
KC	0	0	0	1		1		1
TGFb	0	1	1	0		0		1
ActiveNK	0	NaN	NaN	1		1		1
IFNg	0	NaN	1	1		1		1
ActiveN	0							
IFNab	0	0	1	0		1		1
ActiveCTL	0	NaN	NaN	1		1		1
pDC	0	NaN	NaN	0		0		1
ActivecDC	0							
ActiveTh	0	NaN	NaN	1		1		1
ActiveB	0	NaN	NaN	0		1		1
Ab	0							
Vlow	1	1	1	1		1		1
Vhigh	1	1	1	1		1		1
IEC								

Figure 44: Most often chosen model output from adult mice (top) and elderly mice (bottom).

Table 10: Most-often chosen model from bootstrapping for each age group.

Adult mice most-often chosen model	Elderly mice most-often chosen model
ActiveM ← (MIP1b | MCP1) & IL6	ActiveM ← KC & TNF
TNF ← ActiveM | ActiveN | ActivecDC	TNF ← ActiveM | Vlow
IL1a ← ActiveM | Vhigh	IL1a ← ActiveM
IL1b ← ActiveM	IL1b ← ActiveM
IL6 ← ActiveM | Vlow	IL6 ← ActiveM | ActiveN | ActivecDC
IL10 ← ActiveTh & Vhigh	IL10 ← ActiveTh & Vhigh
IL12p70 ← ActiveTh & Vhigh	IL12p70 ← (ActivecDC & IL1b) | (ActiveTh & Vhigh)
RANTES ← ActiveN	RANTES ← ActivecDC
MCP1 ← ActiveM | Vlow	MCP1 ← ActiveM | Vhigh
MIP1b ← ActiveM | ActiveN | ActivecDC	MIP1b ← ActiveM
KC ← ActiveM | Vhigh	KC ← ActiveM | Vlow
TGFb ← ActiveM & pDC & IL12p70	TGFb ← ActiveM & pDC & Vlow
ActiveNK ← ActiveM	ActiveNK ← ActiveM
IFNg ← ActiveM | ActivecDC	IFNg ← ActiveM
ActiveN ← (KC | MIP1b) & IL6	ActiveN ←(KC | MIP1b) & IL6
IFNab ← (pDC & Vhigh) | (ActivecDC & Vhigh)	IFNab ← (pDC & Vhigh) | (ActivecDC & Vhigh)
ActiveCTL ← IFNg | RANTES	ActiveCTL ← IFNg
pDC ← (Vlow | Vhigh | pDC) & TNF	pDC ← (Vlow | Vhigh | pDC) & TNF
ActivecDC ← ActiveN	ActivecDC ← ActiveNK
ActiveTh ← ActiveM & RANTES	ActiveTh ← ActivecDC | IL12p70
ActiveB ← ActivecDC & MCP1	ActiveB ← ActivecDC & MCP1
Ab ← (ActiveB & TGFb) | Ab	Ab ← (ActiveB & TGFb) | Ab
Vlow ← (IEC | Vlow | Vhigh) & ~(Ab & ~IL10)	Vlow ← (IEC | Vlow | Vhigh) & ~(Ab & ~IL10)
Vhigh ← (IEC | Vhigh) & ~Ab	Vhigh ← (IEC | Vhigh) & ~Ab
IEC ← (Vlow | Vhigh) & ~ActiveCTL & ~ActiveNK	IEC ← (Vlow | Vhigh) & ~ActiveCTL & ~ActiveNK

Table 11: Best fit rule sets for adult and elderly mice from bootstrap experiments.

Adult mice best-fit bootstrap model	Elderly mice best-fit bootstrap model
ActiveM ← (MIP1b | MCP1) & IL6	ActiveM ← KC & TNF
TNF ← ActiveM | ActiveN | ActivecDC	TNF ← ActiveM | Vlow
IL1a ← ActiveM | Vhigh	IL1a ← ActiveM
IL1b ← ActiveM	IL1b ← ActiveM
IL6 ← ActiveM | Vlow	IL6 ← ActiveM | ActiveN | ActivecDC
IL10 ← ActiveTh & Vhigh	IL10 ← ActiveTh & Vhigh
IL12p70 ← ActiveTh & Vhigh	IL12p70 ← (ActivecDC & IL1b) | (ActiveTh & Vhigh)
RANTES ← ActiveN	RANTES ← ActivecDC
MCP1 ← ActiveM | Vlow	MCP1 ← ActiveM | Vhigh
MIP1b ← ActiveM | ActiveN | ActivecDC	MIP1b ← ActiveM
KC ← ActiveM | Vhigh	KC ← ActiveM | Vlow
TGFb ← ActiveM & pDC & IL12p70	TGFb ← ActiveM & pDC & Vlow
ActiveNK ← ActiveM	ActiveNK ← ActiveM
IFNg ← ActiveM | ActivecDC	IFNg ← ActiveM
ActiveN ← (KC | MIP1b) & IL6	ActiveN ←(KC | MIP1b) & IL6
IFNab ← (pDC & Vhigh) | (ActivecDC & Vhigh)	IFNab ← (pDC & Vhigh) | (ActivecDC & Vhigh)
ActiveCTL ← IFNg | RANTES	ActiveCTL ← IFNg
pDC ← (Vlow | Vhigh | pDC) & TNF	pDC ← (Vlow | Vhigh | pDC) & TNF
ActivecDC ← ActiveN	ActivecDC ← ActiveNK
ActiveTh ← ActiveM & RANTES	ActiveTh ← ActivecDC | IL12p70
ActiveB ← ActivecDC & MCP1	ActiveB ← ActivecDC & MCP1
Ab ← (ActiveB & TGFb) | Ab	Ab ← (ActiveB & TGFb) | Ab
Vlow ← (IEC | Vlow | Vhigh) & ~(Ab & ~IL10)	Vlow ← (IEC | Vlow | Vhigh) & ~(Ab & ~IL10)
Vhigh ← (IEC | Vhigh) & ~Ab	Vhigh ← (IEC | Vhigh) & ~Ab
IEC ← (Vlow | Vhigh) & ~ActiveCTL & ~ActiveNK	IEC ← (Vlow | Vhigh) & ~ActiveCTL & ~ActiveNK

Time	0	1	2	3	4	5	6	7	8	9	10	11	12	13	14	15	16	17	18	19
ActiveM	0	NaN	1	NaN		1		1		1		1				1				1
TNF	0	0	0	1		1		1		1		1				1				1
IL1a	0	1	1	1		1		1		1		1				1				1
IL1b	0	0	0	1		1		1		1		1				1				1
IL6	0	1	1	1		1		1		1		1				1				0
IL10	0	0	0	0		1		1		0		0				0				0
IL12p70	0	0	0	0		1		1		1		1				1				0
RANTES	0	0	0	0		1		1		1		1				1				1
MCP1	0	NaN	NaN	1		1		1		1		1				1				1
MIP1b	0	0	0	1		1		1		1		1				1				1
KC	0	1	1	1		1		1		1		1				1				0
TGFb	0	0	0	0		1		1		1		1				0				1
ActiveNK	0	NaN	0	NaN		1		1		1		0				1				1
IFNg	0	0	0	1		1		1		1		1				1				0
ActiveN	0																			
IFNab	0	0	0	0		1		1		1		0				0				0
ActiveCTL	0	NaN	0	NaN		1		1		1		1				1				1
pDC	0	NaN	0	NaN		1		1		1		1				1				1
ActivecDC	0	NaN	1	NaN		1		1		1		1				1				1
ActiveTh	0	NaN	0	NaN		1		1		1		1				1				1
ActiveB	0	NaN	0	NaN		1		1		1		1				1				1
Ab	0	0	0	0		0		1		1		1				1				1
Vlow	1	1	1	1		1		1		0		0				0				0
Vhigh	0																			
IEC	0																			

Time	0	1	2	3	4	5	6	7
ActiveM								
TNF	0	1	1	1		1		1
IL1a	0	1	1	1		1		1
IL1b	0	1	1	1		1		1
IL6	0	1	1	1		1		1
IL10	0	0	0	0		0		1
IL12p70	0	0	0	0		1		1
RANTES	0	0	0	1		1		1
MCP1	0	1	1	1		1		1
MIP1b	0	1	1	1		1		1
KC	0	1	1	1		1		1
TGFb	0	0	0	0				1
ActiveNK	0	0	0	1		1		1
IFNg	0	0	1	1		1		1
ActiveN								
IFNab	0	0	0	1		0		1
ActiveCTL	0	0	1	1		1		1
pDC	0	0	1	1		0		1
ActivecDC								
ActiveTh	0	0	0	0		1		1
ActiveB	0	0	1	1		1		1
Ab								
Vlow	1	1	1	1		1		1
Vhigh	1	1	1	1		1		1
IEC								

Time	0	1	2	3	4	5	6	7	8	9	10	11	12	13	14	15	16	17	18	19
ActiveM	0	NaN	1	1		1		1		1		1				1				1
TNF	0	1	0	1		1		1		1		1				1				1
IL1a	0	0	0	1		1		1		1		1				1				1
IL1b	0	0	1	1		1		1		1		1				1				1
IL6	0	1	1	1		1		1		1		1				1				1
IL10	0	0	0	0		0		1		1		0				0				0
IL12p70	0	1	0	0		0		1		1		1				1				1
RANTES	0	0	0	0		1		1		1		1				1				1
MCP1	0	0	0	1		1		1		1		1				1				1
MIP1b	0	0	0	1		1		1		1		1				1				1
KC	0	1	1	1		1		1		1		1				1				1
TGFb	0	0	0	0		0		1		1		1				0				0
ActiveNK	0	NaN	0	1		1		1		1		1				1				1
IFNg	0	0	0	1		1		1		1		1				1				1
ActiveN	0																			
IFNab	0	0	0	0		1		1		0		0				0				0
ActiveCTL	0	NaN	0	1		1		1		1		1				1				1
pDC	0	NaN	0	0		0		1		1		1				0				0
ActivecDC	0	NaN	0	0		1		1		1		1				1				1
ActiveTh	0	NaN	1	1		1		1		1		1				1				1
ActiveB	0	NaN	0	1		1		1		1		1				1				1
Ab	0	0	0	0		0		1		1		1				1				1
Vlow	1	1	1	1		1		1		1		0				0				0
Vhigh	0																			
IEC	0																			

Time	0	1	2	3	4	5	6	7
ActiveM	0							
TNF	0	NaN	1	1		1		1
IL1a	0	0	0	1		1		1
IL1b	0	0	0	1		1		1
IL6	0	0	0	1		1		1
IL10	0	0	0	0		0		0
IL12p70	0	0	1	1		1		1
RANTES	0	0	0	1		1		1
MCP1	0	NaN	1	1		1		1
MIP1b	0	0	0	1		1		1
KC	0	0	0	1		1		1
TGFb	0	1	1	0		0		1
ActiveNK	0	NaN	NaN	1		1		1
IFNg	0	NaN	1	1		1		1
ActiveN	0							
IFNab	0	0	1	0		1		1
ActiveCTL	0	NaN	NaN	1		1		1
pDC	0	NaN	NaN	0		0		1
ActivecDC	0							
ActiveTh	0	NaN	NaN	1		1		1
ActiveB	0	NaN	NaN	0		1		1
Ab	0							
Vlow	1	1	1	1		1		1
Vhigh	1	1	1	1		1		1
IEC								

Figure 45: Best-fit rule sets from bootstrap replicates from adult (top panels) and elderly (bottom panels).

5.7 EFFECT OF DELETION OF SELECT IMMUNE COMPONENTS ON VIRAL CLEARANCE

We also tested the effect of removing certain elements of the immune response *in silico.* For each age group, one component of immunity was kept off for all steps of the simulation in the sublethal condition. All models identified by the bootstrap replicates were tested in these knockout conditions, and the average results for each age group are summarized in Table 12. In Chapter

4.10, we tested an ODE model of the immune response to influenza virus infection using the experimental data for the adult mice only. In that section, we tested the model's prediction of intrahost immune response in the sublethal condition with several elements of the immune response removed (Figure 35). The Boolean model deletions are compared to the ODE model in Table 12.

Table 12: Selected deletion of immune components in the ODE and Boolean influenza model**s.**

Component kept at baseline	**Adult mouse ODE model result**	**Adult mouse Boolean model result**	**Elderly mouse Boolean model result**
IL-10	Virus clears 2 days faster	Virus clears 1-2 days faster	Virus clears 2 days faster
NK cells	Virus does not clear. Infected cells stay high for longer.	No change in virus clearance	Virus does not clear. Infected cells stay high for 1 day longer.
Antibodies	No significant change in virus clearance	Virus does not clear	Virus does not clear
All inflammation	Virus does not clear. Infected cells peak higher.	Virus does not clear. Infected cells stay high longer.	Virus does not clear. Infected cells stay high longer.

Removing IL-10 from the system causes the virus to be cleared 2 days sooner than with IL-10 on. This result agrees with the prediction from our ODE model, despite the differences in the mechanisms of activation and degradation of IL-10 between the models. In the Boolean models, IL-10 inhibits the activity of antibodies on the virus clearance, and in the ODE model, IL-10 primarily functions to inhibit inflammatory responses (see Section 4.4). Figure 46 shows one example output from an IL-10 deletion simulation.

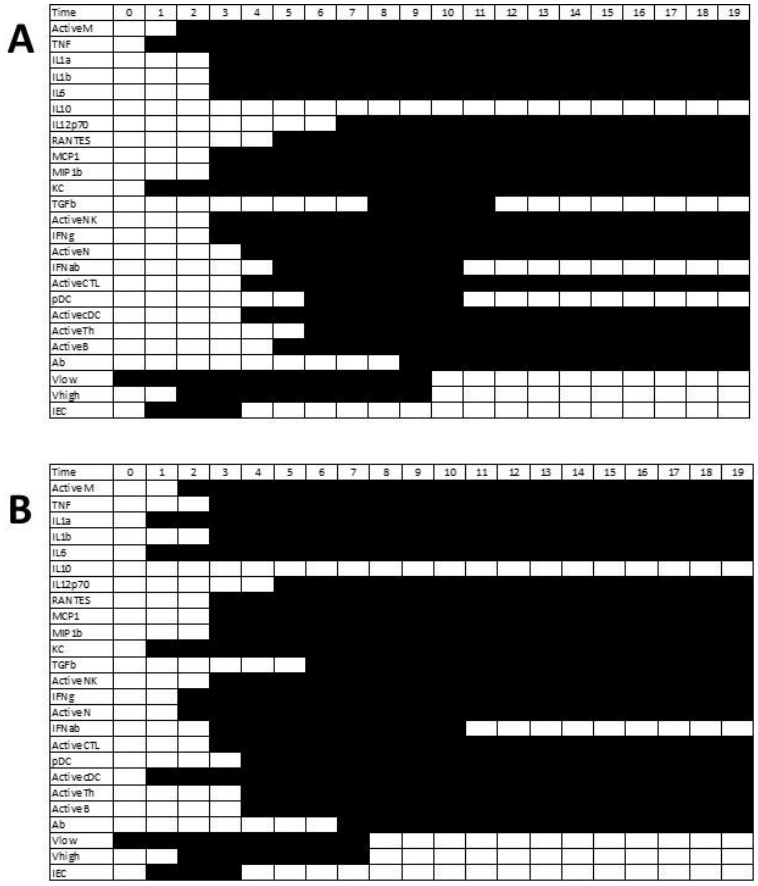

Figure 46: Example output from an IL-10 deletion simulation for (A) adult and (B) elderly mice.

NK cell deletions have different effects between the two age groups. Without NK cells, adult mice are still able to clear the virus fully from the system. NK cells predominantly clear infected cells, but CTLs have a redundant role in clearing the infected cells. CTLs will kill the cells independently and force the virus to clear. This result differs from the ODE model, in which an NK cell deletions will keep the virus from clearing and will force infected cells to stay elevated for a longer time.

In elderly mice, while NK cells are important for clearance of infected cells, they have an additional role aiding in the activation of cDCs. A lack of cDCs causes IL-10, IL-12, RANTES,

and type I IFN all to remain off for the full length of the simulation. Without these cytokines, pDCs, T_H cells, B cells, and antibodies all remain off as well, and without antibodies, the virus cannot clear from the system. NK cells have been shown to increase in number as we age [196], so their loss may be felt more strongly than in younger mice. Figure 47 shows an example output from an NK cell deletions test.

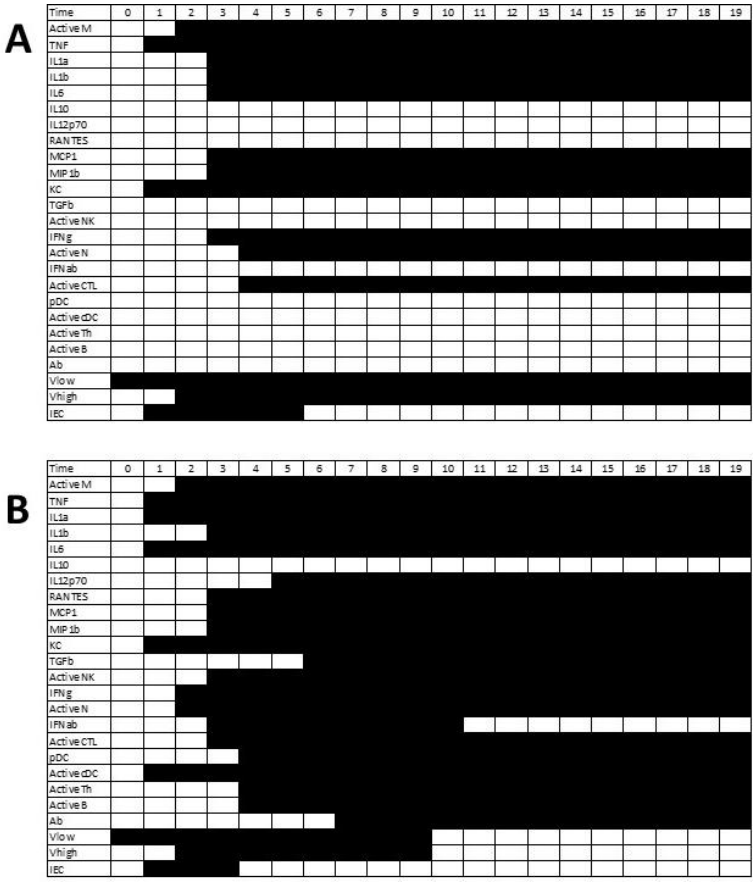

Figure 47: Example output from an NK cell deletions simulation for (A) adult and (B) elderly mice

Removing antibodies keeps virus from clearing in both Boolean models, consistent with biology. In the ODE model, the virus was able to clear even without an increase in antibodies (Figure 35). Infected cells are cleared quickly, removing the source of new virus from the system. Without a large production in virus, the innate responses are able to clear the virus relatively easily, though this may not reflect how the virus would act *in vivo*. The Boolean models better reflect the necessity of antibodies in survival of viral infection. Figure 48 gives an example simulation from an antibody deletion test.

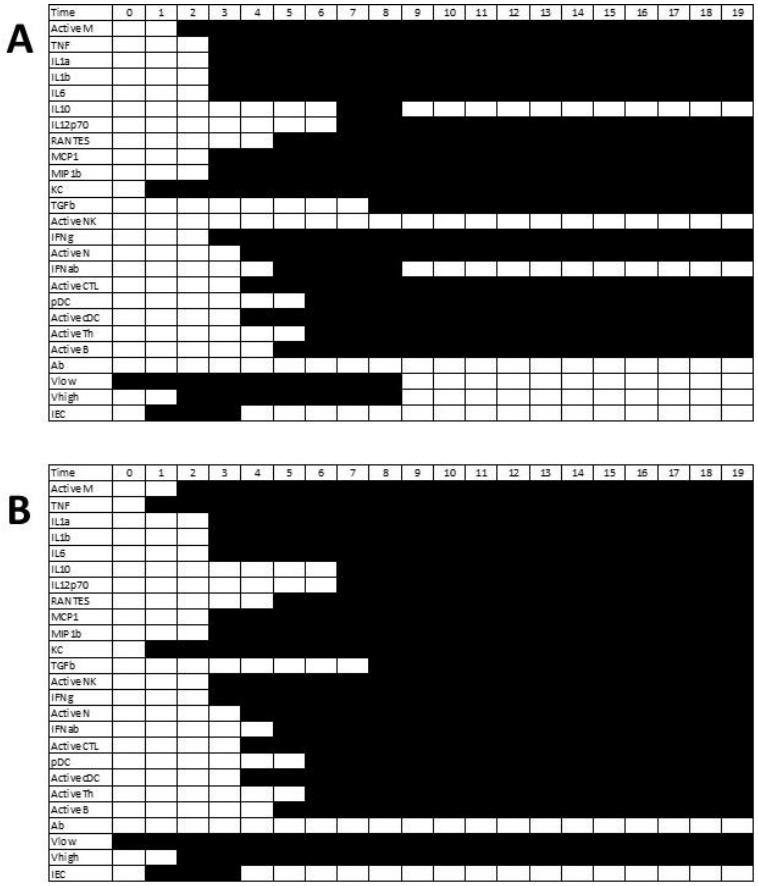

Figure 48: Example output from an antibody deletion simulation for (A) adult and (B) elderly mice.

Removing all inflammatory components from the model has a largely deleterious effect on the host. The final row in Table 12 demonstrates the models' responses when macrophages, cytokines, and chemokines have all been removed from the system. In all three model simulations, the virus cannot be cleared from the system without the onset of inflammation, and infected cells will peak higher and longer than with this arm of the immune system in place.

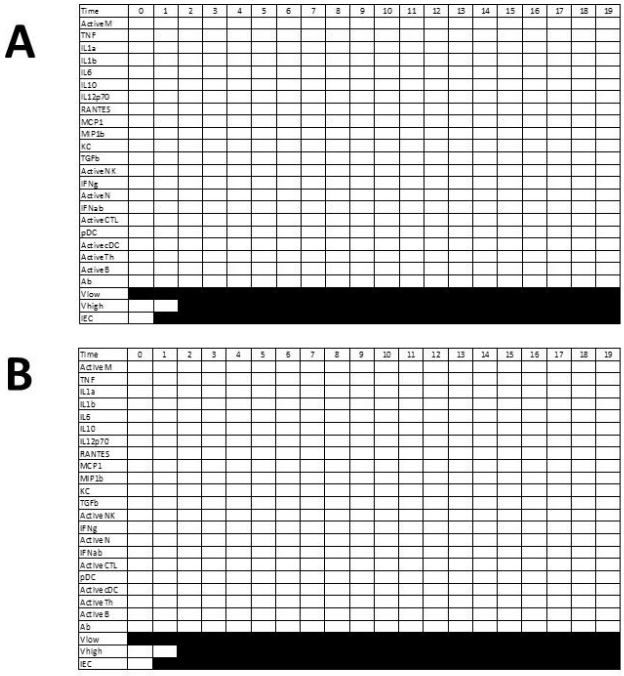

Figure 49: Example output from a total inflammation removal for (A) adult and (B) elderly mice. Without macrophages, cytokines, or chemokines, no branch of immunity can turn on with these rules, and the virus grows in the host unabated.

5.8 DISCUSSION

Immunosenescence in humans is a poorly understood phenomenon. The changes to the immune system in healthy elderly patients can be difficult to ascertain given the wide range of inter-patient variability seen in human subjects, as well as the complex system of interactions between immune components. Discrete, rule-based models allow data-driven discovery of important interactions between components of host-virus response to influenza infection in a way that may be more robust to inter-patient variability than other modeling platforms, such as ODEs. Most previously published Boolean models of the immune response to infection focus exclusively on the steady-state condition of the nodes [176–179]; our model, however, looks at a broad range of time-series data to which the outputs of each variable are matched. Our model thus enables a quantitative analysis of the prediction of the model over time.

Rule-based models allow for an intuitive interpretation of the interactions between variables, making them simpler for non-experts to understand and apply. The rules allow for a representation of complicated biological phenomena with a straightforward combination of ORs, ANDs, and NOTs. Rule-based models also allow for discovery of novel interactions between components of the model.

In comparing activation data between young and elderly mice, it is clear there must be a shift in the cellular source of many cytokines and chemokines as we age. The macrophage Boolean data shows activated macrophages increase on day 2 for both adult and elderly mice. There is disagreement in the literature over how macrophage populations change as we age; some papers report a decrease in bone marrow macrophage counts [197,198], whereas other papers suggest an increase [199]. Defects have also been reported in toll-like receptors (TLRs) on macrophage surfaces [164], which may diminish their ability to react to an infection, affecting the numbers of

macrophages found in the tissue during experiments. Our data suggest age presents no difference in recruitment of macrophages to the site of infection, but there is a difference in the cytokine expression in these cells.

Macrophage-type cells contribute a large amount of the inflammation response in a healthy young host. Because macrophage Boolean data do not indicate a change with age, other cell sources must account for the delay in inflammatory cytokine response. A decrease in macrophage-derived pro-inflammatory cytokines has been previously reported in rodent studies [200], and macrophages have been identified as a primary cause of TNF and IL-6 dysregulation in mice [201]. We see more dependence on dendritic cells in the elderly mice in our analysis, particularly in the production of RANTES, IL-10, IL-12, and MIP-1β. Some studies have reported either no change or an increase in percentage of DCs as we age [194,202,203], so elderly hosts may rely more heavily on these cells to compensate for a decrease in other immune cell functions. Our rules also indicate an important role of macrophages in activation of T helper cells in younger mice. Though dendritic cells are generally considered the major antigen-presenting cell (APC), our model suggests interstitial macrophages also have a critical role bridging the innate and adaptive responses in a healthy younger host [204].

Cytokine dysregulation plays an important role in the rule choices for older mice. Almost every cytokine and chemokine are regulated by rules different from those used in the younger mouse model. In particular, elderly mice are less likely to have inflammatory components respond directly to virus, representing an initial upregulation by lung epithelial cells. Dysregulation of the lung epithelium may account for the slower initiation of many immune responses in elderly hosts. The inflammatory response has been shown to be delayed by about two days in elderly hosts [127]. Bootstrapping also validated T_H cells as a major producer of IL-10 in the elderly. The T_H cell

response is biased toward a T_H-2 phenotype in the elderly, leading to a large production of IL-10 by T cells [205]. It is also likely the experiments measuring the T_H cells included T_{reg} cells in addition to traditional T helper cells, and T_{reg}s are known producers of IL-10 [188]. Our consensus rule set was able to capture the variations in inflammation seen with increased age.

Several cell types had identical rules in the two age groups: CTLs, NK cells, neutrophils, and B cells. Neutrophils had no measured data associated with them in this model, so we could not predict a difference in the neutrophil trajectories over time. NK cells, CTLs and B cell data were all very similar between the young and older mice. Though their function and effect on other components of the model may vary, the Boolean data revealed enough similarity in these components that they were generally able to agree on rule choices. This implies that the differences in activation and recruitment in the innate immune response are more substantial than those in the adaptive and humoral responses in this model.

Some of our results may have been improved with a richer data set. Some variables of the model, such as neutrophils and epithelial cells, did not have accompanying data to which we could match our trajectories. Others, like antibodies and macrophages, had data in some cohorts but not in all. Cells were not measured on every day of the experiment, causing several missing data points at which time our model could predict a cell to be on or off without penalty. Adding to this data set may have strengthened our predictions by removing this ambiguity. We also are unable to obtain truly longitudinal data for a mouse model of influenza, as mice must be sacrificed in order to measure the data [97]. These trajectories then had to be reconstituted from pooled data from three different animals sacrificed at each time point. Results may have been further improved if we had been able to track a single animal over the full course of its infection.

The results can also change significantly if the p-values used to obtain the 0s and 1s are changed. After performing so many statistical tests to generate the Boolean-valued data, we may have needed to perform some correction to the p values, such as a Bonferroni correction. This would have adjusted several of the probabilities and forced some of the predicted 1s to 0s. Future work on this model may take this into account.

Hernandez-Vargas et al. have previously studied this influenza infection data in young and older mice [112]. Using an ODE model, the authors fit data for the virus levels in both age groups. They determined type I interferon, type II interferon, and TNF have redundant roles in mediating antiviral effects post-infection, but they do not consider the different mechanisms by which each of these cytokines helps the host to fight the infection. Our model incorporates many more mechanisms, and as such we are able to capture information about dysregulation in activation and recruitment of cells and cytokines, which tend to vary greatly between age groups. The authors also did not find an important effect of NK cells in improving the fits of their model to the experimental data. Our model, however, presents an important role of NK cells, particularly in the elderly mice simulations. NK cells have been shown to increase greatly with age, likely to compensate for a deficiency in CTLs in older hosts [196].

Boolean models do not model slow dynamics well, as they represent a fast change from "off" to "on". A slow, steady rise in a certain variable is not well accounted for in a Boolean model. Our model also does not handle deactivation well. If all variables are in a steady state for two time points in a row, the Boolean model cannot change its output any further. For that reason, our rules largely ignore variables that have reverted to a 0 at the end of the 19 day simulation. Future work may include improving upon that by possibly including delays or more variables so more changes can occur at the later time points in the sublethal simulations.

5.9 CONCLUSIONS

In conclusion, we have presented an application of optimization methods for Boolean network models with a model of murine influenza A viral infection. We generated a library of potential rules for this complex series of interactions comprising the immune response to viral infection, and using the optimization method outlined in Section 5.4, produced a set of rules that best fits the time-series data. Our model emphasizes differences between younger and older hosts, supporting some documented mechanisms of immunosenescence. Importantly, the Boolean network also led to suggestions of alternative data-driven mechanisms, like those in the rules for TGF-β and IL-12, which could guide further focused experimental work on uncovering the biological bases of immunosenescence.

6.0 DEVELOPMENT OF AN ODE MODEL OF INFLUENZA-PNEUMONIA SUPERINFECTION

6.1 OVERVIEW

Influenza A virus (IAV) infections are often made worse by a secondary bacterial pneumonia infection A *superinfection* occurs when the host suffers a second infection before fully recovering from the initial infection. IAV-pneumonia superinfection is especially evident during flu pandemics. For example, during the 1918 Spanish Flu epidemic, a majority of the 50 million deaths were believed to be caused by a secondary bacterial infection [206–209]. Similar trends have been seen in other influenza pandemics, though the particular bacteria causing the secondary infections has changed over time. The 1918 pandemic was predominantly characterized by *Streptococcus pneumoniae* infections, but recently the emergence of the USA300 and USA400 strains of *Staphylococcus aureus* has led to an increase in staph infections [206,208,210]. A high incidence of bacterial superinfection was also evident in the 2009 H1N1 pandemic [211]. Superinfection causes tens of thousands of excess hospitalizations and deaths each year, particularly among the elderly [212,213].

Multiple theories exist as to which mechanisms are primarily responsible for the increased lethality due to the superinfection of IAV and bacterial pneumonia [214–223], but no one theory has yet satisfactorily explained this phenomenon. Dysregulation of cytokines, neutrophil deactivation, immune system overload, and increased damage to the epithelium have all been identified as potential mechanisms of excess death rates in superinfection. One important factor that many theories overlook is the importance of the time between IAV and bacterial infections.

For many years, the prevailing theory was that the body simply could not fight off two infections simultaneously, leading to decreased survival rates of influenza when bacterial superinfection occurs. However, a 2002 study by McCullers and Rehg [217] proved the probability of survival after superinfection depends largely on the time between primary and secondary infections. Mice in this study were able to survive when bacteria infected the mice a week before the virus, but when IAV was the primary infection, mice had very little chance of survival. The increased likelihood of death after IAV-pneumonia superinfection has been attributed to a "lethal synergism" of the virus and bacteria; when the two are simultaneously present in the host, they can jointly cause morbidity and mortality. Using mathematical modeling techniques similar to those presented in Chapters 2-4, we investigate the mechanisms primarily responsible for this change in survival probability given the time between insults.

6.2 POTENTIAL MECHANISMS OF LETHAL SYNERGISM IN IAV-PNEUMONIA SUPERINFECTION

6.2.1 Excess inflammatory responses

As we have shown in Chapter 4, inflammation can cause excess damage to the host, worsening the outcome of the infection. The presence of the virus causes damage to the epithelium and elicits the inflammatory response, and the corresponding influx of neutrophils increases damage further. Damaged lung tissue allows for bacterial movement between lung and blood compartments, as shown in Chapters 2 and 3, and this increased diffusion enhances bacterial replication and survival in the tissue, diminishing the host's chances of clearing the bacteria.

6.2.2 Neutrophil ineffectiveness

Some studies have also shown that though a large number of neutrophils are activated after IAV infection, these neutrophils become less effective when the secondary infection begins [224,225]. Weakened neutrophils could allow the bacteria to replicate more quickly and overtake the host tissue. This mechanism would be absorbed in the parameters ξ_{nl} and ξ_{nb} (Equations 6.4 and 6.11), where one or both of these parameters would take on a lower value than we would normally see for a BALB/c mouse (see Figure 4). The work in Chapter 2 showed that BALB/c mice have an especially strong neutrophil efficacy in the blood compartment (ξ_{nb}) in response to bacterial infection, so we may see this parameter most strongly affected by the neutrophil weakness reported after superinfection.

6.2.3 Weakened mucociliary responses

The presence of IAV can also cause a weakened mucociliary response in the host. One of the first immune responses to IAV is an increase in type I interferon levels, expressed by infected epithelial cells to generate an antiviral state in surrounding epithelial cells to limit the spread of the infection. High levels of interferon causes a decrease in IL-23 levels, which then reduces IL-17 levels and leads to a reduction in mucociliary action in the lungs [226]. Thus, when virus is the primary infection, type I interferon levels are high when bacteria arrive in the lung, decreasing the initial nonspecific clearance rates and leading to an insurmountable infection. However, when bacteria infect first, interferon levels are low, so mucociliary clearance is unobstructed, leading to a quick depletion of bacteria.

6.3 PREVIOUS WORK

Smith et al. [227] developed an ODE model of IAV-pneumonia superinfection. The model was fit to data for a superinfection of influenza strain PR8 (the same strain used in Toapanta and Ross's experiments detailed in Chapter 4) and *Streptococcus pneumoniae* strain D39. The authors do not identify the same mechanisms by which bacteria worsen a viral infection, as they do not take into account the timing between infections or the high survivability associated with a bacteria-first IAV-pneumonia superinfection. In their model, Smith et al. combine a previous influenza ODE model [102] with a bacterial infection ODE model [40] to create an influenza coinfection model. The model includes terms describing an increased bacterial adherence to infected epithelial cells, increased virus production due to bacterial presence, decreased macrophage phagocytosis rates, and increased carrying capacity of bacteria. The authors cite evidence for increased bacterial adherence to virally infected cells due to increased presence of neuraminidase on the cell surface to which the bacteria can adhere [228]. The authors also include terms for desensitization of the immune system after virus infection, causing decreased macrophage clearance of bacteria [229]. The bacterial carrying capacity is assumed to be larger after viral infection, and virus reproduction is assumed to be stronger in the presence of bacteria as well.

6.4 ODE MODEL

The ODE model used to model IAV-pneumonia superinfection is given in Equations 6.1 –6.11. The structure of the model is designed as a combination of the bacteria model given in Equations 2.1 – 2.4 and a simplified version of the influenza ODE model presented in Equations 4.1 – 4.20.

Target epithelial cells (H) become infected cells (I) after interaction with free virus (V). Healthy cells are killed by interaction with lung bacteria (P_L) or neutrophils (N). They are replenished at a rate proportional to the number of dead epithelial cells ($H_{max} - H - I$). Infected cells can also be killed by bacteria or neutrophils, and they have an additional natural decay rate (δ). Experimental evidence shows neutrophils may interact with infected cells differently than with healthy cells, so we allow two different rates of neutrophil killing, g_H and g_I [230,231].

$$H' = -\beta HV + \lambda(H_{max} - H - I) - \frac{dHP_L}{1 + \kappa P_L} - \frac{g_H HN}{1 + \eta N} \quad 6.1$$

$$I' = \beta HV - \delta I - \frac{dIP_L}{1 + \kappa P_L} - \frac{g_I IN}{1 + \eta N} \quad 6.2$$

Virus is produced by infected cells, but this production is directly inhibited by type I interferon (F) [117]. Virus is cleared by nonspecific clearance (a_{v1}) or by antibodies (c). Antibodies are not explicitly modeled here, so for simplicity we assume a constant rate of clearance for the virus [102].

$$V' = \frac{pI}{1 + qF} - \frac{a_{v1}V}{1 + a_{v2}V} - cV \quad 6.3$$

Lung bacteria are modeled in nearly the same manner as in Equation 2.1, with two exceptions. First, there is an additional term which limits the nonspecific clearance of bacteria proportionally to the presence of type I interferon (F) to reflect one of our hypotheses on lethal synergism. There is also an additional clearance term to represent macrophage phagocytosis rates (ξ_m).

$$P_L^{'} = k_l P_L - \frac{\nu P_L}{(1+\mu P_L)F} - \frac{\xi_{nl} N P_L}{1+\xi_2 P_L} - \frac{\xi_M M P_L}{1+\xi_2 P_L} + f[(b(H_{\max} - H - I) + a)P_B - bDP_L] \quad 6.4$$

TNF (T) is the pro-inflammatory cytokine used in this model, and IL-10 (L) is the anti-inflammatory cytokine. The equations used to describe these variables are significantly simplified from those used in equations 4.5 and 4.6. Both cytokines are produced by macrophages and decay naturally.

$$T' = \gamma_T M - \mu_T T \quad 6.5$$

$$L' = \gamma_L M - \mu_L L \quad 6.6$$

Neutrophils (N) are brought into the infected tissue from a bloodstream source (N_B) after activation by signals from TNF and blood bacteria. Neutrophil recruitment is limited by anti-inflammatory signals from IL-10. Neutrophils decay naturally at rate μ_N.

$$N' = \frac{\left(h_T(T - T_0) + h_p P_B\right) N_B}{1 + \theta_T(T - T_0) + \theta_L(L - L_0)} - \mu_N N \quad 6.7$$

Macrophages are produced by a summation of excitatory signals (Σ_M), composed of interferon [7,117], TNF [128], bacteria, and virus [31,232]. These terms are similar to those proposed in Chapter 4 with Σ_1 and Σ_2. Macrophages decay back to their baseline level M_0, a parameter defined by the experimental data at day 0.

$$\Sigma_M = b_f(F - F_0) + b_T(T - T_0) + b_p P_L + b_v V \quad 6.8$$

$$M' = \frac{\Sigma_M}{1 + \theta_m \Sigma_M} - \mu_M (M - M_0) \tag{6.9}$$

Type I interferon (F) is produced by infected cells to induce viral resistance in surrounding healthy epithelial cells. It decays at rate μ_F to its baseline level F_0, which is defined by the experimental data.

$$F' = \left(\frac{b_i I}{1 + \theta_F F}\right) - \mu_F (F - F_0) \tag{6.10}$$

The equation for blood bacteria is the same as in Equation 2.2, with the addition of a macrophage phagocytosis term.

$$\begin{aligned} P_B' = k_b P_B \left(\frac{P_B - \varepsilon}{P_B + \varepsilon}\right)\left(1 - \frac{P_B}{K}\right) - \frac{\xi_{nb} N P_B}{1 + \xi_2 P_B} - \frac{\xi_{mb} M P_B}{1 + \xi_2 P_B} \\ -(b(H_{\max} - H - I) + a) P_B + bDP_L \end{aligned} \tag{6.11}$$

Figure 50 shows a network diagram demonstrating how these variables interact in the previous equations. Red blunt arrows denote inhibition, while blue arrows represents a source of a variable.

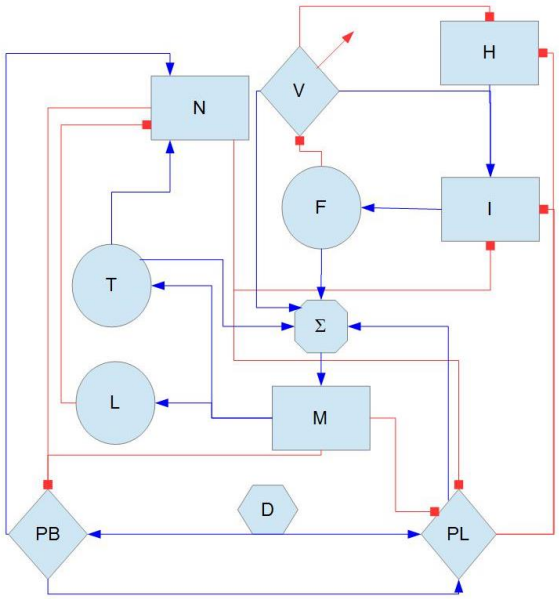

Figure 50: Schematic of variable interactions in IAV-pneumonia superinfection model.

6.5 EXPERIMENTAL DATA

The experimental data to which the model is calibrated comes from a study by McCullers and Rehg [217]. The data includes time of survival post-infection for a variety of different infection scenarios. These data are summarized in Figure 51 and Figure 52. In Figure 51, we summarize five trials in which groups of 20 mice were infected with their primary infection at day -7, followed 7 days later (day 0 on this plot) by a secondary infection.

The mice infected with bacteria then virus (light blue data) showed 100% survival for a week after the experiment, while the mice infected with virus then bacteria (dark blue data) a all died within 24 hours of the secondary infection. The other trials used phosphate-buffered saline (PBS) was as a control for the first infection, then varied what was administered at day 0. The PBS-Pneumonia infected mice (orange data) experienced about 15% deaths, all of which occurred

within the first week post-infection. The PBS-IAV infected mice (gray data) showed about 35% death spread out over the first 10 days post-infection. Finally, one group of mice was given PBS, then a combination of IAV and pneumonia at day 0 (yellow data). These mice had 60% deaths, but they still fared far better than those in the IAV-pneumonia group.

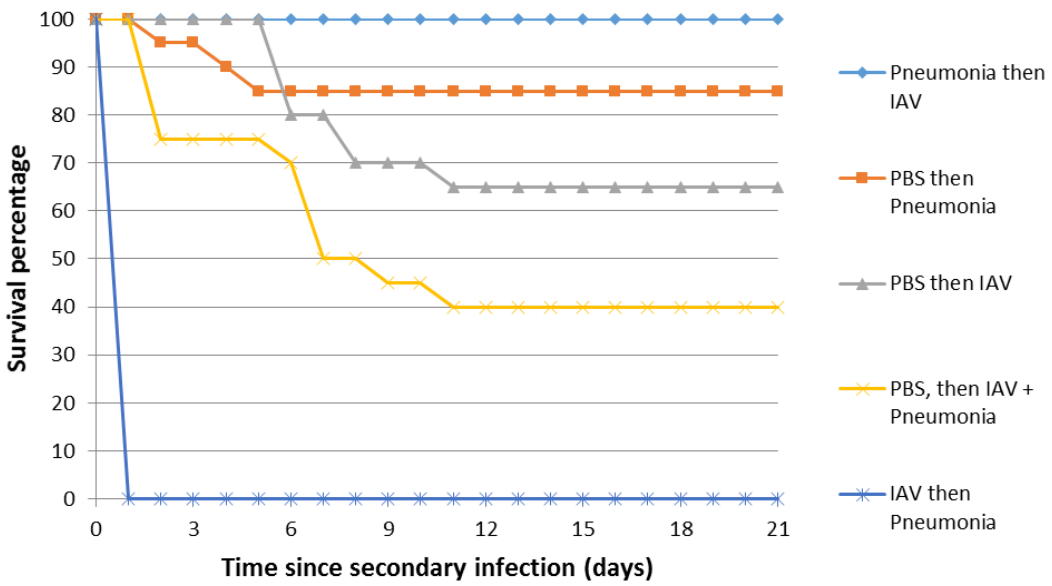

Figure 51: Survival data from five distinct superinfection experiments.

Data reproduced from McCullers and Rehg, J Infect Dis 2002 [217]. Experiments begin on day -7 when the infection listed first in the legend was given to the mice in each group (n=20 per group). All 100 mice survived to day 0, when a second infection was administered, creating a superinfection. Mice were then studied for survival post-secondary infection. The percentage of mice which survived per day is plotted here for each experimental group. IAV = influenza A virus. PBS = phosphate-buffered saline.

The authors also studied the effect of timing of infection on lethal synergism. Groups of 6 mice were challenged with pneumococcus bacteria at different times relative to the viral infection

at day 0. Time to death for each mouse was measured, as well as the percent of mice from each group which survived a full 3 weeks after the secondary infection. Figure 52 shows the results of this experiment. Again, when pneumococcus are administered a week before the virus (data shown at day -7 on Figure 52), 100% of mice survived. The data at day 0 represent a simultaneous infection of virus and bacteria. At each other point, the bacteria are given some number of days after the virus. The data indicate that there is zero likelihood of 21-day survival if bacteria are given 3 to 7 days after the virus. Any other timing tested by these authors presented a nonzero chance of survival. This would indicate a "window of opportunity" exists for the bacteria between 3 and 7 days post-viral infection. The immune response during this time must create an environment conducive to bacterial survival. The goal of the ODE model will be to explain the presence of this window and recreate it *in situ*.

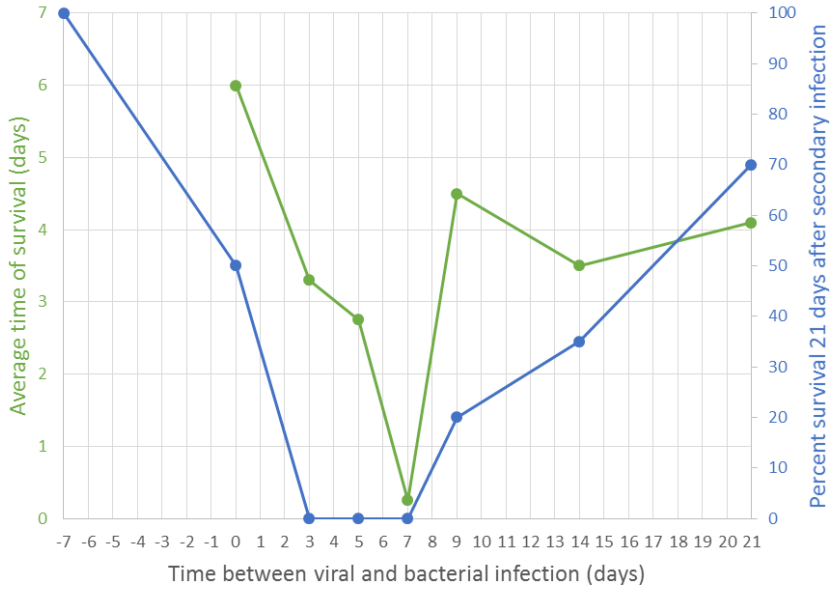

Figure 52: Superinfection experimental data for time to death.

Data reproduced from McCullers and Rehg, J Infect Dis 2002 [217]. The green curve corresponds to the left axis, representing the average time of death in days for mice in each experimental condition. There is no point plotted for

mice in the bacteria-first condition, as all mice survived the full length of the experiment. The blue curve corresponds to the right axis, plotting the percent of mice in each group that survived 21 days post-secondary infection. No mice survived for 21 days in either the 3-, 5-, or 7-day groups.

We were unable to obtain experimental data for the measurements of the variables of the model in a superinfection experiment. Instead, the first portion of the model (before the bacteria have been introduced) can be calibrated with the younger mouse influenza infection data used previously in Chapters 4 and 5 [127]. These data were taken from BALB/c mice, the same strain of mouse used in the McCullers study, an important point since Chapter 2 proved how distinctly mouse strains can respond to identical infections. The bacteria-dependent parameters are fit using heuristics and knowledge of what these trajectories should look like given the work performed in Chapters 2 and 3.

6.6 PARAMETER FITTING

Parameter fitting was performed with the MATLAB function "fminsearchbnd", a bounded search algorithm. Bounds on parameters are derived from literature values where available, and are estimated for the other parameters. Table 13 shows the parameters and their allowed bounds for the superinfection model.

Fits to the data are again determined with a log-likelihood cost function in addition to several heuristics determined from literature. Since the initial viral dose of 50 PFU is known to be a sublethal dose [127], the virus must be cleared by the immune system when no bacteria are administered. From the work done in Section 2.9, we know BALB/c mice can clear a small single

infection of 1000 CFU D39 bacteria. Thus, if only a small bacterial infection is administered, the host must be able to clear the bacteria as well. In addition, the system must return to a healthy state if bacteria are given seven days before the virus.

Death is defined in the model as the time at which lung bacteria reach their peak value and remain at some nonzero steady state. Two heuristics are used to calibrate the time of death. First, when bacteria are administered 14 days after viral infection, the time to death must be between 3 and 5 days [217]. Also, when bacteria are administered 7 days after the virus, time to death must be no more than 2 days.

The model parameters are calibrated to the case when bacteria are administered at day 11, which provides a full 11 days of data to which the model can be trained. All other cases presented in Figure 52 are used as testing data on which to validate our parameter choices.

6.7 RESULTS

6.7.1 Fits to viral infection data: 11 day delay between IAV and pneumonia

Figure 53 shows the best fit of the model to the influenza data. Time to death in this simulation is about 4.4 days, which corresponds to what we see in the McCullers data (Figure 52). The parameters used to generate this fit are given in Table 13. The virus fits reasonably well to the experimental data, though in the superinfection simulation the virus does not clear as quickly as the data imply. Lung bacteria is brought in at day 11 at a level of 1000 CFU. It quickly begins to move into the blood compartment, generating a high population of blood bacteria (PB). Once bacteria levels in the blood are high enough, they begin to move back into the lungs in significant

quantities, generating the fast rise in PL seen at day 14. Bacteria then quickly hit their peak around day 15, leading to death of the host.

Target epithelial cells (H) show only a slight decrease from the viral infection, corresponding to the peak in infected epithelial cells (I), which in turn causes the peak in type I interferon (F) levels. When the bacteria reach their steady-state value, we see a corresponding dip in target epithelial cells that cannot be healed with the bacteria present.

The inflammatory components of the model (TNF, IL-10, macrophages, and neutrophils) all fit reasonably well to the data. The N trajectory misses points at days 1 and 3, but those data points have such large standard deviations their measurements are highly uncertain. Macrophages also begin to fall back to baseline earlier than the mean data would suggest, but still within the standard deviation of the data.

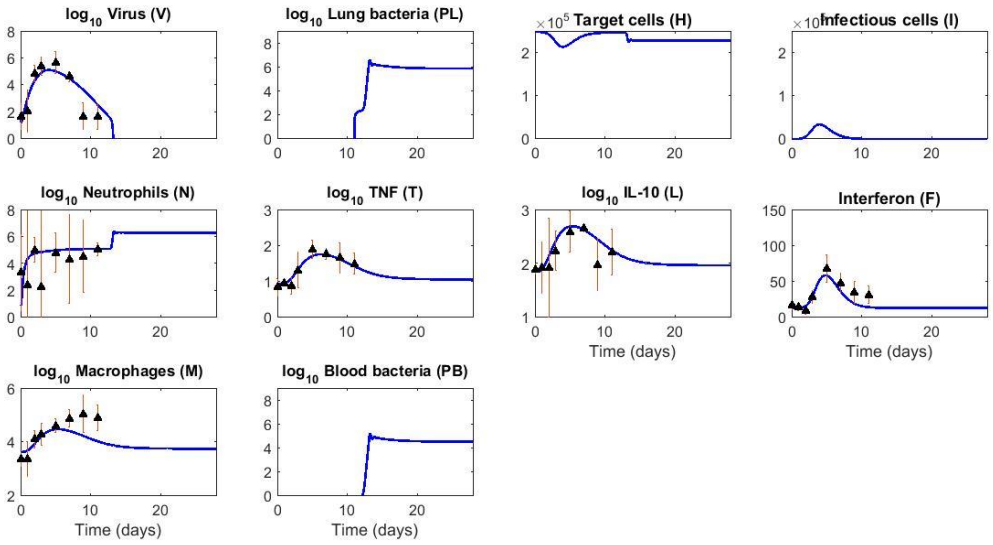

Figure 53: Virus-bacteria superinfection simulation with 11 day delay between infections. Data plotted are experimental data used for calibration of the model up to day 11 post-viral infection. Lines represent single trajectory from a model fit with parameters listed in Table 13.

Table 13: Parameters and their associated values for superinfection model.

Parameter	Meaning	Value	Parameter	Meaning	Value
β	Infectivity of virus	6.27E-6	μ_L	Decay of L	29.96
κ	Saturation parameter for bacterial infection of epithelial cells	1.75E-8	b_F	Activation of M due to F	6.06E4
d	Rate of death of H or I due to bacteria	7.77E-7	μ_F	Decay of F	1.08
g_H	Rate of death of H due to neutrophils	3.07E-4	b_P	Activation of M due to lung bacteria	2.5E-5
η	Saturation parameter for N killing of H	2.17E-7	b_T	Activation of M due to TNF	3.27E3
δ	Natural decay rate of infected cells	0.08	μ_M	Natural death of M	1.07
p	Replication rate of V	90.76	b_V	Activation of M due to V	0.21
q	Rate at which interferon limits V replication	2.27E-5	θ_F	Saturation of F production by I	1.2E-3
ν	Nonspecific clearance of bacteria	30.67	b_I	Production of F by I	20.81
μ	Saturation parameter for bacterial clearance	3.20E-7	σ_M	Saturation of M activation	4.2E-9
λ	Replication rate of H	5.33E3	b	D-dependent movement of P into blood	1.78E-5
ξ_2	Saturation parameter for bacterial clearance by N or M	1.41E-9	f	Volumetric difference between lungs and blood	156.38
k_l	Replication rate of bacteria in lungs	0.61	a	D-independent movement of bacteria from blood to lungs	7.66
K	Carrying capacity of bacteria in blood	5E8	k_b	Replication rate of P in blood	20.81
ξ_{mp}	Clearance of bacteria by M in lungs	1.51E-6	ε	Threshold of P replication in blood	1
ξ_{nl}	Clearance of bacteria by N in lungs	8.44E-7	ξ_{mb}	Clearance of bacteria by M in blood	8E-7
h_T	Activation of N by T	0.71	ξ_{nb}	Clearance of bacteria by N in blood	9.3E-6
μN	Natural death of N	6.28	h_p	Activation of N by PL	0.0011
θL	Limitation of N activation by L	0.22	g_I	Rate of death of I due to N	6.16E-5
γ_T	Production of T	2.3E-3	a_{v1}	Nonspecific clearance of V	2.55E4
μ_T	Decay of T	1.15	a_{v2}	Saturation of av1	3.65E3
γ_L	Production of L	0.48	c	Clearance of V by immune system (antibodies)	21.70

6.7.2 Adjusting day of bacterial infection to day 7

The test case in which bacteria are given to the host at day 7 is shown in Figure 54. The entrance of the bacteria at day 7 leads to a fast clearance of the virus about 2 days later. The lag time between entrance of the bacteria and the peak of lung bacteria also shrinks to about 1 day, compared to about 2 days in 11 day delay case. While the lung bacteria population does fall slowly from its peak, it does not fall quickly enough for the target cells to recover, causing death to the host in our model. Time to death in this simulation is about 1.9 days, around 1 day slower than the McCullers data implies but still a fast death.

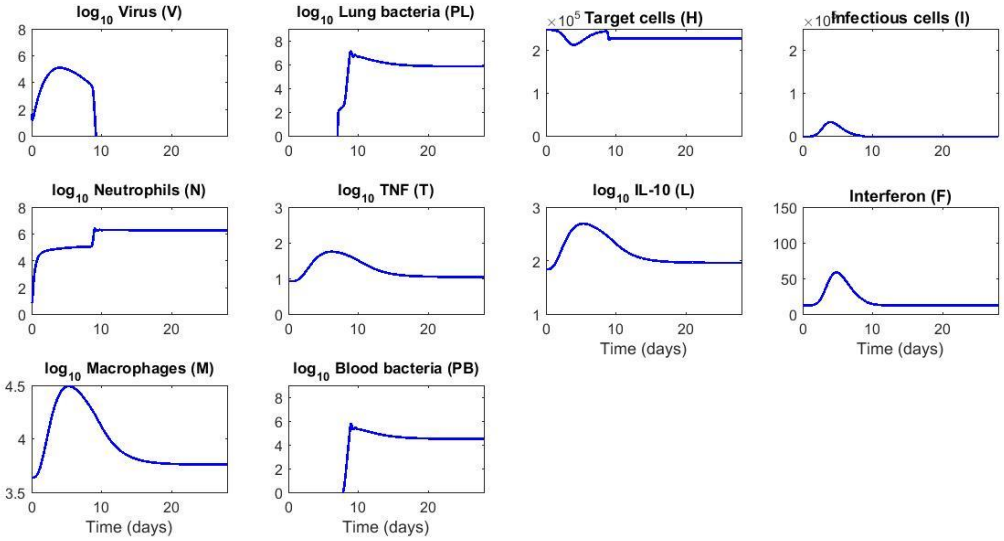

Figure 54: Virus-bacteria superinfection simulation with 7 day delay between infections.

In this case, lung bacteria peak at day 8.9, meaning the time to death predicted by the model is about 2 days. The experimental data indicates death should occur about 1 day after the bacteria are administered, making our model slightly slower than the experiments would indicate. This simulation was used as a validation rather than calibration, so no data are plotted here.

6.7.3 Infection simulation with bacteria administered first

When bacteria are administered a week before the virus in the McCullers experiments, 100% of mice survived a full 21 days, seemingly fully overcoming the infection. In Figure 55, we use the same parameters as in Table 13, but the initial conditions are changed such that the virus is given at day 7 and the bacteria are given at day 0. In the initial parameter fitting procedure, we require that this condition lead to full recovery of the host. Figure 55 shows the bacteria are able to be cleared after about 5 days, and since the dosage of virus given is defined as a sublethal dose, the host can also survive the subsequent viral infection.

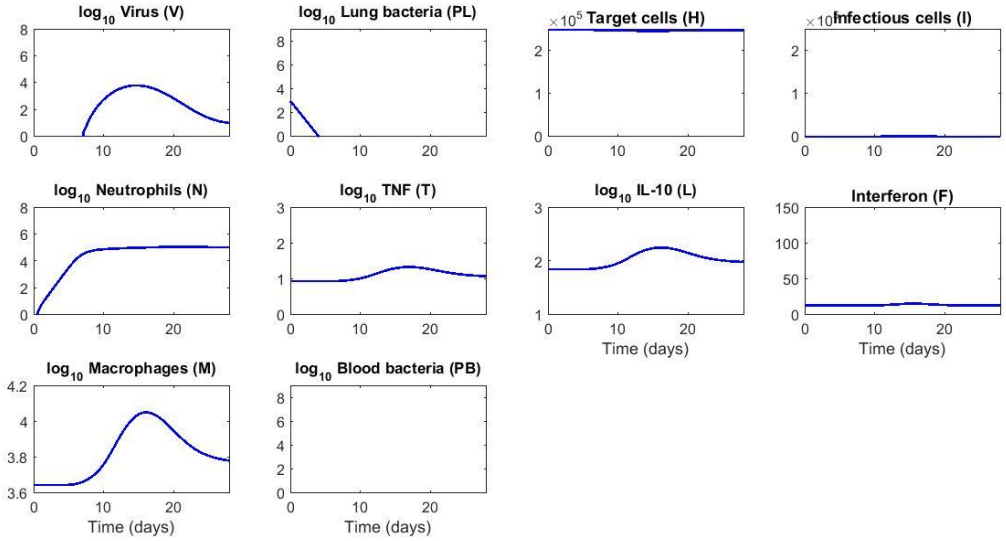

Figure 55: Bacteria-virus superinfection simulation with 7 day delay between infections.

When bacteria are administered first, they clear quickly, causing no significant damage to the system. When the virus is then given, there is a more noticeable immune reaction, but the virus will eventually clear from the host and the system will return to baseline, consistent with experimental evidence.

6.7.4 Comparing survival times to data

We tested each experimental condition provided in Figure 52 from the McCullers experiments, changing only the initial conditions of the lung bacteria and the virus to replicate the experimental conditions. Parameters for the model were kept constant to the values provided in Table 13. In Figure 56, we show a comparison between the expected length of survival of mice from the experimental data (black circles) and from the simulations (red circles).

The predicted trajectories generally match up well to the experimental data. The largest error in our simulations is the day 9 simulation, when the McCullers data predicts about a 5 day survival, while our experiments predict just over 2 days. The McCullers experiments provide only the mean time to survival, not any standard deviations, so we cannot determine if we are within a margin of error for our simulations. Our simulations, however, are a much smoother curve than the experimental data suggest. The increase in survival time at day 9 followed by a decrease at the day 14 condition may be an outlier in the data, making our predictions closer to reality than they might appear. We also miss the time of death by 2 days for a simultaneous IAV-pneumonia infection. There may be other biological phenomena that occur in the body when both pathogens are present concurrently for which our model does not currently account.

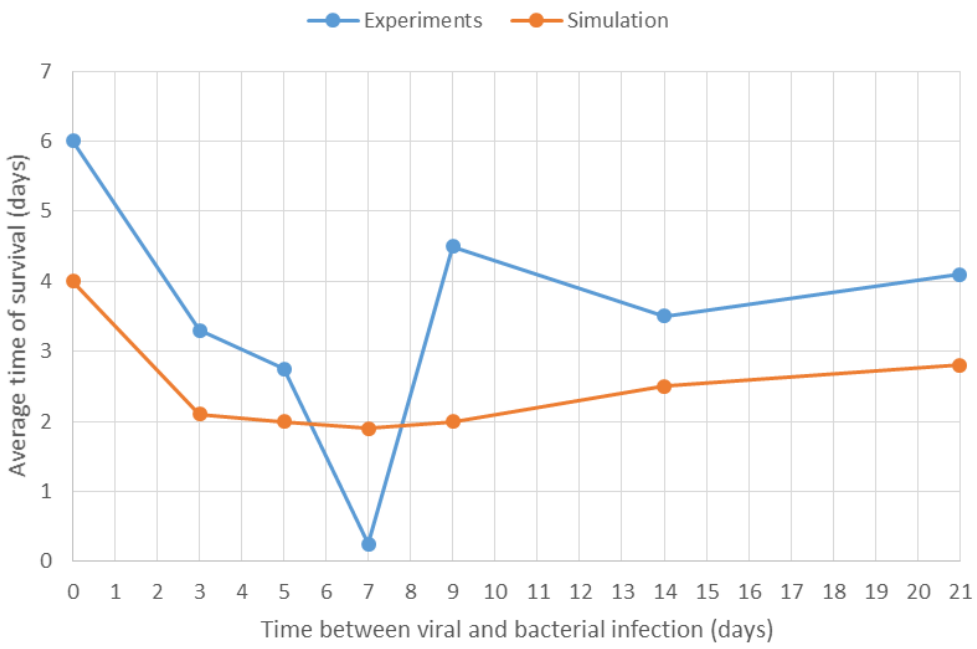

Figure 56: Comparison of survival times between experimental superinfection data (blue) and prediction from simulations (orange).

6.7.5 Testing superinfection mechanisms

We next test the three predicted mechanisms of increased death corresponding to IAV-pneumonia superinfection: excess inflammation, weakened neutrophils, and disrupted mucociliary responses. To test these mechanisms, we either keep a variable at its baseline value (i.e. set dY/dt = 0 for some variable Y in the model), or we change a parameter value to exacerbate its impact on the model behavior. The following three figures demonstrate the outcomes of these tests.

We first test the impact diminished neutrophils have on bacteria and epithelial cells. By changing the parameters associated with neutrophil activity, we can test the effect of weakened neutrophil action. Without loss of generality, parameters ξ_{nl} and ξ_{nb} are decreased by a factor of 5 to demonstrate how weakened neutrophils affect the system as a whole. Figure 57 shows the results of this test (red lines) as compared to the original trajectories (blue lines). Decreasing the bacterial

clearance leads to higher bacterial levels in the lungs and blood, as we would expect. The time to reach this higher steady state is essentially the same as in the original prediction, so time to death is not affected here.

We also see a lower steady-state level of target cells, as more of these will be killed by the increased bacteria. Higher levels of blood bacteria will also lead to higher levels of neutrophils present in the system. Even though we have reduced the efficacy of the neutrophils, they end up rising to a higher level, compensating for their weakened state, and do not change the output much overall. Our model thus does not predict that ineffective neutrophils would be a major contributor to lethal synergism between IAV and pneumonia.

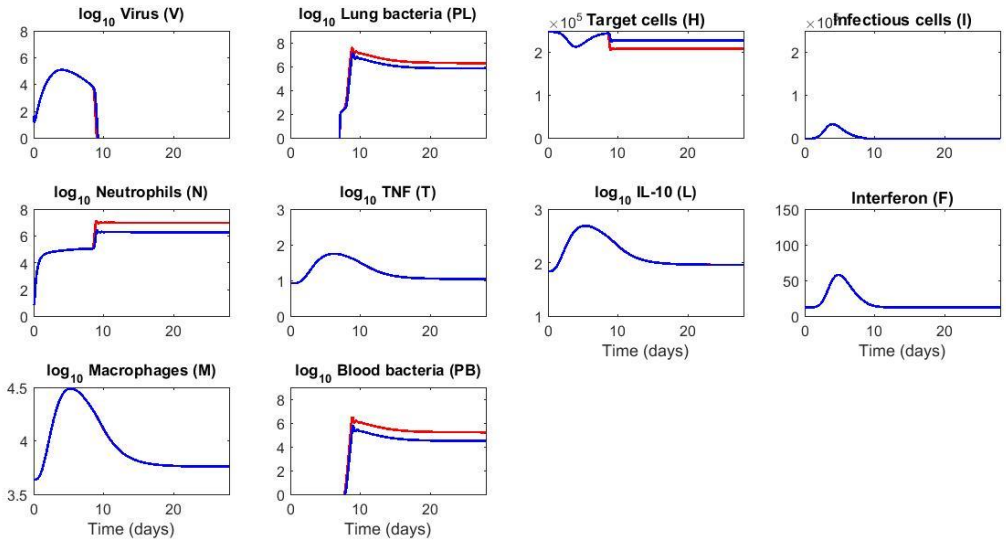

Figure 57: Effect of neutrophil weakening on superinfection model predictions. Blue lines are the original predicted trajectories with virus administered at day 0 and bacteria given at day 7. Red lines represent the new trajectories with parameters ξ_{nl} and ξ_{nb} decreased by a factor of 5 from their original values.

Next we tested the effect of keeping interferon levels at zero. Our hypothesis was that interferon is integral to clearing a viral infection, but it has the side effect of disrupting mucociliary clearance, hindering the initial clearance of bacteria from the lungs. In Figure 58, we show the result of keeping $dF/dt = 0$, which we would hypothesize would improve the survival from bacterial infection but would cause problems in clearance of the viral infection.

Our simulation does not indicate a strong effect of interferon on the bacteria clearance. The largest effect is to the macrophages, which are now missing a component of their summation signal $\Sigma_{M.}$ Macrophages peak a full log lower than in the original simulations, leading to a subsequent decrease in peak value of TNF and IL-10. We also see a higher and faster peak in the virus (2.90 x 10^5 PFU without interferon compared to 1.42 x 10^5 PFU in the original fit), which leads to a greater peak of infected cells as well.

The initial rise of the lung bacteria is also affected by the loss of interferon. The short plateau after lung bacteria are administered is controlled by the nonspecific clearance in the lungs, primarily mucociliary clearance as well as some clearance by resident macrophages and antimicrobial proteins. Interferon decreases the mucociliary clearance, leading to faster rise of the bacteria. That effect is clearly illustrated in these trajectories. The time to death increases by about 1 full day without the interferon present. This would demonstrate that our hypothesis that type I interferon plays a major role in the IAV-pneumonia lethal synergism is validated by our model.

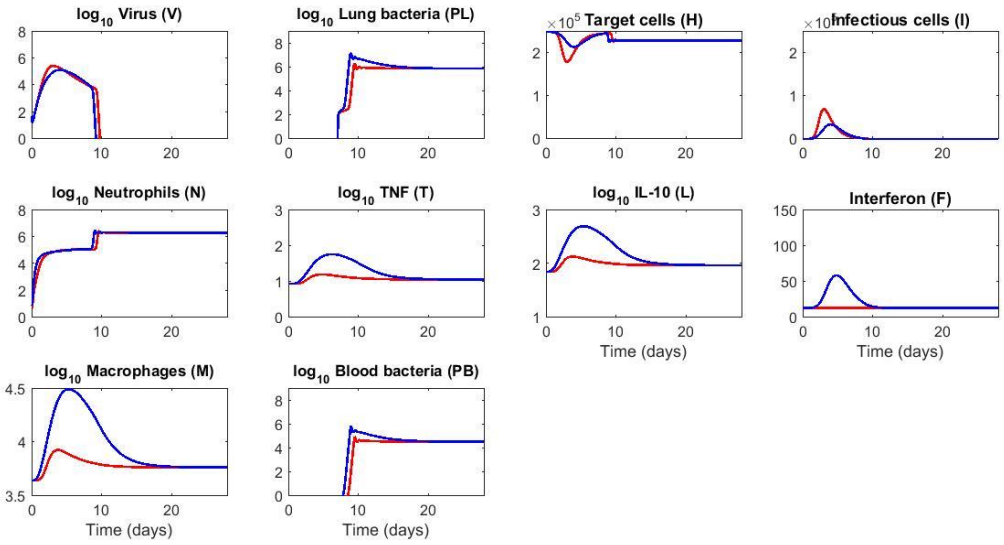

Figure 58: Effect of interferon knockout on superinfection model predictions. Blue lines are the original predicted trajectories with virus administered at day 0 and bacteria given at day 7. Red lines represent the new trajectories with dF/dt = 0 for all t.

Finally, we tested the effect of increased inflammation on survival of superinfection. Increased inflammation in the model is controlled by a parameters governing the increase of TNF and decrease of regulatory effects of IL-10. Therefore we increase the value of parameter γ_T, which controls the rise of TNF trajectories, and decrease the value of parameter θ_L, which controls the anti-inflammatory actions of IL-10 on neutrophil and macrophage activation. Each of these parameter values is changed by a factor of 2.

Figure 59 shows the result of this increased inflammation. Neutrophils rise faster as a result of the decreased effects of IL-10, and the infected cells are unable to sustain any appreciable population. Lack of infected cells leads to a lack of a source for viral replication, so the virus also depletes quickly. The neutrophils and macrophages do not rise high enough to counter the influx

of bacteria into the lungs at day 7, though, and the simulation still predicts a lethal trajectory. This is not the same mechanism of lethality originally predicted, however. Our hypothesis was that increased inflammation would lead to excess death of target cells through excess neutrophils in the lungs. This simulation does not predict any excess target cell deaths; in fact, target cells are kept relatively constant until the bacteria reach the lungs.

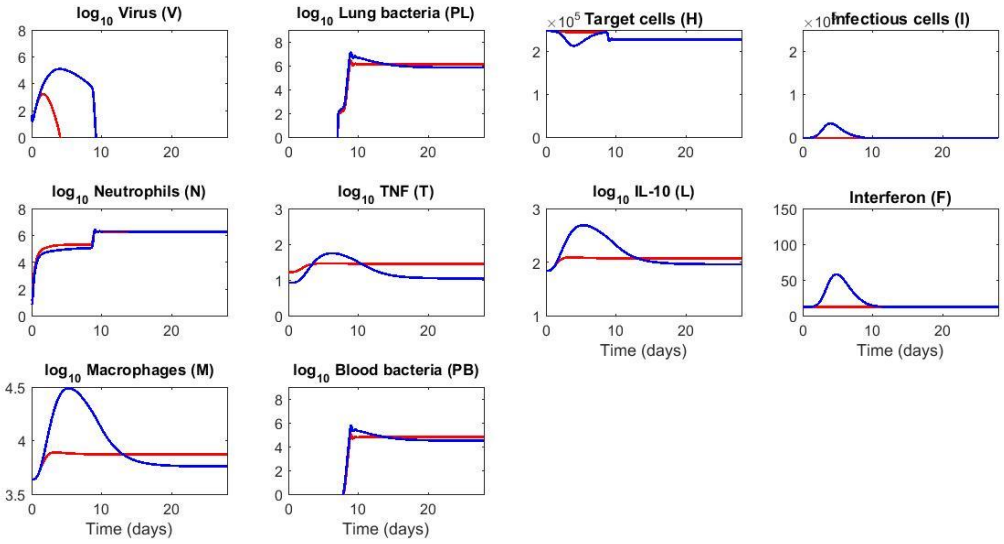

Figure 59: Effect of increased inflammation on lethal synergism. Blue lines are the original predicted trajectories with virus administered at day 0 and bacteria given at day 7. Red lines represent the new trajectories with increased TNF production and decreased IL-10 effects.

6.8 DISCUSSION AND CONCLUSIONS

IAV-pneumonia superinfection is a continuing problem, causing morbidity and mortality in tens of thousands of patients every year, especially in the elderly and immunocompromised populations

[212,213]. We aimed to use mathematical modeling techniques to provide more information on mechanisms leading to the lethal synergism between the virus and bacteria.

This model was developed from a simplified version of the influenza infection model presented in Chapter 4 [97]. That model was highly complex and required weeks to accurately estimate parameters to fit the data. We removed some of the adaptive components that do not directly impact the viral titer trajectories, such as IL-12, T_H-1 cells, type II interferon, and antigen-presenting cells. Because we do not have these adaptive components, we also chose not to include antibodies explicitly in this model, as we do not have a biologically-appropriate source for their production. Instead, we assume a constant rate of clearance of virus with parameter c [102], and another saturating virus removal term representing a nonspecific clearance rate analogous to parameter g_V in equation 4.11.

We suggested three such mechanisms to test in this model: excess inflammation, neutrophil ineffectiveness, and mucociliary disruption via type I interferon upregulation. Our current model demonstrated increased survival time is correlated with a disruption in interferon production, as some experimental research has suggested [222]. Interferon affects the nonspecific clearance term in the lung bacteria equation, controlled by the parameter ν, which was identified as a sensitive parameter in the pneumonia-only model of BALB/c mice infection (see Chapter 2).

Our model did not indicate a strong effect of neutrophil weakening or increased inflammation on survival time. It is important to remember that these effects are directly linked to specific parameter values in this model. Generating an ensemble of parameter values via Markov chain Monte Carlo simulations would yield a distribution of possible values for these parameters. Within this distribution may exist some segment of the population which responds more strongly

to these inflammation effects. Future work should include generating and analyzing the ensemble for other phenotypes which may exist.

The future ensembles should also be performed on data for a true IAV-pneumonia superinfection. One possible source for this data is the Smith et al. paper which proposed a different ODE model for superinfection [227]. This data was not applied to our current model because the mice in their experiments did not reflect the time to death seen the in McCullers experiments; after a 7 day delay between primary and secondary infections, mice were able to survive at least 2 days, whereas the McCullers data suggests these mice should survive less than one day. The difference may lie in the inoculum of the influenza used in each experiment. McCullers and Rehg gave mice a 3000 $TCID_{50}$ dose of H1N1, while Smith et al. administered only a 100 $TCID_{50}$ dose. Since this project was inspired by the timing of infection data, however, we chose not to use the Smith data to calibrate our model. Future research may take the opposite approach, which could change the values and bounds of some of the parameters to allow them to better fit these data.

This study has proposed one possible ODE model of IAV-pneumonia superinfection that may be calibrated to a greater collection of experimental data in future iterations. The model incorporates parameters controlling 3 potential mechanisms of lethal synergism between virus and bacteria in the host. Though much work remains to be completed on this model to fully validate its structure and parameter values, it provides a clear path forward for future work.

7.0 CONCLUSIONS

This project produced several models of varying complexity to better understand the intricacies of the host immune response to respiratory infection. Developing these models requires a balance between biological accuracy and computational feasibility. Increasing the number of variables used in the model may reduce the number of simplifying assumptions used in the generation of the model, but more variables also leads to longer time for parameter estimation and numerical integration of the equations. With the models presented in this work, we have provided a sample of large and small models calibrated to data for bacterial or viral infection.

The first model presented was a four variable model of the intrahost immune response to pneumococcal infection. The 17 parameters in the model allow for many different immune phenotypes to be replicated by changing the value of only a few parameters at a time. The results predicted the importance of maintaining a low bacterial count in the bloodstream in order to control the infection and allow the host to survive.

The 20-variable model of the immune response to influenza infection provides a detailed look at innate, adaptive and humoral immunity as well as inflammation. A well-calibrated inflammatory response was shown to be vital to the survival of the infection, as excess inflammation can cause damage to the host and eventual death. The model's 94 parameters were calibrated such that changing only the initial condition of the viral load will change the output to fit either sublethal or lethal infection data. Both of these models were fit to data using the Metropolis-Hastings Monte Carlo method with parallel tempering to explore the multidimensional parameter space. While this method is effective in finding parameter values which fit the experimental data, it is computationally expensive. The 20-variable model took over two weeks to

fully collect enough samples on our cluster. These time constraints can be prohibitive for some projects, so we next explored this influenza infection data with Boolean network model instead of an ODE model. With this Boolean model we examined differences in immune response between older and younger hosts. Older hosts were shown to experience a delay in the onset of many innate immune responses and a subsequent dysregulation of cellular responses, leading to delayed clearance of the virus from the host. The Boolean model allows for a large, complex model but without the need for parameter estimation techniques, which greatly reduces computation time for calibrating the model. We are, however, limited to only "on/off" levels for our data, which may oversimplify some of the immune responses.

Finally, an ODE model of influenza-pneumonia superinfection was proposed and presented with a single parameter set fit to the influenza infection data. This model is able to replicate the time to death for several experimental conditions changing the time between the primary and secondary infection. More work is needed with this model to see if an ensemble of parameter values could fit well to this data and represent a full population of responses to the infections. Future work will also include getting a better data source to which to calibrate the model. Our experimental collaborators were unable to get this data set for us; future iterations of the model should be calibrated for a full influenza-pneumonia superinfection, rather than just the influenza infection portion.

Fitting mathematical models to experimental data does present several challenges. First, a lack of sufficient data can make parameter estimation far more difficult. All data presented in this work was taken from murine models of infection. When collecting data from mice, their small size necessitates their sacrifice in order to get sufficient samples for measurement. This precludes us from being able to use longitudinal data in our models. Instead, we look at pooled data from many

murine subjects that we assume will react very similarly given the same infection in the same environment. However, large standard errors associated with some of our mean data points suggests a high level of inter-individual variability, particularly in the older mice in the age experiments. Our results could be strengthened if able to follow a single animal through the full course of the infection. In addition, these large models require days or weeks of computation time to fully explore the parameter space used to fit the model to the data. Even though these models are complex, they still simplify the underlying biology of immune response to infection. Some future iterations of these models could try to model explicitly some components which we have not included to keep the models to a reasonable size. These additions may improve some of the fits to data, but may also increase further computation time needed to explore parameter space. Balancing these two aspects of mathematical modeling is fundamental in the creation of a system of ODEs. This project has provided several models that future researchers may use to fit to data for respiratory infections and discover new mechanisms by which hosts defend themselves from disease.

APPENDIX A

PARAMETERS OF THE INFLUENZA MODEL

Table 14: Parameter descriptions and allowed ranges for all parameters in the influenza ODE model.

Parameter	Units	Description	Range	Ref
a_{11}	ml/pg	Signal induced to macrophages by TNF-α	[5.5E-05, 2.2E-02]	[233]
a_{12}	$cells^{-1}$	Signal induced to macrophages by damaged epithelial cells	[4.0E-06, 1.6E-03]	est
a_{21}	dimensionless	Maximal signal induced to macrophages by virus	[1.6E+00, 6.4E+02]	[119]
a_{22}	pfu/ml	Substrate affinity for signal induced by virus	[1.5E+03, 6.0E+05]	[119]
g_1	dimensionless	Inhibitory term for effect of IL-10 on cytokine production	[1.1E+00, 4.5E+02]	est
g_2	pg/ml	Inhibitory term for effect of IL-10 on cytokine production	[3.4E+02, 1.3E+05]	est
δ_2	pg/ml	Inhibitory term for effect of IL-10 on cytokine production	[2.5E+00, 4.0E+02]	[233]
b_{mc}	cells/day	Maximal chemotactic adduction of macrophages	[7.5E+02, 4.1E+04]	[233]
a_{mc}	pg/ml	Substrate affinity for adduction of macrophages	[1.3E+02, 2.0E+03]	[234]
μ_m	day^{-1}	Decay/removal of macrophages	[1.0E-02, 5.0E-01]	[233]
b_m	cells	Baseline number of macrophages	[3.0E+02, 1.2E+04]	[234]
b_t	pg/ml/day	Maximal production rate of TNF-α	[7.8E-02, 3.1E+01]	[233]
k_1	dimensionless	Inhibitory term for pro-inflammatory cytokine production	[2.5E-01, 2.0E+01]	est
k_2	pg/ml	Inhibitory term for pro-inflammatory cytokine production	[2.5E+01, 4.0E+02]	[234]
d_1	pg/ml	Inhibitory term for pro-inflammatory cytokine production	[2.5E+01, 4.0E+02]	[234]
μ_t	day^{-1}	Decay/removal of TNF-α	[2.5E+01, 7.2E+02]	[233]
b_l	pg/ml/day	Maximal production rate of IL-10 by macrophages	[2.1E-02, 8.3E+00]	[233]
μ_l	day^{-1}	Decay/removal of IL-10	[1.8E+00, 1.2E+01]	[233]
b_{lh}	pg/ml/cell	Production rate of IL-10 by target epithelial cells	[5.0E-05, 1.0e-03]	[233]
b_c	pg/ml/day	Maximal production rate of chemokines	[4.0E+00, 1.6E+03]	est
μ_c	day^{-1}	Decay/removal of chemokines	[1.5E+01, 1.8E+02]	[233]
b_{nt}	cells day^{-1}	Maximal activation rate of neutrophils by TNF-α	[4.5E+03, 1.8E+06]	est
a_{nt}	pg/ml	Substrate affinity for activation of neutrophils	[5.0E+00 , 1.6E+02]	[234]
a_{nl}	dimensionless	Inhibitory effect of IL-10 on the activation of neutrophils	[2.5E-02, 1.0E+00]	est
g_{nc}	day^{-1}	Maximal chemotactic adduction of neutrophils	[2.1E+01, 8.4E+03]	est
a_{nc}	pg/ml	Substrate affinity for adduction of neutrophils	[1.8E+01, 7.0E+03]	est
μ_n	day^{-1}	Decay/removal of neutrophils	[1.0E-01, 2.4E+00]	[233]
b_{xn}	pg/ml/day	Maximal production rate of NOS	[1.0E-01, 3.0E+00]	est
a_{xn}	cells	Substrate affinity for production of NOS by neutrophils	[2.0E+02, 8.0E+03]	est
g_{xi}	$cell^{-1}$ day^{-1}	Removal of NOS during infected cell destruction	[1.5E-07, 6.0E-05]	est
g_{xh}	$cell^{-1}$ day^{-1}	Removal of NOS during epithelial cell destruction	[1.5E-07, 6.0E-05]	est

μ_x	day^{-1}	Decay/removal of NOS	[5.0E-01, 1.2E+02]	est
b_h	$cell^{-1}\ day^{-1}$	Replication rate of epithelial cells	[1.7E-05, 6.7E-03]	est
θ	cells	Strong Allee term for the replication of epithelial cells	[6.3E+03, 7.5E+04]	est
g_{hv}	ml/pg/day	Viral infection rate	[5.0E-08, 2.0E-05]	[119]
g_{hx}	cells/day	Maximal destruction rate of epithelial cells by NOS	[2.5E-01, 1.0E+02]	est
a_{hx}	pg/ml	Substrate affinity for destruction of epithelial cells	[1.0E-01, 4.0E+01]	est
g_{ix}	cells/day	Maximal destruction rate of infected cells by NOS	[2.5E-01, 1.0E+02]	est
a_{ix}	pg/ml	Substrate affinity for destruction of infected cells	[7.5E-02, 3.0E+01]	est
g_{ik}	$cell^{-1}\ day^{-1}$	Removal rate of infected cells by NK cells	[2.5E-06, 1.0E-03]	est
g_{ie}	$cell^{-1}\ day^{-1}$	Removal rate of infected cells by effector cells	[5.0E-6, 2.0E-3]	[119]
μ_i	day^{-1}	Decay/removal of infected cells	[2.5E-01, 4.0E+00]	[119]
g_{vi}	pfu/(ml cells day)	Production rate of virus by infected cells	[7.0E+00, 2.8E+03]	[119]
g_{vh}	$cell^{-1}\ day^{-1}$	Removal of virus during infection of epithelial cells	[4.1E-07, 1.6E-04]	[119]
g_{va}	ml/pfu/day	Elimination of virus due to antibody neutralization	[7.5E-05, 3.0E-02]	[119]
g_v	day^{-1}	Removal rate of sub-threshold viral quantities	[1.4E+00, 5.4E+02]	[119]
a_v	ml/pfu	Inverse of lowest viral level capable of infection	[1.0E+00, 4.0E+02]	[119]
μ_v	day^{-1}	Decay/removal of virus	[5.0E-01, 1.2E+01]	[119]
b_{fi}	pg/(ml cell day)	Production rate of IFN-α/β by infected cells	[2.7E-02, 1.1E+01]	est
b_{fp}	pg/(ml cell day)	Production rate of IFN-α/β by APC	[4.7E-04, 1.9E-01]	est
g_{fi}	$cell^{-1}\ day^{-1}$	Excess absorption rate of IFN-α/β by infected cells	[3.2E-4, 1.3E-01]	est
μ_f	day^{-1}	Decay/removal of IFN α/β	[1.0E+00, 8.0E+01]	[119]
a_{rf}	pg/ml	Substrate affinity of epithelial cells to IFN-α/β	[1.0E+01, 1.4E+02]	[234]
b_k	cells	Baseline number of NK cells	[1.1E+02, 4.6E+03]	[234]
b_{kc}	cells/day	Maximal chemotactic adduction of NK cells	[9.0E+03, 3.6E+05]	[234]
a_{kc}	pg/ml	Substrate affinity for adduction of NK cells	[2.0E+02, 2.0E+03]	[234]
g_{ki}	$cell^{-1}\ day^{-1}$	Removal of NK cells during infected cell elimination	[9.5E-09, 3.8E-06]	est
μ_k	day^{-1}	Decay/removal of NK cells	[4.0E-02, 1.6E+00]	[233]
b_{go}	pg/(ml cell day)	Maximal production rate of IFN-γ by Th1 cells	[7.0E-04, 2.8E-01]	est
a_{go}	pg/ml	Substrate affinity in production of IFN-γ by Th1 cells	[7.5E-01, 3.0E+02]	est
b_{gk}	pg/(ml cell day)	Maximal production rate of IFN-γ by NK cells	[1.7E-02, 6.7E+00]	est
a_{gk}	pg/ml	Substrate affinity in production of IFN-γ by NK cells	[2.3E+00, 9.0E+02]	est
μ_g	day^{-1}	Decay/removal of IFN-γ	[1.0E+00, 8.0E+01]	[119]
P_0	cell/day	Inactive APC available for activation	[1.4E+03, 5.6E+05]	est
g_{pv}	dimensionless	Maximal signal for APC from virus	[1.0E-01, 4.0E+01]	est
a_{pv}	pfu/ml	Substrate affinity for signal from virus	[5.0E+02, 2.0E+05]	est
g_{pi}	$cell^{-1}$	Signal for APC from dead infected cells	[4.8E-06, 1.9E-03]	est
g_p	dimensionless	Non-specific activation rate of APC	[2.5E-03, 1.0E+00]	est
b_{pg}	dimensionless	Maximal activation rate of APC by IFN-γ	[5.7E-02, 2.3E+01]	est
a_{pg}	pg/ml	Substrate affinity for activation of APC by IFN-γ	[4.5E+01, 1.1E+03]	[119]
μ_p	day^{-1}	Decay/removal of APC	[5.0E-02, 9.0E-01]	[119]
b_p	cells	Baseline number of activated APC	[3.0E+02, 9.6E+03]	[234]
b_{ep}	cells/day	Maximal activation rate of effector cells	[1.0E+04, 4.0E+05]	[234]
a_{ep}	cells	Substrate affinity in the activation of effector cells	[1.5E+03, 6.0E+04]	[234]
b_{ei}	$cell^{-1}\ day^{-1}$	Removal of effector cells during infected cell elimination	[7.5E-08, 3.0E-05]	[119]

μ_e	day^{-1}	Decay/removal of effector cells	[1.0E-01, 7.0E-01]	[119]
b_{op}	cells/day	Maximal activation rate of Th1 cells	[2.5E+04, 3.0E+05]	[234]
a_{op}	cells	Substrate affinity in the activation of Th1 cells	[1.5E+03, 6.0E+04]	[234]
μ_o	day^{-1}	Decay/removal of Th1 cells	[1.0E-01, 7.0E-01]	[233]
b_{wo}	pg/(ml cell day)	Maximal production rate of IL-12	[3.8E-03, 1.5E-01]	[234]
a_{wo}	cells	Substrate affinity in the production of IL-12	[2.5E+03, 2.0E+05]	[234]
μ_w	day^{-1}	Decay/removal of IL-12	[5.0E-01, 1.0E+01]	est
b_b	cells/day	Non-specific activation of B cells	[5.0E+00, 2.0E+03]	est
b_{bp}	ml/(cell pg day)	APC induced activation of B cells	[6.0E-08, 2.4E-05]	est
B_0	cells	Reservoir number of inactive B cells	[1.5E+04, 3.5E+05]	[234]
μ_b	day^{-1}	Decay/removal of B cells	[5.0E-02, 8.0E-01]	[233]
b_a	pg/ml/day	Non-specific production of antibodies	[1.2E-03, 4.6E-01]	[234]
b_{ab}	pg/(ml cell day)	B cell production of antibodies	[3.3E-04, 1.3E-01]	[119]
g_{av}	ml/(pfu day)	Removal of antibodies during virus elimination	[5.0E-07, 2.0E-04]	[119]
μ_a	day^{-1}	Decay/removal of antibodies	[6.0E-02, 1.2E+01]	[119]
H_0	cells	Total number of epithelial cells	2.5E+05	est
h_m	dimensionless	Hill coefficient for the recruitment of macrophages	3	[234]
h_x	dimensionless	Hill coefficient for the inflammatory removal of epithelial cells	2	[234]
h_e	dimensionless	Hill coefficient for the maturation of NKT cells	2	[234]
h_o	dimensionless	Hill coefficient for the maturation of TH1 cells	2	[234]

BIBLIOGRAPHY

[1] R. Bals, P.S. Hiemstra, Innate immunity in the lung: how epithelial cells fight against respiratory pathogens, Eur Respir J. 23 (2004) 327–333.

[2] T. van der Poll, S.M. Opal, Pathogenesis, treatment, and prevention of pneumococcal pneumonia., Lancet. 374 (2009) 1543–56.

[3] M. Fliegauf, A.F.-P. Sonnen, B. Kremer, P. Henneke, Mucociliary clearance defects in a murine in vitro model of pneumococcal airway infection., PLoS One. 8 (2013) e59925.

[4] N.J. Dimmock, A.J. Easton, K.N. Leppard, Introduction to Modern Virology, 2008.

[5] J. Scheller, A. Chalaris, D. Schmidt-Arras, S. Rose-John, The pro- and anti-inflammatory properties of the cytokine interleukin-6., Biochim Biophys Acta. 1813 (2011) 878–88.

[6] V. Fensterl, G.C. Sen, Interferons and viral infections., Biofactors. 35 (2009) 14–20.

[7] K. Schroder, P.J. Hertzog, T. Ravasi, D.A. Hume, Interferon-gamma: an overview of signals, mechanisms and functions, J Leukoc Biol. 75 (2004) 163–189.

[8] L.N. Carayannopoulos, J.L. Barks, W.M. Yokoyama, J.K. Riley, Murine trophoblast cells induce NK cell interferon-gamma production through KLRK1, Biol Reprod. 83 (2010) 404–414.

[9] L.N. Carayannopoulos, W.M. Yokoyama, Recognition of infected cells by natural killer cells, Curr Opin Immunol. 16 (2004) 26–33.

[10] S. Romagnani, Type 1 T helper and type 2 T helper cells: functions, regulation and role in protection and disease, Int J Clin Lab Res. 21 (1991) 152–8.

[11] M. Lommatzsch, K. Bratke, A. Bier, P. Julius, M. Kuepper, W. Luttmann, et al., Airway dendritic cell phenotypes in inflammatory diseases of the human lung., Eur Respir J. 30 (2007) 878–86.

[12] N. Kadowaki, S. Antonenko, J.Y. Lau, Y.J. Liu, Natural interferon alpha/beta-producing cells link innate and adaptive immunity., J Exp Med. 192 (2000) 219–226.

[13] J. Banchereau, F. Briere, C. Caux, J. Davoust, S. Lebecque, Y. Liu, et al., Immunobiology of Dendritic Cells, Immunology. 18 (2000) 767–811.

[14] D.M. Andrews, A. a Scalzo, W.M. Yokoyama, M.J. Smyth, M. a Degli-Esposti, Functional interactions between dendritic cells and NK cells during viral infection., Nat Immunol. 4 (2003) 175–81.

[15] A. Tarantola, Inverse Problem Theory and Methods for Model Parameter Estimation, SIAM, Philadelphia, 2005.

[16] S. Zenker, J. Rubin, G. Clermont, From inverse problems in mathematical physiology to quantitative differential diagnoses, PLoS Comput Biol. 3 (2007) e204.

[17] S. Chib, E. Greenberg, Understanding the Metropolis-Hastings Algorithm, Am Stat. 49 (1995) 327–335.

[18] K. Mosegaard, A. Tarantola, Monte Carlo sampling of solutions to inverse problems, J Geophys Res. 100 (1995) 12431.

[19] A. Tarantola, Inverse Problem Theory, Elsevier, New York, 1987.

[20] D. Battogtokh, D.K. Asch, M.E. Case, J. Arnold, H.-B. Schuttler, An ensemble method for identifying regulatory circuits with special reference to the qa gene cluster of Neurospora crassa., Proc Natl Acad Sci U S A. 99 (2002) 16904–16909.

[21] M. Allmaras, W. Bangerth, J.M. Linhart, J. Polanco, F. Wang, K. Wang, et al., Estimating Parameters in Physical Models through Bayesian Inversion: A Complete Example, SIAM Rev. 55 (2013) 149–167.

[22] D. Swigon, Ensemble Modeling of Biological Systems, in: Math. Life Sci., 2012: pp. 19–42.

[23] H. Jeffreys, Theory of probability, 3rd ed, 1961.

[24] E. Mochan, D. Swigon, G.B. Ermentrout, S. Lukens, G. Clermont, A mathematical model of intrahost pneumococcal pneumonia infection dynamics in murine strains, J Theor Biol. 353 (2014) 44–54.

[25] World Health Organization, Pneumonia fact sheet, Media Cent. (2013).

[26] V. Kaplan, G. Clermont, M.F. Griffin, J. Kasal, R.S. Watson, W.T. Linde-Zwirble, et al., Pneumonia: Still the Old Man's Friend?, Arch Intern Med. 163 (2003) 317–323.

[27] D. Bogaert, a van Belkum, M. Sluijter, a Luijendijk, R. de Groot, H.C. Rümke, et al., Colonisation by Streptococcus pneumoniae and Staphylococcus aureus in healthy children., Lancet. 363 (2004) 1871–2.

[28] D.R. Cundell, N.P. Gerard, C. Gerard, I. Idanpaan-Heikkila, E.I. Tuomanen, Streptococcus pneumoniae anchor to activated human cells by the receptor for platelet-activating factor, Nature. 377 (1995) 435–438.

[29] R.A. Hirst, A. Kadioglu, C. O'Callaghan, P.W. Andrew, The role of pneumolysin in pneumococcal pneumonia and meningitis, Clin Exp Immunol. 138 (2004) 195–201.

[30] S.B. Gordon, G.R. Irving, R. a Lawson, M.E. Lee, R.C. Read, Intracellular trafficking and killing of Streptococcus pneumoniae by human alveolar macrophages are influenced by opsonins., Infect Immun. 68 (2000) 2286–93.

[31] H.M. Marriott, D.H. Dockrell, The role of the macrophage in lung disease mediated by bacteria., Exp Lung Res. 33 (2007) 493–505.

[32] B.J.P. Mizgerd, B.B. Meek, G.J. Kutkoski, D.C. Bullard, A.U. Beaudet, C.M. Doerschuk, Selectins and Neutrophil Traffic: Margination and Streptococcus Pneumoniae-induced Emigration in Murine Lungs, J Exp Med. 184 (1996) 639–645.

[33] G. Fang, M. Fine, J. Orloff, D. Arisumi, V. Yu, W. Kapoor, et al., New and emerging etiologies for community-acquired pneumonia with implications for therapy. A prospective multicenter study of 359 cases, Med. 69 (1990) 307–316.

[34] S. Knapp, J.C. Leemans, S. Florquin, J. Branger, N.A. Maris, J. Pater, et al., Alveolar macrophages have a protective antiinflammatory role during murine pneumococcal pneumonia, Am J Respir Crit Care Med. 167 (2003) 171–9.

[35] I. Fillion, N. Ouellet, M. Simard, Y. Bergeron, S. Sato, M.G. Bergeron, Role of chemokines and formyl peptides in pneumococcal pneumonia-induced monocyte/macrophage recruitment, J Immunol. 166 (2001) 7353–61.

[36] D.H. Dockrell, H.M. Marriott, L.R. Prince, V.C. Ridger, P.G. Ince, P.G. Hellewell, et al., Alveolar macrophage apoptosis contributes to pneumococcal clearance in a resolving model of pulmonary infection., J Immunol. 171 (2003) 5380–8.

[37] A. Kadioglu, N.A. Gingles, K. Grattan, A. Kerr, T.J. Mitchell, P.W. Andrew, et al., Host Cellular Immune Response to Pneumococcal Lung Infection in Mice Host Cellular Immune Response to Pneumococcal Lung Infection in Mice, Infect Immun. 68 (2000) 492–501.

[38] N.A. Gingles, J.E. Alexander, A. Kadioglu, P.W. Andrew, A. Kerr, T.J. Mitchell, et al., Role of Genetic Resistance in Invasive Pneumococcal Infection : Identification and Study of Susceptibility and Resistance in Inbred Mouse Strains, Infect Immun. 69 (2001) 426–434.

[39] A. Kadioglu, A.M. Cuppone, C. Trappetti, T. List, A. Spreafico, G. Pozzi, et al., Sex-based differences in susceptibility to respiratory and systemic pneumococcal disease in mice., J Infect Dis. 204 (2011) 1971–9.

[40] A.M. Smith, J.A. McCullers, F.R. Adler, Mathematical model of a three-stage innate immune response to a pneumococcal lung infection., J Theor Biol. 276 (2011) 106–16.

[41] A.A. Romanyukha, S.G. Rudnev, I.A. Sidorov, Energy cost of infection burden: an approach to understanding the dynamics of host-pathogen interactions., J Theor Biol. 241 (2006) 1–13.

[42] S.S. Pilyugin, R. Antia, Modeling immune responses with handling time., Bull Math Biol. 62 (2000) 869–90.

[43] H. Spencer, Interstitial pneumonia., Annu Rev Med. 18 (1967) 423–42.

[44] S.J. Jay, W.G. Johanson, A.K. Pierce, J.S. Reisch, Determinants of lung bacterial clearance in normal mice., J Clin Invest. 57 (1976) 811–7.

[45] K. Todar, Todar's Online Textbook of Bacteriology, 2008.

[46] R. Corteling, D. Wyss, A. Trifilieff, In vivo models of lung neutrophil activation. Comparison of mice and hamsters, BMC Pharmacol. 8 (2002) 1–8.

[47] D. Battogtokh, D.K. Asch, M.E. Case, J. Arnold, H.-B. Schuttler, An ensemble method for identifying regulatory circuits with special reference to the qa gene cluster of Neurospora crassa., Proc Natl Acad Sci U S A. 99 (2002) 16904–9.

[48] N. Metropolis, A.W. Rosenbluth, M.N. Rosenbluth, A.H. Teller, E. Teller, Equation of State Calculations by Fast Computing Machines, J Chem Phys. 21 (1953) 1087.

[49] W.K. Hastings, Monte Carlo sampling methods using Markov chains and their applications, Biometrika. 57 (1970) 97–109.

[50] D.J. Earl, M.W. Deem, Parallel tempering: theory, applications, and new perspectives., Phys Chem Chem Phys. 7 (2005) 3910–6.

[51] A. Gelman, D. Rubin, Inference from iterative simulation using multiple sequences, Stat Sci. 7 (1992) 457–511.

[52] J. Geweke, Evaluating the Accuracy of Sampling-Based Approaches to the Calculation of Posterior Moments, University Press, 1992.

[53] J. Casellas, Inbred mouse strains and genetic stability: a review., Animal. 5 (2011) 1–7.

[54] T. Toni, D. Welch, N. Strelkowa, A. Ipsen, M.P.. Stumpf, Approximate Bayesian computation scheme for parameter inference and model selection in dynamical systems, J R Soc Interface. 6 (2009) 187–202.

[55] S. Manco, F. Hernon, H. Yesilkaya, J.C. Paton, P.W. Andrew, A. Kadioglu, Pneumococcal neuraminidases A and B both have essential roles during infection of the respiratory tract and sepsis., Infect Immun. 74 (2006) 4014–20.

[56] D. Proud, Pulmonary Epithelium in Health and Disease, 2008.

[57] A. Craig, J. Mai, S. Cai, S. Jeyaseelan, Neutrophil recruitment to the lungs during bacterial pneumonia., Infect Immun. 77 (2009) 568–75.

[58] E.B. Eruslanov, I. V Lyadova, T.K. Kondratieva, K.B. Majorov, I. V Scheglov, M.O. Orlova, et al., Neutrophil Responses to Mycobacterium tuberculosis Infection in Genetically Susceptible and Resistant Mice, Infect Immun. 73 (2005) 1744–1753.

[59] T.E. Mandel, C. Cheers, Resistance and susceptibility of mice to bacterial infection: histopathology of listeriosis in resistant and susceptible strains., Infect Immun. 30 (1980) 851–61.

[60] J.C. Alves-Filho, A. de Freitas, M. Russo, F.Q. Cunha, Toll-like receptor 4 signaling leads to neutrophil migration impairment in polymicrobial sepsis, Crit Care Med. 34 (2006) 461–470.

[61] M. Kovach, T. Standiford, The function of neutrophils in sepsis, Curr Opin Infect Dis. 25 (2012) 321–327.

[62] C.G. Harford, M. Hara, Pulmonary Edema in Influenzal Pneumonia of the Mouse and the Relation of Fluid in the Lung To the Inception of Pneumococcal Pneumonia., J Exp Med. 91 (1950) 245–60.

[63] J.M. Prince, R.M. Levy, J. Bartels, A. Baratt, J.M. Kane, C. Lagoa, et al., In silico and in vivo approach to elucidate the inflammatory complexity of CD14-deficient mice., Mol Med. 12 (2006) 88–96.

[64] R.B. Ashman, J.M. Papadimitriou, Genetic resistance to Candida albicans infection is conferred by cells derived from the bone marrow., J Infect Dis. 166 (1992) 947–8.

[65] J. Day, A. Friedman, L.S. Schlesinger, Modeling the immune rheostat of macrophages in the lung in response to infection., Proc Natl Acad Sci U S A. 106 (2009) 11246–51.

[66] H.P. Ludewick, L. Aerts, M.-E. Hamelin, G. Boivin, Long-term impairment of Streptococcus pneumoniae lung clearance is observed after initial infection with influenza A virus but not human metapneumovirus in mice., J Gen Virol. 92 (2011) 1662–5.

[67] R.H. Buckley, R.I. Schiff, S.E. Schiff, M.L. Markert, L.W. Williams, T.O. Harville, et al., Human severe combined immunodeficiency: genetic, phenotypic, and functional diversity in one hundred eight infants., J Pediatr. 130 (1997) 378–87.

[68] R. Jounblat, A. Kadioglu, T.J. Mitchell, W. Peter, P.W. Andrew, Pneumococcal Behavior and Host Responses during Bronchopneumonia Are Affected Differently by the Cytolytic

and Complement-Activating Activities of Pneumolysin, Infect Immun. 71 (2003) 1813–1819.

[69] J. McCluskey, J. Hinds, S. Husain, A. Witney, T.J. Mitchell, A two-component system that controls the expression of pneumococcal surface antigen A (PsaA) and regulates virulence and resistance to oxidative stress in Streptococcus pneumoniae, Mol Microbiol. 51 (2004) 1661–1675.

[70] E. Mochan-Keef, D. Swigon, G.B. Ermentrout, G. Clermont, A Three-Tiered Study of Differences in Murine Intrahost Immune Response to Multiple Pneumococcal Strains, PLoS One. 10 (2015) e0134012.

[71] A. Kadioglu, S. Taylor, F. Iannelli, T.J. Mitchell, P.W. Andrew, G. Pozzi, Upper and Lower Respiratory Tract Infection by Streptococcus pneumoniae Is Affected by Pneumolysin Deficiency and Differences in Capsule Type, Infect Immun. 70 (2002) 2886–2890.

[72] T. Kelly, J.P. Dillard, J. Yother, Effect of genetic switching of capsular type on virulence of Streptococcus pneumoniae., Infect Immun. 62 (1994) 1813–9.

[73] J. Mohler, E. Azoulay-Dupuis, C. Amory-Rivier, J.X. Mazoit, J.P.P. Bédos, V. Rieux, et al., Streptococcus pneumoniae strain-dependent lung inflammatory responses in a murine model of pneumococcal pneumonia., Intensive Care Med. 29 (2003) 808–16.

[74] O.T. Avery, R. Dubos, The protective action of a specific enzyme against type III pneumococcus infection in mice, J Exp Med. 54 (1931) 73–89.

[75] D.A. Watson, D.M. Musher, Interruption of capsule production in Streptococcus pneumoniae serotype 3 by insertion of transposon Tn916, Infect Immun. 17 (1990) 913–924.

[76] C.-J. Lee, S.D. Banks, J.P. Lee, Virulence, immunity, and vaccine related to Streptococcus pneumoniae, Crit Rev Immunol. 18 (1991) 89–114.

[77] G. a Bruyn, B.J. Zegers, R. van Furth, Mechanisms of host defense against infection with Streptococcus pneumoniae., Clin Infect Dis. 14 (1992) 251–62.

[78] D.P. Fine, Pneumococcal type-associated variability in alternate complement pathway activation., Infect Immun. 12 (1975) 772–8.

[79] G.S. Giebink, J. Verhoef, P.K. Peterson, P.G. Quie, Opsonic requirements for phagocytosis of Streptococcus pneumoniae types VI, XVIII, XXIII, and XXV., Infect Immun. 18 (1977) 291–7.

[80] M.K. Hostetter, Serotypic variations among virulent pneumococci in deposition and degradation of covalently bound C3b: implications for phagocytosis and antibody production., J Infect Dis. 153 (1986) 682–93.

[81] D.S. Chudwin, S.G. Artrip, a Korenblit, G. Schiffman, S. Rao, Correlation of serum opsonins with in vitro phagocytosis of Streptococcus pneumoniae., Infect Immun. 50 (1985) 213–7.

[82] M. Kalin, Pneumococcal serotypes and their clinical relevance., Thorax. 53 (1998) 159–62.

[83] D.M. Weinberger, Z.B. Harboe, E. a M. Sanders, M. Ndiritu, K.P. Klugman, S. Rückinger, et al., Association of serotype with risk of death due to pneumococcal pneumonia: a meta-

analysis., Clin Infect Dis. 51 (2010) 692–9.

[84] M. Kalin, K. Kanclerski, M. Granström, R. Möllby, Diagnosis of pneumococcal pneumonia by enzyme-linked immunosorbent assay of antibodies to pneumococcal hemolysin (pneumolysin)., J Clin Microbiol. 25 (1987) 226–9.

[85] J.S. Braun, J.E. Sublett, D. Freyer, T.J. Mitchell, J.L. Cleveland, E.I. Tuomanen, et al., Pneumococcal pneumolysin and H 2 O 2 mediate brain cell apoptosis during meningitis, J Clin Invest. 109 (2002) 19–27.

[86] J.C. Paton, B. Rowan-Kelly, a Ferrante, Activation of human complement by the pneumococcal toxin pneumolysin., Infect Immun. 43 (1984) 1085–7.

[87] G.J. Boulnois, J.C. Paton, T.J. Mitchell, P.W. Andrew, Structure and function of pneumolysin, the multifunctional, thiol-activated toxin of Streptococcus pneumoniae, Mol Microbiol. 5 (1991) 2611–2616.

[88] T.J. Mitchell, J.E. Alexander, P.J. Morgan, P.W. Andrew, Molecular analysis of virulence factors of Streptococcus pneumoniae., Soc Appl Bacteriol Symp Ser. 26 (1997) 62S–71S.

[89] M. Camara, G.J. Boulnois, P.W. Andrew, T.J. Mitchell, A neuraminidase from Streptococcus pneumoniae has the features of a surface protein, Infect Immun. 62 (1994) 3688–3695.

[90] J.E. Alexander, a M. Berry, J.C. Paton, J.B. Rubins, P.W. Andrew, T.J. Mitchell, Amino acid changes affecting the activity of pneumolysin alter the behaviour of pneumococci in pneumonia., Microb Pathog. 24 (1998) 167–74.

[91] A.B. Dalia, A.J. Standish, J.N. Weiser, Three surface exoglycosidases from Streptococcus pneumoniae, NanA, BgaA, and StrH, promote resistance to opsonophagocytic killing by human neutrophils., Infect Immun. 78 (2010) 2108–16.

[92] C.J. Orihuela, G. Gao, K.P. Francis, J. Yu, E.I. Tuomanen, Tissue-specific contributions of pneumococcal virulence factors to pathogenesis., J Infect Dis. 190 (2004) 1661–9.

[93] J. a Lanie, W.-L. Ng, K.M. Kazmierczak, T.M. Andrzejewski, T.M. Davidsen, K.J. Wayne, et al., Genome sequence of Avery's virulent serotype 2 strain D39 of Streptococcus pneumoniae and comparison with that of unencapsulated laboratory strain R6., J Bacteriol. 189 (2007) 38–51.

[94] A. Brooks-Walter, D.E. Briles, S.K. Hollingshead, The pspC Gene of Streptococcus pneumoniae Encodes a Polymorphic Protein , PspC , Which Elicits Cross-Reactive Antibodies to PspA and Provides Immunity to Pneumococcal Bacteremia, Infect Immun. 67 (1999) 6533–6542.

[95] R.C. Read, R. Wilson, A. Rutman, V. Lund, H.C. Todd, A.P.R. Brain, et al., Interaction of Nontypable Haemophilus influenzae with Human Respiratory Mucosa In Vitro, J Infect Dis. 163 (1991) 549–558.

[96] S. Sethi, T.F. Murphy, Bacterial Infection in Chronic Obstructive Pulmonary Disease in 2000 : a State-of-the-Art Review, Clin Microbiol Rev. 14 (2001) 336–363.

[97] I. Price, E.D. Mochan-Keef, D. Swigon, G.B. Ermentrout, S. Lukens, F.R. Toapanta, et al., The inflammatory response to influenza A virus (H1N1): An experimental and mathematical study, J Theor Biol. 374 (2015) 83–93.

[98] C.A.A. Beauchemin, A. Handel, A review of mathematical models of influenza A infections within a host or cell culture: lessons learned and challenges ahead., BMC Public Health. 11 Suppl 1 (2011) S7.

[99] H. Miao, X. Xia, A.S. Perelson, H. Wu, On Identifiability of Nonlinear ODE Models and Applications in Viral Dynamics., SIAM Rev. 53 (2011) 3–39.

[100] A.M. Smith, A.S. Perelson, Influenza A virus infection kinetics: quantitative data and models., Wiley Interdiscip Rev Syst Biol Med. 3 (2011) 429–45.

[101] A. Smith, R. Ribeiro, Modeling the viral dynamics of influenza A virus infection, Crit Rev Immunol. 30 (2010) 291–298.

[102] P. Baccam, C. Beauchemin, C. a Macken, F.G. Hayden, A.S. Perelson, Kinetics of influenza A virus infection in humans., J Virol. 80 (2006) 7590–9.

[103] C. Beauchemin, Probing the Effects of the Well-mixed Assumption on Viral Infection Dynamics, J Theor Biol. 242 (2006) 464–477.

[104] R.A. Saenz, M. Quinlivan, D. Elton, S. Macrae, A.S. Blunden, J.A. Mumford, et al., Dynamics of influenza virus infection and pathology., J Virol. 84 (2010) 3974–83.

[105] A. Tridane, Y. Kuang, Modeling the interaction of cytotoxic T lymphocytes and influenza virus infected epithelial cells., Math Biosci Eng. 7 (2010) 171–85.

[106] G.A. Bocharov, A.A. Romanyukha, Mathematical Model of Antiviral Immune Response III. Influenza A Virus Infection, J Theor Biol. 167 (1994) 323–360.

[107] B. Hancioglu, D. Swigon, G. Clermont, A dynamical model of human immune response to influenza A virus infection., J Theor Biol. 246 (2007) 70–86.

[108] H.Y. Lee, D.J. Topham, S.Y. Park, J. Hollenbaugh, J. Treanor, T.R. Mosmann, et al., Simulation and prediction of the adaptive immune response to influenza A virus infection., J Virol. 83 (2009) 7151–65.

[109] H.M. Dobrovolny, M.B. Reddy, M. a Kamal, C.R. Rayner, C. a a Beauchemin, Assessing mathematical models of influenza infections using features of the immune response., PLoS One. 8 (2013) e57088.

[110] L. Canini, F. Carrat, Population modeling of influenza A/H1N1 virus kinetics and symptom dynamics., J Virol. 85 (2011) 2764–70.

[111] A. Handel, I.M. Longini, R. Antia, Towards a quantitative understanding of the within-host dynamics of influenza A infections., J R Soc Interface. 7 (2010) 35–47.

[112] E. a Hernandez-Vargas, E. Wilk, L. Canini, F.R. Toapanta, S.C. Binder, A. Uvarovskii, et al., Effects of aging on influenza virus infection dynamics., J Virol. 88 (2014) 4123–31.

[113] A. Handel, I.M. Longini, R. Antia, Neuraminidase inhibitor resistance in influenza: assessing the danger of its generation and spread., PLoS Comput Biol. 3 (2007) e240.

[114] H. Manchanda, N. Seidel, A. Krumbholz, A. Sauerbrei, M. Schmidtke, R. Guthke, Within-host influenza dynamics: a small-scale mathematical modeling approach., Biosystems. 118 (2014) 51–9.

[115] L.A. Reperant, T. Kuiken, B.T. Grenfell, A.D.M.E. Osterhaus, A.P. Dobson, Linking influenza virus tissue tropism to population-level reproductive fitness., PLoS One. 7 (2012)

e43115.

[116] K.A. Pawelek, G.T. Huynh, M. Quinlivan, A. Cullinane, L. Rong, A.S. Perelson, Modeling within-host dynamics of influenza virus infection including immune responses., PLoS Comput Biol. 8 (2012) e1002588.

[117] P.L. Smith, G. Lombardi, G.R. Foster, Type I interferons and the innate immune response--more than just antiviral cytokines, Mol Immunol. 42 (2005) 869–877.

[118] R.A. Saenz, M. Quinlivan, D. Elton, S. Macrae, A.S. Blunden, J.A. Mumford, et al., Dynamics of influenza virus infection and pathology., J Virol. 84 (2010) 3974–83.

[119] B. Hancioglu, D. Swigon, G. Clermont, A dynamical model of human immune response to influenza A virus infection., J Theor Biol. 246 (2007) 70–86.

[120] H. Miao, J.A. Hollenbaugh, M.S. Zand, J. Holden-Wiltse, T.R. Mosmann, A.S. Perelson, et al., Quantifying the early immune response and adaptive immune response kinetics in mice infected with influenza A virus., J Virol. 84 (2010) 6687–98.

[121] E.A. Hernandez-Vargas, E. Wilk, L. Canini, F.R. Toapanta, S.C. Binder, A. Uvarovskii, et al., Effects of aging on influenza virus infection dynamics., J Virol. 88 (2014) 4123–31.

[122] G. Nieman, D. Brown, J. Sarkar, B. Kubiak, C. Ziraldo, J. Dutta-Moscato, et al., A two-compartment mathematical model of endotoxin-induced inflammatory and physiologic alterations in swine., Crit Care Med. 40 (2012) 1052–63.

[123] J. Day, J. Rubin, Y. Vodovotz, C.C. Chow, A. Reynolds, G. Clermont, A reduced mathematical model of the acute inflammatory response II. Capturing scenarios of repeated endotoxin administration, J Theor Biol. 242 (2006) 237–256.

[124] R. Kumar, G. Clermont, Y. Vodovotz, C.C. Chow, The dynamics of acute inflammation, J Theor Biol. 230 (2004) 145–155.

[125] A. Reynolds, J. Rubin, G. Clermont, J. Day, Y. Vodovotz, G. Bard Ermentrout, A reduced mathematical model of the acute inflammatory response: I. Derivation of model and analysis of anti-inflammation., J Theor Biol. 242 (2006) 220–36.

[126] S. Tamura, T. Kurata, Defense mechanisms against influenza virus infection in the respiratory tract mucosa., Jpn J Infect Dis. 57 (2004) 236–47.

[127] F.R. Toapanta, T.M. Ross, Impaired immune responses in the lungs of aged mice following influenza infection., Respir Res. 10 (2009) 112–131.

[128] J. Mizgerd, Acute lower respiratory tract infection, N Engl J Med. 358 (2008) 716–727.

[129] L. Sun, R.F. Guo, M.W. Newstead, T.J. Standiford, D.R. Macariola, T.P. Shanley, Effect of IL-10 on neutrophil recruitment and survival after Pseudomonas aeruginosa challenge, Am J Respir Cell Mol Biol. 41 (2009) 76–84.

[130] R.B. Goodman, J. Pugin, J.S. Lee, M.A. Matthay, Cytokine-mediated inflammation in acute lung injury, Cytokine Growth Factor Rev. 14 (2003) 523–535.

[131] M. Brandes, F. Klauschen, S. Kuchen, R.N. Germain, A systems analysis identifies a feedforward inflammatory circuit leading to lethal influenza infection., Cell. 154 (2013) 197–212.

[132] J.C. Kash, C.F. Basler, A. Garcia-Sastre, V. Carter, R. Billharz, D.E. Swayne, et al., Global

host immune response: pathogenesis and transcriptional profiling of type A influenza viruses expressing the hemagglutinin and neuraminidase genes from the 1918 pandemic virus, J Virol. 78 (2004) 9499–9511.

[133] D.C. Clarke, M.D. Betterton, X. Liu, Systems theory of Smad signalling, 153 (2006).

[134] M.E. Bianchi, DAMPs, PAMPs and alarmins: all we need to know about danger., J Leukoc Biol. 81 (2007) 1–5.

[135] R. Medzhitov, C. Janeway, Innate Immunity, N Engl J Med. 343 (2000) 338–334.

[136] K.W. Moore, M.R. de Waal, R.L. Coffman, A. O'Garra, Interleukin-10 and the interleukin-10 receptor, Annu Rev Immunol. 19 (2001) 683–765.

[137] S.J. van Deventer, C.O. Elson, R.N. Fedorak, Multiple doses of intravenous interleukin 10 in steroid-refractory Crohn's disease. Crohn's Disease Study Group., Gastroenterology. 113 (1997) 383–389.

[138] E.J. Fernandez, E. Lolis, Structure, function, and inhibition of chemokines, Annu Rev Pharmacol Toxicol. 42 (2002) 469–499.

[139] C. Asselin-Paturel, A. Boonstra, M. Dalod, I. Durand, N. Yessaad, C. Dezutter-Dambuyant, et al., Mouse type I IFN-producing cells are immature APCs with plasmacytoid morphology, Nat Immunol. 2 (2001) 1144–1150.

[140] S. Pestka, C.D. Krause, M.R. Walter, Interferons, interferon-like cytokines, and their receptors, Immunol Rev. 202 (2004) 8–32.

[141] L. Berec, E. Angulo, F. Courchamp, Multiple Allee effects and population management, Trends Ecol Evol. 22 (2007) 185–191.

[142] B.G. Radden, J.H.P. Main, A.R. Ten Cate, Electron microscopic studies of organ cultures of tooth germs infected with polyoma virus, J Oral Pathol Med. 2 (1973) 272–279.

[143] A. Reynolds, J. Rubin, G. Clermont, J. Day, Y. Vodovotz, G. Bard Ermentrout, A reduced mathematical model of the acute inflammatory response: I. Derivation of model and analysis of anti-inflammation., J Theor Biol. 242 (2006) 220–36.

[144] C. Janeway, Immunobiology: the immune system in health and disease, 6th ed (2005).

[145] W.M. Yokoyama, Betting on NKT and NK cells, Immunity. 20 (2004) 363–365.

[146] D. Moskophidis, F. Lechner, H. Pircher, R.M. Zinkernagel, Virus persistence in acutely infected immunocompetent mice by exhaustion of antiviral cytotoxic effector T cells., Nature. 362 (1993) 758–761.

[147] S. Mankarious, M. Lee, S. Fischer, K. Pyun, H. Ochs, V. Oxelius, et al., The half-lives of IgG subclasses and specific antibodies in patients with primary immunodeficiency who are receiving intravenously administered immunoglobulin, J Lab Clin Med. 112 (1988) 634–640.

[148] T. Walzer, L. Chiossone, J. Chaix, A. Calver, C. Carozzo, L. Garrigue-Antar, et al., Natural killer cell trafficking in vivo requires a dedicated sphingosine 1-phosphate receptor, Nat Immunol. 8 (2007) 1337–1344.

[149] W.M. Yokoyama, S. Kim, A.R. French, The dynamic life of natural killer cells, Annu Rev Immunol. 22 (2004) 405–429.

[150] Y.J. Liu, Dendritic cell subsets and lineages, and their functions in innate and adaptive immunity., Cell. 106 (2001) 259–262.

[151] M. Merad, M.G. Manz, Dendritic cell homeostasis, Blood. 113 (2009) 3418–3427.

[152] M. Hellerstein, M.B. Hanley, D. Cesar, S. Siler, C. Papageorgopoulos, E. Wieder, et al., Directly measured kinetics of circulating T lymphocytes in normal and HIV-1-infected humans., Nat Med. 5 (1999) 83–89.

[153] G. Bocharov, A. Romanyukha, Mathematical model of antiviral immune response. III. Influenza A virus infection., J Theor Biol. 167 (1994) 323–60.

[154] G.P. Rangaiah, Multi-Objective Optimization Applications in Chemical Engineering, in: Multi-Objective Optim. Tech. Appl. Chem. Eng., 2008: pp. 1–51.

[155] H. Miao, J. a Hollenbaugh, M.S. Zand, J. Holden-Wiltse, T.R. Mosmann, A.S. Perelson, et al., Quantifying the early immune response and adaptive immune response kinetics in mice infected with influenza A virus., 2010.

[156] A.M. Smith, F.R. Adler, J.L. McAuley, R.N. Gutenkunst, R.M. Ribeiro, J.A. McCullers, et al., Effect of 1918 PB1-F2 expression on influenza A virus infection kinetics., PLoS Comput Biol. 7 (2011) e1001081.

[157] W. Pan, Z. Dong, F. Li, W. Meng, L. Feng, X. Niu, et al., Visualizing influenza virus infection in living mice., Nat Commun. 4 (2013) 2369.

[158] J.J. Sedmak, S.E. Grossberg, Interferon bioassay: reduction in yield of myxovirus neuraminidases, J Gen Virol. 21 (1973) 1–7.

[159] R. Gazit, R. Gruda, M. Elboim, T.I. Arnon, G. Katz, H. Achdout, et al., Lethal influenza infection in the absence of the natural killer cell receptor gene Ncr1., Nat Immunol. 7 (2006) 517–23.

[160] H.D. Neff-LaFord, B. a. Vorderstrasse, B.P. Lawrence, Fewer CTL, not enhanced NK cells, are sufficient for viral clearance from the lungs of immunocompromised mice, Cell Immunol. 226 (2003) 54–64.

[161] C. Sanders, P. Doherty, P. Thomas, Respiratory Epithelial Cells in Innate Immunity to Influenza Virus Infection, Cell Tissue Res. 343 (2011) 13–21.

[162] I. Cinel, S.M. Opal, Molecular biology of inflammation and sepsis: a primer., Crit Care Med. 37 (2009) 291–304.

[163] Centers for Disease Control and Prevention, Prevention and control of influenza: recommendations of the Advisory Committee on Immunization Practices (ACIP), MMWR. 55 (2006) 1–42.

[164] J. Plowden, M. Renshaw-Hoelscher, C. Engleman, J. Katz, S. Sambhara, Innate immunity in aging: impact on macrophage function., Aging Cell. 3 (2004) 161–7.

[165] U.N. Population Division, Department of Economic and Social Affairs, World Population Ageing: 1950 - 2050, 2001.

[166] C. Franceschi, M. Bonafè, S. Valensin, Human immunosenescence: the prevailing of innate immunity, the failing of clonotypic immunity, and the filling of immunological space., Vaccine. 18 (2000) 1717–20.

[167] L. Ginaldi, M.F. Loreto, M.P. Corsi, M. Modesti, M. De Martinis, Immunosenescence and infectious diseases., Microbes Infect. 3 (2001) 851–7.

[168] A.C. Shaw, D.R. Goldstein, R.R. Montgomery, Age-dependent dysregulation of innate immunity., Nat Rev Immunol. 13 (2013) 875–87.

[169] C. Franceschi, M. Bonafè, S. Valensin, F. Olivieri, M. De Luca, E. Ottaviani, et al., Inflamm-aging. An evolutionary perspective on immunosenescence., Ann N Y Acad Sci. 908 (2000) 244–254.

[170] D. Krone, C. L., Trzciński, K., Zborowski, T., Sanders, E. A. M., & Bogaert, Impaired Innate Mucosal Immunity in Aged Mice Permits Prolonged Streptococcus pneumoniae Colonization, Infect Immun. 81 (2013) 4615–4625.

[171] P. Mancuso, R. McNish, M. Peters-Golden, T. Brock, Evaluation of phagocytosis and arachidonate metabolism by alveolar macrophages and recruited neutrophils from F344xBN rats of different ages, Mech Ageing Dev. 122 (2001) 1899–1913.

[172] M. De La Fuente, Changes in the macrophage function with aging, Comp Biochem Physiol A. 81 (1985) 935–938.

[173] M. De La Fuente, S. Medina, M. Del Rio, M. Ferrandez, A. Hernanz, Effect of aging on the modulation of macrophage functions by neuropeptides, Life Sci. 67 (2000) 2125–2135.

[174] F.G. Ferguson, A. Wikby, P. Maxson, J. Olsson, B. Johansson, Immune parameters in a longitudinal study of a very old population of Swedish people: a comparison between survivors and nonsurvivor, J Gerontol Ser A Biol Sci Med Sci. 50 (1995) B378 –B382.

[175] K.C. Meyer, The role of immunity in susceptibility to respiratory infection in the aging lung., Respir Physiol. 128 (2001) 23–31.

[176] K. Raman, A.G. Bhat, N. Chandra, A systems perspective of host-pathogen interactions: predicting disease outcome in tuberculosis., Mol Biosyst. 6 (2010) 516–530.

[177] J. Thakar, M. Pilione, G. Kirimanjeswara, E.T. Harvill, R. Albert, Modeling systems-level regulation of host immune responses, PLoS Comput Biol. 3 (2007) 1022–1039.

[178] J. Thakar, A. Saadatpour-Moghaddam, E.T. Harvill, R. Albert, Constraint-based network model of pathogen-immune system interactions., J R Soc Interface. 6 (2009) 599–612.

[179] J. Thakar, A.K. Pathak, L. Murphy, R. Albert, I.M. Cattadori, Network model of immune responses reveals key effectors to single and co-infection dynamics by a respiratory bacterium and a gastrointestinal helminth, PLoS Comput Biol. 8 (2012).

[180] D.G. Brooks, M.J. Trifilo, K.H. Edelmann, L. Teyton, D.B. McGavern, M.B. a Oldstone, Interleukin-10 determines viral clearance or persistence in vivo., Nat Med. 12 (2006) 1301–1309.

[181] N. Atias, M. Gershenzon, K. Labazin, R. Sharan, Experimental design schemes for learning Boolean network models, Bioinformatics. 30 (2014) i445–i452.

[182] C.J. Langmead, S.K. Jha, Symbolic Approaches for Finding Control Strategies in Boolean Networks, J Bioinform Comput Biol. 15 (2009).

[183] I.E. Grossmann, L.T. Biegler, Part II. Future perspective on optimization, Comput Chem Eng. 28 (2004) 1193–1218.

[184] W.E. Hart, C. Laird, J.-P. Watson, D.L. Woodruff, Pyomo–optimization modeling in python, Springer Sci Bus Media. (2012).

[185] W.E. Hart, J.-P. Watson, D.L. Woodruff, Pyomo: modeling and solving mathematical programs in python, Math Program Comput. 3 (2011) 219–260.

[186] P. Trairatphisan, A. Mizera, J. Pang, A.A. Tantar, T. Sauter, optPBN: An optimisation toolbox for probabilistic Boolean networks, PLoS One. 9 (2014).

[187] S. Matsukura, F. Kokubu, H. Noda, H. Tokunaga, M. Adachi, Expression of IL-6, IL-8, and RANTES on human bronchial epithelial cells, NCI-H292, induced by influenza virus A, J Allergy Clin Immunol. 98 (1996) 1080–1087.

[188] A.O. Garra, P.L. Vieira, P. Vieira, A.E. Goldfeld, Review series IL-10 – producing and naturally occurring CD4 + Tregs : limiting collateral damage, J Clin Invest. 114 (2004) 1–7.

[189] A. Rizzitelli, R. Berthier, V. Collin, S.M. Candéias, P.N. Marche, T lymphocytes potentiate murine dendritic cells to produce IL-12., J Immunol. 169 (2002) 4237–4245.

[190] A.K. Wesa, A. Galy, IL-1 beta induces dendritic cells to produce IL-12., Int Immunol. 13 (2001) 1053–1061.

[191] D.A. Lebman, J.S. Edmiston, The role of TGF-beta in growth, differentiation, and maturation of B lymphocytes., Microbes Infect. 1 (1999) 1297–1304.

[192] J.J. Letterio, a B. Roberts, Regulation of immune responses by TGF-beta., Annu Rev Immunol. 16 (1998) 137–161.

[193] G. Jego, A.K. Palucka, J.-P. Blanck, C. Chalouni, V. Pascual, J. Banchereau, Plasmacytoid dendritic cells induce plasma cell differentiation through type I interferon and interleukin 6., Immunity. 19 (2003) 225–234.

[194] Y. Jing, E. Shaheen, R.R. Drake, N. Chen, S. Gravenstein, Y. Deng, Aging is associated with a numerical and functional decline in plasmacytoid dendritic cells, whereas myeloid dendritic cells are relatively unaltered in human peripheral blood, Hum Immunol. 70 (2009) 777–784.

[195] S.C. Castle, Clinical Relevance of Age-Related Immune Dysfunction, Clin Infect Dis. 31 (2000) 578–585.

[196] R. Solana, M.C. Alonso, J. Pena, Natural killer cells in healthy aging, Exp Gerontol. 34 (1999) 435–443.

[197] T. Ogawa, M. Kitagawa, K. Hirokawa, Age-related changes of human bone marrow: a histometric estimation of proliferative cells, apoptotic cells, T cells, B cells and macrophages, Mech Ageing Dev. 117 (2000) 57–68.

[198] I. Takahashi, E. Ohmoto, S. Aoyama, M. Takizawa, Y. Oda, K. Nonaka, et al., Monocyte chemiluminescence and macrophage precursors in the aged, Acta Med Okayama. 39 (1985) 447–451.

[199] C. Wang, K. Udupa, H. Xiao, D. Lipschitz, Effect of age on marrow macrophage number and function, Aging (Milano). 7 (1995) 379–384.

[200] Y. Higashimoto, Y. Fukuchi, Y. Shimada, K. Ishida, M. Ohata, T. Furuse, et al., The effects of aging on the function of alveolar macrophages in mice, Mech Ageing Dev. 69 (1993)

207–217.

[201] N.F. Spencer, R. a Daynes, IL-12 directly stimulates expression of IL-10 by CD5+ B cells and IL-6 by both CD5+ and CD5- B cells: possible involvement in age-associated cytokine dysregulation, Int Immunol. 9 (1997) 745–754.

[202] A. Agrawal, S. Agrawal, J.-N. Cao, H. Su, K. Osann, S. Gupta, Altered Innate Immune Functioning of Dendritic Cells in Elderly Humans: A Role of Phosphoinositide 3-Kinase-Signaling Pathway, J Immunol. 178 (2007) 6912–6922.

[203] S. Della Bella, L. Bierti, P. Presicce, R. Arienti, M. Valenti, M. Saresella, et al., Peripheral blood dendritic cells and monocytes are differently regulated in the elderly, Clin Immunol. 122 (2007) 220–228.

[204] D.A. Hume, Macrophages as APC and the Dendritic Cell Myth, J Immunol. 181 (2008) 5829–5835.

[205] L. Ginaldi, M. De Martinis, A. D'Ostilio, L. Marini, M.F. Loreto, D. Quaglino, The Immune System in the Elderly, Immunol Res. 20 (1999) 117–126.

[206] D.M. Morens, J.K. Taubenberger, A.S. Fauci, Predominant role of bacterial pneumonia as a cause of death in pandemic influenza: implications for pandemic influenza preparedness., J Infect Dis. 198 (2008) 962–70.

[207] Y.-W. Chien, K.P. Klugman, D.M. Morens, Bacterial pathogens and death during the 1918 influenza pandemic., N Engl J Med. 361 (2009) 2582–3.

[208] K.P. Klugman, Y.-W. Chien, S. a Madhi, Pneumococcal pneumonia and influenza: a deadly combination., Vaccine. 27 Suppl 3 (2009) C9–C14.

[209] J.F. Brundage, G.D. Shanks, Deaths from bacterial pneumonia during 1918-19 influenza pandemic., Emerg Infect Dis. 14 (2008) 1193–9.

[210] L. Finelli, A. Fiore, R. Dhara, L. Brammer, D.K. Shay, L. Kamimoto, et al., Influenza-associated pediatric mortality in the United States: increase of Staphylococcus aureus coinfection., Pediatrics. 122 (2008) 805–11.

[211] P. James R. Gill , MD, Zong-Mei Sheng , MD, PhD, Susan F. Ely , MD, MPHTM, Donald G. Guinee Jr , MD, Mary B. Beasley , MD, James Suh , MD, Charuhas Deshpande , MD, Daniel J. Mollura , MD, David M. Morens , MD, Mike Bray , MD, William D. Travis , MD, and Jeff, Pulmonary Pathologic Findings of Fatal 2009 Pandemic Influenza A/H1N1 Viral Infections, Arch Pathol Lab Med. 134 (2010).

[212] L. Simonsen, K. Fukuda, L.B. Schonberger, N.J. Cox, The impact of influenza epidemics on hospitalizations., J Infect Dis. 181 (2000) 831–7.

[213] L. Simonsen, M.J. Clarke, G.D. Williamson, D.F. Stroup, N.H. Arden, L.B. Schonberger, The impact of influenza epidemics on mortality: introducing a severity index., Am J Public Health. 87 (1997) 1944–50.

[214] C. Small, S. Mccormick, N. Gill, K. Kugathasan, M. Santosuosso, D.E. Heinrichs, et al., NK cells play a critical protective role in host defense against acute extracellular Staphylococcus aureus bacterial infection in the lung, J Immunol. 180 (2013) 5558–68.

[215] K. Sun, D.W. Metzger, Inhibition of pulmonary antibacterial defense by interferon-gamma during recovery from influenza infection., Nat Med. 14 (2008) 558–64.

[216] L.N. Lee, P. Dias, D. Han, S. Yoon, A. Shea, V. Zakharov, et al., A mouse model of lethal synergism between influenza virus and Haemophilus influenzae., Am J Pathol. 176 (2010) 800–11.

[217] J.A. McCullers, J.E. Rehg, Lethal synergism between influenza virus and Streptococcus pneumoniae: characterization of a mouse model and the role of platelet-activating factor receptor., J Infect Dis. 186 (2002) 341–50.

[218] J.A. McCullers, K.C. Bartmess, Role of neuraminidase in lethal synergism between influenza virus and Streptococcus pneumoniae., J Infect Dis. 187 (2003) 1000–9.

[219] M.J. Tuvim, B.E. Gilbert, B.F. Dickey, S.E. Evans, Synergistic TLR2/6 and TLR9 activation protects mice against lethal influenza pneumonia., PLoS One. 7 (2012) e30596.

[220] A.R. Iverson, K.L. Boyd, J.L. McAuley, L.R. Plano, M.E. Hart, J. a McCullers, Influenza virus primes mice for pneumonia from Staphylococcus aureus., J Infect Dis. 203 (2011) 880–8.

[221] S.A. Khader, S.L. Gaffen, J.K. Kolls, Th17 cells at the crossroads of innate and adaptive immunity against infectious diseases at the mucosa., Mucosal Immunol. 2 (2009) 403–11.

[222] A. Kudva, E. V Scheller, K.M. Robinson, C.R. Crowe, S.M. Choi, S.R. Slight, et al., Influenza A inhibits Th17-mediated host defense against bacterial pneumonia in mice., J Immunol. 186 (2011) 1666–74.

[223] K.F. van der Sluijs, L.J.R. van Elden, M. Nijhuis, R. Schuurman, J.M. Pater, S. Florquin, et al., IL-10 is an important mediator of the enhanced susceptibility to pneumococcal pneumonia after influenza infection., J Immunol. 172 (2004) 7603–9.

[224] A.M. LeVine, V. Koeningsknecht, J.M. Stark, Decreased pulmonary clearance of S. pneumoniae following influenza A infection in mice., J Virol Methods. 94 (2001) 173–86.

[225] M. Seki, K. Yanagihara, Y. Higashiyama, Y. Fukuda, Y. Kaneko, H. Ohno, et al., Immunokinetics in severe pneumonia due to influenza virus and bacteria coinfection in mice, Eur Respir J. 24 (2004) 143–149.

[226] A. Peck, E.D. Mellins, Precarious balance: Th17 cells in host defense., Infect Immun. 78 (2010) 32–8.

[227] A.M. Smith, F.R. Adler, R.M. Ribeiro, R.N. Gutenkunst, J.L. McAuley, J. a McCullers, et al., Kinetics of coinfection with influenza A virus and Streptococcus pneumoniae., PLoS Pathog. 9 (2013) e1003238.

[228] V.T. Peltola, K.G. Murti, J. a McCullers, Influenza virus neuraminidase contributes to secondary bacterial pneumonia., J Infect Dis. 192 (2005) 249–57.

[229] J.L. McAuley, F. Hornung, K.L. Boyd, A.M. Smith, R. McKeon, J. Bennink, et al., Expression of the 1918 influenza A virus PB1-F2 enhances the pathogenesis of viral and secondary bacterial pneumonia., Cell Host Microbe. 2 (2007) 240–9.

[230] J.A. Smith, Neutrophils, host defense, and inflammation: a double-edged sword., J Leukoc Biol. 56 (1994) 672–686.

[231] Y. Hashimoto, T. Moki, T. Takizawa, A. Shiratsuchi, Y. Nakanishi, Evidence for phagocytosis of influenza virus-infected, apoptotic cells by neutrophils and macrophages in mice., J Immunol. 178 (2007) 2448–2457.

[232] M. Population, B.L. Bronchoalveolar, The alveolar macrophage, 60 (1986) 353–369.

[233] J. Day, A. Friedman, L.S. Schlesinger, Modeling the immune rheostat of macrophages in the lung in response to infection., Proc Natl Acad Sci U S A. 106 (2009) 11246–51.

[234] F.R. Toapanta, T.M. Ross, Impaired immune responses in the lungs of aged mice following influenza infection., Respir Res. 10 (2009) 112–131.